Tailored synthesis of ultra-small nanoparticles for biomedical applications

A thesis submitted for the degree of Materials Science

Doctor of Philosophy



Dominique Piché

Hertford College, University of Oxford

April 4, 2019

Dedicated to my dad

Wayne Roland Piché

16/11/1946 - 28/07/2003

Abstract

Accurate and early diagnosis of disease is a critical worldwide challenge in healthcare. The emergence of nanomaterials has opened up the possibility of engineering new and improved diagnostic and therapeutic tools which can interact on a sub-cellular level. Ultra-small ($<$ 3 nm) metal-oxide nanoparticles (NPs) have been highlighted as particularly strong candidates for enhancing positive (T_1) image contrast in magnetic resonance imaging (MRI), an important and powerful diagnostic imaging tool. Current T_1 gadolinium contrast agents are limited by long-term toxicity issues, and cannot be given to patients with kidney disease, which represents 16% of the UK population. Metal-oxide NPs, such as iron oxide, are more biocompatible, and below 3 nm, they present the ideal magnetic properties to enhance T_1 image contrast, offering a potential alternative to current gadolinium-based agents.

However, several roadblocks must be overcome to reach clinical application of ultra-small NPs. The primary challenge lies in the development of suitable synthesis methods that offer the exquisite control over particle size and composition that is required to produce ultra-small NPs. Furthermore, their properties need fine-tuning in order to achieve T_1-weighted contrast that is more comparable with gadolinium. An additional important consideration is that the NPs are designed with core and surface features that enable excellent stability, performance and biocompatibility *in vivo*.

This thesis details the synthesis, characterisation, and functionalisation of ultra-small iron oxide and cobalt ferrite NPs for application as T_1 MRI contrast agents. The main findings of this thesis concern the investigation of 2.4 nm cobalt ferrite NPs for T_1 MRI. Cobalt ferrite NPs may be excellent candidates for T_1-weighted contrast as they offer beneficial properties in comparison to iron oxide, such as lower magnetisation and greater chemical stability.

Size-controlled synthesis of ultra-small NPs was addressed with a simple and fast thermal decomposition approach using oleylamine and acetylacetonate precursors. Sub-nm size control in the range of 2.4-5 nm was achieved by tailoring the oleylamine-to-precursor ratio. Annular dark-field scanning transmission electron microscopy revealed highly-crystalline cubic spinel particles 2.4 nm in size with atomic-resolution. Both iron oxide and cobalt ferrite NPs displayed size and coating-dependent superparamagnetic properties.

In consideration for *in vivo* applications, two strategies were explored to obtain water-dispersible NPs. A novel phase transfer method with bovine serum albumin proved unsuitable as the NPs quickly flocculated. Ligand exchange with dimercaptosuccinic acid rendered the particles stable in physiological conditions with an average hydrodynamic diameter of $\sim$12 nm. It was found that dialysing the particles prior to ligand exchange to remove excess oleylamine and alkalising the particles after ligand exchange were key steps to obtain reproducible results.

The potential toxicity of the NPs was investigated with cytotoxicity and oxidative stress assays comparing the effect of particle size and metal composition. Neither iron oxide nor cobalt ferrite NPs of any size displayed cytotoxicity towards HepG2 liver cells. However, both NP types produced reactive oxygen species (ROS), and it was found that cobalt ferrite produced significantly more. Serendipitously, ROS generation was effectively alleviated through conjugation to a bile acid derivative, cholic acid. Conjugation was achieved by EDC-NHS coupling, following which the ROS levels reduced by 62% and 67% for iron oxide and cobalt ferrite NPs respectively. This new insight reveals the potential of cholic acid to mitigate ROS generation, a common issue encountered in metal-oxide NPs. Furthermore, the cholic acid coating could promote active liver-targeting *in vivo*.

Finally, the MRI application of DMSA-coated iron oxide and cobalt ferrite NPs was assessed with phantom studies using 3.0 T and 9.4 T scanners. Cobalt ferrite NPs were found to have a low r_2/r_1 ratio suitable for a T_1 contrast agent. The work described in this thesis demonstrates the potential of ultra-small ferrite NPs towards application as liver-targeted T_1 MRI contrast agents. The synthesis and functionalisation methods described may open up the possibility of applying ultra-small ferrite NPs in other exciting areas of biomedicine.

Acknowledgements

My DPhil journey has brought with it the pleasure of meeting and working with many extraordinary people, all of whom have contributed towards making this thesis possible. First, I would like to thank my supervisor, Professor Nicole Grobert, for accepting me into her lab with open arms, for giving me the freedom to explore my own research direction and facilitating the process, and for her support and encouragement through the tough and the good times.

The Nanomaterials By Design lab felt like a second home, thanks to the warmth, laughter and all-round great atmosphere the group created. I am so grateful to the nano-family, Albert, Pablo, Jesus, Pierre, Ruth, Koen, and Santamon for the lunchtime laughter, the mug-pong tournaments, and for helping and inspiring me scientifically. Thank you all for making the lab a place I looked forward to going to everyday. A special shout out goes to the 'As-in-NBD' team, for so many hilarious memories. I'd also like to thank Frank for introducing me to the wonderful world of nanoparticle synthesis (and health and safety!).

An important aspect of my DPhil was the chance to collaborate with, visit, and learn from other research groups. In this regard, I would like to express my deep gratitude towards Dr. Isabella Taverano, Dr. Jana Fleddermann, and Dr. Annette Krageloh from the Nano Cell Interaction group at the INM for their valuable scientific contribution and support. I would like to extend my thanks to other members of the INM, to Dr. Marcus Koch for his support with TEM and thought-provoking scientific discussions, to the INM technical team for their assistance with many measurements, and to Günther and Juraj for welcoming me into a new lab environment.

I would also like to thank Professor Toru Maekawa sensei from the BioNano Electronics Research Centre for his collaboration and support, and for the incredi-

ble opportunity to visit Japan. I'd like to extend my thanks to his team members, Tomofumi Ukai san and Yutaka Nagaoka san, for their assistance with magnetic measurements. I'd further like to thank several talented microscopists in the Materials department at Oxford, Dr. Aakash Varambhia, Dr. Juan Lozano and Professor Peter Nellist, for assisting with the characterisation of my nanoparticles.

The MRI experiments in my thesis were both exciting and challenging, and for that I'd like to thank Dr. Mahon Maguire for helping me to acquire and understand the data I needed, Dr. Sebastian Riegler and Dr. Daniel Papp for their help with the 3.0 T MRI experiment, and my new friends Professor Evelio González Dalmau, Armando Hernández Rodríguez and Israel Reyes Molina from the Cuban Neuroscience Centre for their help with the data analysis. I'd also like to warmly acknowledge Professor Sonia Conterra, for inspiring me with nano-biomedicine, and for her encouragement and advice during a difficult time. Furthermore, this thesis would not have been possible without the generous financial support of the Engineering & Physical Sciences Research Council, Hertford College and Santander Academic Award and Scatcherd European scholarships, for which I am very appreciative.

Oxford has provided me with the good fortune of making many friendships which I will treasure beyond my PhD years. I'd like to thank my CocoHut roomie Gaby, for her support, kindness, and inspirational positivity. I'm also extremely thankful to Ilija and Martin, for many good times as 'The Endohedral Starfish', and for sharing their intelligence and wit (either in the form of scientific knowledge, or pub quizzes). I'd also like to thank Lea for brightening up Begbroke, and supporting me each work day, be it with coffee, or entertaining coffee breaks.

I'm also extremely grateful for my wonderful network of friends beyond Oxford for their support, guidance and encouragement throughout my PhD. I'd like to especially thank Nik for his support and encouragement during the early years, and for the many good times (and hard lessons) that came from our time with UPROSA. I'd like to give a big thanks to Lukas for consistently providing me with sound advice, encouragement and tears of laughter. I further give many thanks to Jamie Walters and Professor Lisa Hall from the University of Cambridge, for providing me with the foundation in science, (and the foot in the door), that I needed to be able to complete this PhD. I'm of course forever grateful to my 'Be Fri' Vicky, for always

lending her support and kindness, and for lifting my spirits whenever I needed it. A special thanks also goes to Tony for his unwavering friendship and belief in me. And Val, what can I said about Val, you've kept me going through the difficult times, calming me down when I needed it most, thank you for always being there for me. Not forgetting some additional thesis helpers, I'm thankful for Percy and Buddy, for acting as comforting little footrests and keeping me company during the lonely writing hours.

My biggest thanks must go to mi Pistachio, Pablo, for making sure I always had the biggest smile on my face, for his stellar scientific advice and input, and for supporting me in every way possible, particularly through my writing journey. Finally, I'd like to thank my parents, for having led by example with their hard work and strength, and for providing me with the life lessons, skills, and opportunities I would need to reach this point. Thank you all!

Declaration

This thesis is submitted for the degree of Doctor of Philosophy in Materials Science at the University of Oxford. No part of this thesis has been accepted or is currently being submitted for any degree, diploma, certificate or other qualification in this University or elsewhere. This thesis is wholly my own work, except where indicated.

Publication

The following published journal article relates to the work conducted in this thesis:

Chapters 2,3,4,5,6

Dominique Piché, Isabella Tavernaro, Jana Fleddermann, Juan G. Lozano, Aakash Varambhia, Mahon L. Maguire, Marcus Koch, Tomofumi Ukai, Armando J. Hernaández Rodríguez, Lewys Jones, Frank Dillon, Israel Reyes Molina, Mai Mitzutani, Evelio R. González Dalmau, Toru Maekawa, Peter D. Nellist, Annette Kraegeloh, and Nicole Grobert. *Targeted T_1 Magnetic Resonance Imaging Contrast Enhancement with Extraordinarily Small $CoFe_2O_4$ Nanoparticles.*
ACS Applied Materials & Interfaces, 11(7): 6724–40, February 2019.

Contents

Abstract i

Acknowledgements iii

Declaration vi

Publication vii

1 Introduction: Magnetic nanoparticles in biomedicine 1

1.1 Metal-oxide nanoparticles: why iron oxide and cobalt ferrite 2

1.2 The effect of nanoparticle size 3

1.3 Nanoparticles for MRI: The potential of 'ultra-small' 5

1.4 Other considerations in the design of NPs for *in vivo* applications . . 8

1.4.1 Particle stability 8

1.4.2 Nanotoxicity 8

1.5 How to synthesise ultra-small nanoparticles 9

1.6 Aim of thesis 11

2 Size-controlled synthesis of ultra-small MFe_2O_4@OLA nanoparticles 13

2.1 Size-controlled nanoparticle synthesis by thermal decomposition . . . 13

2.1.1 Introduction to nanoparticle synthesis 13

2.1.2 Nanoparticle nucleation and growth mechanisms 14

2.1.3 Important parameters for thermal decomposition 21

2.1.4 Thermal decomposition to synthesise metal-oxide and ultra-small NPs 23

2.1.5 The role of oleylamine in nanoparticle synthesis 26

2.2 Materials and methods 28
2.2.1 Materials 28
2.2.2 Nanoparticle synthesis method 28
2.3 Characterisation 29
2.3.1 Transmission electron microscopy 29
2.4 Results and discussion 31
2.4.1 Size-controlled synthesis of iron oxide NPs with oleylamine . . 31
2.4.2 Effect of other synthesis parameters on iron oxide NP size . . 36
2.4.3 Size-controlled synthesis of cobalt ferrite NPs with oleylamine 41
2.4.4 Synthesis of cobalt oxide NPs with oleylamine 47
2.5 Conclusion 49

3 Properties of ultra-small MFe_2O_4@OLA nanoparticles 51
3.1 Introduction to iron oxide and spinel ferrites 51
3.1.1 Iron oxides: Structure and properties 51
3.1.2 Spinel ferrites: Structure and properties 53
3.1.3 Nanoscale magnetic properties 56
3.2 Characterisation methods to analyse MFe_2O_4 NPs 60
3.2.1 Scanning transmission electron microscopy 61
3.2.2 Superconducting quantum interference device measurements of magnetic properties 63
3.2.3 X-ray diffraction 64
3.3 Results and discussion 65
3.3.1 Crystal structure determination of synthesised USNPs 65
3.3.2 Composition and oxidation state of synthesised USNPs 69
3.3.3 Magnetic properties of synthesised USNPs 71
3.4 Conclusion 75

4 Phase transfer and stability studies for water-dispersible ultra-small ferrite NPs 76
4.1 Introduction 77
4.1.1 The effect of NP characteristics on their *in vivo* behaviour . . 79
4.1.2 Ligand exchange with dimercaptosuccinic acid 82

4.1.3 Direct phase transfer with bovine serum albumin 82
4.2 Materials and methods 83
4.2.1 Materials 83
4.2.2 Nanoparticle preparation (dialysis) for phase exchange 84
4.2.3 DMSA ligand exchange method 84
4.2.4 BSA phase transfer method 85
4.2.5 Characterisation 85
4.2.6 Stability tests 89
4.3 Results and discussion 90
4.3.1 Direct phase transfer with BSA 90
4.3.2 Ligand exchange with DMSA 100
4.3.3 Conclusions 112

5 Cytotoxicity and oxidative stress of ultra-small MFe_2O_4@DMSA and MFe_2O_4@BSA NPs 114

5.1 Introduction to measuring nanotoxicity 115
5.1.1 Toxicity of ferrite NPs: oxidative stress and size-dependence . 116
5.2 Materials and methods 117
5.2.1 Chemicals 117
5.2.2 Nanoparticle preparation 117
5.2.3 HepG2 cell culture 118
5.2.4 Cytotoxicity assay method 118
5.2.5 Oxidative stress assay method 119
5.2.6 Inductively coupled plasma optical emission spectrometry . . . 119
5.3 Results and discussion 121
5.3.1 Determination of NP concentrations 121
5.3.2 Evaluation of potential NP assay interference 122
5.3.3 Cytotoxicity of ultra-small NPs towards HepG2 cells 127
5.3.4 Oxidative stress of ultra-small NPs towards HepG2 cells . . . 128
5.4 Discussion 129
5.5 Conclusions 132

6 Magnetic resonance imaging and bile-acid functionalisation studies of ultra-small MFe_2O_4@DMSA NPs towards liver-targeted MRI 134

6.1 MRI phantom testing of MFe_2O_4@DMSA NPs 135

6.1.1 Introduction to MRI 135

6.1.2 MRI contrast agents: Gadolinium-based and magnetic NPs . . 137

6.1.3 MRI phantom methods 142

6.1.4 Results and discussion 145

6.1.5 Conclusions 157

6.2 Bile-acid functionalisation of MFe_2O_4@DMSA NPs 159

6.2.1 Introduction 159

6.2.2 Materials and methods 162

6.2.3 Results and discussion 166

6.2.4 Conclusions 174

7 Summary and Outlook 176

Bibliography 181

Appendix A List of Abbreviations 203

Appendix B Additional results 207

Chapter 1

Introduction: Magnetic nanoparticles in biomedicine

Nanoparticles (NPs) are a class of material which have led to important technological advances in recent years. Frequently defined as particles 1-100 nm in size, NPs are of significant interest from both the fundamental science and applied technology perspective. The interest in NPs arises from their small size and enhanced surface-to-volume ratio in comparison to their bulk counterparts. This leads to two beneficial phenomena: an increase in their reactivity, and/or, a size-dependent change in their properties.[1]

One application in which NPs can make a significant impact is biomedicine, where NPs can overcome some of the limitations of current therapeutic and diagnostic agents.[2] Below 100 nm, they are within the size range of biological entities such as cells (10–100 µm), viruses (20–450 nm) and proteins (5–50 nm).[3] As such, they are able to penetrate or interact with biological components. Their large surface-to-volume ratio presents a considerable amount of surface available for interactions *in vitro* or *in vivo*. Functionalisation of their surface with targeting molecules that seek specific interaction with a biological entity of interest is highly beneficial for improving the treatment and diagnosis of diseases. NPs have already demonstrated utility in biosensing,[4] drug delivery,[5] cell tracking,[6] magnetic hyperthermia,[7] and biomedical imaging.[8]

1.1 Metal-oxide nanoparticles: why iron oxide and cobalt ferrite

One important class of NPs which have been particularly useful in biomedicine are magnetic NPs, typically metallic or metal-oxide of which iron oxide is the most popular.[9] Due to the wide scope of literature, this introduction focuses on the NPs of interest in this work: magnetic iron oxide (γ-Fe_2O_3, Fe_3O_4) and cobalt ferrite ($CoFe_2O_4$) NPs. Other metal-oxide NPs such as ZnO and TiO_2 and their clinical applications are described elsewhere.[10] Magnetic metal-oxide NPs are a popular choice due to their chemical versatility, biocompatibility and intriguing size-dependent physical properties.[11,12] The main property that makes iron oxide and cobalt ferrite NPs promising biomedical candidates is their unique nanoscale magnetism. Below a critical size where the NPs are composed of a single magnetic domain (approximately 25 nm for magnetite[13] and 10 nm for cobalt ferrite[14]), the NPs exhibit superparamagnetism. Iron oxide NPs within this size range are typically referred to as SPIONs (superparamagnetic iron oxide nanoparticles). In the presence of an external magnetic field, the magnetic moments of the particles tend to align along the field leading to a net magnetisation, however their magnetisation is zero in the absence of a field. Thus their magnetism is switchable, a property which enables their manipulation *in vivo*.[15] Superparamagnetism and spinel ferrites are discussed in depth in chapter 3 of this thesis.

The magnetic properties of metal-oxide NPs is being explored in research to address some of the key challenges facing the treatment and diagnosis of disease. Such challenges include improving the efficacy of drug delivery,[5] developing more targeted cancer treatments to avoid damage to healthy disease,[15] improving the resolution of imaging techniques to enable earlier diagnosis of diseases,[16] and improving the sensitivity of biosensors to better detect the presence of diseases and pathogens.[4] Chertok et al. demonstrated targeted delivery of iron oxide NPs to brain tumours in rats through magnetic guiding.[17] Thus if conjugated to drugs, the NPs could be effective delivery vehicles. SPIONs conjugated with targeting molecules can also be used to detect DNA, tumour cells, proteins and pathogens with extremely high-sensitivity in a technique called diagnostic magnetic resonance (DMR).[4] The detection scheme

is based on the ability of the magnetic moment of SPIONS to alter the relaxation behaviour of nearby water molecules, causing a change in the magnetic resonance signal and thus indicating binding events. Analogously, the ability of SPIONs to alter the relaxation behaviour of protons has proved highly useful in MRI, where SPIONs >5 nm act as effective contrast agents to improve negative image contrast, aiding diagnosis.[18]

The magnetic properties of iron-oxides with cubic spinel crystal structures can be fine-tuned for specific applications by substituting ferrous ions with other metal ions following the formula MFe_2O_4 (where M = Fe, Co, Mn, Zn etc.). Substitution with cobalt ions (Co^{2+}) changes both the magnetic saturation and anisotropy of the NPs. In comparison to magnetite (Fe_3O_4), bulk $CoFe_2O_4$ possesses 90% saturation magnetization (M_s).[19] The same was observed at the nanoscale, where 6 nm Fe_3O_4 and $CoFe_2O_4$ nanoparticles had an M_s of 55 and 50 emu g^{-1} respectively.[20] The Co^{2+} ions also increase the magnetic anisotropy, which has proved useful for magnetic hyperthermia. In an applied magnetic field, their superparamagnetism and large magnetic anisotropy is effective for releasing heat energy, destroying cells in a localised region.[21] Cobalt ferrite NPs have also recently demonstrated high potential for MRI with > 5 nm NPs acting as negative contrast agents.[22] Furthermore, $CoFe_2O_4$ is more resistant to oxidation,[23] which can affect the magnetic properties,[24] as well as toxicity.[25] Asides from the metal composition of the NP core, an extremely important parameter for MRI and other biomedical applications is the NP size.

1.2 The effect of nanoparticle size

The size of a NP has a drastic effect on its properties and behaviour, as evidenced by the emergence of superparamagnetism below a critical size range. However, the size of a NP can also strongly affect how and where it interacts with biological components of the body, influencing circulation time, toxicity, cellular uptake, and clearance route.[26] This begs the question: *is there an ideal NP size?* The answer is dependent upon the application of interest. For applications such as magnetic particle imaging (MPI) and magnetic hyperthermia, which harness the superparamagnetic 'switching' behaviour of NPs to produce a signal or to release energy,

the largest magnetic moment possible whilst still maintaining superparamagnetic properties, is desired.[27,28] For drug delivery applications, NPs which are too small are unfavourable as they may be quickly eliminated renally and thus reduce the amount of drug absorbed in the system.[5] Conversely, NPs that are too large may be recognised and removed from circulation by the immune system before reaching the target destination.[29] Therefore a size range of 5-50 nm is suggested as optimal.[5] Figure 1.1 outlines the size-dependent applications of ferrite NPs.

In MRI, iron oxide NPs were found to have different effects on image contrast depending on their core size, which gave rise to the interest in ultra-small NPs (USNPs) in this study. Below 3 nm, NPs can increase positive, as opposed to negative, image contrast.[30] This phenomenon had not been explored for ultra-small cobalt ferrite NPs prior to this work. The next section is focused on MRI and the benefits of USNPs.

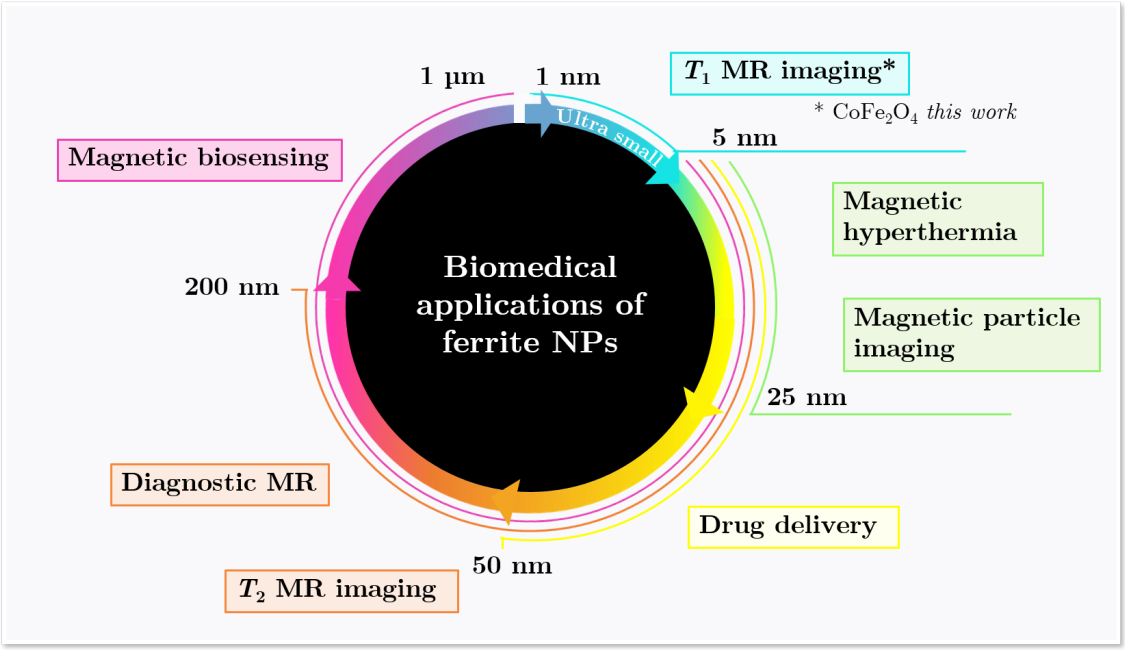


Figure 1.1: Overview of the main biomedical applications of spinel ferrite NPs according to their core size. Information sources:[5,21,31–34]

1.3 Nanoparticles for MRI: The potential of 'ultra-small'

MRI is a powerful imaging tool that utilises the water content of the human body and large magnetic fields to generate a contrast-based internal image to diagnose injury or disease. In order to improve image contrast and thus the accuracy of diagnosis, contrast agents are administered.[18] Contrast agents serve to either increase the positive (white) contrast, known as T_1, or the negative (black) contrast, known as T_2. Chapter 6 covers the fundamentals of MRI and contrast agents in greater detail. SPIONs have demonstrated excellent utility as T_2 MRI contrast agents, and some received FDA approval for clinical use.[35] Their large magnetic moment was effective for shortening the T_2 relaxation times of nearby water protons, creating greater contrast between surrounding tissue.[18] Iron oxide NPs 5-200 nm in size typically accumulate in the liver following intravenous administration,[29] thus they were particularly suitable for liver T_2 MRI.

Despite their strong promise, SPIONs had limited commercial success in clinical practice. Their large magnetic moment was prone to inducing susceptibility artefacts and the diagnostic value of increasing negative contrast as opposed to positive was questionable.[36] Positive (T_1) contrast agents, which are typically gadolinium-based (Gd-agents), are preferred for non-specific and liver MRI and remain commercially more successful.[37] Gd effectively shortens T_1 relaxation through dipole interactions afforded by its 7 unpaired electrons. Furthermore, Gd-agents have long circulation times which is very useful for imaging blood vessels.[38] However, Gd-agents suffer from a significant drawback which is the inherent toxicity of Gd ions. In 2018, the UK government suspended the licenses of Omniscan®and Magnevist®, two main commercial Gd-based contrast agents, following the discovery of Gd deposits in the brains of past MRI patients.[39,40]

With growing concerns regarding the use of Gd, and a general desire to improve image resolution and enable more targeted approaches, alternative T_1 contrast agents are highly sought after. In 2011, ultra-small iron-oxide NPs were highlighted as a potential more biocompatible approach.[41] Kim et al. showed that T_1-weighted contrast could be achieved with iron-oxide NPs by reduction of their size below 3

nm.[30] In a size-dependent study with 1.5, 2.2, 3.0 and 12 nm maghemite NPs, they found the magnetic core of NPs smaller than 3 nm was greatly reduced as they were composed mostly of surface atoms, which are magnetically disordered due to spin canting (figure 1.2). This led to a decrease in T_2 effect, whilst the five unpaired electrons of Fe^{3+} provided effective shortening of T_1. Their 3 nm NPs proved useful for high-resolution MR angiography in mice, and no toxic effects were observed. Similar studies have since emerged that echo this finding.[42–44]

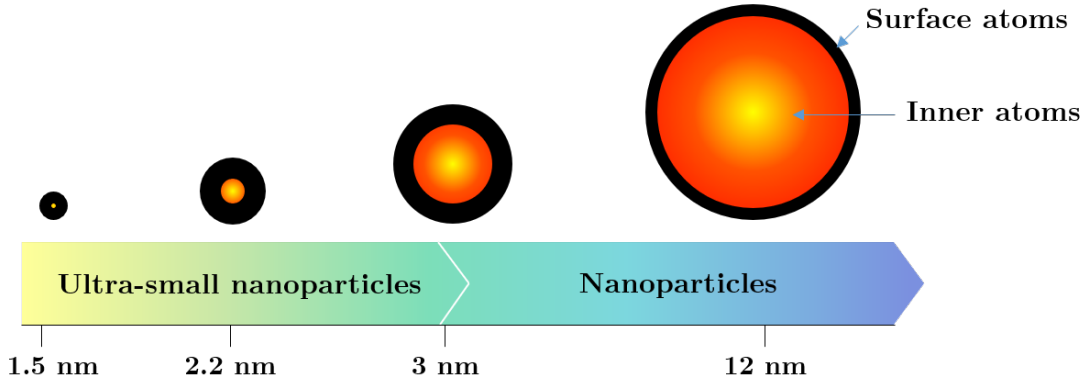


Figure 1.2: Schematic representing the ratio of surface to core atoms in various NP sizes. As the size decreases to the ultra-small range, the particles become increasingly composed of surface atoms which are magnetically disordered, thus decreasing the overall magnetisation of the NP. Figure adapted from ref[30]

Ultra-small NPs, also distinguished as 'extremely-small',[30] 'exceedingly-small'[42] and 'extraordinarily-small',[45] offer additional advantages for *in vivo* applications in comparison to larger NPs:

· They can be eliminated renally, thus reducing the risk of toxic effects that arise from accumulation in the body.[42]

· They offer an even larger surface-to-volume ratio for greater surface interactions.

· Their small size enables good tissue penetration.[26]

For clarity purposes, NPs $\leq$3 nm will be referred to herein as USNPs and only metal-oxide NPs will be discussed. A comprehensive review on USNPs of other materials can be found elsewhere.[26] The large surface area of USNPs combined with the flexible surface chemistry of ferrite NPs presents an opportunity to create ultra-small targeted probes for more specific *in vivo* applications such as liver-targeted

MRI. Although larger SPIONs are passively liver-targeting due to their uptake by the reticuloendothelial system, Gd-based liver-specific agents demonstrated better practicality and diagnostic performance for liver cancer and are currently preferred by clinicians.[37] For liver-MRI, T_1-weighted contrast agents are beneficial for detecting metastases and liver lesions.[46]

USNPs may solve the issue of preferring *T_1* contrast agents for imaging liver lesions, however their small size means they are within the threshold for renal clearance (hydrodynamic diameters < 15 nm) and thus may not reach the liver.[29] For liver targeted MRI, conjugation to a hepatospecific functional group for active-targeting could thus be beneficial. Bile acids are amphipathic molecules with a hydrophilic chain and a functional head group which are up-taken into the liver via the hepatic pathway.[47] As such they have been proposed as ideal surface modifiers for liver-targeted *in vivo* applications. Kramer et al. effectively demonstrated the use of bile acids as 'Trojan horses' to deliver drugs specifically into the liver.[48] Similarly, Zhang et al. found that functionalising chitosan nanoparticles with cholic acid, a primary bile acid, remarkably improved the efficacy of insulin delivery, owing to cholic acid's liver-targeting properties.[49] Others have functionalised Gd-chelates with cholic acid towards liver-targeted MRI[50].[51] Bile acid functionalised ferrite NPs could thus be promising candidates for liver-targeted MRI and are explored in chapter 6 of this thesis.

For MRI contrast enhancement, USNPs offer the combined advantages of shortening T_1, long blood circulation times, efficient clearance from the body, a large surface area which can be conjugated to targeting ligands, and potentially minimised toxicity. However to date, only a handful of studies have been conducted and they are yet to be as efficient as Gd-based agents in enhancing T_1 contrast, prompting the need for their fine-tuning and further development. In addition, no liver-targeting *T_1* ferrite NPs have been developed yet. To optimise the performance of USNPs in T_1 MRI, additional factors which influence their behaviour *in vivo* such as their stability and toxicity must be considered. The next section discusses these points and considers how one can optimise a NP for a specific biomedical application such as T_1 MRI. The pharmacokinetic behaviour of NPs *in vivo* are discussed in greater detail in chapter 4.

1.4 Other considerations in the design of NPs for *in vivo* applications

1.4.1 Particle stability

A key requirement for the good clinical performance of NPs is their colloidal stability in aqueous and physiological media, both in terms of retaining stability *in vivo*, and during long-term storage. The stability of NPs in a dispersion is influenced by their ability to repel one another in a variety of conditions such as high concentration, pH, temperature etc. NPs may repel one another by steric repulsion, or electrostatically by surface charges, both of which are largely governed by the surface ligand.[52] The surface ligand is also at the forefront of interaction with biological components *in vivo*, and thus strongly influences its circulation, distribution and elimination. NPs which aggregate *in vivo* will be quickly recognised by the immune system and cleared from distribution, leading to a short circulation time.[29] The surface ligands on USNPs have an additional strong influence on their magnetic properties. Depending on their bonding mechanism and chemical properties, the ligands can increase or decrease the magnetisation saturation of the NPs by varying the degree of spin canting in the surface layer.[20] Thus for T_1 MRI applications, the surface ligand is extremely important. Chapter 4 of this study explores two different surface coatings for ultra-small cobalt ferrite and iron oxide NPs and discusses the role of surface ligand on the stability of NPs in more detail.

1.4.2 Nanotoxicity

An important consideration in the synthesis of NPs for biomedical applications is their potential toxicity. This is highlighted by the issues surrounding Gd-based contrast agents. Iron-oxide NPs offer a more biocompatible route than Gd as its degradation products can be stored by ferritin in the body. Co^{2+} ions were recently shown to follow the same ferritin remediation pathway as iron.[53] Whilst generally considered safe, there are toxicity concerns surrounding iron-oxide, and particularly cobalt-ferrite, due to their potential to generate reactive oxygen species which pose a risk to human health.[25] Reactive oxygen species have potentially harmful effects

on cells, and have been linked to DNA damage, apoptosis, and even carcinogenesis.[54] The toxicity of metal-oxide nanoparticles however, can be effectively mitigated through a biocompatible surface coating, and many different functionalisation approaches have emerged.[29,55]

Understanding the toxicity of NPs *in vivo* presents a major research challenge as many different factors influence the interaction between NPs and biological components. NP size,[56] shape,[57] surface charge, metal composition,[58] oxidation state,[25] dose[59] and administration route[60] can all affect toxicity. Moreover, it is not just chemical processes which govern the interactions between NPs and biological components. Mechanical forces also play a role, further complicating our interpretation and understanding of *in vivo* behaviour. For example, magnetic NPs attached to cell membranes can be used to initiate the biochemical reactions within a cell to promote the functional growth of bone or cartilage *in vitro*. A magnetic force was applied which activated the ion channels responsible for promoting growth of these tissues, demonstrating that mechanical forces can directly influence cellular behaviour.[61] The complex nature of nanoscale interactions means that all new nanomaterials developed for biomedical applications require thorough toxicity screening. Initial toxicity testing is typically conducted *in vitro* by analysing the viability or death of cells following exposure to the NPs of interest. Chapter 5 of this thesis discusses nanotoxicity in more detail and compares the effect of different NP sizes and iron oxide to cobalt ferrite NPs on their toxicity.

1.5 How to synthesise ultra-small nanoparticles

The ultra-small size of USNPs makes them promising candidates for T_1 MRI, however it also makes them very difficult to synthesise and characterise. Due to their large surface-to-volume ratio, the properties of USNPs are sensitive to slight changes in their size, shape and composition. Therefore, producing USNPs requires extremely strict control over their size and monodispersity. As the cost of a diagnostic or therapeutic product impacts its clinical utility, synthesis methods should also ideally be simple, fast and scalable to minimise costs. Thus, development of a suitable synthesis method is one of the major roadblocks preventing the application of

USNPs in clinical practice.[26]

To date, multiple different techniques have been developed to synthesise ferrite NPs. Such methods include micro-emulsion,[62] co-precipitation,[13] sol-gel,[63] mechanical alloying,[64] and solvothermal[65] techniques. Each method has its advantages, however thermal decomposition synthesis offers unprecedented control over NP size. Thermal decomposition involves decomposing organometallic precursors at high temperature in non-polar solvents and surfactants, yielding NPs which are highly crystalline and of a narrow size distribution.[66] In 2004, Sun et al. pioneered the use of this technique to synthesise ferrite NPs using acetylacetonate (acac) precursors.[67] Since then several parameters such as reaction time,[68] temperature,[69] and precursor concentration[70] have been explored as a means to control the particles shape, size and composition. Notably, the use of surfactants, typically oleic acid and oleylamine, have shown to play a key role in controlling nanoparticle size.[71]

Whilst many existing methods have demonstrated fine control over particle size and shape at larger scales (>5 nm) , control of these features at the ultra-small scale remains a challenge.[67,72–74] Moreover, achieving size control often requires the use of multiple solvents, surfactants and accelerating agents, which limits the method's scalability. Oleylamine, a long-chained alkylamine with a weak affinity for transition metals, can play a triple role of solvent, surfactant and reducing agent, mitigating the need for additional reagents. Nevertheless, to date only a handful of studies have reported synthesis of NPs with oleylamine alone, and its role in controlling nanoparticle size is still not well understood.[68,75,76] Chapter 2 of this thesis explores the role of oleylamine in the size-controlled synthesis of USNPs.

Synthesis by thermal decomposition offers superior size control, however the NPs produced are only dispersible in non-polar solvents. One strategy to overcome this is to exchange the hydrophobic ligands for a hydrophilic ligand. Dimercaptosuccinic acid (DMSA), a small molecule composed of carboxylate and thiol groups, has a high affinity for transition metal ions and thus is effective at replacing ligands via a simple ligand exchange technique.[77] Additionally, DMSA is non-toxic and provides a chemically versatile surface for further functionalisation.[78] Ligand exchange with DMSA, and a novel direct phase transfer method with bovine serum albumin (BSA), a natural biocompatible protein, are explored in chapter 4 of this thesis.

1.6 Aim of thesis

The aim of this thesis is to detail the synthesis, characterisation, and functionalisation of ultra-small iron oxide and cobalt ferrite nanoparticles for application as MRI contrast agents. The lower magnetisation saturation and greater chemical stability of $CoFe_2O_4$ NPs could be particularly beneficial for T_1 MRI. Figure 1.3 summarises the main research considerations in the design of NPs for biomedical applications as discussed in the introduction. From figure 1.3, it can be deduced that achieving the aim of this thesis requires a multidisciplinary approach. Therefore, a combination of objectives were derived as follows:

1. Develop a tailorable synthesis method capable of controlling the size of both iron-oxide and cobalt-ferrite NPs in the ultra-small range (chapter 2).
2. Thoroughly characterise the material properties of the NPs (chapter 3).
3. Explore two surface functionalisation strategies to obtain water-dispersible, stable, and biocompatible NPs (chapter 4).
4. Evaluate their toxicity *in vitro*, comparing the effect of size and metal composition (chapter 5).
5. Evaluate their performance as MRI contrast agents (chapter 6).
6. Conjugate the NPs to a targeting ligand towards liver-specific MRI (chapter 6).

The following chapter describes the results of objective 1 concerning the synthesis of ultra-small ferrite NPs and how size control can be achieved with a simple thermal decomposition approach.

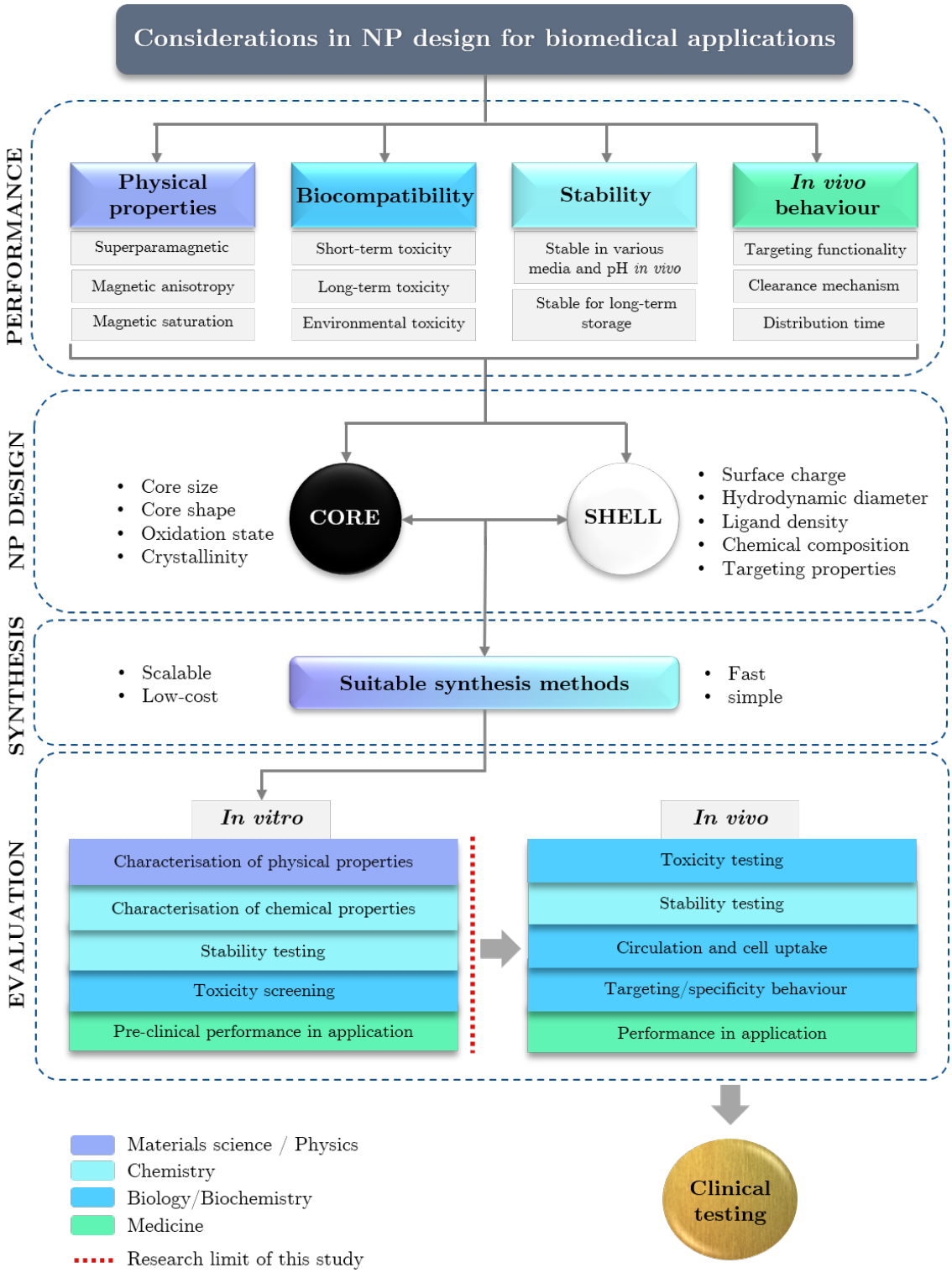


Figure 1.3: Overview of key considerations in the development of NPs for biomedical applications.

Chapter 2

Size-controlled synthesis of ultra-small MFe_2O_4@OLA nanoparticles

2.1 Size-controlled nanoparticle synthesis by thermal decomposition

This section details the method developed to synthesise iron oxide and cobalt ferrite NPs with fine size control. First, the background and underlying principles behind NP nucleation and growth are discussed. Important parameters for controlling NP size in thermal decomposition are then detailed, accompanied by a review of published methods focusing on metal-oxide NP synthesis and ultra-small NPs. The method and experimental details are then described; followed by the results which detail the effect of oleylamine, reaction time, temperature and heating rate on iron oxide, cobalt ferrite and cobalt oxide NP size. The focus of this chapter is on size control, and not on the structure or properties of the NPs, both of which are addressed in the succeeding chapter.

2.1.1 Introduction to nanoparticle synthesis

NPs have enormous potential for application in a range of fields from biomedicine to catalysis. The properties of NPs strongly depend on their dimension, therefore one

of the most fundamental parameters to control in their synthesis is their size. For MRI applications, the NPs must have a narrow size distribution, superparamagnetic properties, and be small enough to facilitate efficient blood circulation and clearance from the body. For T_1 MRI contrast enhancement in particular, the NPs must be smaller than ca. 5 nm to reduce their magnetic moment and thus suppress T_2 effect.[30]

Numerous methods to synthesise NPs are available, namely micro-emulsion,[62] co-precipitation,[13] sol-gel,[63] mechanical alloying,[64] and solvothermal[65] approaches. Due to their simplicity and practicality, co-precipitation and thermal decomposition are the dominant methods in use. Co-precipitation, where NPs are precipitated from a stoichiometric mixture of ferrous and ferric salts in alkaline medium, is simple, efficient and immediately yields water-soluble NPs. However, as crystal growth is driven kinetically, control over NP size, size distribution and morphology is poor.[79] In comparison, the thermal decomposition method offers superior size control and thus was chosen to synthesise NPs in this work. The remainder of this section will focus on the thermal decomposition method and the most important parameters for controlling NP size, shape and composition. First, background on NP nucleation and growth in solution is given. The reaction kinetics governing crystal growth are still poorly understood in the scientific community, and hence are not described in detail in this thesis. Instead, the two most prominent theories for NP nucleation and growth, the LaMer mechanism and Ostwald ripening are discussed.

2.1.2 Nanoparticle nucleation and growth mechanisms

The formation of NPs occurs in two stages: nucleation and growth. Nucleation refers to the formation of solid seeds or nuclei from a liquid phase. Growth of the nuclei then occurs to form NPs. Nucleation can happen heterogeneously, whereby seeds form on a pre-existing surface, either from impurities present in solution or container surfaces. Homogeneous nucleation is a spontaneous process whereby nuclei form uniformly throughout the liquid phase. The formation of nuclei occurs once the solid phase becomes thermodynamically more favourable than the liquid phase. This can be the result of a supercooled liquid, or supersaturation. In the 1950s, LaMer developed a theory on NP nucleation and growth based on Classi-

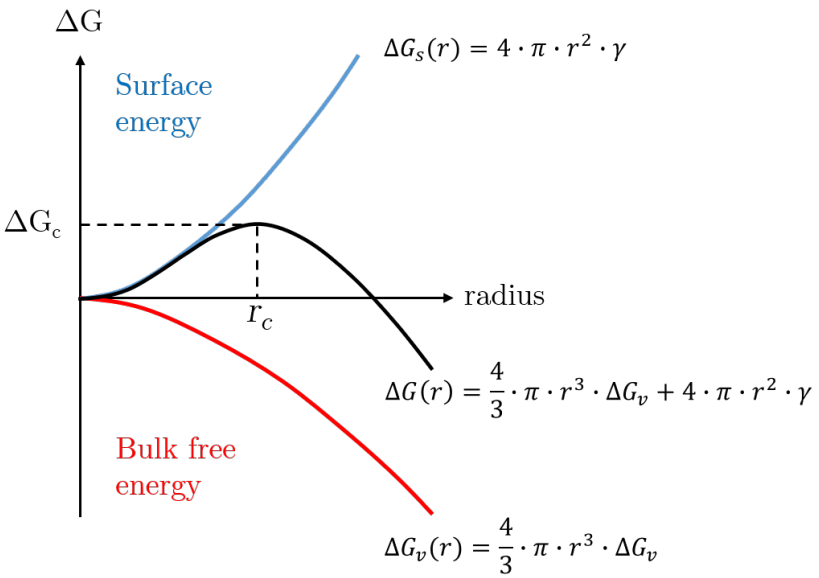


Figure 2.1: Thermodynamic nucleation of NPs and the 'critical radius'.

cal Nucleation Theory (CNT) which forms the basis of our understanding of NP synthesis today.[80,81]

CNT is based on a thermodynamic model where the nucleation of a solid phase is driven by the minimisation of the Gibbs free energy of the system. For homogeneous nucleation, the Gibbs free energy of a nucleus $\Delta G(r)$ is the sum of a positive term, which describes free surface energy, and a negative term, which takes into account the energy contribution from the inner volume of the nucleus (assuming spherical shape):

$$\Delta G(r) = \frac{4}{3} \cdot \pi \cdot r^3 \cdot \Delta G_v + 4 \cdot \pi \cdot r^2 \cdot \gamma \tag{2.1}$$

where r is the radius of the nucleus, γ is the interfacial energy per unit area and $\Delta G(v)$ is the free energy of the bulk crystal. The bulk crystal energy $\Delta G(v)$ itself is dependent upon temperature (T), Boltzmann constant (k_B), saturation of the solution (S) and its molar volume (v):

$$\Delta G(v) = \frac{-k_B T \ ln(S)}{v} \tag{2.2}$$

Due to γ always being positive and $\Delta G(v)$ negative in the case of supersaturation, a maximum free energy for formation of a stable nucleus exists called the critical radius (r_c) (Figure 2.1). This critical radius is the size at which a nuclei is stable

in solution and will not redissolve. When $r < r_c$, the surface energy is higher than the volume energy so nucleation is not thermodynamically favoured and any nucleus smaller than r_c will redissolve into the solution. When nuclei with a radius of at least r_c form, nucleation is favoured as further growth decreases the Gibbs free energy, leading to thermodynamically stable NPs. The size of r_c can be found from equation 2.1 by differentiating ΔG with respect to r and setting it to zero ($d\Delta G/dr = 0$):

$$r_c = \frac{-2\gamma}{\Delta G_v} = \frac{2\gamma v}{k_B T \; ln \; S} \tag{2.3}$$

By substituting r in equation 2.1 with r_c from equation 2.3 the critical free energy (ΔG_c)is given:

$$\Delta G_c = \frac{16\pi\gamma^3}{(\Delta G_v)^2} \tag{2.4}$$

Equation 2.3 shows that the temperature and saturation of a solution affects the critical radius size. By lowering γ of the new solid phase, the critical radius size decreases. It will be shown later in this work that the synthesis of ultra-small NPs was achieved using the surfactant oleylamine as it reduces the surface energy, thus lowering the r_c required for stable NP formation. The r_c also decreases with an increase in supersaturation, (as this increases $\Delta G(\upsilon)$).

Using the CNT model, LaMer proposed that in order to achieve monodisperse NPs, nucleation and growth had to occur separately, and ideally nucleation would occur as a single event (burst nucleation). In burst nucleation, seeds nucleate simultaneously and then grow without further nucleation occurring. If nucleation and growth were to occur simultaneously, NPs of different sizes would be obtained as one NP is growing in size whilst another is just nucleating. The LaMer model in figure 2.2 depicts that to achieve burst nucleation, the concentration of solute must increase rapidly (region 1), then rise above the minimum supersaturation concentration for a brief period (region 2). Following a burst nucleation event, the nuclei initially grow rapidly which lowers the solute concentration and prevents further nucleation events (region 3). The growth rate eventually slows and monodisperse NPs are obtained.

The LaMer concept of separating nucleation and growth has been used to achieve

monodisperse NPs in 'one-pot', 'hot-injection' and 'seed-mediated' thermal decomposition approaches, the latter whereby smaller NPs are used as templates for larger NP growth. Seed approaches facilitate a growth-only phase by suppressing additional nucleation by slow reduction of the metal-source and thus avoiding supersaturation.[82] Sun et al. used this approach to synthesise monodisperse MFe_2O_4 (M = Fe, Co, Mn) NPs using 8 nm NPs as seeds.[67] Park et al. applied the LaMer nucleation and growth model to synthesise monodisperse iron oxide NPs by a one-pot method using an iron-oleate complex formed *in situ* from iron chloride and sodium oleate.[66] Size uniformity was achieved due to the separation of nucleation and growth phases by temperature-dependent dissociation of iron-oleate ligands. Applying this knowledge, they also separated nucleation and growth by preparing a metal-oleate complex *ex situ*, and then heating it with pre-formed smaller NPs to grow NPs from 6-13 nm in a similar fashion to a seed-mediated approach.[72]

Others have applied a 'hot-injection' method to separate nucleation and growth phases. Metal precursors are injected into a solution containing surfactants, solvents and reducing agents which have been heated to a temperature higher than the decomposition temperature of the precursors. Following injection, the precursors rapidly decompose and instantly supersaturate the solution, initiating burst nucleation. Murray et al. developed this concept to synthesise monodisperse CdE (E = S, Te, Se) NPs.[83] Rockenberger et al. subsequently used the hot-injection approach to controllably synthesise metal-oxide NPs. NP size was controlled by lowering the injection temperature or lowering the injected precursor concentration.[84]

Although the LaMer mechanism is widely accepted to describe NP formation in a range of synthesis approaches, it is not a reliable model which can be used to predict the outcome of different synthesis parameters. For example in this work, it was found that a larger ratio of oleylamine-to-precursor led to smaller NPs. This contradicts the notion that greater supersaturation leads to smaller NPs, as more precursor and thus more monomer saturation resulted in larger NPs. It should also be mentioned that the model assumes the NP is spherical with a smooth surface and bulk-like properties. Analogously, growth mechanisms and their effect on NP size and shape are not taken into account. The following section will discuss NP growth and its role in controlling NP size and size distribution.

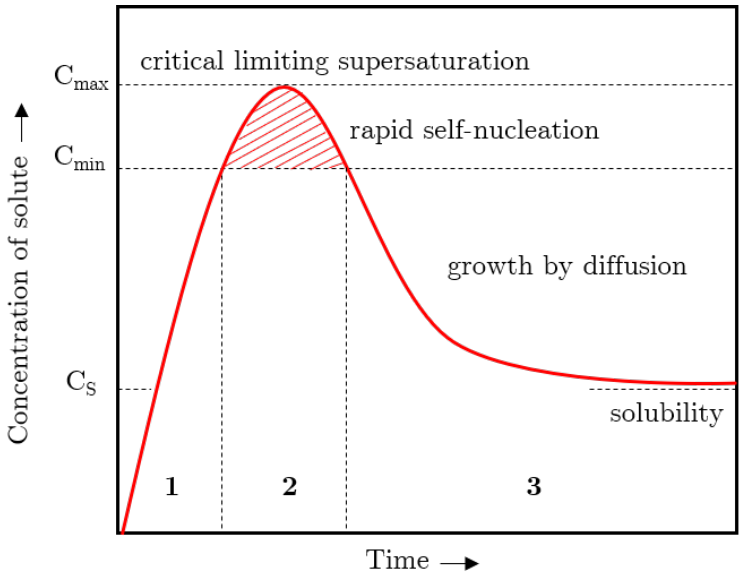


Figure 2.2: The LaMer mechanism for NP nucleation. As the concentration of solute increases it reaches a minimum supersaturation for rapid self-nucleation of nuclei. Following burst nucleation the concentration of solute is decreased sufficiently to prevent further nucleation. NP growth then occurs.

NP growth mechanisms

Following nucleation, NPs grow in size from remaining monomers in the solution. Growth is controlled either by the diffusion or reaction rate of monomers at the surface of the NPs.[81] NP growth takes into account the bulk concentration of monomers in solution (C_b), the monomer concentration at the solid/liquid interface (C_i), and the NP solubility (C_r). Diffusion-controlled growth was first modelled by Reiss[85] following the work of LaMer, whereby Fick's first law of diffusion is applied to describe the flux of monomers towards the NPs surface.

If diffusion of monomers to the NP surface is the limiting factor for growth, then change in NP radius with time is given by:

$$\frac{dr}{dt} = \frac{Dv}{r}(C_b - C_i) \tag{2.5}$$

where r is the NP radius, D the diffusion coefficient of the monomer, which is affected by the solvent, and k is the rate of surface reaction, which is assumed to be independent of NP size.

In the Reiss diffusion-controlled growth model (equation 2.5), the growth rate is inversely proportional to the NP radius, thus smaller NPs grow faster than larger

ones. As the size distribution becomes narrower with NP growth, this model is referred to as the 'size focussing method'. Reiss developed this model to explain the NP monodispersity achieved by the LaMer synthesis model. Conversely, if the rate at which monomers react with the NP surface is the limiting factor for growth, then the growth is the same regardless of NP size. Change in NP radius with time is thus given by:

$$\frac{dr}{dt} = kv(C_b - C_i) \tag{2.6}$$

where v is NP volume. In the event that NP growth is not diffusion or surface reaction limited, then change in NP radius with time is given by:

$$\frac{dr}{dt} = \frac{Dv(C_b - C_r)}{r + D/k} \tag{2.7}$$

Aggregation, coalescence, and Ostwald ripening

Whilst the Reiss diffusion-controlled growth model offered an explanation for monodisperse NPs, it did not explain why wide size distributions are often obtained. Ostwald ripening, introduced by Ostwald in 1900,[86] is a diffusion-limited process whereby smaller NPs are 'consumed' by larger NPs, often leading to a wider size distribution (Figure 2.3).

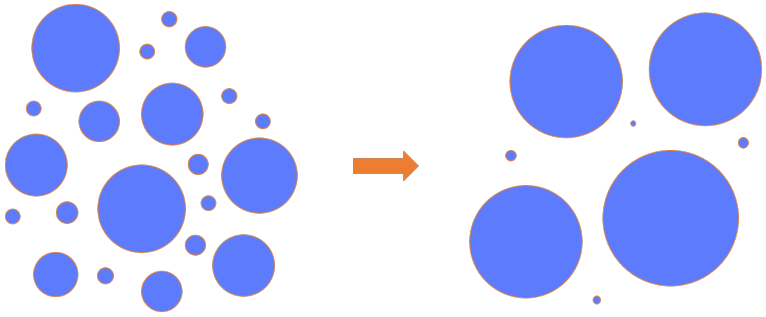


Figure 2.3: Diagram depicting the Ostwald ripening process. Smaller NPs are 'consumed' by larger NPs, until they eventually vanish. Larger NPs typically grow faster than smaller NPs, leading to a broadening of the size distribution.

The chemical potential of atoms at the interface between the NP solid surface and liquid solution is higher than that of atoms in either bulk phases. As smaller NPs offer a larger surface-to-volume ratio, their interfacial energy has a larger contribution than bigger NPs. The presence of a concentration gradient is responsible for

the thermodynamically-driven transfer of material. The concentration of solubilised material around the interface of smaller NPs is larger than the average concentration in bulk solution, whereas the opposite is true for larger NPs, leading to the transfer of material from the smaller NP interface to the larger NP. The Ostwald-ripening process can be described by the Gibbs-Thomson equation:

$$\Delta\mu = \frac{2\gamma v}{r} \tag{2.8}$$

where $\Delta\mu$ is the chemical potential, and v is the NP's molar volume. Expressing a NP's solubility as a function of its radius then gives:

$$C_r = C_b \; exp\frac{2\gamma v}{r k_B T} \tag{2.9}$$

where k_B is the Boltzmann constant and T is the temperature.

Lifschiz, Slyozov[87] and Wagner[88] developed a kinetic description of Ostwald ripening referred to as LSW theory, which explains that the mean radius of NPs increases in size over time as well as the overall size distribution.[89] LSW theory assumes a dilute system where NPs are infinitely separated from one another. Although Ostwald ripening has been demonstrated experimentally (example shown in Figure 2.4), NP size distributions are often wider then LSW predicts, thus several adaptions to LSW and other theories have since emerged to describe NP dissolution, which are summarised elsewhere.[89,90]

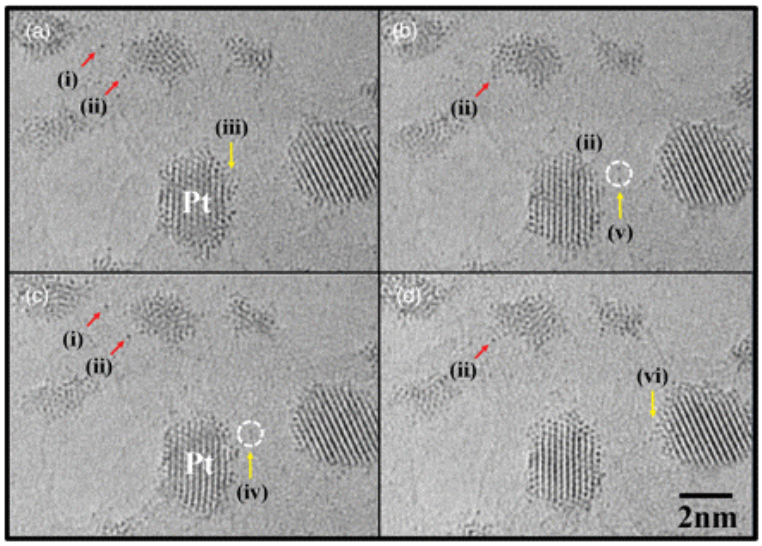


Figure 2.4: Ostwald ripening of platinum NPs captured by *in situ* aberration-corrected TEM.[91]

Ostwald ripening and NP aggregation can be limited or promoted by stabilising agents such as OLA and OA.[92] Aggregation is a blanket term used to describe another growth mechanism where NPs fuse or cluster together to form larger NPs, driven by interparticle forces. Some crystals with high energy facets can self-orientate to align with a neighbouring crystal at the same facet, then crystallographically fuse together in order to minimise free surface energy. This is known as 'oriented aggregation' and was coined by Penn and Banfield and has been demonstrated experimentally.[93,94] When NPs have not perfectly aligned their crystallographic orientations, defects such as twinning and grain boundaries can occur.[95] Coalescence is another aggregation-based growth that specifically describes the fusing of nuclei or NPs with no particular preference for direction to form a single NP.[96] In literature, aggregation, coalescence and agglomeration are often used interchangeably to generally describe NP growth.

Growth can occur by a combination of the previously-described mechanisms, and can also occur simultaneously with nucleation.[89] In general, NP growth is dominated by surface energy, which in turn is dependent upon a wide variety of physical and chemical factors.[97] As a result, no model currently exists that can be applied to accurately identify synthesis parameters required to obtain a specific NP size and morphology, although some inferences can be done. Instead, desired NP characteristics are obtained through trial and error. It is also important to note that non-classical theories for NP nucleation and growth have emerged which take into account the potential formation of an intermediate species such as a molecular cluster.[95] The pre-nucleation intermediate species may have lower surface/bulk energies than potential NPs and thus lower the critical free energy (ΔG_c) for nucleation. However non-classical nucleation and growth theories are currently lacking significant experimental support due to the current limitations of characterisation methods.

2.1.3 Important parameters for thermal decomposition

Thermal decomposition is a widely used synthesis technique to produce NPs. Employing the LaMer mechanism, organometallic precursors are decomposed rapidly at high temperatures to instigate burst nucleation, forming monodisperse NPs. Typi-

cally the precursors are heated with a mixture of solvents, surfactants and reducing agents which serve to facilitate nucleation and subsequently stabilise the NPs. Figure 2.5 illustrates the method.

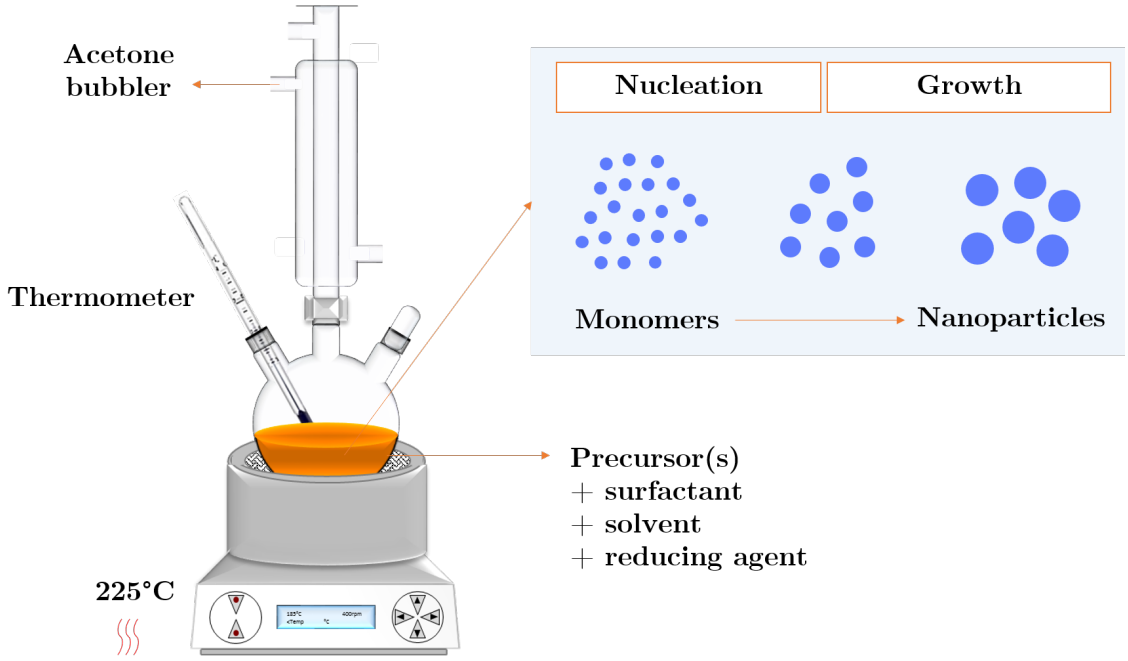


Figure 2.5: Schematic of NP synthesis by thermal decomposition.

The most important parameters considered to influence NP size and size distribution are listed below:

1. The metal precursor and its concentration (which influences saturation), ratio to other reagents, and decomposition temperature. For example, iron acetylacetonate decomposes at a lower temperature than iron carbonyl or iron oleate, and has generally produced smaller NPs.[98] Using a different molar ratio of cobalt and iron precursors led to a change in NP size distribution in this work.

2. The heating rate can affect precursor decomposition and thus the onset of nucleation.[99]

3. The reaction temperature can influence the nucleation and growth by controlling precursor or ligand decomposition.[66]

4. Surfactants: surfactants play a crucial role of lowering surface free energy and capping the NPs to limit aggregation. Their ratio in comparison to the precursors also influences NP size, as will be discussed later in this chapter.

5. Reaction time: generally, longer reaction times lead to larger NPs as NPs continue to grow from the remaining monomer supply.

6. The solvent can affect the diffusion of nuclei, thus NP growth.

7. Reducing agents: they serve to facilitate decomposition of the metal precursor and thus affect nucleation. For example Yu et al. (2014) found by adding a stronger reducing agent they reduced their metal salt faster in comparison to a weaker reducing agent producing smaller NPs.[75]

2.1.4 Thermal decomposition to synthesise metal-oxide and ultra-small NPs

Through a variety of the synthesis parameters listed previously, thermal decomposition has been successfully applied to make metal oxide NPs with excellent control over NP size. In 2001, Hyeon pioneered the 'heat-up' thermal decomposition method to make monodisperse iron oxide NPs from 4 to 16 nm in size.[65] NPs were synthesised by heating iron pentacarbonyl with oleic acid (OA) and octyl ether to 300℃. NP size was tuned by adjusting the ratio of precursor to oleic acid. Hyeon's group later improved the method by using a less expensive and non-toxic precursor, iron chloride, in conjunction with sodium oleate and OA to form an *in situ* iron oleate complex. NP size was controlled from 5-22 nm by changing the solvent and concentration of OA.[66] Sun et al. subsequently introduced a flexible approach in 2004 for synthesising MFe_2O_4 NPs (M = Co, Ni, Mn, Mg, etc.) by using low-cost metal acetylacetonates as precursors.[67] NPs from 3-20 nm were obtained by using solvents with different boiling points (thus changing the reaction temperature). Although fine size control was achieved, multiple reagents and different synthesis parameters were required. For example, applying the same synthesis conditions used for Fe_3O_4 NPs to synthesise $CoFe_2O_4$ and $MnFe_2O_4$ NPs produced different NP sizes.

Several researchers expanded on the method of using acetylacetonate precursors. Guardia et al. synthesised iron oxide NPs from 5 to 30 nm using iron acetylacetonate ($Fe(acac)_3$), decanoic acid and dibenzyl ether.[100] The NP size increased as the relative amount of decanoic acid decreased, however their morphology also changed. Lu et al. synthesised a range of $CoFe_2O_4$ NPs with a mixture of 1-octadecene, 1,2-

hexadecanediol (HDD), oleylamine (OLA), OA and iron and cobalt acetylacetonate precursors.[68] Monodisperse NPs in the range of 4-30 nm were obtained by varying the reaction time. Longer reaction times led to larger NPs, however Ostwald ripening occurred and polydisperse NPs were obtained if extended for too long. NP morphology was controlled by changing the ratio of OA/OLA to the precursors to produce spherical, cube or star-shaped NPs. Through a systematic trial and error approach, they found that HDD was key to achieving smaller NP sizes and narrow size distributions. Considering that HDD is expensive, they tried octadecanol instead but obtained larger NP sizes.

Nakaya et al. reported a similar but solvent-less method to produce Fe_3O_4 NPs using HDD, OA, OLA and $Fe(acac)_3$.[69] No solvents were used in order to encourage the formation of a metal-ligand complex by surrounding the precursor with excess ligands. Raising the reaction temperature and time led to an increase in NP size to obtain a range of sizes from 5.3-20.4 nm. Maity et al. also used a solvent-less approach to synthesise Fe_3O_4 NPs from $Fe(acac)_3$, OA and OLA.[101] NP size was tunable from 5-11 nm by either adjusting the reaction time from 30 minutes to 24 hours, and/or by adjusting the temperature from 300-330 ℃.

The purpose of developing methods that can control metal oxide NP size is to design NPs with the ideal size and magnetic properties for specific applications. Recently, researchers introduced a different approach to tailor the magnetic properties: rather than control the size of the NPs, Unni et al. controlled the size of the magnetically 'dead' surface layer by addition of molecular oxygen during synthesis.[102] In comparison to synthesis under argon, which yielded 18.5 nm NPs with a 10.7 nm magnetic diameter, reacting iron oleate, OA and trioctylamine under the controlled addition of oxygen produced 15.4 nm Fe_3O_4 NPs with a 14.1 nm magnetic diameter. Their method significantly reduced the size of the 'dead' layer in comparison to post-synthesis thermal annealing procedures, however the addition of oxygen introduced a fire hazard, therefore the flow rate of oxygen must be carefully controlled.

The above methods have demonstrated effective control over NP size, however this often involved changing the reagents and synthesis conditions in order to produce different NP sizes. This inevitably introduces the potential for inconsistencies between batches. Furthermore, the methods are suitable to produce NPs 3-30 nm in

size, but not for NPs smaller than 3 nm. The following section will discuss current synthesis methods for ultra-small NPs.

Synthesis of ultra-small nanoparticles

Synthesis of NPs below 3 nm demands strict control over nucleation to achieve a burst of small nuclei, and restricted growth in order to retain a small NP size. Several strategies to synthesise USNPs have been reported so far: Park et al. synthesised 1.7 nm iron oxide NPs by a polyol thermal decomposition method. They heated ferric chloride hexahydrate, triethylene glycol and polyethylene glycol diacid (PEG) for 24 hours at 260 ℃.[103] The advantage of their method was that the NPs were immediately dispersible in water due to the PEG coating. However their TEM image appears to show agglomerates and no stability testing was conducted. Furthermore it is unclear whether NP size could be controlled. Similarly, Hu et al. synthesised water-soluble 3 nm iron oxide NPs by heating $Fe(acac)_3$ and diethylene glycol for 3 hours.[104] NP size could be increased to 5 nm by extending the reaction time to 6 hours.

In 2011, the Hyeon group used their iron oleate complex to synthesise 3 nm iron oxide NPs following heating with OA, oleyl alcohol and diphenyl ether.[30] NP size was reduced to 2.2 nm by replacing OA with more oleyl alcohol, and further reduced to 1.5 nm by decreasing the reaction temperature from 250 to 200 ℃. Hufschmid et al. tried a similar approach using iron pentacarbonyl, octyl ether and OA, controlling NP size down to 2 nm by reducing the amount of OA.[105] However the NPs were poorly crystalline and wüstite phase with anti-ferromagnetic properties, therefore a subsequent oxidation step was required to improve the properties. More recently, Wei et al. synthesised 3 nm iron oxide NPs using iron oleate, OA, 1-tetradecene and 1-hexadecene for 1 hour at 270 ℃.[42] The mixture was further heated with an trimethylamine N-oxide for 1 hour to obtain maghemite.

Existing methods have demonstrated the ability to synthesise iron oxide NPs $\leq$3 nm, however this is often at the expense of using multiple different reagents or unfavourable conditions such as long reaction times. Mohapatra et al. introduced a flexible approach to synthesise MFe_2O_4 (where M = Mn, Fe, Co, Ni and Zn) NPs in the range of 2 to 9 nm.[20] Nearly monodisperse NPs were obtained by

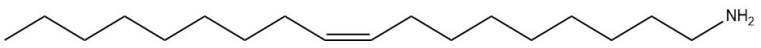


Figure 2.6: chemical structure of oleylamine.

decomposing metal chloride precursors in OLA alone for 4 hours. NP size decreased as the relative amount of OLA increased as the higher content of OLA promoted a diffusion-controlled growth process (due to a low concentration of growth species). The use of OLA alone proposes a potential route to both restrict NP growth and reduce the amount of reagents required for synthesis. The following section discusses oleylamine in more detail.

2.1.5 The role of oleylamine in nanoparticle synthesis

The use of surfactants (also referred to as capping agents or stabilising agents) in thermal decomposition is critical in NP nucleation and growth. The formation of surfactant-precursor complexes can influence nucleation by reducing interfacial free energy and thus reducing the size of r_c (equation 2.3), as well as influence the supersaturation level by reducing the amount of free metal atoms.[92] In terms of NP growth, surfactants can affect both the diffusion rate, influencing NP radius according to equation 2.5, and the surface reaction rate (equation 2.6), due to covering the NP surface. A theoretical study considering the effect of surfactants is detailed elsewhere.[106] In addition, surfactants can act as a barrier to prevent further growth through steric or electrostatic repulsion according to the theory of Derjaguin, Landau, Verwey, and Overbeek.[107,108]

The most frequently used surfactants are oleic acid and oleylamine. Both have long-chained hydrocarbon tails, but OA has a carboxylic head group whereas OLA has an amine head group (figure 2.6), which differentiates their binding modes.[71]

Typically OA and OLA are used in conjunction with one another, and until recently, their interaction was not well-known. Harris et al. modelled the adsorption behaviour of OA and OLA combined on 2.6 nm magnetite NPs and found that a surfactant double layer is formed.[71] Oleic acid binds via its carboyxlic group to the NP surface, OLA then binds to OA. OLA forms an acid-base complex with OA in the solution which helps to form stable NPs by promoting adsorption of OA, thus it is recommended that OA and OLA are used together. However the study did not

assess the use of OLA alone.

OA is known to bind more strongly to NPs than OLA and has a preference for specific crystal facets leading to directional growth. OLA binds weakly and isotropically typically leading to spherical NPs, whereas OA binds strongly and selectively to the (110) crystal plane and has been shown to produce cubic shapes.[68] Importantly, OA has been shown to promote NP growth: several reports have shown that as the amount of OA increases the NP size increases, thus it may not be suitable for the synthesis of USNPs.[30,65,66,105]

Only a few studies on NP synthesis using OLA alone currently exist. In addition to the study by Mohapatra et al. mentioned previously,[20] Yu et al. used OLA to synthesise MPt (M = Fe, Co, Ni, Cu, Zn) NPs from heating acac precursors at 300 ℃ for one hour.[75] Using the same reaction conditions with different metal precursors led to NPs of various metal compositions but also different sizes (ranging from 5-10 nm). Smaller NPs with sizes down to 3.5 nm were obtained with the addition of borane t-butylamine, a stronger reducing agent. Georgiadou et al. synthesised cobalt ferrite NPs in OLA, however the NPs' shape was not consistent and the size distribution was wide (9.0 ± 3.8 nm). Furthermore the reaction time was in excess of 24 hours.[76] Lastly Seo et al. synthesised hexagonal and cubic CoO NPs from cobalt acetylacetonate ($Co(acac)_3$) in OLA alone.[109] Hexagonal CoO NPs 47 nm in side edge length were obtained when a solution of 1:100 molar ratio of $Co(acac)_3$ and OLA was used. Larger NPs 83 nm in side edge length were grown from a 1:50 molar ratio solution.

OLA alone can play an effective triple role as solvent, surfactant and reducing agent. It acts as an electron donor at high temperatures, and its hydrocarbon chain makes it a good capping agent.[76] Moreover it is low-cost, and has a high boiling point of ca. 350 ℃, allowing flexibility in synthesis.[110] Despite the prevalent use of OLA, its effect in NP synthesis is still poorly understood.

Previous research conducted by Karl Mandel in the Nanomaterials By Design group focused on the synthesis of metal-oxide NPs with a variety of surfactants including OLA.[111] Mandel concluded that OLA promoted growth of CoO NPs from 10.0 to 14.3 and 19.7 nm, contrary to that observed by Mohapatra et al.[20] However, following a closer look at his experimental parameters, it can be seen that

only the 10 nm NPs were synthesised in OLA alone, the two larger sizes were both synthesised with 1 mmol of triphenylphosphine as well as different reaction temperatures. Furthermore, from his appendix of reaction parameters, it appeared that when more OLA was used, smaller NPs were obtained in the case of iron oxide NPs. This prompted the study of OLA alone in this work, with the hypothesis that OLA could restrict NP growth if used in the absence of oleic acid or other surfactants, and thus be suitable for the production of ultra-small NPs in conjunction with rapidly-decomposing acetylacetonate precursors. Concomitantly, using oleylamine alone simplifies thermal decomposition and reduces costs, facilitating potential scale-up.

In this study, synthesis of iron oxide and cobalt ferrite NPs was investigated using oleylamine alone. The aim was to identify a method that can produce ultra-small NP sizes under the same synthesis conditions to allow for future comparative studies on their properties, toxicity, and MRI application.

2.2 Materials and methods

2.2.1 Materials

Iron (III) acetylacetonate ($\geq$ 99.9 % trace metals basis), cobalt (II) acetylacetonate (97 %), oleylamine (technical grade 70 %) and cyclohexane (ACS reagent $\geq$ 99 %) were all purchased from Sigma Aldrich. Ethanol (analytical reagent grade) was purchased from Fisher Scientific. TEM grids (400 mesh copper, lacey, holey, or just carbon) were purchased from Agar Scientific.

2.2.2 Nanoparticle synthesis method

In a typical reaction, x mmol of M(II,III)acetylacetonate ($M(acac)_{2,3}$ where M = Fe(III) or Co(II)) and y ml of oleylamine were placed into a three neck funnel flask fitted with a magnetic stir bar, reflux cooler and thermometer. The amount of metal precursor and oleylamine was varied to examine their effect; full details of the parameters are detailed in the next section. The mixture was stirred at 400 rpm under argon for 15 minutes at room temperature, before being heated to 225 ℃ at a heating rate of ca. 16 ℃ min^{-1}. The solution was kept at this temperature for 10

minutes, before allowing to cool. An excess of ethanol was added and the NPs were magnetically separated. After discarding the supernatant, the NPs were washed in ethanol two times with centrifugation at 4600 rpm for 15 minutes. The NPs were re-dispersed in cyclohexane and stored at 4 ℃.

The standard conditions for synthesising 2.4 nm MFe_2O_4 NPs (M = Fe or Co) were as follows: 0.03 mmol of $Fe(acac)_3$ for iron oxide NPs or 0.02 mmol of $Fe(acac)_3$ and 0.01 mmol of $Co(acac)_2$ for cobalt ferrite NPs were heated with 60 mmol of OLA as described above.

Full details of parameters used for each experiment can be found in the appendix (B.1.1).

2.3 Characterisation

The NPs were characterised by a JEOL 3000F transmission electron microscope operating at 300 kV acceleration voltage. Samples were prepared by placing a 3 μl drop of NP suspension onto a TEM grid. NP diameters were measured from TEM micrographs using automated nanomaterials software developed by Vitaly Babenko. NP size refers to the average NP diameter measured from a minimum of 100 NPs.

2.3.1 Transmission electron microscopy

Transmission electron microscopy (TEM) was used to characterise the size, size distribution, shape and crystal structure of the NPs. TEM employs an electron beam which is focussed onto the sample and camera by a series of objective, condenser, intermediate, and projective lenses to record images. Upon reaching the sample, electrons interact in a variety of ways depending on the atomic weight, density, thickness and crystal structure of the sample. TEM primarily uses electrons which forward scatter (<90°) from the sample, and thus requires thin (<100 nm) samples.[112]

The spatial distribution of electron scattering as a result of the sample can be observed as contrast in TEM. Thicker areas lead to more scattering events, thus appear darker than thinner areas, providing *thickness* contrast. Heavier elements induce more scattering than lighter elements as the likelihood that an electron is

deviated from its direct path by an interaction with an atom increases with the number of charges that the atom carries.[112] Thus areas of heavier atoms will appear darker than those with lighter areas, which is known as *mass* contrast. The combined effects of *mass-thickness* contrast is a type of amplitude contrast that provides the contrast for the images in this section and is achieved by using an objective aperture that allows only the incident beam to come through (high-angle scattered electrons are thus blocked). Iron and cobalt are heavy elements and as such provide good contrast in this imaging mode.

TEM is capable of achieving high resolution, and the JEOL 3000F has a point resolution of 0.16 nm, which makes it suitable for the characterisation of USNPs. A limitation of TEM is the sampling size; only a small proportion of the sample can be feasibly measured and therefore NP sizes and distributions are statistically less significant. Alternative techniques to measure NP size include dynamic light scattering (DLS), however this does not provide a direct measurement of the crystal core but rather the layer of solvated ions surrounding NPs. X-ray based techniques such as X-ray diffraction (XRD) and small angle X-ray scattering (SAXS) are also useful for measuring NP size and size distribution. Both measure the bulk of a sample, providing better statistical significance than TEM. A study on spherical $CoPt_3$ NPs smaller than 10 nm compared TEM, XRD and SAXS for analysis of NP size and distribution and found the results between techniques were in good agreement.[113] TEM however allows one to better assess the degree of homogeneity of the sample, such as polydisperse NP sizes and irregular shapes.

2.4 Results and discussion

The first study details the synthesis of iron oxide NPs by oleylamine in order to elucidate the role and effect of OLA on NP size. The effect of other parameters on iron oxide NP size such as reaction time, temperature and heating rate are then discussed. After identifying the ideal conditions for USNP synthesis, the method was then extended to synthesise other metal-oxides, namely cobalt ferrite and cobalt oxide.

2.4.1 Size-controlled synthesis of iron oxide NPs with oleylamine

NPs were successfully synthesised using $Fe(acac)_3$ and oleylamine alone. Upon heating the mixture, a colour change from orange-brown to dark brown/black occurred at around 180 °C due to the formation of nuclei (figure 2.7). The final dispersions obtained contained no visible aggregates and could be stored for months at 4 °C without sedimentation occurring. An example batch synthesised with 0.71 mmol of $Fe(acac)_3$ and 60 mmol of oleylamine for 10 minutes at 225℃ is shown in figure 2.7. The NPs were spherical and nearly monodisperse, with an average size of 4.6 ± 0.6 nm. Spherical NPs were anticipated considering that OLA is known to bind isotropically.[68] The narrow size distributions of the NPs suggests that burst nucleation had occurred. This could have resulted from a combination of factors: iron acetylacetonate decomposes rapidly, and OLA can act as a mild reducing agent which may also encourage rapid precursor decomposition, thus the monomer concentration could be decreased below the supersaturation level quickly enough to limit further nucleation events according to equation 2.3.

To investigate the role OLA plays in determining NP size, iron oxide NPs were synthesised with 15, 30, 60 and 120 mmol of oleylamine. The amount of $Fe(acac)_3$ was fixed at 1 mmol, and the reaction temperature, time and heating rate were fixed as described in section 2.2.2. Figure 2.8 shows the effect of increasing amounts of OLA on the average NP diameter. The NP size decreased from 6.4 nm to 3.2 nm as the amount of OLA increased.

According to the LaMer theory, the critical nuclei size required to initiate nucle-

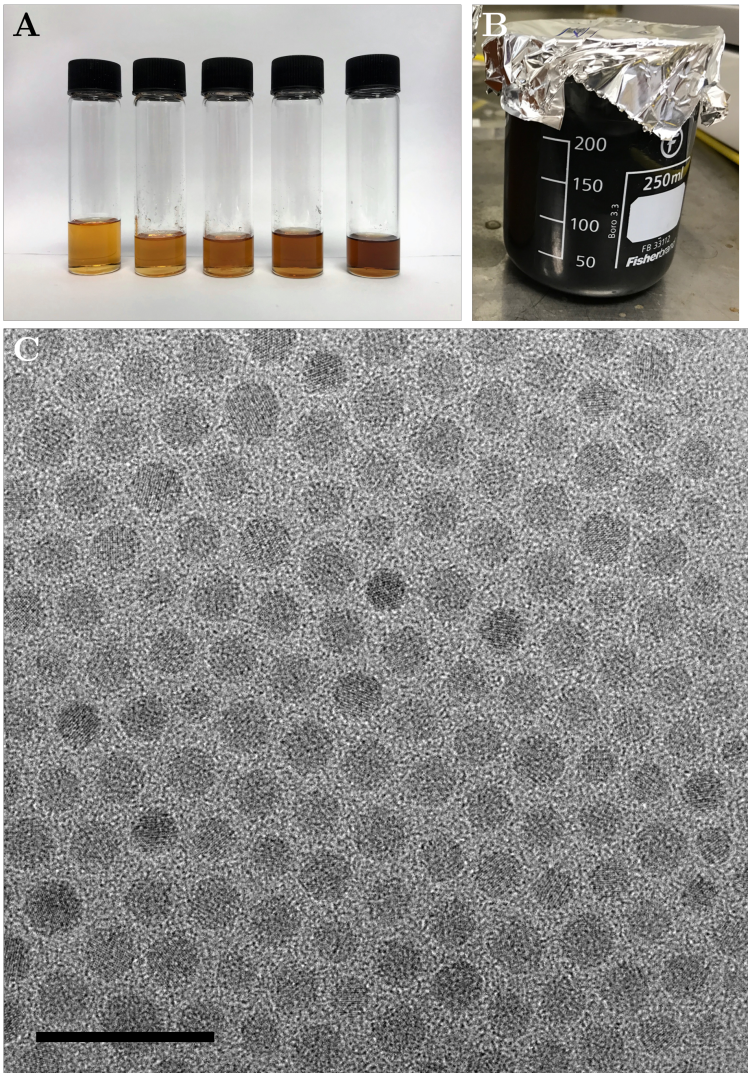


Figure 2.7: (A) Aliquots of NPs drawn at 100, 150, 180, 200 and 220 °C (from left to right) showing colour change. (B) Black colour of NPs in cyclohexane. (C) TEM micrograph of iron oxide NPs synthesised with $Fe(acac)_3$ and oleylamine alone (scale bar = 20 nm).

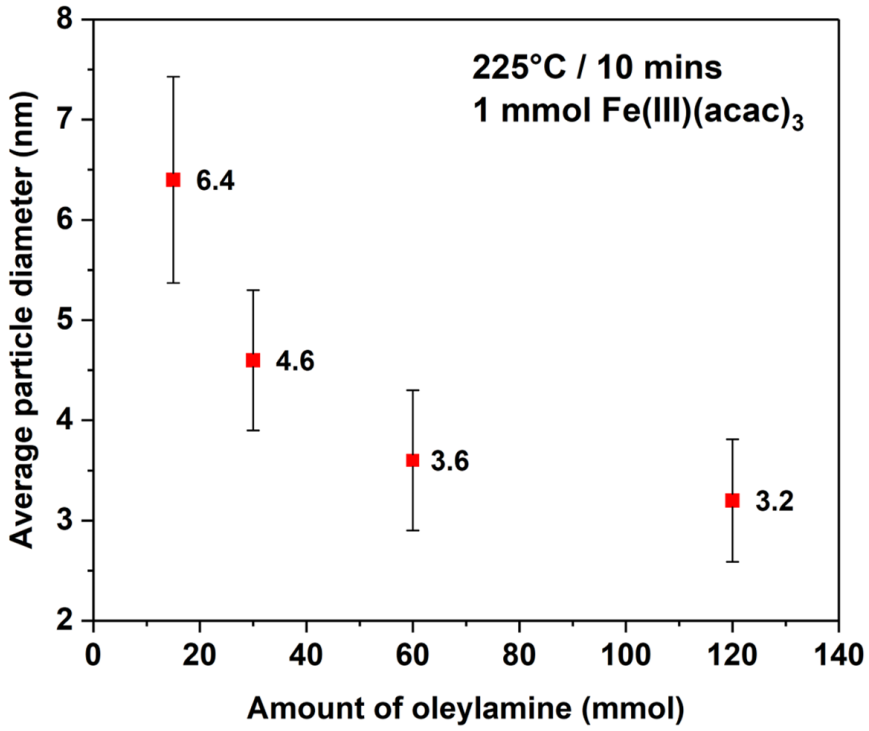
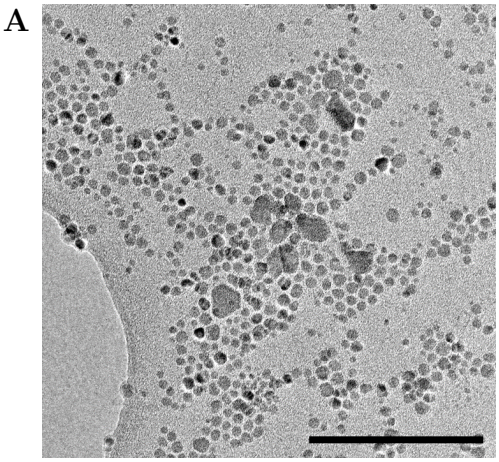


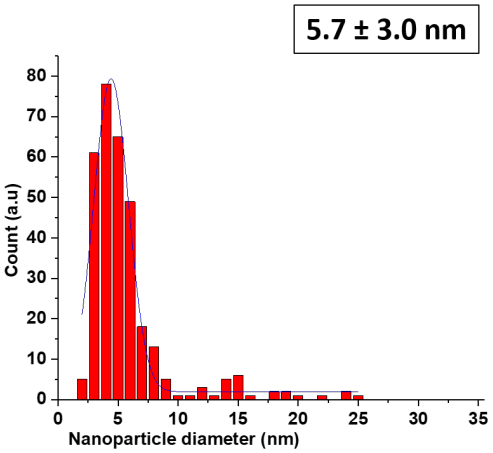
Figure 2.8: Iron oxide NP size in relation to the amount of OLA.

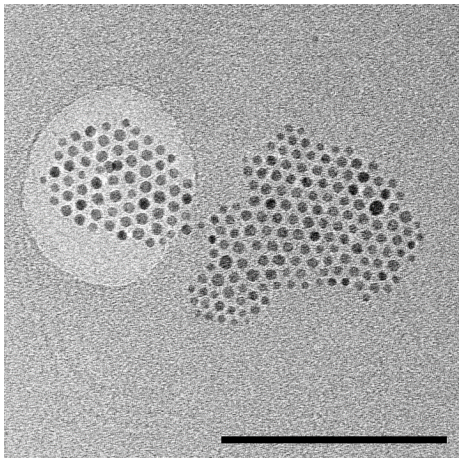
ation is influenced by the saturation of the solution (equation 2.3). Higher monomer saturation reduces the critical nuclei size required for nucleation to occur, leading to the generation of smaller NPs. However in this experiment, a lower volume of liquid, and thus higher saturation of precursor monomers, resulted in larger-sized NPs. This trend suggests that the change in NP size was not influenced by nucleation under these synthesis conditions, but was determined during the growth phase. This could be explained using the growth models proposed by Reiss (equation 2.5): a lower volume of liquid could have facilitated faster diffusion of monomers to a nuclei surface, and/or increased the concentration of monomers at the nuclei/liquid interface, promoting growth and leading to larger NP sizes.

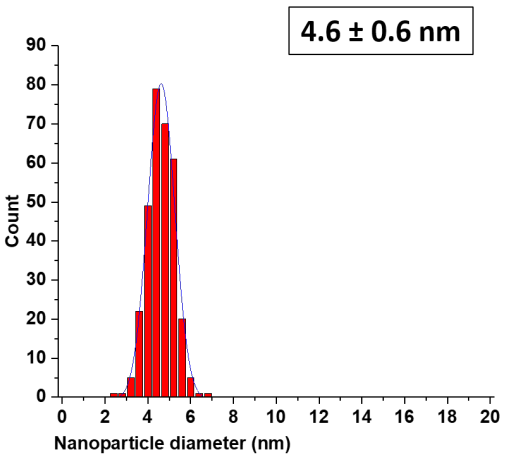
To further examine the role of the precursor-to-OLA ratio, the amount of OLA was kept constant at 60 mmol and instead the amount of precursor was varied from 1.4 mmol to 0.03 mmol. Figure 2.9 shows TEM micrographs and size distributions of the NPs obtained. As the amount of precursor decreased, thus the ratio of precursor-to-OLA increased, the NPs decreased in size from 5.7 $\pm$ 3.0 to 2.4 $\pm$ 0.4 nm.

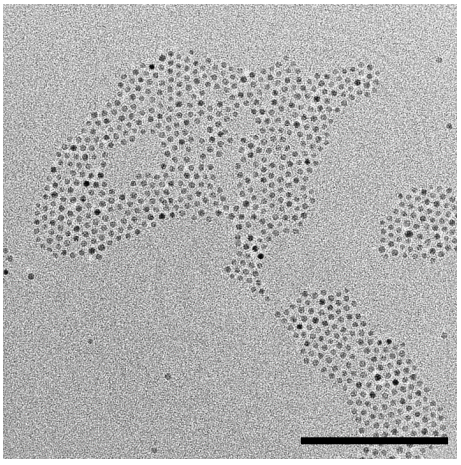
Thus by varying the precursor-to-OLA ratio, iron oxide NP size could be finely

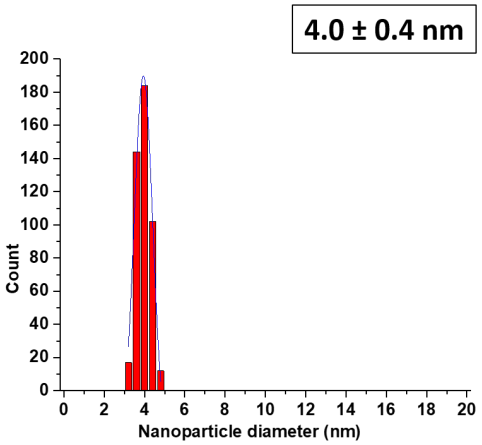



5.7 ± 3.0 nm
Count (a.u)
Nanoparticle diameter (nm)




4.6 ± 0.6 nm
Count
Nanoparticle diameter (nm)




4.0 ± 0.4 nm
Count
Nanoparticle diameter (nm)

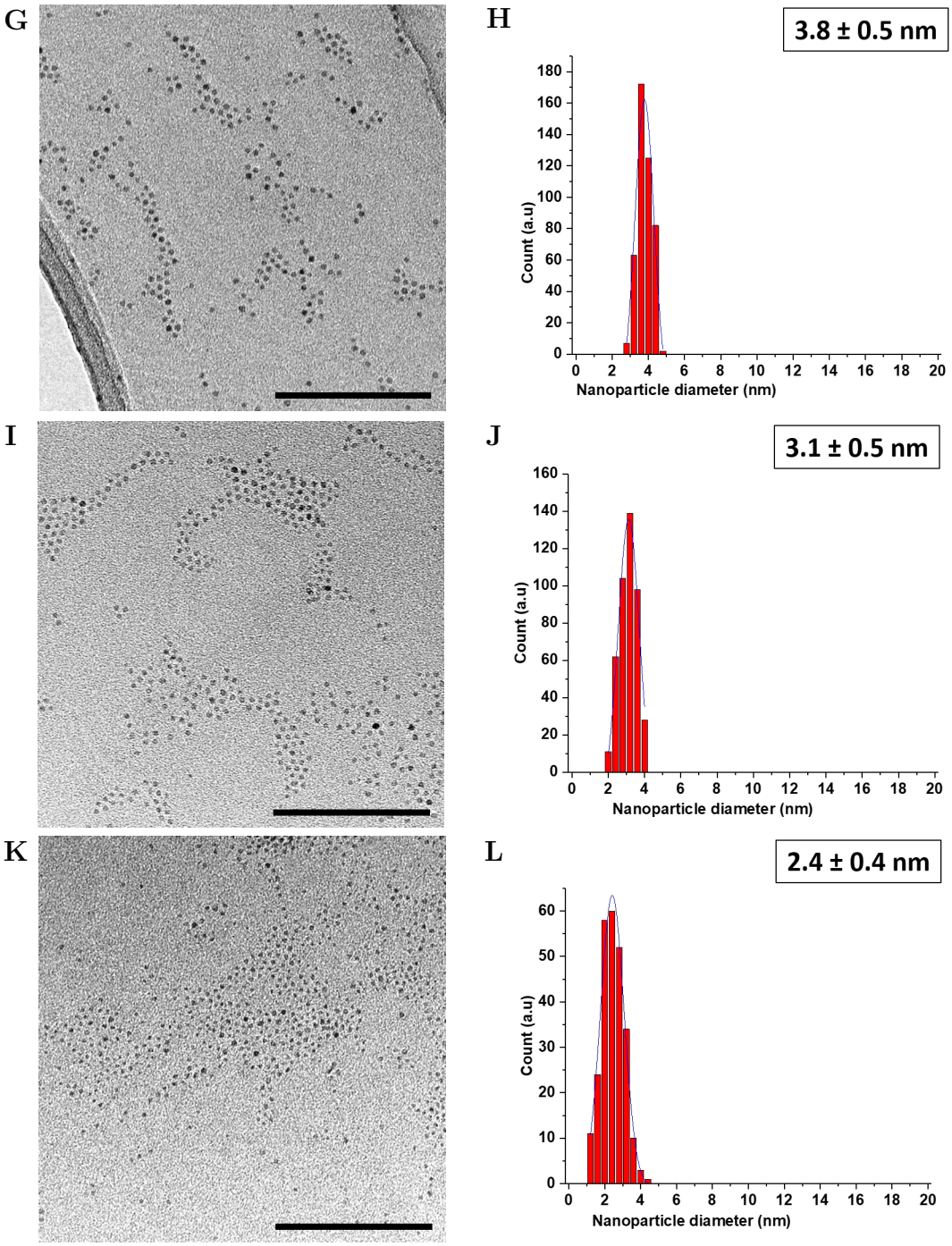


Figure 2.9: TEM micrographs and corresponding size distribution graphs of iron-oxide NPs synthesised with 60 mmol OLA and A-B: 1.4 mmol, C-D: 0.7 mmol, E-F: 0.3 mmol, G-H: 0.15 mmol, I-J: 0.07 mmol, K-L: 0.03 mmol of precursor. Scale bar is 100 nm. The NP size decreases from 5.7 nm (A) to 2.4 nm (K) as the precursor:OLA ratio increases.

controlled. The upper threshold for size control however was a precursor-to-OLA ratio of approximately 1:50, below which the size distribution was wide due to the formation of aggregates (figure 2.9 A,B precursor-to-OLA ratio = 1:43). Aggregate formation was likely due to an insufficient amount of OLA present to cap the NPs and restrict growth, allowing Ostwald ripening to occur. Irregular NP sizes at low precursor-to-OLA ratios have also been observed by others.[114] Conversely, in the presence of an excessive amount of OLA, (0.03 mmol precursor to 60 mmol OLA) USNPs 2.4 ± 0.4 nm in size were obtained (figure 2.9K,L). Thus it can be deduced that by either varying the volume of OLA or the amount of precursor to increase the ratio between them, a greater proportion of OLA led to smaller NP sizes, most likely by limiting the growth phase. Similar observations were reported by others.[20,115]

The small size range of the NPs obtained infers OLA perhaps had a general influence on nucleation and growth: OLA may have lowered the surface free energy of the system through formation of an OLA-precursor intermediate complex, allowing generation of smaller nuclei by reducing the critical nuclei size required to initiate nucleation r_c (see equation 2.3). The formation of an OLA-precursor complex is plausible through binding of OLA to the metal cations via its nitrogen head group. An attempt was made to gather experimental evidence showing formation of an OLA-precursor complex by conducting Fourier transform infrared (FTIR) studies on aliquots drawn during various stages of the synthesis reaction. However, the results were inconclusive (see appendix B.1.2). In addition to affecting nucleation, OLA could also have restricted NP growth by Ostwald ripening through steric repulsion.

2.4.2 Effect of other synthesis parameters on iron oxide NP size

Heating rate

The precursor-to-OLA ratio was found to influence NP size, however other parameters such as the heating rate can also impact NP size. The heating rate can affect the rate of precursor decomposition, thus potentially influencing nucleation.[99] To explore the effect of heating rate in synthesis of iron oxide NPs in OLA alone, NPs were synthesised using the same conditions for 2.4 nm NPs, except different heating

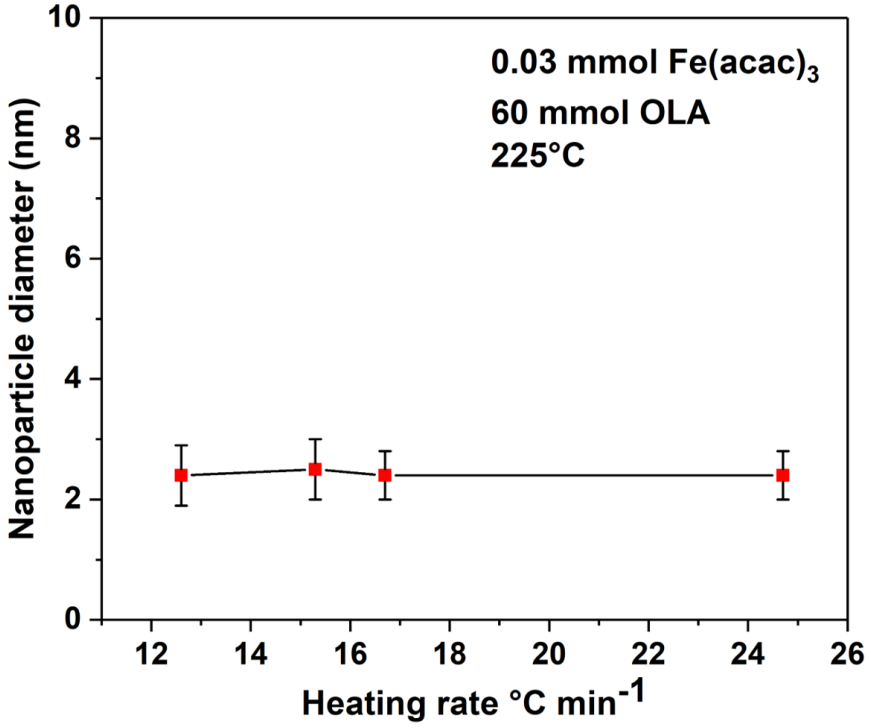


Figure 2.10: Iron oxide NP size in relation to the heating rate. The NP size did not change in response to an increase in heating rate.

rates of 12.6, 15.3, 16.7 and 24.7 ℃ min^{-1} were employed. The resulting NPs were analysed with TEM for any variation in NP size, size distribution or morphology (see appendix B.1.4). As shown in figure 2.10, there was no significant change in NP size in relation to the heating rate. Furthermore, no change in morphology was observed.

A slower heating rate could lead to a wider window for nucleation events to occur as precursor decomposition happens more gradually.[99] This principle is why some researchers opt to use the hot-injection method to ensure rapid precursor decomposition. Slower heating rates did not affect NP size in this study possibly due to the reducing capability of OLA in combination with using rapidly-decomposing acetylacetonate.

Reaction time

The synthesis experiments conducted in this subsection were carried out by Mai Mitzutani under my supervision. I conducted the subsequent TEM investigations and data analysis.

In addition to the heating rate, the period of time for which the reaction is held has been shown to influence NP size. Longer reaction times have typically led to larger NP sizes in similar studies due to Ostwald ripening, or additional NP growth from remaining monomers in solution occurring over time.[68,69,101,104] Generally, others have used reaction times ranging from 1-24 hours. In this study, the incentive to use shorter reaction times was to reduce the window for growth and also to speed up the synthesis process to facilitate scalability. To investigate the influence of time on iron oxide NP characteristics, the reaction was held at 225 ℃ for 10, 30 or 60 minutes whilst all other conditions were kept the same. The average NP sizes obtained were 4.4 ± 0.9, 4.8 ± 0.9 and 4.3 ± 0.9 nm for 10, 30 and 60 minutes respectively. Figure 2.11 shows the TEM micrographs and corresponding size distributions.

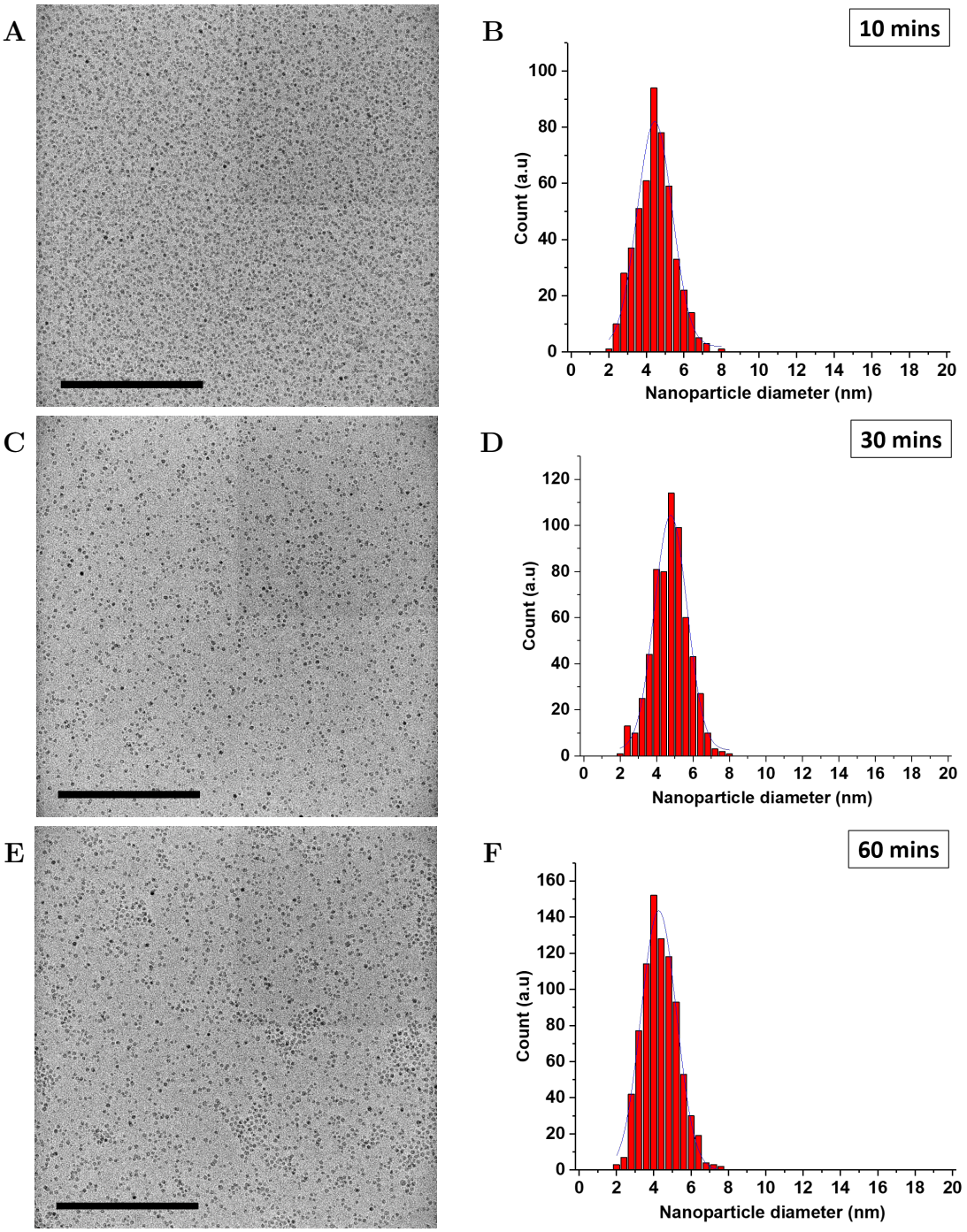


Figure 2.11: TEM micrographs and corresponding size distribution graphs of iron-oxide NPs synthesised with 60 mmol OLA and 0.85 mmol of $Fe(acac)_3$ for reaction times of A-B: 10, C-D: 30, and E-F: 60 minutes. Scale bar is 200 nm. There was no significant difference in NP size between reaction times.

As shown in figure 2.11, varying the reaction time from 10 to 60 minutes did not affect NP size. This implies that after 10 minutes, the precursor monomer supply has already been exhausted and no subsequent growth occurs according to equation 2.5. Alternatively, using an excess of OLA may have ensured that the NPs are sufficiently

capped to prevent Ostwald ripening and other aggregation from occurring.

Reaction temperature

The temperature of the reaction is an important parameter in thermal decomposition. Depending on the reagents used, the temperature can be used to separate nucleation and growth, as well as control NP size.[66] Higher temperatures have been shown to increase NP size by preventing NP dissolution and promoting the growth phase.[30] Conversely the opposite has also been reported, whereby higher reaction temperatures helped to promote precursor decomposition and obtain smaller NP sizes.[69] Such conflicting reports show that CNT cannot always be used to predict NP size due to the influence of multiple parameters.

To assess the influence of reaction temperature on the synthesis of iron oxide NPs in OLA alone, the standard conditions developed for synthesis of 2.4 nm NPs were used (section 2.2.2), however the temperature was varied from 225, to 230 and 250 ℃. Figure 2.12 shows the NP sizes obtained; synthesis conducted at these reaction temperatures did not affect NP size. NP shape was also not affected. However, NP size could be influenced by other reaction temperatures that were not tested. An aliquot of the synthesis mixture was withdrawn at 180 ℃ to assess whether NPs had already formed (hypothesised by the visible colour change) and thus the precursor/precursor-OLA complex had decomposed (see appendix B.1.3). TEM analysis revealed that NPs had already formed by 180 ℃, indicating that precursor decomposition had occurred by this temperature. The low decomposition temperature of $Fe(acac)_3$ in OLA signifies that temperatures >225 ℃ are not required to promote decomposition, and therefore do not affect nucleation. This reinforces the concept that size control in this synthesis is primarily governed by the precursor-to-OLA ratio.

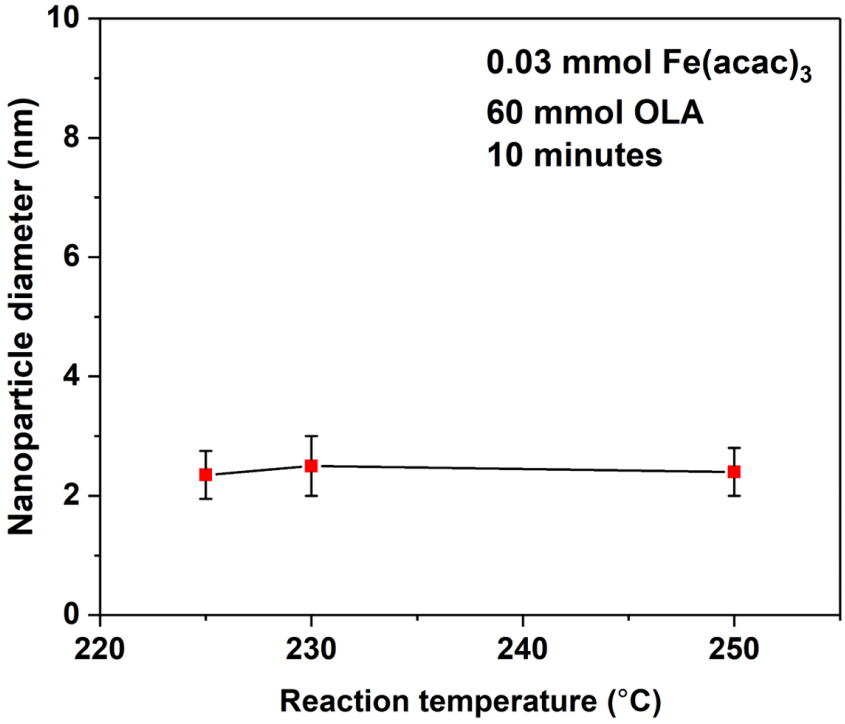
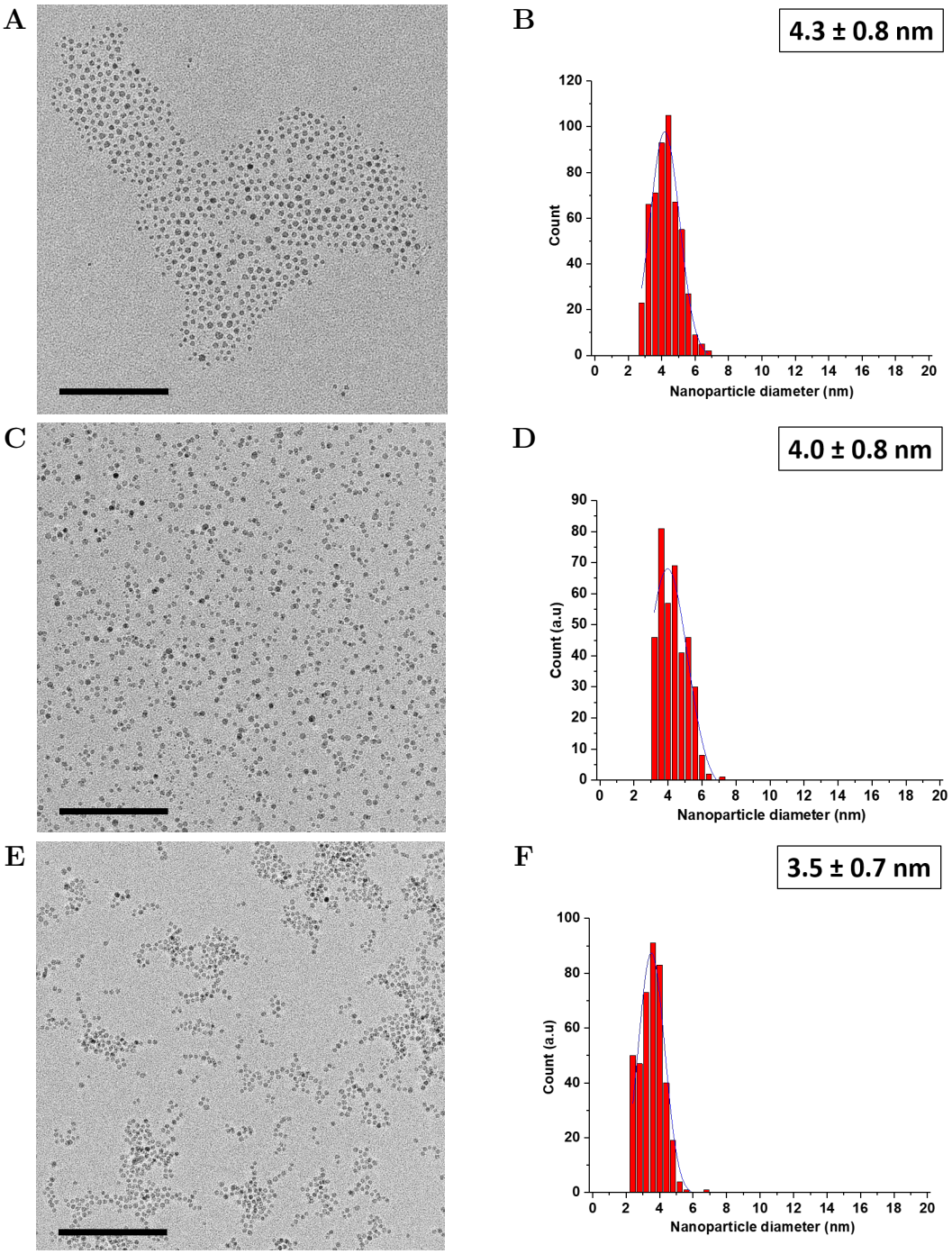


Figure 2.12: Iron oxide NP size in relation to the reaction temperature. The NP size did not change in response to an increase in the reaction temperature from 225 to 250 ℃.

2.4.3 Size-controlled synthesis of cobalt ferrite NPs with oleylamine

The properties of iron-oxide NPs can be tailored towards their target application by substitution of ferrous ions with different metal ions. Substitution with cobalt ions (Co^{2+}) introduces magnetic anisotropy and lowers magnetisation saturation which could be beneficial for T_1 MRI.[19,116] Following investigations with iron-oxide NPs, the same synthesis method was applied to make cobalt ferrite NPs (figure 2.9 section 2.4.1). Confirmation that the NPs were $CoFe_2O_4$ is detailed in the next chapter. A portion of the $Fe(acac)_3$ precursor was substituted for $Co(acac)_2$ so that a molar ratio of 2:1 (Fe:Co) was used. To assess the effect of OLA on cobalt-ferrite NP size, the amount of OLA was kept constant at 60 mmol, and the amount of precursor was varied from 1.4 mmol to 0.03 mmol. Figure 2.13 shows TEM micrographs and corresponding size distribution graphs of cobalt-ferrite NPs synthesised with increasing OLA-to-precursor ratios.


A
B
4.3 ± 0.8 nm
Count
Nanoparticle diameter (nm)
C
D
4.0 ± 0.8 nm
Count (a.u)
Nanoparticle diameter (nm)
E
F
3.5 ± 0.7 nm
Count (a.u)
Nanoparticle diameter (nm)

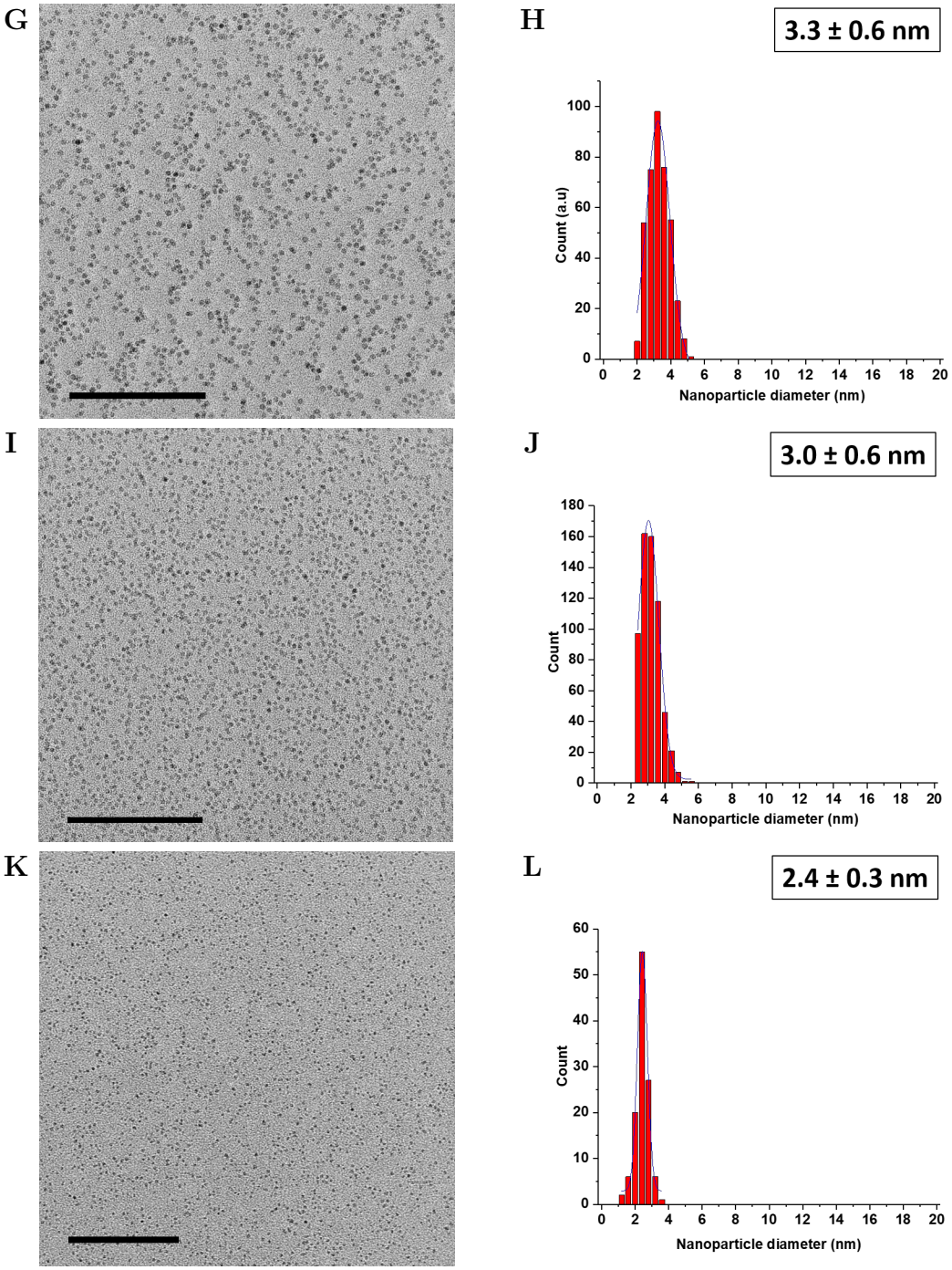


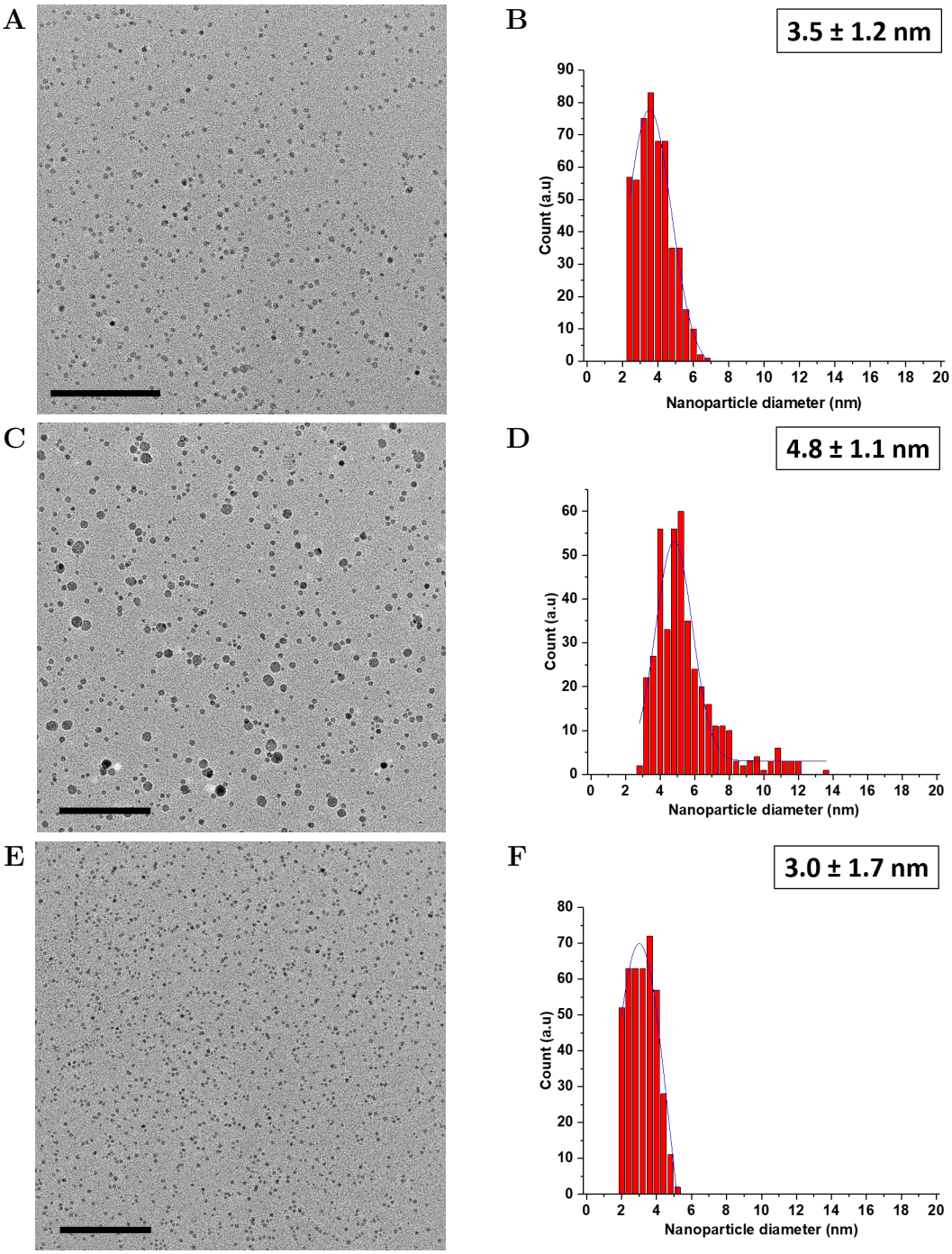
Figure 2.13: TEM micrographs and corresponding size distribution graphs of cobalt-ferrite NPs synthesised with 60 mmol of OLA and A-B: 1.4, C-D: 0.7, E-F: 0.3, G-H: 0.15, I-J: 0.07, and K-L: 0.03 mmol of precursors ($Fe(acac)_3$:$Co(acac)_2$ ratio of 2:1). Scale bar is 100 nm. The NP size decreases from 4.3 nm (A) to 2.4 nm (K) with an increasing oleylamine-to-precursor ratio.

Cobalt ferrite NP size decreased as the precursor-to-OLA ratio increased in the same fashion as iron-oxide NPs. The average NP diameter decreased from 4.3 ± 0.8 nm to 2.4 ± 0.3 nm when synthesised with 60 mmol OLA and 1.4 mmol and 0.03 mmol of precursors respectively. The NPs were also spherical and had a narrow size distribution. Unlike iron oxide NPs where aggregates were observed at a precursor-to-OLA ratio of <1:50, no visible aggregation occurred in the cobalt ferrite sample synthesised under the same conditions (figure 2.13 A,B). To obtain the 2.4 nm cobalt ferrite NPs, the same synthesis conditions used to yield 2.4 nm iron oxide NPs were applied (section 2.4.1)), except 0.01 mmol of $Fe(acac)_3$ was replaced with 0.01 mmol of $Co(acac)_2$. Varying the precursor-to-OLA ratio thus had the same effect on cobalt ferrite NP size as was observed for iron oxide NPs. As the same synthesis conditions could be applied to synthesise both iron oxide and cobalt ferrite NPs, future comparative studies of these materials are possible which may contribute towards identifying the optimum NP for MRI applications.

Effect of Fe:Co precursor ratio on cobalt ferrite NP size

The magnetic properties of cobalt ferrite NPs can be further fine-tuned by varying the ratio of cobalt and iron ions.[116] Chapter 3 explains this further. In this context, experiments using a different molar ratio of Fe:Co precursors were carried out in an attempt to modulate magnetic properties without affecting NP size and size distributions. To examine the effect of the Fe:Co molar ratio on NP size, the same synthesis conditions applied to vary cobalt ferrite and iron oxide NP size were employed (60 mmol OLA, 1-4-0.03 mmol total precursor), however the $Fe(acac)_3$:$Co(acac)_2$ ratio was decreased to 1.5:1. Figure 2.13 shows TEM micrographs and corresponding size distribution graphs of cobalt ferrite NPs synthesised with a $Fe(acac)_3$:$Co(acac)_2$ ratio of 1.5:1.

Figure 2.14 reveals an increase in the precursor-to-OLA ratio led to an overall but inconsistent decrease in NP size. Additionally, NP size distributions were wider in comparison to those synthesised with a 2:1 $Fe(acac)_3$:$Co(acac)_2$ ratio, particularly for larger NPs (>3 nm). A possible source for the increase in polydispersity could be the formation of two distinct crystalline phases as observed by Lu et al.[68] OLA seemed ineffective at controlling NP size in $Co(acac)_2$-rich synthesis. To further explore


A
B
3.5 ± 1.2 nm
Count (a.u)
Nanoparticle diameter (nm)
C
D
4.8 ± 1.1 nm
Count (a.u)
Nanoparticle diameter (nm)
E
F
3.0 ± 1.7 nm
Count (a.u)
Nanoparticle diameter (nm)

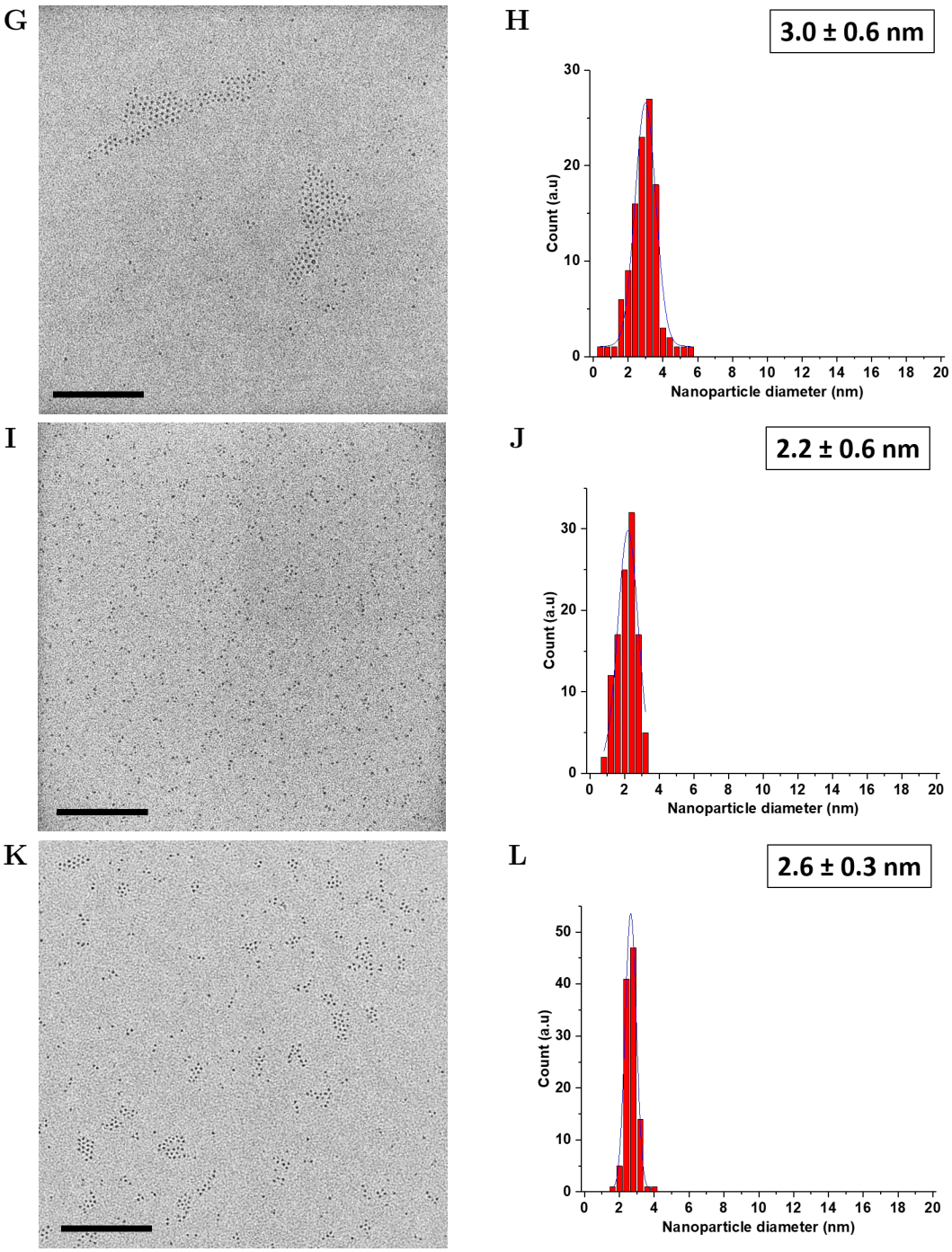


Figure 2.14: TEM micrographs and corresponding size distribution graphs of cobalt-ferrite NPs synthesised with 60 mmol of OLA and A-B: 1.4, C-D: 0.7, E-F: 0.3, G-H: 0.15, I-J: 0.07, and K-L: 0.03 mmol of precursors ($Fe(acac)_3$:$Co(acac)_2$ ratio of 1.5:1). Scale bar is 100 nm. The NP size tends to decrease with an increase in precursor-to-OLA ratio, however the size distribution is wide. Control over NP size with OLA is less effective than when a Fe:Co molar ratio of 2:1 was used.

this, these experiments were repeated using only the $Co(acac)_2$ precursor (detailed below). Due to the wide size distributions obtained, no further experiments using a precursor molar ratio of 1.5:1 were carried out. All cobalt ferrite NPs henceforth were synthesised with a molar ratio of 2:1 Fe:Co.

2.4.4 Synthesis of cobalt oxide NPs with oleylamine

Cobalt oxide NPs were synthesised under the same conditions used for cobalt ferrite and iron oxide NPs, whereby the precursor amount was varied from 1.4 mmol to 0.03 mmol and all other conditions were fixed as described in section 2.4.1. The resulting NPs were analysed with TEM for any variation in NP size, size distribution or morphology (see appendix B.1.5). Figure 2.15 shows the effect of the precursor-to-OLA ratio on cobalt oxide NP size.

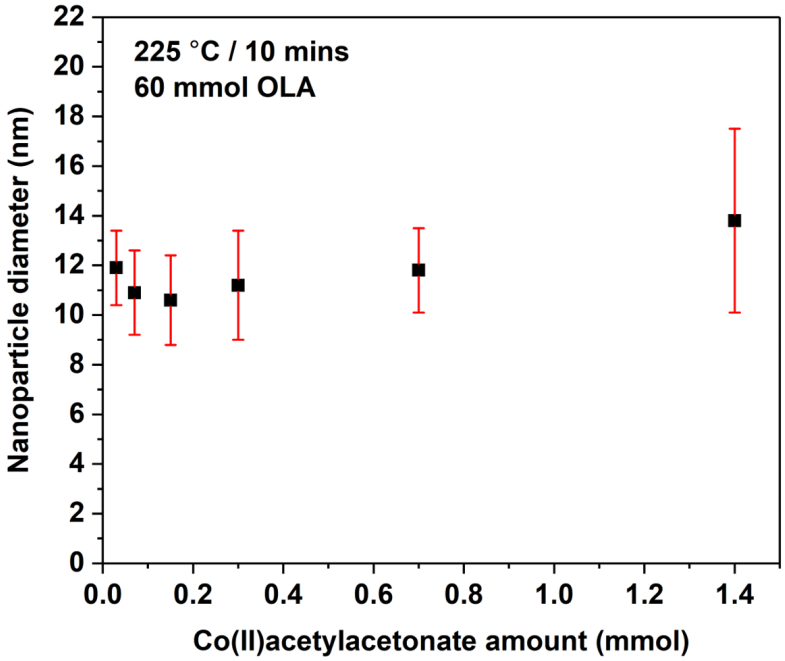


Figure 2.15: Cobalt oxide NP size in relation to amount of precursor. The precursor-to-OLA ratio did not affect NP size.

Changing the precursor-to-OLA ratio did not influence NP size; in all samples NPs were 10-14 nm which is much larger than those obtained for iron oxide and cobalt ferrite. This finding conflicts with results obtained previously in the Nanomaterials by Design Group. Mandel et al. reported an increase in CoO NP size from 10 nm to 19 nm with increasing amounts of OLA.[111,117] However, triphenylphosphine

was used in addition to OLA in his experiments. Thus, it is possible that the observed change in size was due to the amount of triphenylphosphine, and not OLA.

In addition to a larger average size in comparison to iron oxide and cobalt ferrite NPs, the NPs were more faceted and cubic in shape. As all the CoO samples were similar, a representative TEM image of CoO NPs synthesised with 0.07 mmol of $Co(acac)_2$ and 60 mmol OLA is shown in figure 2.16(A). Closer inspection with high-resolution TEM (HR-TEM) revealed that the NPs had voids (figure 2.16 (C)), which are likely created by the diffusion of oxygen anions, due to OLA-induced oxidation at the NP surface.[118,119] This phenomenon is known as the 'Kirkendall effect', which describes the formation of voids due to the difference in diffusivity rates at an interface between different atoms.[120] This effect was also reported in the previous work of Mandel concerning synthesis of CoO with OLA and triphenylphosphine.[117]

The difference in effect of OLA on MFe_2O_4 (M = Fe, Co) and CoO NPs could be due to the binding of OLA to specific crystal facets. OLA typically binds non-selectively and weakly to NPs, thus producing a spherical shape in the case of MFe_2O_4. However, CoO has a rock salt structure and thus a high energy polar (111) facet consisting of solely Co^{2+} ions. Consequently, OLA may selectively bind to this surface to minimise the free energy, encouraging growth along the (111) plane forming a cubic shape. HR-TEM of CoO reveals the crystal structure in more detail (figure 2.16 (D)). The dominance of (111) facets in cubic CoO NPs has been reported previously.[109,121]

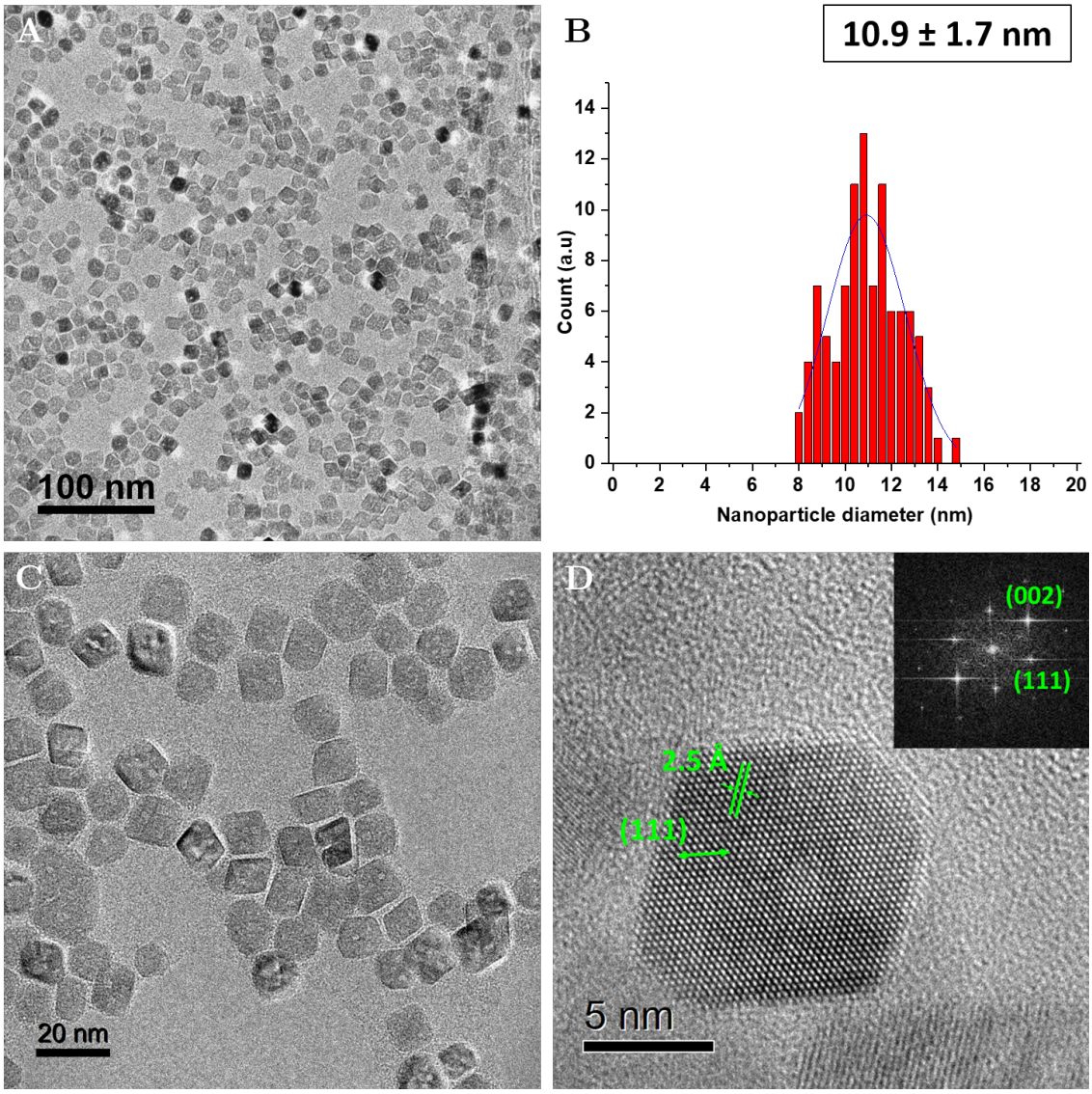


Figure 2.16: *Cobalt oxide NPs synthesised from Co(acac)2 and OLA alone. (A) TEM micrograph of NPs and (B) corresponding size distribution. (C) HRTEM displaying cubic shape and voids. (D) HRTEM of a NP in the [110] zone axis orientation and corresponding fast Fourier transform. The interplanar spacing measured 2.5 Å which matches well with the (111) plane of CoO.*

2.5 Conclusion

The aim of this chapter was to develop a synthesis method capable of producing both iron oxide and cobalt ferrite NPs smaller than 3 nm. In this context, iron oxide, cobalt ferrite and cobalt oxide NPs were synthesised by thermal decomposition of metal acetylacetonates in oleylamine. It was found that the size of iron oxide and cobalt ferrite NPs could be finely tuned from 2.4-5 nm by varying the precursor-to-OLA ratio. Other parameters such as the heating rate, reaction temperature and

time were found to have no significant effect on iron oxide NP size.

OLA was thus primarily responsible for achieving small sizes, with ultra-small (2.4 nm) NPs obtained in a high proportion of OLA. It was hypothesised that varying the precursor-to-OLA ratio controlled NP size in the growth phase, as more OLA restricted growth by limiting the diffusion and/or reaction rate of remaining monomers in the system. It was also hypothesised that small NP sizes were obtained in general as OLA lowered the free surface energy of the system through formation of an OLA-precursor complex, reducing the critical radius required for nucleation to occur. However, FTIR studies to detect the formation of an OLA-precursor complex were inconclusive. Future studies on the decomposition of OLA and acetylacetonate precursors by thermogravimetric analysis (TGA) may be beneficial in this context. Modelling of the thermodynamics of the reaction could also be useful. Interestingly, OLA was not effective at controlling the growth of cobalt oxide NPs, nor cobalt ferrite NPs synthesised with an Fe:Co precursor ratio of 1.5:1. These findings could contribute towards understanding the role of OLA in NP synthesis.

A limitation to this study was that in order to achieve ultra-small NP sizes, small amounts of precursor were required. As a result, the amount of NPs obtained was low (ca. 5 mg per batch). This hampers the ability to conduct multiple characterisations on each batch considering techniques such as TGA and XRD require milligram quantities of dried NPs.

The synthesis method described was rapid, with only 10 minutes reaction time required to yield spherical NPs with narrow size distributions. A key benefit was that ultra-small iron oxide and cobalt ferrite NPs could be synthesised using the same conditions, therefore allowing direct comparison of their properties and toxicity in future studies. This method proved suitable to obtain the ultra-small sizes demanded for application as T_1 MRI contrast agents, however the NPs produced were only soluble in non-polar solvents. Their stability in water was addressed by ligand exchange of hydrophobic oleylamine to hydrophilic dimercaptosuccinic acid which will be discussed in chapter 4. First, the iron oxide and cobalt ferrite NPs produced were characterised to identify their properties, particularly in relation to size and metal composition.

Chapter 3

Properties of ultra-small MFe_2O_4@OLA nanoparticles

Chapter 2 outlined the synthesis of iron oxide and cobalt ferrite NPs by thermal decomposition in oleylamine. Particular focus was given to controlling NP size, as this has a significant effect on the resulting properties. In addition to particle size, the properties of NPs can be dependent on other factors, including overall synthesis conditions, their surface coating, crystallinity and morphology. Thus all nanomaterials require thorough characterisation.

In this chapter, the crystal structure, composition, and magnetic properties of iron oxide and cobalt ferrite NPs are discussed. As there are no previous reports detailing the synthesis of ultra-small ferrite NPs using oleylamine and acetylacetonate precursors, emphasis is given to particles < 3 nm. Following an outline of the analysis methods used, the results of their characterisation by transmission electron microscopy, X-ray diffraction and magnetic measurements are detailed.

3.1 Introduction to iron oxide and spinel ferrites

3.1.1 Iron oxides: Structure and properties

Iron oxide is a widespread naturally-occurring mineral found in soils, rocks and the earth's crust. With 16 different phases (including hydroxides), the four main oxide forms are: magnetite (Fe_3O_4), maghemite (γ-Fe_2O_3), hematite (α-Fe_2O_3) and wüstite ($Fe_{1-x}O$). Hematite is the most abundant form and has a hexagonal close-

packed (HCP) crystal structure with type $R3c$ rhombohedral space group.[122] Bulk hematite is a canted antiferromagnet above -10 ℃ and thus exhibits low magnetization.[123] Wüstite (FeO) is a rock salt structure with a stable cation deficient phase ($Fe_{1-x}O$) which exists at pressures of 0.1 MPa and temperatures higher than 567 ℃, below which it readily oxidises to magnetite.[124] As this study is concerned with the synthesis of spinel ferrites, focus is placed on magnetite and maghemite.

Magnetite and maghemite both have face centered cubic (FCC) spinel structures. Magnetite has a lattice parameter of 8.396 Å and type $Fd3m$ spacegroup following the inverse spinel crystal structure shown in figure 3.2 with the formula $Fe_8^{(3+)}[Fe_8^{(2+)}Fe_8^{(3+)}]O_{32}$ (square brackets denote octahedral sites).[125] Maghemite is a Fe^{2+} deficient form of magnetite and has a similar crystal structure with 32 cubic close packed oxygen anions, 8 Fe^{3+} ions in tetrahedral sites and remaining Fe^{3+} ions situated in octahedral sites according to the formula: $Fe_8^{(3+)}[Fe_{13.3}^{(3+)}\square_{2.67}]O_{32}$, where $\square$= cation vacancies. Vacancies compensate for the oxidation of Fe divalent cations.[124]

Considering the structural similarity of maghemite and magnetite, distinguishing between them can be challenging, particularly on the nanoscale. Identification of magnetite or maghemite particles can be qualitatively estimated by their characteristic colours, with their dispersions appearing black or brown-red respectively (figure 3.1).[126] However mixed phases are often obtained in their synthesis making differentiation difficult. A combination of analytical techniques such as x-ray diffraction, electron energy loss spectroscopy[127,128] and Mössbauer spectroscopy[129] can identify between phases (more details will be given in the next section).[130]

Iron oxide	Color
Hematite (α-Fe_2O_3)	Dark Red
Magnetite (Fe_3O_4)	Jet black
Maghemite (γ-Fe_2O_3)	Brownish-red

Figure 3.1: Characteristic colours of different iron oxide particles (source:[126])

Depending on their size, iron oxide NPs often exist as a combination of magnetite and maghemite. Thermal decomposition synthesis of acetylacetonate typically produces magnetite NPs initially.[67] However, magnetite NPs are susceptible to oxidation in air; the smaller the particles, the more readily they are oxidised due to their larger surface area to volume ratio.[131] Iron oxide NPs are therefore often considered to be composed of a magnetite core surrounded by an oxidised maghemite shell.[30,129,130] The proportion of this oxidised shell is particularly significant in particles smaller than 20 nm due to their large surface-to-volume ratio.[129] The effect of the maghemite shell on the magnetic properties of iron oxide NPs is discussed in section 3.1.3.

3.1.2 Spinel ferrites: Structure and properties

Crystal structure

Ferrites are a class of iron-containing compounds that typically have a FCC spinel crystal structure with the formula AB_2O_4.[132] 'A' represents divalent cations positioned at tetrahedral sites and 'B' trivalent iron ions in octahedral positions (figure 3.2). In tetrahedral sites, four oxygen atoms surround 'A' cations so that lines drawn from each O atom form a tetrahedral shape with the A atom in the centre. Six oxygen atoms surround 'B' sites such that an octahedron shape is formed from their centre lines.[132]

A spinel unit cell consists of 32 oxygen anions, 64 tetrahedral and 32 octahedral sites for cations. To maintain a neutral charge, only 8 of the tetrahedral and 16 of the octahedral sites are filled with cations. If 'A' sites are filled with divalent cations, and 'B' sites trivalent cations, the ferrite is known as a 'normal' spinel. If the 'A' site is filled with trivalent cations, and the 'B' site mixed with divalent and trivalent ions, the spinel is 'inverse'. Spinels with a mixed distribution of ions are called 'mixed' spinels.[62]

The structure of spinel ferrites with cubic close packed oxygens allows for substitution of iron cations with other metal cations. Cobalt ferrite is an inverse spinel obtained by substitution of divalent iron ions with divalent cobalt ions. In comparison, some metal-oxides such as CoO adopt a rock salt structure: the octahedral sites are all filled but the tetrahedral sites are empty and the unit cell is smaller.[133]

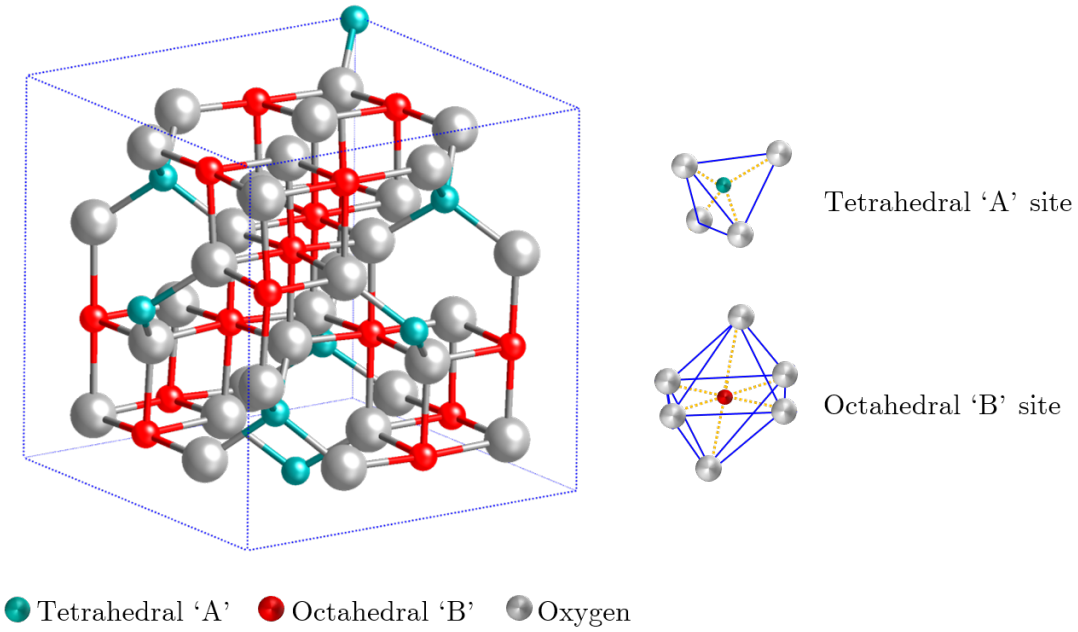


Figure 3.2: The crystal structure of inverse spinel ferrite with 8 divalent cations and 8 trivalent cations occupying octahedral 'B' sites, and 8 trivalent cations occupying tetrahedral 'A' sites.

Magnetite is also an inverse spinel.[62]

Magnetic properties

Spinel ferrites have ferrimagnetic properties due to the cation distribution in A and B sites. Ferrimagnetism differs from ferromagnetism, as exhibited in iron, cobalt and nickel, where all electron spins are aligned parallel with a net magnetisation even in the absence of a magnetic field (hence spontaneous magnetisation). In ferrimagnets, the magnetic moments of cations in the A sites are aligned anti-parallel to those on B sites (figure 3.3). This coupling is a superexchange interaction due to the contribution from oxygen anions between the anti-parallel cations.[134] As there are twice as many B sites to A sites, there is an overall net magnetisation. Ferrimagnets are thus similar to ferromagnets but have lower saturation magnetisation. Antiferromagnets such as hematite have an equal amount of anti-parallel spins thus no overall magnetisation.

The cation composition and distribution in spinel ferrites therefore has a significant effect on the magnetic properties. Ferrite NPs of the same size can have different saturation magnetisation (M_s) values due to varying distributions of cations

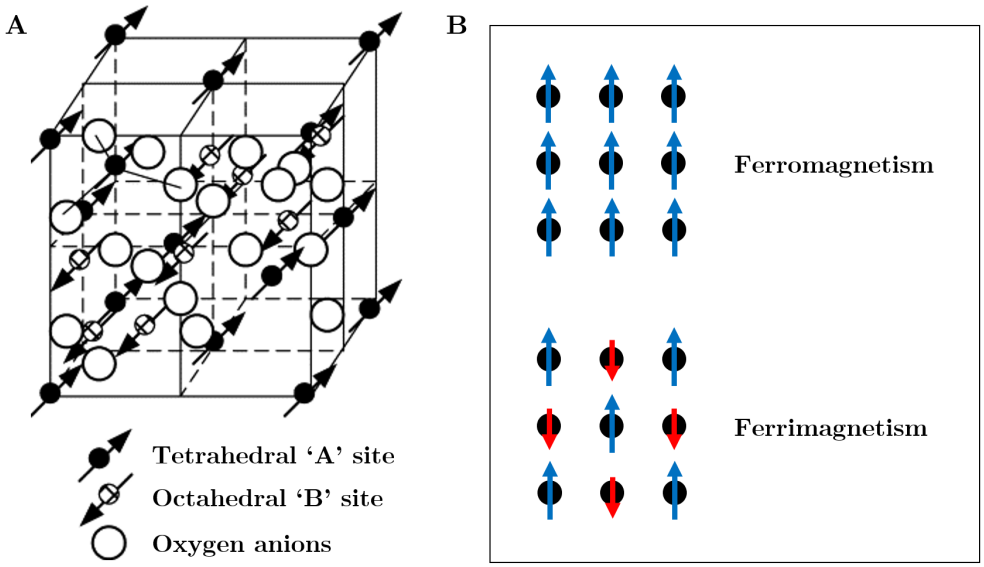


Figure 3.3: A. Schematic of ferrimagnetism in spinel ferrites, with anti-parallel spins in tetrahedral and octahedral sites. B. Difference between ferromagnetism and ferrimagnetism. Adapted from:[62]

in A and B sites.[135] Table 3.1 compares the bulk magnetic properties for common spinel ferrites.

It can be seen from table 3.1 that cobalt ferrite has a slightly lower saturation magnetisation compared to magnetite and maghemite, but has a significantly larger magnetic anisotropy. This magnetocrystalline anisotropy arises due to spin-orbit coupling of cobalt ions, where the spin of the electron is coupled with the magnetic field created by its own orbital motion around the nucleus. The orbit is in turn coupled with the crystal lattice via electric potential of the ions. Coupling of the orbit to the crystal lattice results in a preference for magnetisation along a certain plane, named the 'easy' axis. In the presence of an external field, the strong orbit-lattice coupling resists re-orientation to the 'hard' axis.[136] The energy required to overcome this spin-orbit coupling is the anisotropy energy.

In magnetite, the anisotropy energy originates from the Fe^{3+} ions in the A and B sites and Fe^{2+} ions in the B sites,[147] and the easy axis is [111] due to the lower density of atoms in this direction.[148] In cobalt ferrite, the anisotropy from Fe ions is almost negligible in comparison to that of cobalt ions, and the easy axis is the [100] whilst [111] is the hard axis.[147] The large magnetocrystalline anisotropy of

Table 3.1: Comparison of bulk magnetic properties of common spinel ferrites

Material	Spinel type	Magnetism (300 K)	M_s at 300 K (emu/g)	Curie temp (K)	Anisotropy constant K1 300 K (erg/cm^3)	Refs
Fe_3O_4	inverse	ferrimagnetic	92	858	-1.36×10^5	[137,138]
γ-Fe_2O_3	inverse	ferrimagnetic	80	820–986*	-4.6×10^4	[139,140]
$CoFe_2O_4$	inverse	ferrimagnetic	74.1	793	2.0×10^6	[62,141,142]
$MnFe_2O_4$	mixed	ferrimagnetic	80	573	-33×10^3	[141,143,144]
$ZnFe_2O_4$	normal	paramagnetic	5	-	-	[145]

*Difficult to measure as irreversibly transitions to hematite at 400 ℃[146]

cobalt ferrite means its magnetic moment relaxes much slower than magnetite or maghemite NPs of similar size.[149] This feature highlighted cobalt ferrite NPs for applications in magnetic hyperthermia.

3.1.3 Nanoscale magnetic properties

The magnetism of bulk ferrimagnets is the collective contribution of magnetic domains separated by walls, which have a characteristic width and energy and form to minimise the internal energy of the material. At the nanoscale, there is a size at which it is no longer energetically favourable for the material to consist of several magnetic domains, thus a single domain particle is formed. Single-domain ferrite NPs give rise to a magnetic phenomenon called superparamagnetism.

Superparamagnetism

Superparamagnetic NPs behave similarly to paramagnets, where their magnetic moments align with an overall net magnetisation in the presence of an external magnetic field, however their magnetisation is zero in the absence of a field. The term *super*paramagnetism is derived because the collective magnetic moments of individual particles is much larger than that of atoms.[150]

As previously discussed, in nano-crystalline structures like magnetite and cobalt ferrite, there is magnetocrystalline anisotropy resulting in a preference to align magnetic moments along the easy axis. Therefore, an anisotropy energy barrier (E_B) exists which must be overcome to flip magnetisation from an easy axis to a hard axis. In NPs of small size, thermal fluctuations overcome this anisotropy energy barrier (E_B), causing the direction of magnetisation to randomly flip (figure 3.4). The time

between flips is known as the Néel relaxation time. The resulting fluctuations in the direction of magnetization cause the magnetic field to average to zero.

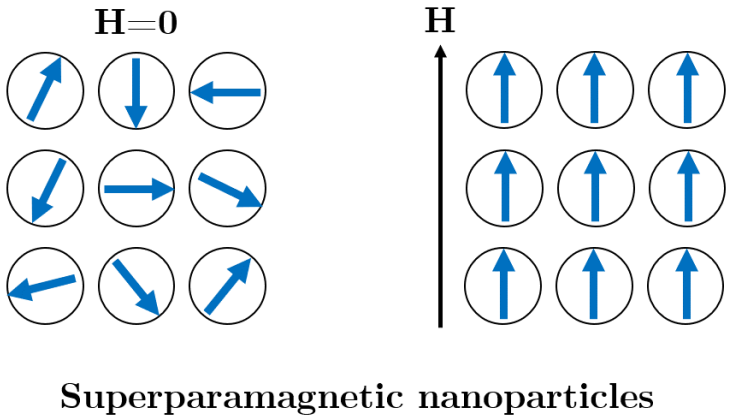


Figure 3.4: Behaviour of superparamagnetic NPs in absence (H=0) and presence of external magnetic field.

Superparamagnetism is thus dependent upon temperature. The temperature at which thermal fluctuation is no longer comparable with E_B in zero magnetic field is known as the superparamagnetic blocking temperature (T_B). Above (T_B), the particles are superparamagnetic. Below (T_B), the magnetic anisotropy energy is greater than thermal fluctuations thus their superparamagnetic state is 'blocked' and the particles act as ferrimagnets again. As particles decrease in size, so does their anisotropy energy, thus (T_B) also decreases with particle size. Evidence of this will be shown later in this chapter.

Superparamagnetic behaviour can be described by the Néel-Brown equation as:

$$\tau = \tau_0 \; exp(KV/k_bT) \tag{3.1}$$

where τ is the Néel relaxation time, τ_0 is the relaxation time constant (ca. $10^{-9}s$), KV is the anisotropy energy, k_B is Boltzmann's constant and T is the temperature. For an arbitrary measurement time of 100 s, and a particle of uniaxial anisotropy (one easy axis), the anisotropy energy barrier is give as:[151]

$$KV = In(\tau/\tau_0)k_BT \tag{3.2}$$

$In(\tau/\tau_0)$ is in the order of 20-25, thus

$$KV = 25k_BT_B \tag{3.3}$$

Rearranging equation 3.3 to find the blocking temperature (T_B) gives:

$$T_B = KV/25k_B \tag{3.4}$$

The size limit for superparamagnetism in magnetite and cobalt ferrite NPs is approximately 25 nm[152] and 10 nm respectively.[14] Table 3.2 compares the blocking temperatures and saturation magnetisations reported in literature for different iron oxide and cobalt ferrite NPs that displayed superparamagnetic properties.

Table 3.2: Comparison of nanoscale magnetic properties of superparamagnetic spherical cobalt ferrite and iron oxide NPs

NP type	Synthesis method	D_{TEM} (nm)	M_s at 300 K (emu/g)	T_B (K)	Ref
Cobalt ferrite	thermal decomposition	4	35	90	[14]
Cobalt ferrite	polyol	5.5	86	200	[149]
Cobalt ferrite	thermal decomposition	6	55	210	[20]
Cobalt ferrite	polyol	6.7	78	289	[149]
Cobalt ferrite	thermal decomposition	7	64	225	[14]
Cobalt ferrite	thermal decomposition	10.5	64	125	[68]
Cobalt ferrite	coprecipitation	15	53	247	[153]
Cobalt ferrite	coprecipitation	21	65	262	[153]
Magnetite	polyol	4.5	43	n/a	[43]
Magnetite	thermal decomposition	6	65	130	[20]
Maghemite	thermal decomposition	2.2	25	5	[30]
Maghemite	thermal decomposition	3	32	8	[30]
Maghemite	thermal decomposition	3	50	n/a	[30]
Maghemite	thermal decomposition	5	23	30	[154]
Maghemite	thermal decomposition	11	42	215	[154]
Maghemite	thermal decomposition	12	49	197	[30]

It can be seen in table 3.2 that an increase in particle size does not necessarily

correlate to an increase in M_s and T_B as anticipated. At the nanoscale, the magnetic properties are sensitive to additional parameters such as the synthesis method. For example, co-precipitation methods tend to produce particles with more defects and lower degrees of crystallinity than high temperature methods such as thermal decomposition and polyol synthesis.[155] In addition, due to their large surface-to-volume ratio, surface effects also contribute towards defining the magnetic properties, therefore the capping agent and surface oxidation play a role.[20]

Spin canting/surface effects

Due to their large surface-to-volume ratio, the relative number of atoms at the surface increases as particle size decreases. In ferrite NPs, the atoms at the surface are subject to a phenomenon known as spin canting, whereby their spins are tilted by an angle about their axis rather than being co-parallel. Spin canting is ascribed to magnetic frustration due to a lower number of neighbour atoms and reduced symmetry at the surface.[156] Spin canting at the surface creates a magnetically disordered layer, decreasing the overall magnetisation (M_s) of the particle. As such, Coey proposed that superparamagnetic ferrite NPs should be thought of as core/shell structures, with a magnetic core and magnetically 'dead' shell (figure 3.5).[157]

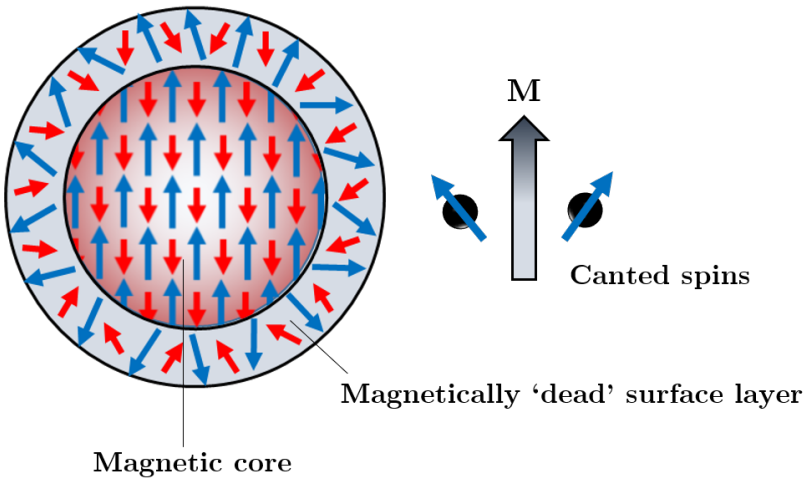


Figure 3.5: Schematic demonstrating the core/shell structure of an iron oxide NP. The particle is composed of a magnetic core with aligned spins which gives rise to its magnetisation. Atoms at the surface are subject to spin canting resulting in a magnetically 'dead' surface layer.

The degree of spin canting can vary depending on the cation distribution,[158] syn-

thesis method,[102] capping agent[20] and particularly particle size.[30,159,160] As particles decrease to the ultra-small scale, they become composed almost entirely of surface atoms (figure 3.6). Therefore, there is a decrease in the saturation magnetisation due to a greater proportion of spin canting, as evidenced by Kim et al. who found that below 3 nm, surface spin canting was responsible for dramatically decreasing the magnetic moment of maghemite NPs from 24,800 μB for 12 nm particles to 83.9 μB and 3.91 μB for 2.2 and 1.5 nm particles respectively.[30] The thickness of the spin canted layer in maghemite is estimated to be 0.5-0.9 nm,[30] thus particle sizes of 1.5 nm were predominantly composed of surface atoms. It will be shown later in chapter 6 of this thesis how this is beneficial for T_1 MRI applications.

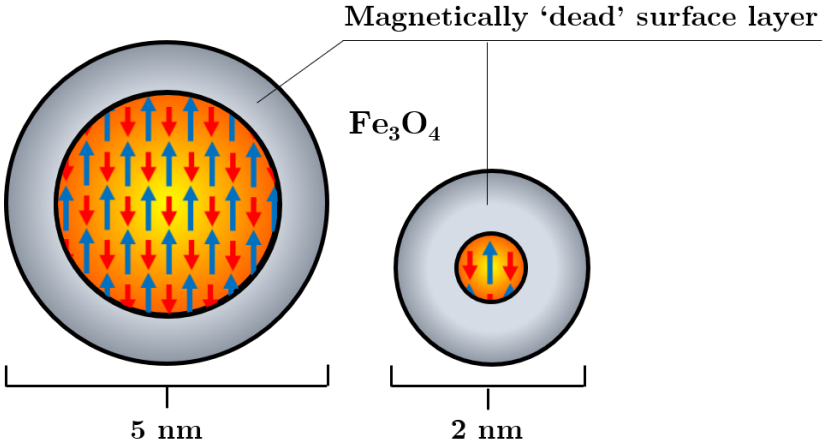


Figure 3.6: The thickness of a magnetically disordered surface layer as a function of NP size. The effect of spin canting is increased in ultra-small NPs due to a larger proportion of atoms being surface atoms.

3.2 Characterisation methods to analyse MFe_2O_4 NPs

The characterisation in this chapter was performed in collaboration with other research groups. Annular dark-field scanning transmission electron microscopy (ADF-STEM) and electron energy loss spectroscopy (EELS) experiments were carried out by Dr. Juan Lozano and Dr. Aakash Varambhia under the supervision of Professor Peter Nellist from the Department of Materials at the University of Oxford. Analysis of the L_2/L_3 intensity ratio was done by Dr. Juan Lozano. EELS elemental

mapping was performed by Dr. Aakash Varambhia. Superconducting quantum interference device (SQUID) measurements were performed by Dr. Tomofumi Ukai and Dr. Yutaka Nagaoka under the supervision of Professor Toru Maekawa at the Bio-Nano Electronics Research Centre at Toyo University, Japan. Finally, X-ray diffraction (XRD) analysis was performed by Rudolf Karos and Dr. Marcus Koch from the Leibniz Institute for New Materials (INM) in Saarbrücken, Germany.

3.2.1 Scanning transmission electron microscopy

STEM is a transmission electron microscopy technique where the electron beam is focussed to a fine point and scanned over the sample in a raster fashion. Image resolution is determined by the probe size and lens aberrations; atomic resolution can be achieved with spherical aberration (C_s) correctors and probe sizes smaller than interatomic distances (0.2-0.5 nm).[112] As in TEM, information about the material is determined from the interaction of the electron beam with the sample.

Annular dark-field (ADF) imaging is a STEM mode whereby a detector consisting of a plate with a hole (annulus) detects signal from incoherent elastic scattered (Rutherford) electrons (>10-50 mrad).[161] Contrast in this imaging mode is called Z-contrast, and is directly related to the atomic number (Z) of the atoms in the sample.[162] ADF-STEM allows visualisation of the crystal structure of materials which is directly interpretable.[163]

The small probe size of STEM presents some challenges for imaging NPs. The electron beam can cause sample damage, and NPs of ultra-small size are particularly beam-sensitive. Furthermore, the sample or stage can drift during scanning, distorting the image. Additionally, the electron beam can cause deposition of amorphous carbon from the TEM grid onto the sample, clouding the resulting image. Contamination can also arise from residual organic solvents on the TEM grid. Strategies to mitigate these issues include baking samples prior to use, using a lower beam voltage (80 kV), or pre-irradiating the sample via a 'beam shower',[164] all of which were employed in the analysis of USNPs in this work. In addition, software tools can be used to correct for drift and to acquire images by a succession of short frames to minimise exposure. Such software used in this work was Smart Align, which was developed by researchers in the Materials department.[165]

The crystal structure of MFe_2O_4@OLA NPs was characterised with ADF-STEM using an aberration-corrected JEOL ARM200F microscope operating at both 80 and 200 kV. NPs in cyclohexane were drop-cast onto a lacey or holey TEM grid and baked at 135 ℃ for 1 hour using a Fischione 1020 plasma cleaner. The inner and outer ADF collection angles spanned ca. 50-242 mrad and a 22.48 mrad probe forming aperture was used with a ca. 17.5 pA beam current. Thirty frames were taken at a 4µs dwell time and then averaged after non-rigid alignment using Smart Align software.[165] CrystalMaker® was used as a visualisation tool to compare observed crystal structures with known structures obtained from the Crystallography Open Database.

Electron energy loss spectroscopy

EELS was performed in conjunction with ADF-STEM to analyse the elemental composition and oxidation state of the NPs. EELS uses the signal from inelastically scattered electrons which pass through the hole in the ADF-detector and travel to the EELS spectrophotometer where they are separated according to their kinetic energies.[166] Inelastically scattered electrons have lost energy, and the amount of energy lost is characteristic for different elements and bonding states.[166] For the EELS spectrum images, a beam current of ca. 88 pA was used with ca. 40 mrad and 90 mrad inner and outer ADF detector collection angles respectively.

Identification of transition metal elements such as iron and cobalt can be achieved by their characteristic ionisation edges, which are formed when an inner-shell electron absorbs enough energy from a beam electron to be excited to a state above the Fermi level.[167] These ionisation edges, known as $L_{2,3}$ 'white-lines', result from transitions from $2p$ levels to unoccupied $3d$ density of states,[168] and can be used to construct elemental maps, giving information about the distribution of different transition metals in the sample. To identify the elemental distribution within the NPs, the acquired images were masked using thresholding and the Fe $L_{2,3}$ and Co $L_{2,3}$ peaks were integrated. This signal was then represented as a multi-coloured binary image. Analysis of TEM micrographs and EELS spectroscopic data was conducted using Gatan DigitalMicrograph® software.

Fitting of the cross-sections of white lines can yield an estimation of the atomic

ratios of Fe, Co and O present in the sample, as well as the oxidation state. Cross-sectional fitting can be done using a hydrogenic white lines model or a Hartree-Slater model. The latter offers a more realistic approximation to the electronic configuration, however the error is approximately 10%.[169] The Hartree Slater model was used to estimate the atomic and intensity ratios of the USNPs from the obtained white lines following background subtraction using Gatan DigitalMicrograph® software.

Fast Fourier transform

Information on the crystal structure can be obtained through analysis of a fast Fourier transform (FFT) of a TEM micrograph. A FFT gives the diffraction pattern (reciprocal space) of a selected region in a TEM image.[170] The diffraction pattern can be interpreted to find the symmetry of the crystal and measure the spacings of atomic planes. Analysis of FFTs cannot reliably distinguish between maghemite or magnetite, but can identify if a structure is cubic spinel ferrite, and only a small area of an image is required, thus it is suitable for analysing the structure of USNPs.

3.2.2 Superconducting quantum interference device measurements of magnetic properties

The magnetic properties of the NPs were assessed using a SQUID (MPMS3, Quantum Design, Inc.). A SQUID is a highly sensitive technique for measuring magnetic flux which consists of a superconducting loop interrupted by two Josephson junctions separated by a thin insulating layer.[171] Any external magnetic field causes a current imbalance that leads to a voltage across the Josephson junction,[172] which is a function of the magnetic flux and can therefore be measured and used to calculate the magnetic flux. Other techniques exist for measuring magnetic flux, such as vibrating sample magnetometers (VSM) which offer the advantage of faster measurements, however SQUID is the most sensitive commercially-available technique.[172] The SQUID used in this work is capable of measuring magnetic fields of less than 1 x 10^{-8} emu.[173] Therefore it is suitable for the measurement of USNPs with potentially weak magnetic properties. It is important to note that SQUID measures the collective magnetic properties of a bulk powder sample and not that of individual NPs. Sophisticated methods such as magnetic force microscopy[174] and nano-SQUID[175]

are in development for single-particle measurements.

SQUID can measure a variety of quantities to determine the magnetic behaviour of NPs, such as saturation magnetisation (M_s), coercivity (H_C), and blocking temperature (T_B). The M_s can be measured by applying an external magnetic field to align spins in one direction until a plateau is reached (spins are saturated), then reversing the direction of the field to return the magnetisation to zero. The magnitude of the field required to reverse magnetisation gives the coercivity, and the magnetic field at zero magnetisation indicates the remanent magnetisation. A superparamagnetic state is indicated by loss of remanent magnetisation.[151] The blocking temperature is obtained by measuring the magnetisation in zero-field and a small applied field as a function of temperature.[176]

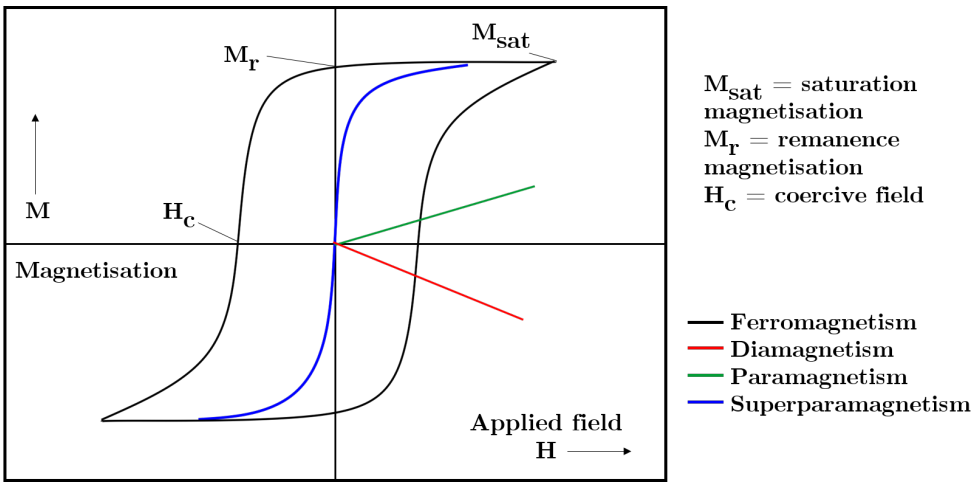


Figure 3.7: Diagram illustrating typical hysteresis curves of different magnetic behaviours

For SQUID measurements, the NPs were dialysed to remove excess OLA as outlined in section 4.2.2 of chapter 4, then dried at 150 ℃.

3.2.3 X-ray diffraction

To further analyse the crystal structure of the NPs, powder XRD was conducted on NPs (prepared as described for SQUID above) in Theta-2-Theta geometry using a Bruker AXS Advance D8 diffractometer operating with copper K-alpha line and equipped with a Lynxeye detector. XRD is a technique used to give information about the crystalline structure of a material such as phase, purity and also particle size. An X-ray directed to a crystalline sample will interact with the atomic nuclei.

Some x-rays will diffract, and interference of these waves can be destructive, or in a few directions, constructive when conditions satisfy Braggs law:[177]

$$2dsin\theta = n\lambda \tag{3.5}$$

where d is the spacing between diffracting planes, Θ the incident angle, n is any integer and λ is the beam wavelength.

X-rays are used for diffraction as their wavelength is around the same size as the interatomic distances of crystal lattice planes (0.15-0.4 nm).[177] The diffraction peaks obtained can be compared to standard reference materials to identify the crystal structure. Although XRD can calculate particle size using the Scherrer equation (eq. 3.6), the formula used does not take size distribution into account, therefore XRD is best used in conjunction with electron microscopy for this purpose.[178]

$$\tau = \frac{K\lambda}{\beta cos\theta} \tag{3.6}$$

where τ is the mean crystallite size and K is a dimensionless shape factor (0.9 for spheres[179]).

3.3 Results and discussion

3.3.1 Crystal structure determination of synthesised USNPs

Following investigations using an ARM200F microscope, atomic-resolution ADF-STEM micrographs of 2.4 nm iron oxide and cobalt ferrite NPs were obtained. Figure 3.8(A) shows a NP obtained from synthesis with 0.03 mmol of $Fe(acac)_3$ and 60 mmol of oleylamine (OLA). The crystal structure corresponds to that of a FCC cubic spinel in the [110] zone axis orientation. Measurement of the lattice fringe revealed a distance of 4.8 Å, which corresponds to the interplanar d-spacing of the (111) plane of magnetite or maghemite. The corresponding FFT (Figure 3.8(B)) shows diffraction spots which can be indexed to the (220) and (111) planes.

Figure 3.8(C,D) shows an ADF-STEM micrograph and corresponding FFT of a particle obtained from synthesis of 0.01 mmol $Co(acac)_2$, with 0.02 mmol $Fe(acac)_3$ and 60 mmol of OLA. The particle also had a FCC cubic spinel structure, and a lat-

tice fringe spacing of 2.4 Å which is in good agreement with the interplanar d-spacing of the (311) plane of $CoFe_2O_4$. The FFT was indexed to the [013] crystallographic orientation of $CoFe_2O_4$.

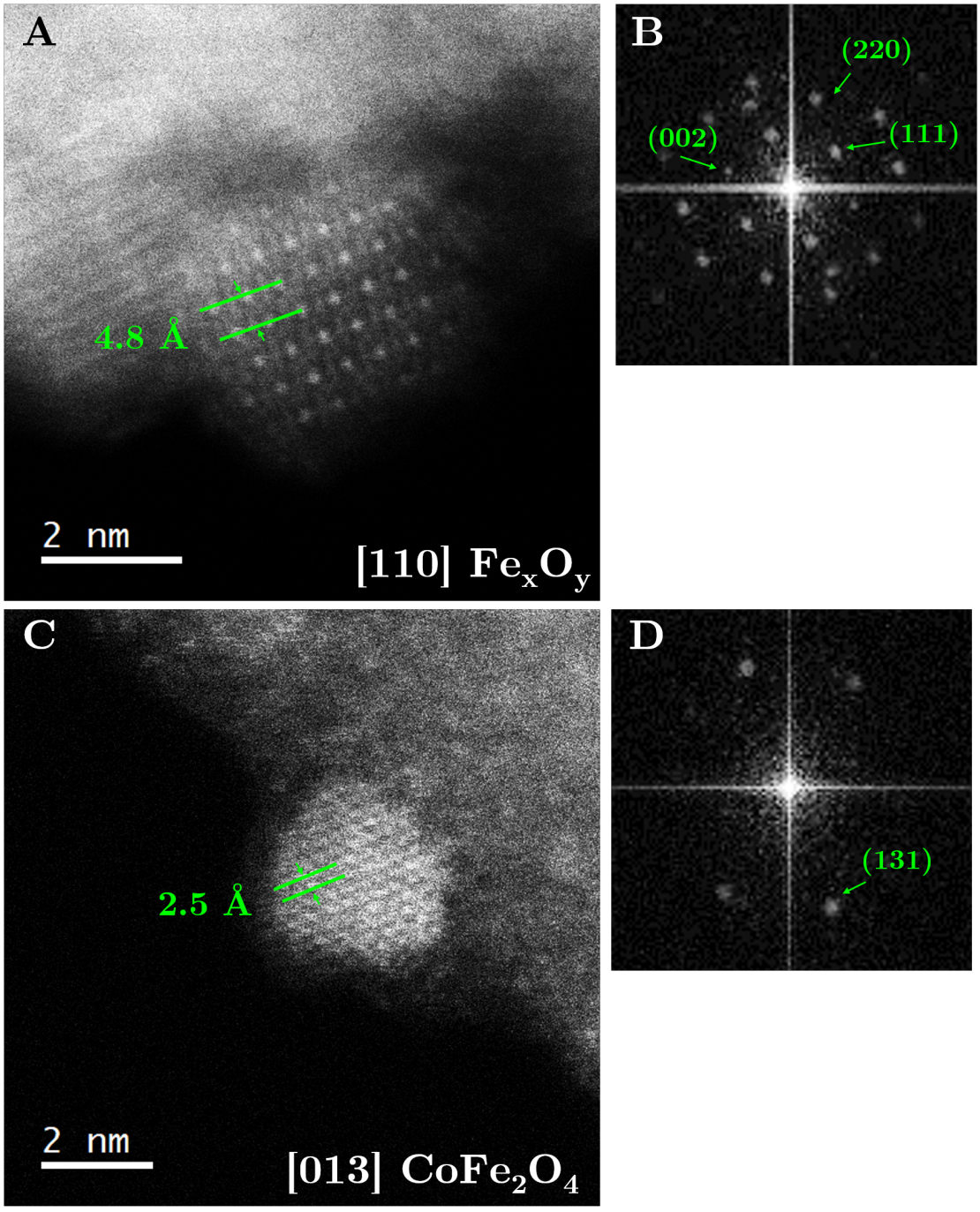


Figure 3.8: ADF-STEM micrographs of (A) iron oxide NP and corresponding FFT (B), and (C) cobalt ferrite NP and corresponding FFT (D).

To inspect the crystal structure in closer detail, multi-frame fast-acquisition and subsequent non-rigid alignment and averaging using Smart Align software were employed on a representative 4.3 nm $CoFe_2O_4$ particle. Figure 3.9(A) reveals a FCC spinel structure in the [110] zone axis orientation with atomic resolution. For comparison, figure 3.9(C) shows the position of cobalt and iron atoms in the inverse spinel cobalt ferrite [110] zone axis orientation where the same periodic arrangement can be seen in the NP. The interplanar d-spacing was measured as 5.96 Å, which corresponds well with the (111) plane of cobalt ferrite.

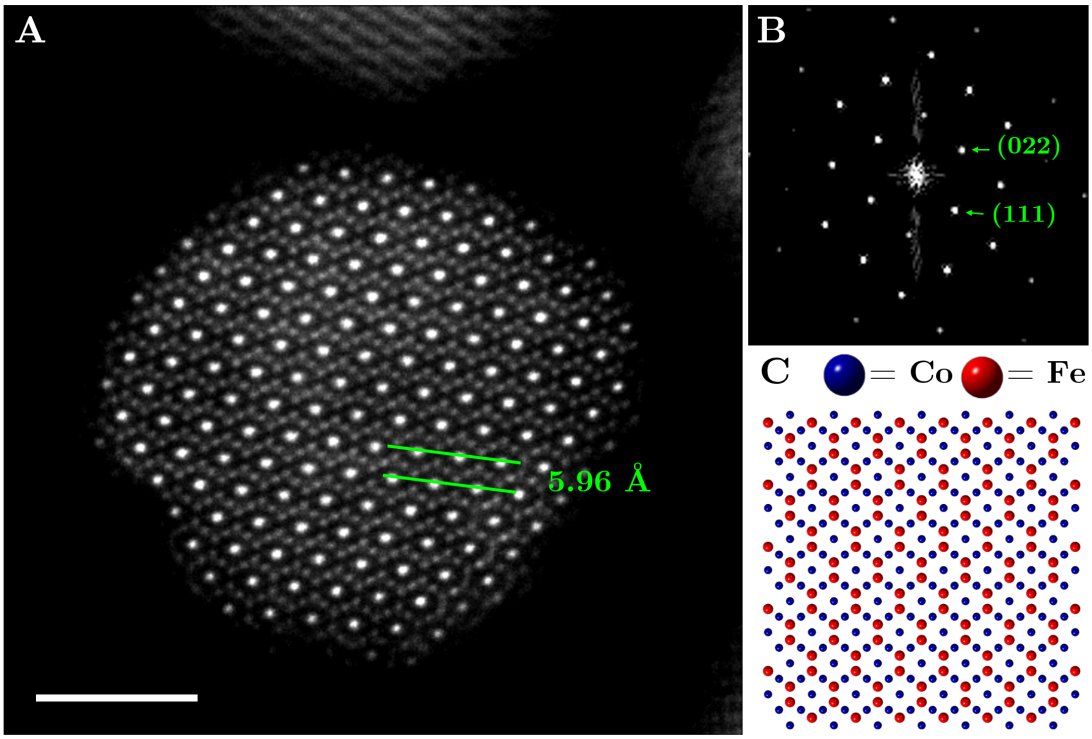


Figure 3.9: (A) Smart Align ADF-STEM micrograph of a 4.3 nm cobalt ferrite NP and corresponding FFT (B). Scale bar = 2 nm. (C) Modelled crystal structure of inverse spinel cobalt ferrite in the the [110] orientation.

XRD was performed as a complementary technique to probe the crystal structure of iron oxide and cobalt ferrite NPs. Particles were synthesised with 1 mmol of precursor and 60 mmol of OLA.

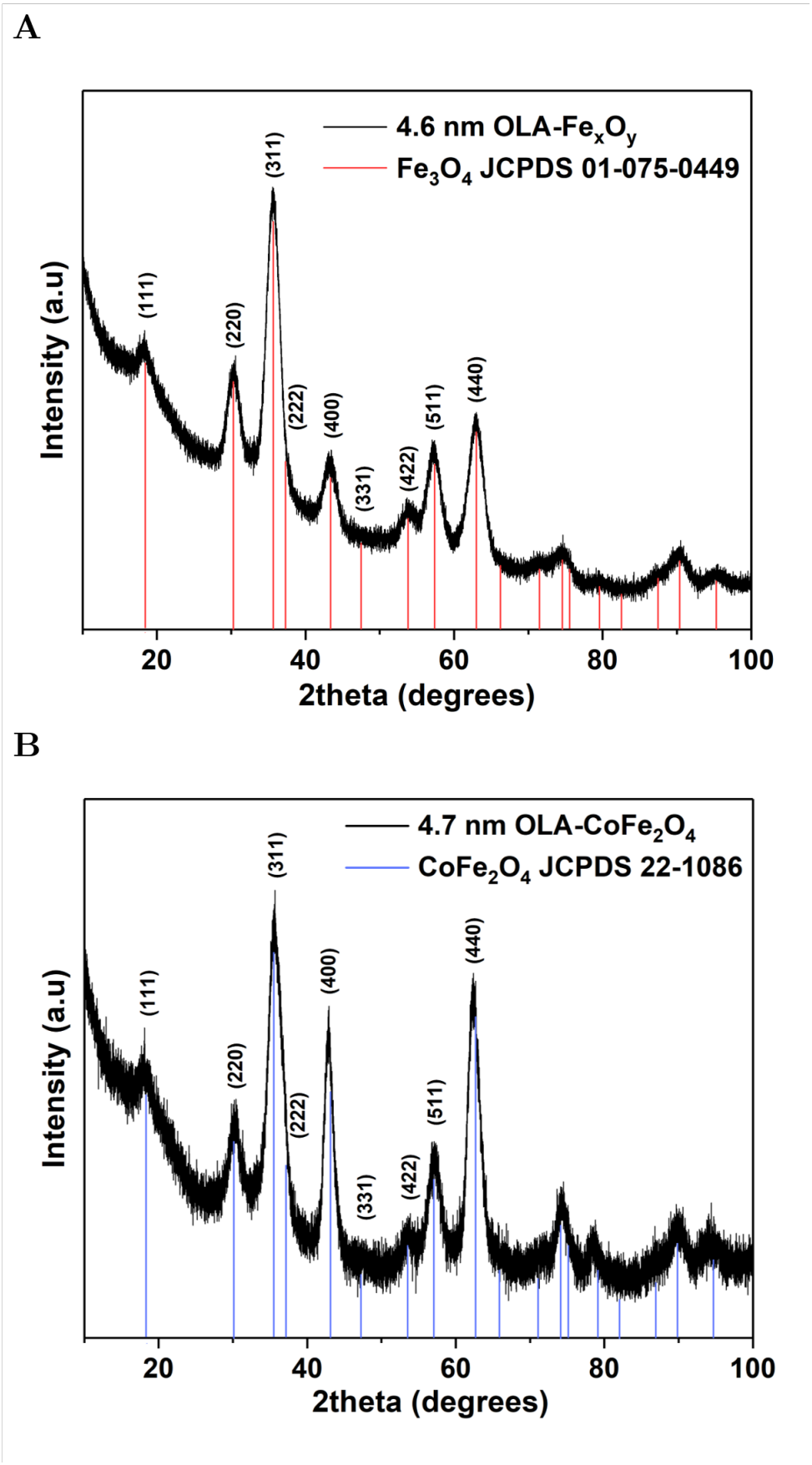


Figure 3.10: XRD pattern of (A) iron oxide NPs and (B) cobalt ferrite NPs synthesised in oleylamine.

Figure 3.10(A) shows the XRD pattern obtained for the iron oxide NPs. The peaks were indexed to the cubic spinel phase of magnetite (JCPDS card 01-075-0449). The lattice parameter of 8.35 Å is also close to that of magnetite (8.34 Å). The particle diameter was calculated to be 4.6 nm which matches well with that obtained by TEM (4.5 ± 0.7 nm). Figure 3.10(B) displays the XRD pattern obtained for cobalt ferrite NPs. The peaks were indexed to the cubic spinel phase of cobalt ferrite with a lattice parameter of 8.40 Å which closely matches the reference (8.39 Å) (JCPDS card 22-1086). The particle diameter was calculated to be 4.7 nm which is similar to that measured from TEM studies (4.8 ± 1.1 nm).

3.3.2 Composition and oxidation state of synthesised USNPs

To determine the elemental composition and oxidation state of the NPs, EELS was performed. The EELS spectrum obtained for 2.4 nm iron oxide NPs is shown in figure 3.11. Peaks corresponding to the K ionisation edge of oxygen (530 eV) and the L ionisation edges of iron (710 eV) are present, confirming the NPs are composed of iron and oxygen. Quantification using the Hartree-Slater model showed an atomic ratio (/O) of 0.68 ± 0.07 for iron, which matches best with maghemite.[127,169] Quantitative analysis of the Fe-$L_{2,3}$ ionisation edges can also indicate the oxidation state of iron-oxide, as the (L_3/L_2) intensity ratio can vary depending on the oxidation state.[128] The intensity ratio of L_3/L_2 was found to be 4.49, which is in good agreement with the value for magnetite.[128]

To further investigate oxidation state, the shape of the Fe 2p L edges were examined in closer detail. Magnetite presents a shapeless L_3 peak and an L_2 edge with three distinct features, whereas maghemite displays a pre-shoulder on the L_3 peak and a post-peak on the L_3 edge.[180] The inset of figure 3.11(A) shows the L_3 peak in closer detail; the L_3 edge is smooth without a shoulder and the L_2 edge looks similar to that obtained by Almeida et al., further suggesting the composition of the NPs is Fe_3O_4. Due to their small size it is possible that the NPs are a mixture of magnetite and maghemite, or that they oxidise to maghemite over time. Differentiating between the two is notoriously challenging at the nanoscale, and it was not possible to quantitatively distinguish between them. Nonetheless, the black colour of the iron oxide NPs (see figure 2.7 section 2.4.1) suggests that the NPs are

predominantly magnetite.[126] Thus for the purpose of clarity, synthesised iron oxide NPs in this work will be referred to as Fe_3O_4 for the remainder of this thesis.

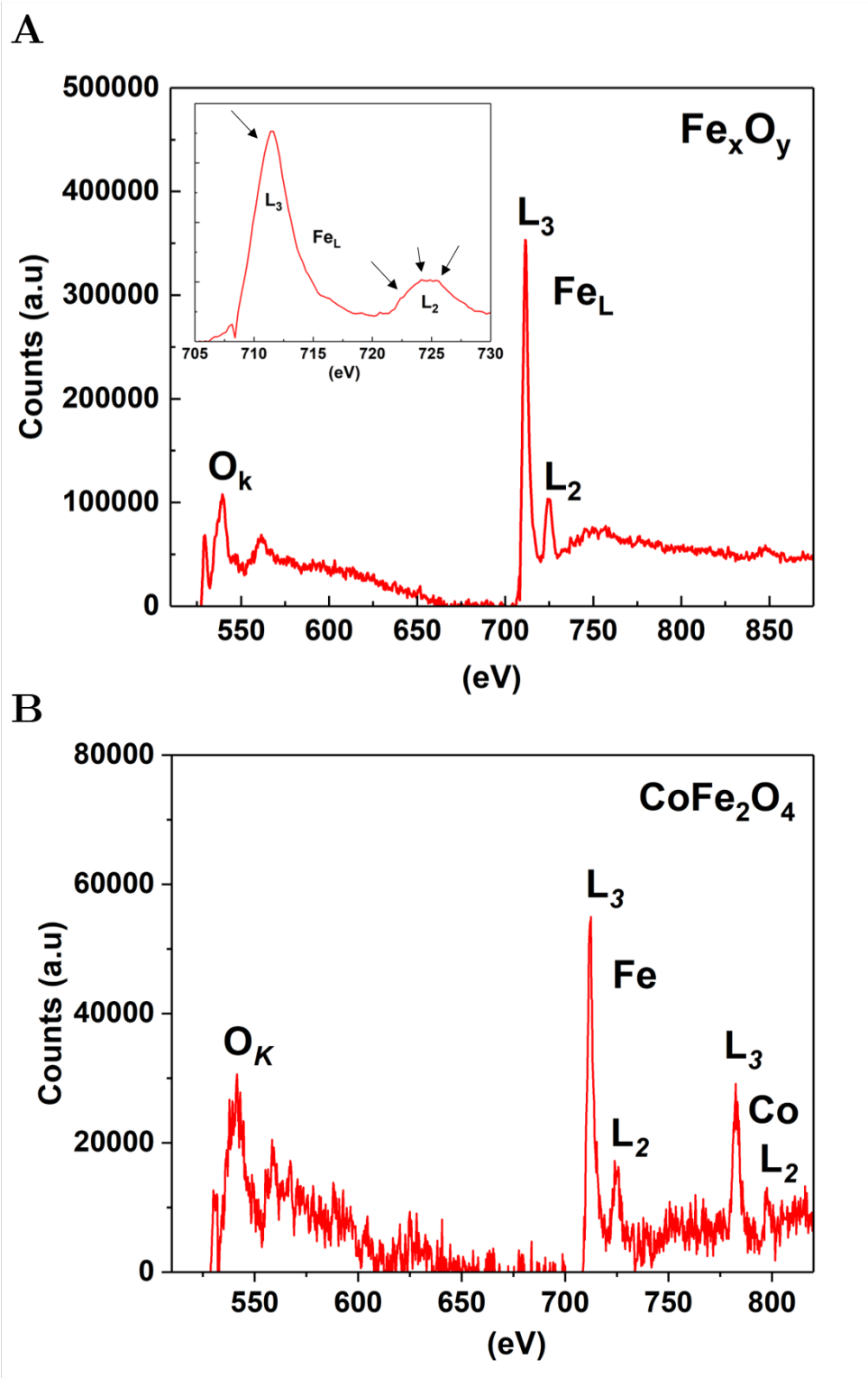


Figure 3.11: (A) EELS spectrum of 2.4 nm iron oxide NPs showing the oxygen K and iron L ionisation edges and (inset) the L edges in the range of 705-730 eV presenting a smooth L_3 peak. (B) EELS spectrum of 2.4 nm cobalt ferrite NPs showing three peaks corresponding to the oxygen K, and iron and cobalt L ionisation edges.

EELS spectroscopy of 2.4 nm cobalt ferrite NPs revealed three peaks corresponding to the K ionisation edge of oxygen, the L ionisation edge of iron, and an additional peak at 780 eV which is the L ionisation edge cobalt, confirming the presence of cobalt in the particles (figure 3.11(B)). Quantitative analysis of the EELS spectrum using the Hartree-Slater model revealed a relative composition of 56 ± 6% oxygen, 27 ± 3% iron and 17 ± 2% cobalt, which corresponds well with the composition of cobalt ferrite ($CoFe_2O_4$).

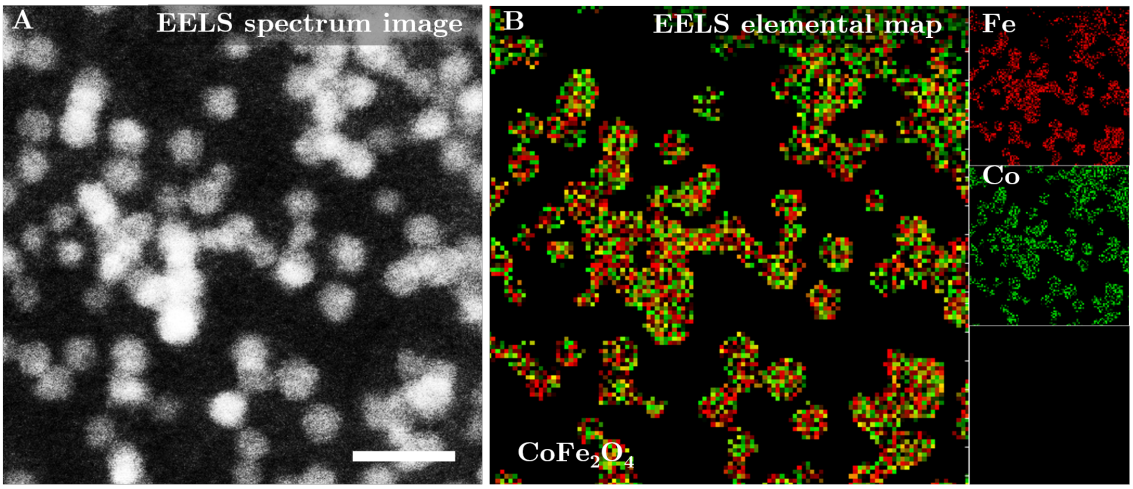


Figure 3.12: (A) EELS spectrum image of 2.4 nm cobalt ferrite NPs and (B) corresponding elemental map (red = iron, green = cobalt) showing a homogeneous distribution of cobalt and iron atoms in 3 nm $CoFe_2O_4$ NPs. (scale bar = 10 nm).

To probe the distribution of iron and cobalt in the NPs to see if it is one phase of cobalt ferrite and not a mix of iron and cobalt oxides, EELS elemental mapping was conducted. Figure 3.12 shows the EELS spectrum image before and after elemental mapping, displaying a homogeneous distribution of cobalt and iron in the particles.

3.3.3 Magnetic properties of synthesised USNPs

Following investigation into their crystal structure and elemental compositions, the magnetic properties of the NP were assessed. Emphasis was given to the effect of NP size on the magnetic properties of cobalt ferrite NPs since size-dependent studies on the magnetic properties of iron oxide NPs have been well described elsewhere.[30]

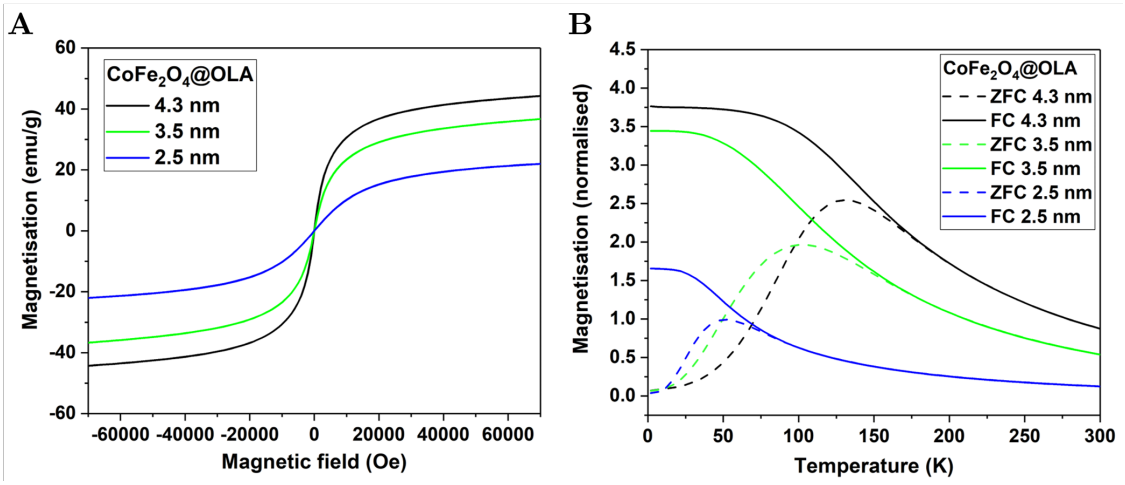


Figure 3.13: (A) Magnetisation curves of 4.3, 3.5 and 2.5 nm $CoFe_2O_4$@OLA NPs at 300K. (B) Corresponding temperature-dependent magnetisation (zero-field cooling (ZFC) and field-cooling (FC)) curves. The FC curves were obtained at an applied field of 100 Oe.

The magnetic properties of 4.3, 3.5 and 2.5 nm cobalt ferrite ($CoFe_2O_4$@OLA) NPs were assessed at 300 K and 4 K. The particles displayed typical superparamagnetic behaviour with zero remanence and coercivity (figure 3.13(A)). The magnetisation saturation (M_s) decreased with particle size as anticipated, with 4.3, 3.5 and 2.5 nm particles having (M_s) of 44, 37 and 22 emu/g respectively at 300 K. Analogously, the blocking temperature (T_B) decreased with particle size from 131 to 101 and 52 K for 4.3, 3.5 and 2.5 nm particles (figure 3.13(B)).

At low temperature (4 K), the particles displayed large coercivities with 4.3, 3.5 and 2.5 nm particles having (H_C) values of 14.5, 15.3 and 17.0 KOe respectively 3.14. Hysteresis was observed at 4 K as their superparamagnetic state is blocked and they act as ferrimagnets. Interestingly, as particle size decreased the coercivity increased. Previous studies into the size dependence of coercivity in ferrite NPs state that a nonmonotomic pattern should be observed where above the single domain size, coercivity decreases with increasing particle size due to the formation of multi-domains.[181] Below the single domain size however, coercivity should decrease with decreasing particle size owing to a smaller overall magnetic volume.[13,14] The increase in H_C with decreasing particle size observed in this work can be explained by the enhanced contribution of surface magnetocrystalline anisotropy to the coercivity. Spin canting at the surface of ferrite NPs creates magnetic disorder, as described in section 3.1.3. Due to the ultra-small size of the particles, surface effects strongly

influence the magnetic properties, and at 2.5 nm, the particles are composed largely of surface atoms. The larger contribution of magnetocrystalline anisotropy in 2.5 nm NPs has therefore increased the coercivity. Theoretical and experimental studies support this observation.[182–184]

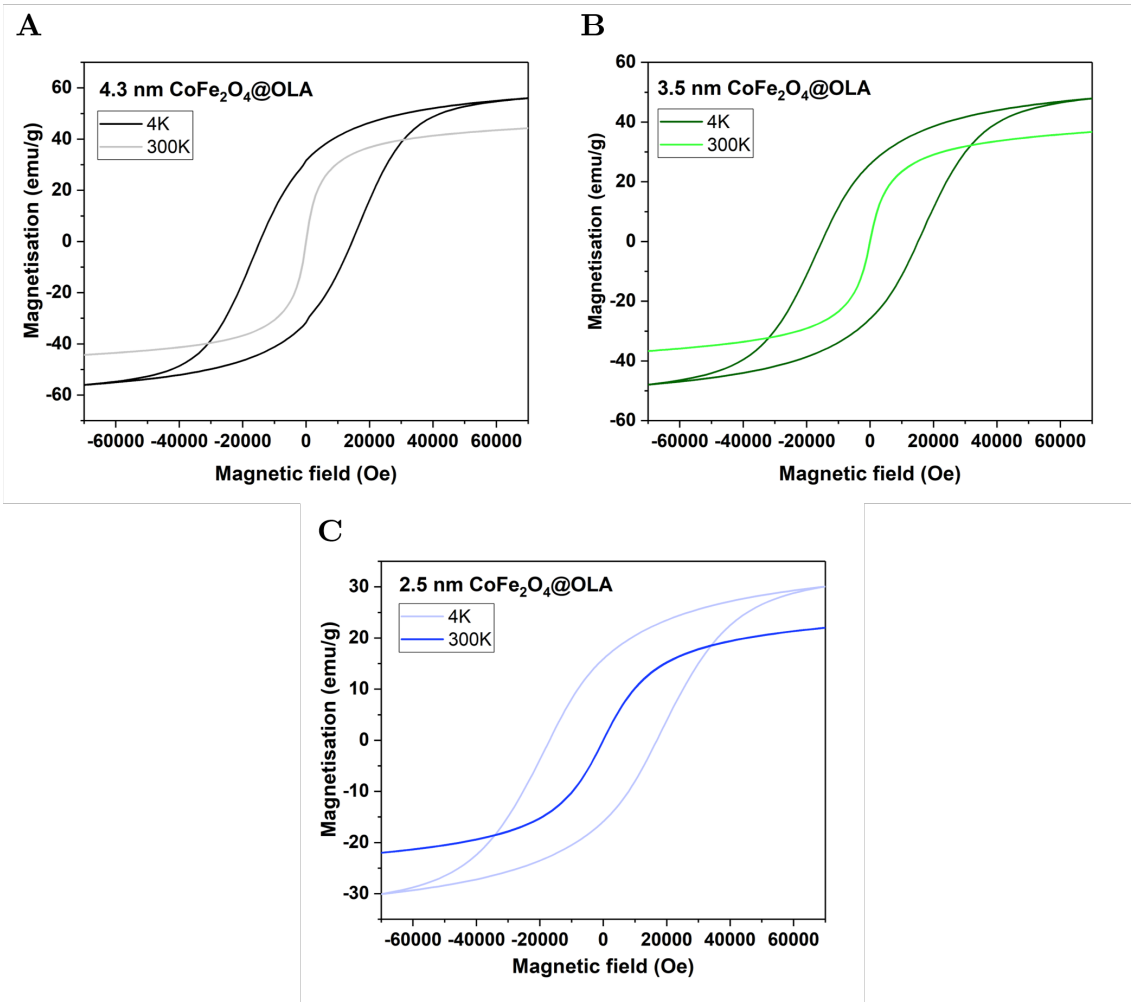


Figure 3.14: Magnetisation curves of (A) 4.3, (B) 3.5 and (C) 2.5 nm $CoFe_2O_4$@OLA NPs at 300 K and 4 K.

For comparison, the magnetic properties of 4.0 nm iron oxide NPs were measured at 300 K. Figure (figure 3.15(A)) shows the particles also displayed typical superparamagnetic behaviour with no coercivity or remanence. Their M_S was 55 emu/g, which is slightly larger than that obtained for 4.3 nm cobalt ferrite NPs (44 emu/g). In comparison to magnetite, bulk cobalt ferrite possesses 90% saturation magnetisation,[19] thus lower M_s values for $CoFe_2O_4$ NPs were expected, and similar results have been reported previously.[20] The T_B of Fe_3O_4@OLA NPs however was much lower in comparison to cobalt-ferrite particles, at 44 K compared to 131 K.

This rise in T_B is characteristic for $CoFe_2O_4$ due to an increase in anisotropy energy courtesy of Co^{2+} ions.[153]

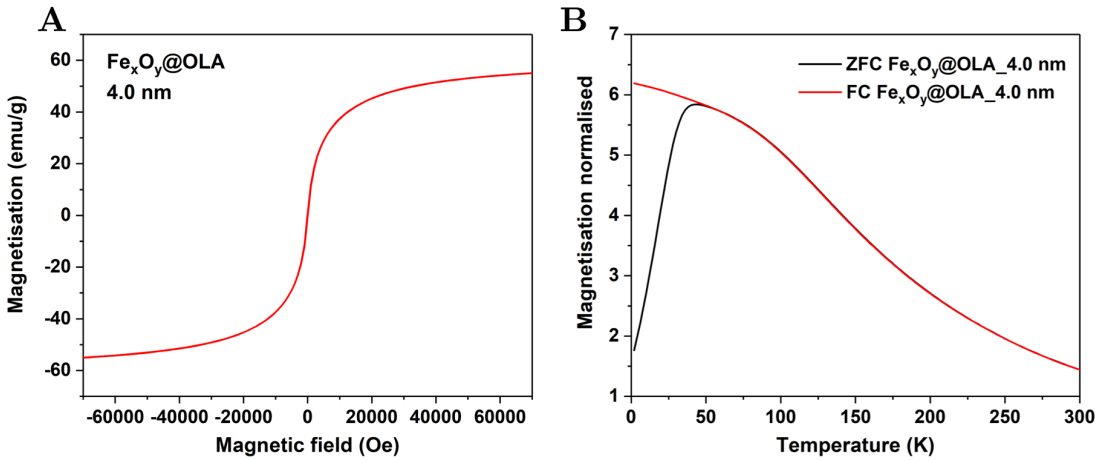


Figure 3.15: (A) Magnetisation curve of 4.0 nm iron oxide NPs at 300K. (B) Corresponding temperature-dependent magnetisation (zero-field cooling (ZFC) and field-cooling (FC)) curves. The FC curves were obtained at an applied field of 100 Oe.

The magnetic moments (m) of the NPs were calculated from the following equation:

$$m = \frac{M\rho V}{\mu_B} \tag{3.7}$$

where M is mass magnetisation, ρ is the material density, V is particle volume and μ_B is the Bohr magneton value.[30] Table 3.3 summarises the results for oleylamine-coated ferrite NPs. 2.5 nm cobalt ferrite NPs have a very small magnetic moment of 103 μB. This small magnetic moment arises due to the large surface-to-volume ratio and thus prominence of the magnetically dead surface layer.[185]

Table 3.3: Table outlining the magnetic properties of oleylamine-coated cobalt ferrite and iron oxide NPs

NP type	D_{TEM} (nm)	M_s 300 K (emu/g)	T_B 100 Oe (K)	H_C 300 K (KOe)	M_s 4 K (emu/g)	H_C 4 K (KOe)	Magnetic moment (μB)
Iron oxide	4.0 ± 0.8	55	44	0	-	-	1029
Cobalt ferrite	4.3 ± 0.8	44	131	0	60	14.5	976
Cobalt ferrite	3.5 ± 1.7	37	101	0	48	15.3	471
Cobalt ferrite	2.5 ± 0.4	22	52	0	30	17.0	103

At the ultra-small scale, the surface properties of NPs play an important role in their magnetic behaviour. In chapter 4 of this thesis, the effect of surface coating on the magnetic properties of USNPs is addressed with SQUID measurements following ligand exchange of OLA with dimercaptosuccinic acid and bovine serum albumin (section 4.3.2).

3.4 Conclusion

In this section, the structural and magnetic properties of iron oxide and cobalt ferrite NPs were investigated. ADF-STEM revealed both particle types had highly crystalline FCC spinel type structures. Good agreement was found between the EELS and XRD studies that the cobalt ferrite NPs were a homogeneous mixture of cobalt, iron and oxygen with a stoichiometric ratio resembling that of $CoFe_2O_4$. The iron oxide NPs presented a crystal structure that could be indexed to either magnetite or maghemite. XRD and EELS studies were also inconclusive as to which oxidation state the particles were. It is likely that the particles were either a) a mixture of maghemite/magnetite, or b) were initially magnetite but oxidised to maghemite over time. Due to their ultra-small size it was not possible to distinguish them. Mössbauer spectroscopy is a technique which may offer further insight,[126] however is beyond the scope of this work.

The magnetic properties of the particles were assessed using SQUID magnetometry. Both iron oxide and cobalt ferrite NPs were superparamagnetic in the size range of 2.5-4.3 nm. Cobalt ferrite NPs displayed size-dependent high coercivity values at low temperature. 2.5 nm particles exhibited the highest coercivity of 17.0 KOe owing to the greater influence of surface magnetocrystalline anisotropy due to their larger surface-to-volume ratio. Similarly, the saturation magnetisation and blocking temperature were found to be dependent on particle size, reducing with smaller particle sizes. The magnetic properties are important for potential application as MRI contrast agents, whereby low saturation magnetisation values are desirable for T_1 imaging. In this context, 2.5 nm cobalt ferrite NPs could be suitable candidates, offering a very small magnetic moment of 103 μB.

Chapter 4

Phase transfer and stability studies for water-dispersible ultra-small ferrite NPs

Chapters 2 and 3 have described the synthesis and properties of ultra-small ferrite NPs using oleylamine as the capping ligand. Oleylamine is hydrophobic, therefore it is unsuitable for biomedical applications where biocompatibility and particle stability in aqueous media are critical. This chapter describes two methods explored to transfer hydrophobic oleylamine-capped particles from a non-polar to polar phase in consideration for *in vivo* imaging applications. The two methods detailed are: a new direct phase transfer method using bovine serum albumin (BSA), and an established ligand exchange method using dimercaptosuccinic acid (DMSA). First, background is given on the key processes which govern the fate of the NPs *in vivo*. The dependence of these processes on the hydrophilicity, surface ligand and other particle characteristics are then discussed. The method section outlines both routes and the characterisation tools used to evaluate the general properties and stability of the particles. In the results section, both method's ability to yield NPs with the desired characteristics for *in vivo* imaging applications (no changes to particle core size, small hydrodynamic diameters and excellent stability in storage and physiological conditions) are evaluated.

The work in this chapter was conducted in collaboration with the Nano Cell Interaction Group at the Leibniz Institute for New Materials (INM).

4.1 Introduction

NPs which are intended for biomedical applications are subject to strict design parameters in order to ensure their optimum performance and minimised toxicity *in vivo*. To understand which NP characteristics are desirable for the intended application, it is important to know the pharmacokinetics of particles intravenously delivered, known as 'particokinetics'.[186] In the human body, the NPs will encounter a complex media composed of salts, sugars, proteins, and lipids, all of which are likely to interact with the NPs. In addition, NPs will encounter cells, macrophages, organs, and other biomolecules which can trigger an immune response or have an adverse effect on health. With a plethora of surface interactions happening between NPs and biomolecules *in vivo*, the choice of ligand is very important. The complex interaction of NPs *in vivo* is an ongoing and critical area of research and there are many fundamental unknowns. However, research has identified key processes involved with the uptake, transport, distribution, and degradation of NPs *in vivo* (outlined in figure 4.1, detailed information can be found elsewhere[29]). These processes are discussed below in the context of iron oxide NPs intravenously delivered for imaging purposes.

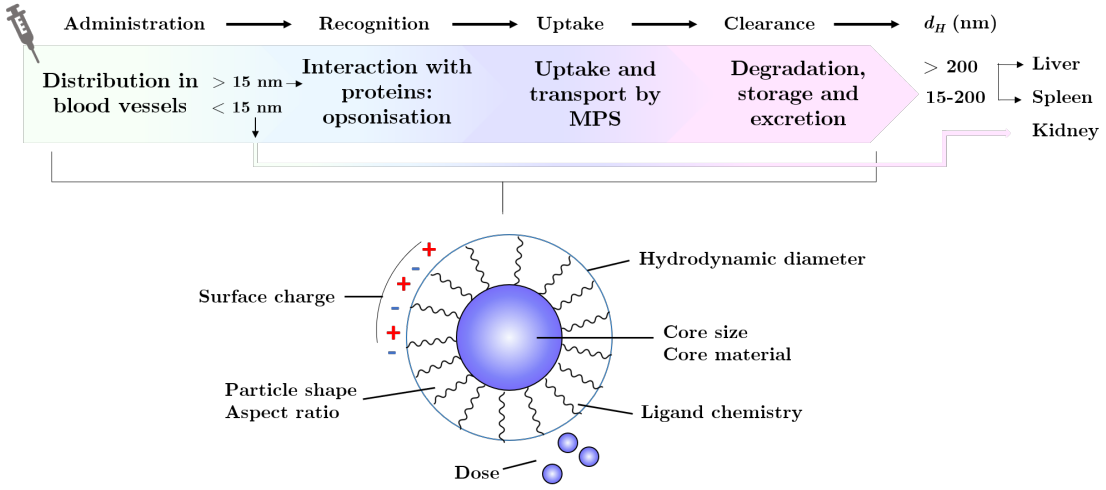


Figure 4.1: Overview of main *in vivo* pathway of iron oxide NPs. Particles with a hydrodynamic diameter smaller than 15 nm can escape detection and follow elimination via the kidneys. Larger particles are engulfed by macrophages in the liver and/or spleen, then degraded by lysosomes.

Blood distribution For NPs which are intravenously delivered, their fluid dynamics in blood vessels influences their circulation times. The blood or plasma

half-life ($t_{1/2}$) of the NPs is the time it takes for the concentration of the injected NPs in the blood to decrease to half its initial value.[29] SPIONs larger than 40 nm have a plasma half-life of 30 minutes, making them suitable for liver-imaging MRI as they rapidly accumulate there after administration. SPIONs smaller than 40 nm have a half-life of two hours, enabling their application as blood-pool agents for MR angiography.[187]

Protein corona The protein corona describes the adsorption of plasma proteins, albumin, immunoglobulins and other biomolecules onto the surface of NPs following *in vivo* administration.[188] The biomolecules that form the protein corona can interact with receptors on the surface of phagocytes, after which they are internalized, transported to phagosomes and fused with lysosomes.[188] NP size, surface modification and surface charge influences which and how many opsonins adsorb, thereby influencing the fate of NPs *in vivo*. If the NP is coated with a targeting ligand, formation of a protein corona can inhibit its functionality. Conversely, the protein corona can be harnessed to help NPs cross the blood brain barrier if desired.[186]

Immune response and clearance The mononuclear phagocyte system (MPS), also known as the reticuloendothelial system (RES), is the major NP clearance route. The first stage of the MPS system is opsonization, where plasma proteins and opsonins adsorb onto the surface of a NP or other invading species. The opsonins and proteins on the NPs surface then interact with surface receptors on macrophages, triggering their clearance from circulation.[187] These macrophages are responsible for phagocytosis, where particles are engulfed and then degraded. Kupffer cells located inside the liver and macrophages in the spleen are the most active phagocytes in uptaking the SPIONs. When the walls of macrophages come into contact with lysosomes, enzymes are released that degrade the NPs in an acidic environment. Degradation by-products, such as Fe^{2+} ions, can form protein complexes such as ferritin and transferrin which are stored and recycled by the body. The mechanism of clearance is dependent on the hydrodynamic diameter (d_H) of the NPs. NPs with a d_H 15-200 nm in size typically accumulate in the liver and spleen, particles >200 nm predominately end up in the spleen. NPs with a d_H smaller than 15 nm can follow a different pathway altogether, whereby they are filtered through the kidney

via the blood vessels of nephrons and excreted in urine.[29]

Toxicity Degradation of ferrite NPs into metal ions such as Co^{2+} or Fe^{2+} can have a detrimental effect on health, potentially causing cytotoxicity, DNA damage, oxidative stress, epigenetic events and inflammatory processes.[25] The degree of damage is affected by the cellular uptake of NPs, which can be dependent on many NP characteristics. Information on toxicity, and systematic studies into the role of NP size, coating and composition on the viability of liver cells are addressed in chapter 5.

4.1.1 The effect of NP characteristics on their *in vivo* behaviour

The processes described in the previous section are known to be influenced by the characteristics of the NPs such as:

Core material and composition The metal composition and oxidation state of NPs can influence their fate *in vivo*. Differences in toxicity between iron oxide and other ferrite NPs have been reported. Cobalt ions (Co^{2+}) have demonstrated toxic effects, but the mechanism behind them is not clear.[189] It was recently shown that Co^{2+} ions can follow the same ferritin remediation pathway as iron ions.[53] Due to the potential for magnetite/maghemite NPs to undergo oxidation and reduction reactions *in vivo*, differences between their cellular uptake and toxicity have also been reported.[25]

Core size Asides from influencing magnetic properties, NP core size can also affect their degradation rate. Larger NPs may degrade slower, increasing their exposure time and thus potential toxic effects.[190]

Surface charge The surface charge of NPs strongly affects the type of proteins that adsorb onto the surface, thus potentially changing the function of the protein corona.[191] NPs which are highly cationic have exhibited shorter blood circulation times than anionic particles.[188] Neutrally-charged NPs have demonstrated less protein adsorption and longer blood circulation times,[192] thus development of zwitteri-

onic coatings and use of neutral ligands such as polyethylene glycol (PEG) has been of interest.[42,193] Cole et al. hypothesised that their neutral PEG coating prevented uptake by Kupffer cells leading to longer blood circulation times which is useful for blood-pool imaging.[194] Surface charge also influences cellular uptake and toxicity, with charged NPs showing greater transportation across the plasma membrane.[195]

Hydrodynamic diameter (d_H) As outlined in the previous section, the d_H of NPs governs their blood distribution and clearance pathway.[186] Aggregation of NPs *in vivo* will increase their d_H and lead to their rapid entrapment and clearance by the MPS.[29]

Surface coating/ligand As the interface between NPs and the surrounding biosystem, the surface coating has a significant impact on their *in vivo* behaviour. The surface ligands directly influence the NP's surface charge, hydrodynamic diameter, stability and hydrophilicity. As a result, the surface coating inevitably impacts protein adsorption and NP degradation rate.[196] The size, density and spatial configuration of the coating molecules has also been shown to influence the NPs distribution.[193] Careful selection of the surface coating is therefore paramount to achieving the desired *in vivo* behaviour.

Shape The shape of NPs affects their flow through blood vessels, clearance and cellular uptake. NPs with spherical geometry have demonstrated less contact with blood vessel walls than non-spherical NPs.[197] This is advantageous for efficient circulation, but disadvantageous for drug delivery applications where adhesion is required for blood-tissue exchange.[198] Oblate-shaped NPs however have demonstrated longer circulation times than spherical NPs owing to their lesser uptake by macrophages.[199] Some studies have shown greater uptake of spherical NPs into cells than rod-shaped NPs.[192,193] The opposite has also been reported, where rod-shaped NPs demonstrated greater uptake owing to their sharp shape facilitating permeation through cell membranes.[57,195]

Hydrophilicity The degree of hydrophilicity can impact the particokinetics. Hydrophobic NPs are known to elicit an immune response.[200] Hydrophobic NPs will

also inevitably lead to aggregation in plasma, increasing the likelihood for opsonization and rapid clearance.[201]

Concentration Dose-dependent toxicity of NPs is well established. High doses of SPIONs can lead to their distribution in lungs and adipose tissue in addition to the liver and spleen.[29] A high dose can be considered as >5 mg Fe/kg body weight for human in one injection. The recommended dose of Feridex, an MRI contrast agent that received clinical approval, was 0.56 mg Fe/kg.[202]

Due to the complexity of potential NP interactions, predicting *in vivo* behaviour is a major challenge. Nonetheless, considering the aforementioned processes and the existing knowledge of NP *in vivo* interactions, the following can be considered as desirable surface properties for positive MRI imaging applications:

- **Small hydrodynamic diameter (<20 nm)** to avoid uptake by macrophages and prolong blood circulation time. For effective T_1 relaxation, small hydrodynamic diameters are also desired to allow water molecules to come into close proximity with the paramagnetic species.

- **Negative or neutral surface charge** to increase blood circulation times, avoid uptake by cells and reduce potential toxicity.

- **A biocompatible and stabilising ligand** that enables minimised protein adsorption to prolong blood circulation time, and confers excellent colloidal stability. A further consideration is that the ligand should not adversely affect the magnetic properties of the particles. DMSA has been shown to reduce the magnetic saturation of SPIONs,[203] which is beneficial for T_1 MRI (further discussed in chapter 5)

In this study, two different ligands are explored as potentially suitable coatings: bovine serum albumin (BSA) and dimercaptosuccinic acid (DMSA). Two different phase methods are subsequently explored to evaluate their ability to transfer the NPs from non-polar to polar phase, and render stability in water and cell media.

4.1.2 Ligand exchange with dimercaptosuccinic acid

Dimercaptosuccinic acid (DMSA) ligand-exchange is a well-established method for transferring metal-oxide NPs from non-polar solvents to water. The principle of DMSA thiolation of maghemite NPs was first described by Fauconnier et al. in 1997.[77] Jun et al. subsequently applied this in 2005 to develop the ligand exchange technique, demonstrating its efficiency to yield stable water-dispersible NPs that provide an ideal canvas for further functionalisation.[204] DMSA, a small molecule composed of carboxylate and thiol groups, has a high affinity for transition-metals which causes it to replace the existing ligand, typically oleic acid. DMSA binds to the metal centre via its carboxylate groups, subsequent oxidation of DMSA leads to a cage of disulphide cross-linked DMSA molecules around the NP [5]. Free carboxyl and thiol groups offer a stable negatively-charged surface which can be further functionalised with targeting ligands, drugs or fluorescent molecules.[205] Thus DMSA could be ideal for conjugating to a liver-specific ligand towards liver-targeted MRI. Additionally, DMSA is non-toxic, providing a suitable route to obtain biocompatible water-dispersible NPs.[78]

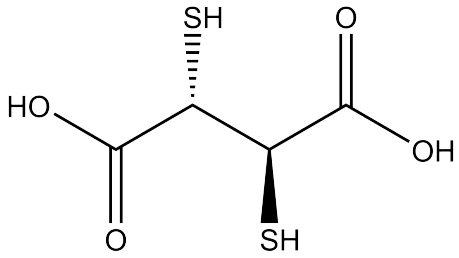


Figure 4.2: Chemical structure of dimercaptosuccinic acid

4.1.3 Direct phase transfer with bovine serum albumin

Bovine serum albumin (BSA) is a large hydrophilic protein composed of a mixture of 607 amino acids produced by cows. It is non-reactive and stable, which has led to its use in many biological applications.[206,207] BSA is structurally similar to human serum albumin, containing 76% of the same amino acids.[208] Thus, BSA-coated NPs have demonstrated excellent biocompatibility in blood, permitting comparatively longer blood circulation times which is desirable for MRI imaging applications.[207] Furthermore, albumin-conjugated gadolinium MRI contrast agent Ablavar® is 4-

5 times more efficient than its un-conjugated version, as albumin has the ideal molecular weight for T_1 relaxation (detailed further in chapter 6).[209] An additional benefit of BSA is that the potential for other proteins adsorbing and forming an uncontrolled protein corona is minimized.[210]

Aires et al. functionalised DMSA coated iron-oxide NPs with BSA to act as a chemotherapeutic agent.[207] The NPs demonstrated excellent stability in a range of media, however their method required functionalisation with DMSA first in order to attach BSA. Similarly, Samanta et al. demonstrated BSA-coated iron-oxide NPs were stable and viable thermal therapeutic agents.[211] Their method is currently the only reported direct functionalisation with BSA, and was achieved by sonicating bare SPIONs with BSA. For BSA to be directly coated however, the NPs were synthesised by the co-precipitation method which yields water-dispersible NPs with poor crystallinity and a wide size distribution.

As BSA has demonstrated potential as a biocompatible protective coating, a novel method for directly coating BSA onto oleylamine-coated iron-oxide and cobalt-ferrite NPs has been explored. The direct coating approach serves to offer a simple phase exchange solution as well as a suitable coating for biomedical application.

4.2 Materials and methods

4.2.1 Materials

Snakeskin® dialysis tubing (3.5 kDa molecular weight cut-off, 22 mm x 35 feet diameter) was purchased from Thermo Scientific. Bovine serum albumin (Albumin Fraction V pH 7.0) was purchased from AppliChem. Dimethyl sulfoxide (anhydrous, ≥99.9%), toluene (ACS reagent, ≥99.5%), and chloroform (puriss. p.a., reag. ISO, reag. Ph. Eur., 99.0-99.4%) were all purchased from Sigma Aldrich. Hydrochloric acid (HCl) (37% techn), Sodium hydroxide (NaOH) (≥99%), ethanol (ROTIPURAN® ≥99.8%, p.a, 9065.4) and sterile filters (Rotilab 668.1) were purchased from Carl Roth GmbH. Dimercaptosuccinic acid (D1722) was purchased from TCI Chemicals. Dulbecco's Modified Eagle Medium (DMEM) (1885023, Life technologies), fetal bovine serum (FBS) (PAN-Biotech 3302-P291205), Dulbecco's Phosphate Buffered Saline (D-PBS), (Invitrogen 14190169) and holey carbon TEM

grids (type S147-4, Plano, Wetzlar, Germany) were purchased as stated. Unless otherwise specified, ultrapure Milli-Q water was used throughout.

4.2.2 Nanoparticle preparation (dialysis) for phase exchange

Initial phase transfer experiments were conducted on MFe_2O_4@OLA NPs as produced after synthesis. The results section will show that both BSA and DMSA phase exchange methods yielded water-dispersible aggregates of NPs when as-prepared particles were used (sections 4.3.1 and 4.3.2). This was most likely caused by excess oleylamine on the particles hindering ligand exchange. To remove the excess oleylamine, a pre-transfer dialysis step was introduced. To dialyse the particles, 10 mg of particles in 10 ml of cyclohexane were added to Snakeskin® dialysis tubing. The tubing was placed into a 500 ml glass beaker and 300 ml of chloroform was added. The chloroform and tubing was stirred for 1.5 hours, then the chloroform was discarded and 300 ml of fresh chloroform was added. Following stirring for a further 1.5 hours, the chloroform was discarded and the NPs were extracted from the tubing.

4.2.3 DMSA ligand exchange method

The ligand exchange method was adapted from a previously reported protocol.[78] Dialysed or undialysed MFe_2O_4@OLA NPs were evaporated by rotary evaporation and re-dispersed in toluene at a concentration of 5 mg/mL. 5 ml of the particle dispersion was added to a glass vial and sonicated for 5 minutes in an ultrasonic bath. A DMSA solution was prepared by mixing 200 mg of DMSA in 12 ml of dimethyl sulfoxide (DMSO) by sonication for 5 minutes. The DMSA solution was added to the NPs and sonicated for 15 minutes, then stirred at room temperature for 48 hours at 200 rpm. To terminate the reaction, 20 ml of ethanol was added and the particles magnetically separated. The supernatant was discarded and the particles were washed three times in ethanol with centrifugation at 4600 rpm for 15 minutes. Following re-dispersion in water, the pH was adjusted to 10 using NaOH solution, and the particles were dialysed in 500 ml water for 24 hours to remove excess DMSA. Finally, the pH was re-adjusted to 7 with NaOH solution and the particles were filtered through a sterile 0.22 μm membrane and stored at 4 ℃.

4.2.4 BSA phase transfer method

The direct coating method with BSA involved the generation of an oil-in-water emulsion to encourage BSA to electrostatically bind to the NPs. To form the water phase, 80-220 mg of BSA was dissolved in 20 ml of water in a 50 ml Schott bottle and vortexed for 5 minutes. To form the oil phase, dialysed or un-dialysed MFe_2O_4@OLA NPs in cyclohexane were evaporated by rotary evaporation and re-dispersed in cyclohexane at a concentration of 5 mg/mL. 4 ml of the oil phase was then added to the water phase and sonicated with a probe tip at amplitude 50 for 15 minutes to form an emulsion. An ice bath was placed around the bottle during sonication to prevent any generated heat degrading the BSA. The emulsion was then transferred to a water bath at 40 ℃ and stirred for 20 minutes at 200 rpm to promote evaporation of cyclohexane. The sonication and heating steps were repeated three further times. The emulsion was then left in the water bath at 40 ℃ to stir overnight. Following complete evaporation of cyclohexane, a clear, brown dispersion of NPs in water was obtained. The particles were centrifuged at 14,000 rpm for 30 minutes and washed three times in water to remove excess BSA before re-dispersing in water.

4.2.5 Characterisation

Cryo Transmission Electron Microscopy

Cryo transmission electron microscopy (Cryo-EM) is a valuable tool to image NPs in their native state in liquid, giving rise to information about their agglomeration behaviour. Conventional TEM images NPs which are dried onto a grid, and are therefore subject to drying artefacts. Cryo-EM employs the same TEM principles in section 2.3.1, however the sample is plunge-frozen so that the NPs are frozen in water to maintain their state in solution, and imaged under liquid nitrogen using a specialised holder.

Cryo-EM in this study was performed by Dr. Marcus Koch from the INM. For Cryo-EM investigations, 3 µl of NP solution were deposited onto a holey carbon TEM grid and then plunged into liquid ethane using a Gatan (Pleasanton, CA, USA) CP3 Cryoplunger. The frozen sample was transferred under liquid nitrogen to

a Gatan Cryo-EM holder (model 914). TEM investigations were performed at liquid nitrogen temperature using a JEOL (Akishima, Japan) JEM-2100 (HR) with LaB6 cathode operating at 200 kV accelerating voltage and a Gatan Orius SC1000 camera (acquisition time 2 s, image size 1024x1024 pixel at binning 2). NPs were found both on the amorphous ice-covered carbon film and on the amorphous ice-covered holes. The contrast in TEM bright-field images was enhanced on the ice-covered holes due to the missing carbon film.

Thermogravimetric Analysis

Thermogravimetric analysis (TGA) is a thermal measurement technique that measures the change in mass of a sample over time, in response to temperature. The sample of interest is loaded onto a pan and placed on a precision balance in a furnace. TGA was employed to determine the amount of ligand on the surface of the NPs using a Perkin-Elmer Pyris Diamond TG/DTA6300. 5 mg of dried NPs were heated to 900°C at a heating rate of 10 °C min^{-1}. The measurement was performed under nitrogen gas flowing at 80 ml/min to avoid any mass losses from oxidation.

Dynamic Light Scattering

Dynamic light scattering (DLS) is a useful tool for measuring the hydrodynamic diameter (d_H) and thus the colloidal stability of NPs in solution. DLS measures the scattering of light caused by NPs undergoing Brownian motion in a dispersion. A laser is directed onto a NP sample in a cuvette, and scattered light is detected by a photomultiplier. The Brownian motion of NPs causes their scattering to fluctuate over time, the rate of which is measured by DLS and depends on the diffusion behaviour of NPs; smaller NPs cause the intensity to fluctuate more rapidly than larger ones. The d_H of a NP is given by the Stokes-Einstein equation:[212]

$$d(H) = \frac{kT}{3\pi\eta D} \tag{4.1}$$

where k is Boltzmann's constant, T is absolute temperature, η is viscosity and D is the translational diffusion coefficient. The d_H is thus a value that represents the diffusion of a particle in a fluid and includes the particle core, surface coating, and layer of solvated ions around the particle.

The d_H is typically obtained by cumulant analysis to give the 'z-average' or intensity-weighted particle size distribution. This is suitable only for monodisperse samples, as it provides the mean values of the diffusion coefficient but not the distribution of diffusion coefficients.[212] The intensity-distribution can be converted to a volume-weighted distribution which is based on the relative proportion of particles based on their volume and size, and thus is more suitable for larger particles. If the majority of the sample is composed of smaller NPs, however a few aggregates are present, volume-weighted distribution will be biased towards the larger particles and thus would not provide an accurate representation of the sample. In this case, number-weighted distribution, which represents the number of each particle of a given size, is more suitable and thus was the analysis method used in this study. Parameters such as particle concentration, material, type of dispersant, and temperature need to be taken into consideration to ensure an accurate measurement. Further information on these effects and DLS in general is described elsewhere.[213]

d_H measurements in this study were obtained using a Nanotrac® NPA 250 with an external probe. Calibration checks were conducted using 80 nm latex beads. Samples were diluted to approximate concentrations of 30 μg/ml and irradiated with a HeNe laser (red light, 780 nm) and the intensity fluctuations of the scattered light (detected at a backscattering angle of 180°) was analysed. Three independent measurement runs of 60 seconds were collected for each sample at a temperature of 20 °C. The mean hydrodynamic diameter was obtained using cumulant analysis and a size distribution using a regularization scheme by number. The parameters used for measurements are detailed in table 4.1.

Table 4.1: Parameters used for DLS measurements of NPs in this work.

Media/material	Refractive index	Density at 20°C (g/cm^3)	Viscosity at 20°C (cP)
Toluene	1.497	0.867	0.59
Cyclohexane	1.43	0.779	0.93
Water	1.33	0.989	1.002
DMEM w/ 10% FBS	1.34	1.04	1.07
Cobalt ferrite NPs	2.23[214]	4.91[214]	-
Iron-oxide NPs	2.34[215]	5.18[216]	-

Zeta-potential measurements

The zeta-potential is an indicator of the electrokinetic potential of a NP. A charged particle will attract oppositely-charged ions present in the dispersant, which form an initial layer around it called the Stern layer. An additional diffuse layer of ions forms around this layer, creating what's known as an 'electrical double layer' (figure 4.3). The zeta potential is the difference in electric potential between the interface of this double layer (slipping plane), and the surrounding bulk dispersant. Higher zeta-potentials (+/- 30 mV) are indicative of strongly cationic or anionic particles, thus indicate the dispersion is stable.[217]

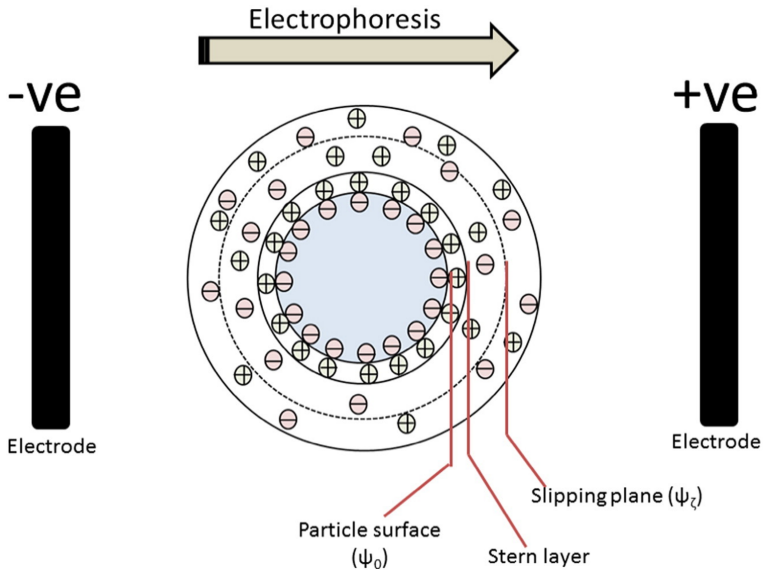


Figure 4.3: Diagram illustrating the electrical double layer surrounding a charged particle in liquid. Image source:[218]

Zeta-potential is calculated by measuring the speed at which particles in an electrolyte-containing dispersion travel to the oppositely charged electrode in an electric field. Measurements are obtained by measuring the scattering of laser light as a function of the particle velocity. The frequency of the scattered beam will have shifted in comparison to the incident beam proportionally to the speed of the particles (Doppler shift).[218] From the known applied electric field and measured particle velocity, the particle mobility is readily determined. Zeta potential is then calculated from mobility by using a model, the most common of which is the Smoluchowski model which is suitable for particles dispersed in water.[218]

Zeta-potential (ζ) measurements were performed using a Malvern Zetasizer Nano

ZSP equipped with a 633 nm laser. Samples were diluted 1:10 in water/relevant solvent. Three independent measurement runs with several subruns of 10 seconds per subrun were performed for each sample at a temperature of 25 °C. The ζ-potential was calculated from the NP electrophoretic mobility using the Smoluchowski theory.

Fourier-transform infrared spectroscopy

Fourier-transform infrared spectroscopy (FTIR) is a spectroscopic technique that measures the absorbance of infrared light by a sample to yield information on its chemical composition. Inorganic and organic compounds can absorb light in the infrared range, caused by the interaction of the vibration of electronic bonds with light. If the vibrations lead to a net change in the dipole moment of the molecule, the bonds will transition to a vibrational excited state by the absorption in a particular region of the infrared spectrum. Since the vibrational energy is quantized, the position of a absorption band can be specified by a particular wave number. Bonds can undergo six different vibration notions, such as stretching and bending.[219] The frequencies of such vibrations can be assigned to the mode of vibration and atoms involved.

Thus FTIR can identify the presence of ligands or functional groups, and their binding modes to a NP. FTIR is fast and highly-sensitive, requiring only a few milligrams of sample and thus is ideal for small NP samples.[220] To verify ligand coating, FTIR was employed on dried NP samples using a Varian Excalibur FTS 3500 FTIR.

Superconducting quantum interference device measurements of magnetic properties

The magnetic properties of MFe_2O_4 NPs following phase transfer were measured using the method described in section 3.2.2.

4.2.6 Stability tests

To measure the stability of the aqueous NP dispersions in different pH, the NPs were diluted in water 1:10, and the pH adjusted to 3, 5, 7, or 9 by addition dropwise of sodium hydroxide or hydrochloric acid. To measure the stability of the particles

in cell culture, the samples were diluted 1:5 in DMEM supplemented with 10% FBS. DLS and zeta-potential measurements were then performed following the protocols described above.

4.3 Results and discussion

4.3.1 Direct phase transfer with BSA

Rationale behind experimental design

The first method explored to transfer the NPs from non-polar solvent to water is by direct coating with the hydrophilic protein BSA. The schematic of the process is outlined in figure 4.4. The formation of an oil-in-water emulsion serves to promote electrostatic binding of BSA to the NP surface in order to minimise free energy in the system. Theoretically, both electrostatic and hydrophobic interactions are possible, as the positively charged MFe_2O_4@OLA NPs could induce anionic interaction with BSA, whilst the hydrophobicity of the particle and the process of generating an oil-in-water emulsion could induce hydrophobic interaction.

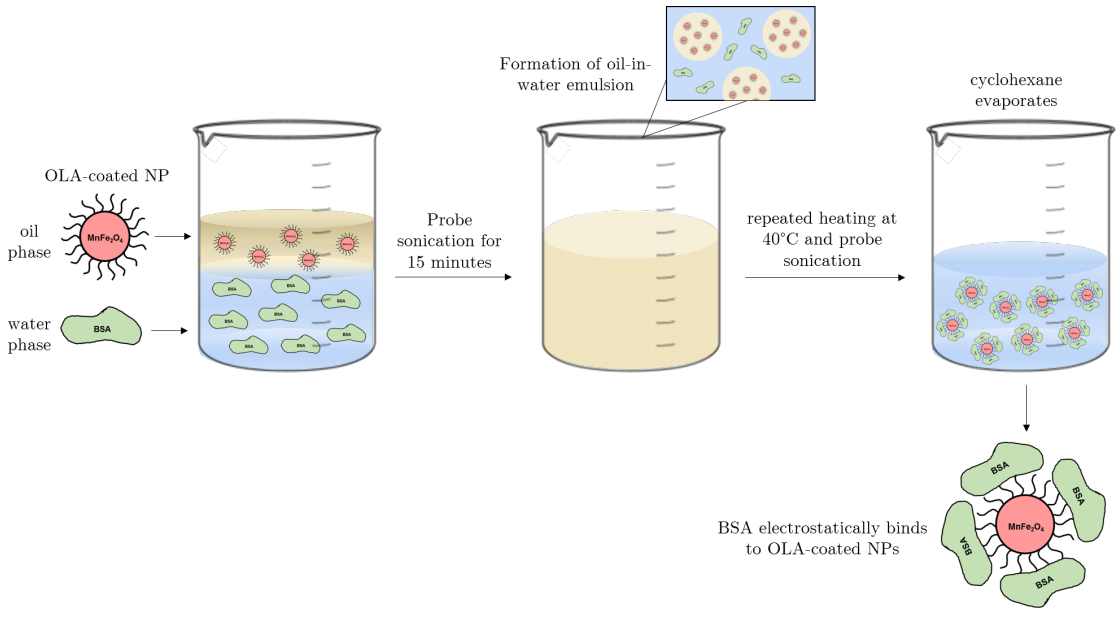


Figure 4.4: Schematic of BSA phase transfer for MFe_2O_4@OLA NPs.

Binding via electrostatic interaction is hypothesised due to the presence of multiple free carboxyl groups on BSA,[221] which are known to interact with metals.[222,223] This is further supported by the work of Yang, Liang and Han (2009)[224] who ob-

served that BSA interacted with oleic-acid capped iron-oxide NPs spontaneously via electrostatic interaction. In the case of a positively-charged surface, an electrostatic interaction was energetically more favourable than a hydrophobic interaction.[225,226] Notably, hydrophobic interactions induced the most amount of structural changes, which can adversely affect the function of BSA.[226]

To assess whether the amount of BSA impacts the phase transfer process, two different quantities, 80 mg and 160 mg of BSA were evaluated. The dimensions of BSA are approximated to be 7.5 x 6.5 x 4 nm.[227] If bound side-on, one BSA molecule occupies roughly 56 nm^2, and end-on, 16 nm^2 (figure 4.5).[225] BSA has three differently-charged domains: domains I and II are negatively charged, with domain I containing the most negatively charged -COO- groups, and domain III is neutral.[226] Given the location of the carboxyl groups on BSA, both side-on and end-on binding interaction is possible.

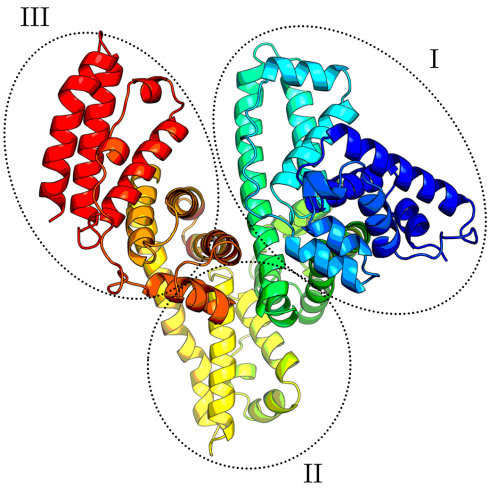


Figure 4.5: Structure of BSA showing different domain regions. Adapted from[228]

To ensure sufficient coverage of the NPs, an end-on tighter packing arrangement is desirable due to their small size and thus limited surface area available for binding. Phan et al. concluded that low concentrations of BSA resulted in looser packing on self-assembled monolayers, as opposed to tighter packing at high concentrations ($>$ 1 mg/ml).[225] An excess of BSA was thus added to encourage closer end-on packing on the surface and to ensure that full coverage would be obtained. For a 4 nm particle, 80 mg roughly equates to a 3-fold excess of BSA necessary for full coverage if bound side-on, and a 1-fold excess if all BSA is bound end-on. 160 mg roughly

equates to a 6-fold excess of BSA necessary for full coverage if bound side-on, and a 2-fold excess if bound end-on. Several assumptions were made for these calculation, the details of which can be found section B.2.3 of the appendix.

Results of direct phase transfer with BSA

Following repeated sonication and heating with BSA, aqueous dispersions of NPs were obtained, indicating that phase transfer was successful. Both iron-oxide and cobalt-ferrite NPs of different sizes were tested to assess if the metal core composition or size affects BSA binding. Figure 4.6 shows representative aqueous dispersions of iron-oxide and cobalt-ferrite NPs obtained via the BSA direct coating method. From first appearance, the dispersions were opaque, which indicated aggregation or agglomeration may have occurred. To assess the degree of aggregation, the zeta-potential and hydrodynamic diameter of the particles were measured. Table 4.2 details the results and the experimental parameters.

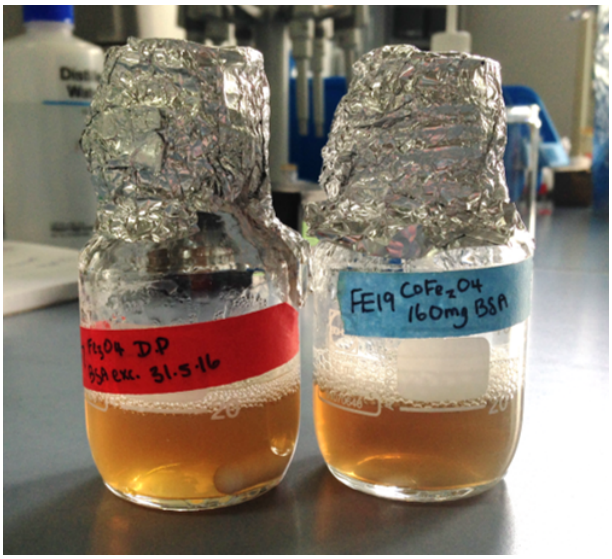


Figure 4.6: $CoFe_2O_4$@BSA and Fe_3O_4@BSA showing opaque aqueous dispersions following phase transfer with BSA.

Hydrodynamic diameters in excess of 94 nm were obtained for all samples. The core size and composition appeared to have no effect on the d_H obtained. Larger amounts of BSA (160 or 220 mg) tended to decrease the d_H slightly: for example the d_H of 4.1 nm $CoFe_2O_4$@BSA NPs was 187 nm when 80 mg of BSA was used and 124 nm when 160 mg of BSA was used. However, this improvement was not sufficient to achieve monodisperse NPs.

Table 4.2: Parameters used for phase transfer experiments with BSA and measured d_Hs and ζ-potentials (at pH 7). Particles were either not dialysed prior to phase transfer or dialysed according to the method in section 4.2.2.

Sample	Core size (TEM) (nm)	NPs dialysed?	Amount of BSA (mg)	d_H (nm)	ζ-potential (mv)
$CoFe_2O_4$@BSA 1	2.5 ± 0.6	Yes	80	142 ± 43	-29 ± 0.9
$CoFe_2O_4$@BSA 2	4.1 ± 1.2	No	80	187 ± 54	-31 ± 0.2
$CoFe_2O_4$@BSA 3	4.1 ± 1.2	No	160	124 ± 31	-17 ± 0.5
$CoFe_2O_4$@BSA 4	2.3 ± 0.4	Yes	220	96 ± 18	-27 ± 0.2
$CoFe_2O_4$@BSA 5	4.3 ± 0.6	Yes	220	94 ± 28	-38 ± 0.2
Fe_3O_4@BSA 1	5.2 ± 1.2	No	80	167 ± 72	-32 ± 0.7
Fe_3O_4@BSA 2	5.2 ± 1.2	No	160	129 ± 52	-35 ± 0.5
Fe_3O_4@BSA 3	4.0 ± 0.4	No	160	158 ± 51	-
Fe_3O_4@BSA 4	4.7 ± 0.7	No	80	195 ± 55	-
Fe_3O_4@BSA 4	4.7 ± 0.7	Yes	80	125 ± 55	-32 ± 0.3

Furthermore, dialysing the NPs prior to phase transfer did not significantly reduce the hydrodynamic diameter. Figure 4.7 compares the d_H of representative Fe_3O_4@BSA samples. The d_H decreased from 195 to 125 nm with a pre-phase transfer dialysis step included, however NP aggregation or agglomeration had still occurred. In section 4.3.2 of this study, it will be shown however that dialysis much improved the results of DMSA ligand exchange.

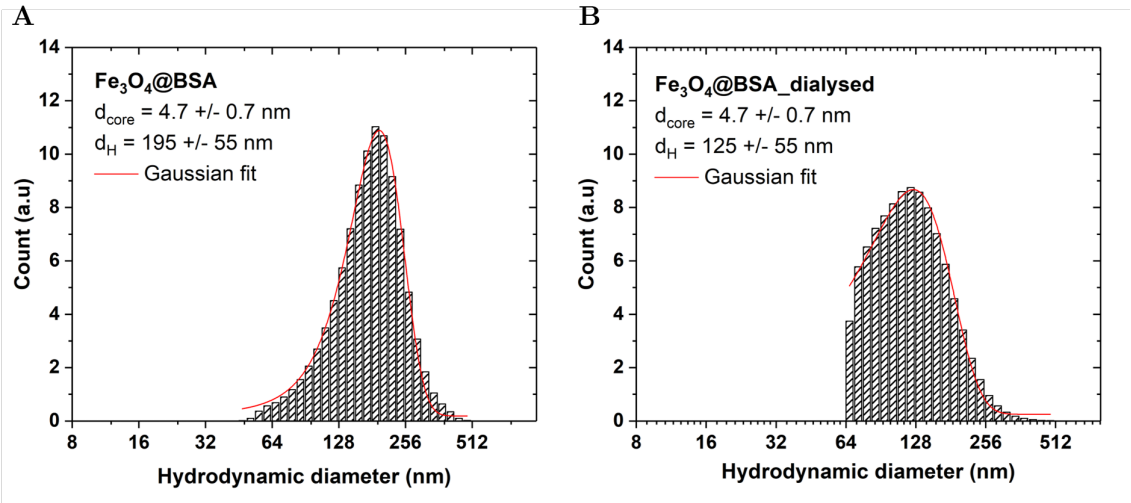


Figure 4.7: Hydrodynamic diameter size distributions of 4.7 nm Fe_3O_4@BSA NPs (A) with no prior dialysis (B) with dialysis step.

Negative zeta-potentials in the range of -17 to -38 mV were obtained for all samples, indicating moderate to good colloidal stability. As the hydrodynamic diameters measured were large (>100 nm), the low zeta-potentials indicated the agglomerates themselves were stable and not individual NPs, which highlights the issue with reporting zeta-potential results alone to indicate 'good colloidal stability'. Chen et al. also described discrepancies in their DLS and zeta results for SPIONs following phase transfer.[229,230] Zeta-potential is the measurement of surface charge, which indicates colloidal stability depending on the ability of the particles to repel one-another. If sufficient negative or positive surface charge is present, the colloidal solution is deemed 'stable'. However, there is no difference in the surface charge of 10 nm particles versus 220 nm agglomerates, hence zeta-potential will indicate both samples are equally stable. This explains the discrepancy between DLS and ζ-potential results for the stability of MFe_2O_4@BSA NPs and highlights an issue in this field. Many published articles on water-dispersible NPs measure stability by ζ-potential only, thus no indication is given as to whether the particles exist as monodisperse NPs or agglomerates, yet literature points towards biomedical applications as the intended use of the NPs. Accordingly, there is a lack of definition of the term 'stable' in reference to water-dispersible NPs intended for biomedical use. This is an important term to clarify considering the influence of stability on *in vivo* behaviour.

To investigate the state of the NPs further, cryo-EM was performed. Cryo-EM of 4.3 nm $CoFe_2O_4$@BSA NPs is shown in Figure 4.8(A). Agglomerates/clusters ranging from ca. 15-150 nm are visible, with the majority approximately 100 nm in size which corresponds to the measured d_H of 94 nm (table 4.2). The metal-oxide cores were not aggregated as there was no change in their average diameter.

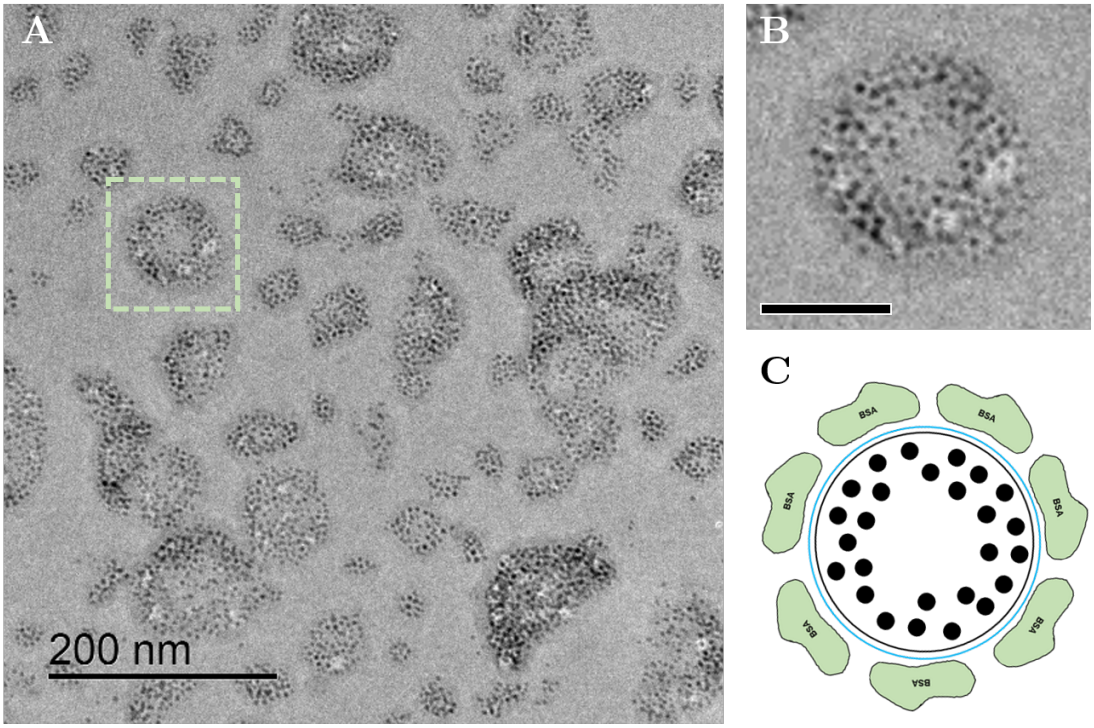


Figure 4.8: (A) Cryo-EM image of $CoFe_2O_4$@BSA NPs. Particles are agglomerated in clusters 15 to 150 nm in size. (B) Enlarged cryo-EM image of a particle cluster showing a higher concentration of particles at the cluster boundary with a hollow centre (scale bar is 50 nm). (C) Proposed schematic of BSA-NP cluster.

The formation of clusters may be caused by BSA inducing NP agglomeration upon interacting with them. Recent research suggested that BSA can unfold when interacting with a NP, exposing its hydrophobic core and inducing NP agglomeration.[231] Alternatively, the formation of an emulsion during phase-transfer could have induced cluster formation: instead of interacting with individual NPs, BSA interacted with bubbles of NPs prior to evaporation of the oil phase. This is supported by the observation of some 'hollow' clusters. Figure 4.8(B) shows that particles appear to be more concentrated around the cluster edge. This suggests that the particles have gathered at the oil-water interface during the emulsion process. The Peclet number can explain this effect:

$$Pe = \frac{r^2}{D\tau} \tag{4.2}$$

where τ is the evaporation time of a droplet, r is the droplet radius, and D is the diffusion coefficient of the particles in liquid. Depending on the time it takes for a droplet to evaporate, and the radius of the droplet, the particles either accumulate at

the interface, or diffuse into the remaining volume of oil as the liquid-liquid interface moves inwards. If Pe $\gg$1, particles cannot diffuse and will gather at the droplet interface. Smaller emulsion droplets and a slow evaporation rate therefore favour the diffusion of particles into the remaining volume. The Kraus group from the INM synthesised controlled 'supraparticle' gold NP clusters using this principle. In their case, homogeneous clusters were formed by slowly evaporating the oil droplets in an oil-in-water emulsion.[232]

To test whether the clusters were created by the emulsion process or induced by BSA interacting with the NPs, the direct coating method was repeated without NPs. Cryo-EM revealed the presence of similar agglomerates, verifying that BSA agglomerates were formed independently of the NPs (figure 4.9). Protein aggregation may have occurred due to BSA unfolding upon contact with the solvent in the oil-phase,[233] or by the mechanical forces induced by sonication.[234] Aggregation was also observed by Samanta et al. who sonicated water-soluble NP iron-oxide NPs with BSA to coat them.[211] Too high a concentration of BSA may also be a causation,[235] although smaller hydrodynamic diameters were obtained when 160-220 mg of BSA was used as opposed to 80 mg (table 4.2). The results suggest that a combination of protein aggregation, and particles accumulating at the liquid-liquid interface, has led to the formation of the BSA-particle clusters.

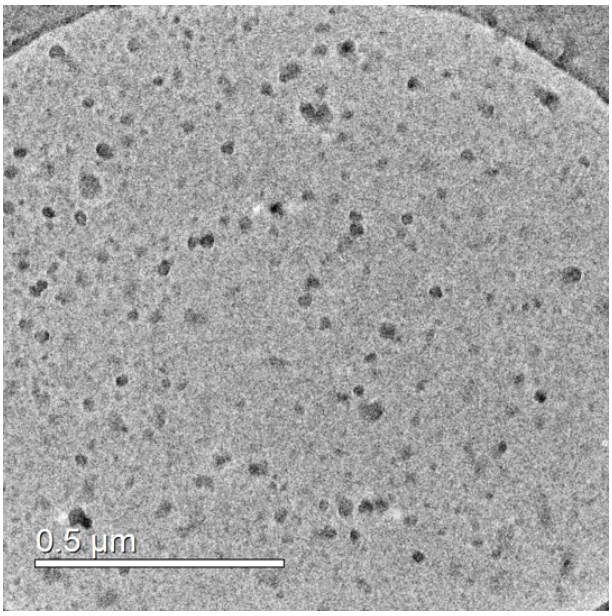


Figure 4.9: Cryo-EM image of a blank BSA sample: the direct coating method performed without NPs. Agglomerates of BSA are present.

Nanoparticle stability studies

To further investigate the stability of the BSA-coated clusters, zeta-potential measurements were taken in a pH range of 3-9. The stability of NPs in different pH is important for *in vivo* applications as the pH varies within different cellular environments. Figure 4.10 shows the ζ-potential results of MFe_2O_4@BSA clusters in response to different pH. The clusters were stable in pH 7-9 with ζ-potentials below -25 mV, however below pH 7 the stability decreased and at pH 3 the ζ-potentials were 25-36 mV. The optimum pH conditions for BSA-coated particles therefore were 7-9, which corroborates the findings of a study into pH stability of BSA by Michnik, Michalik and Drzazga.[236]

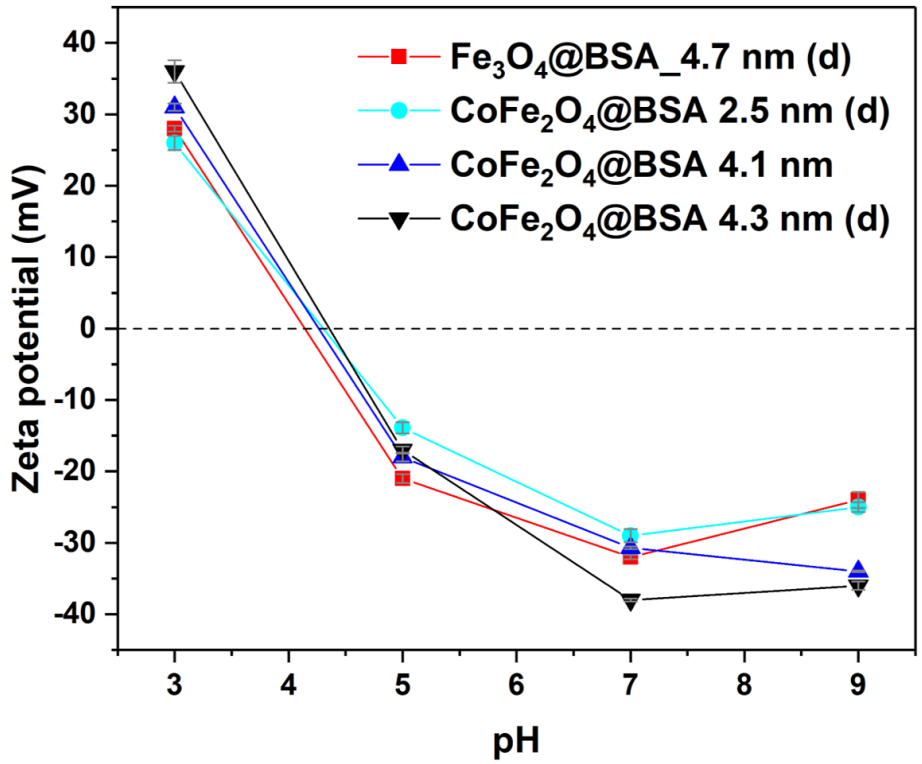


Figure 4.10: ζ-potential of MFe_2O_4@BSA clusters in response to different pH. (d) indicates the particles were dialysed prior to phase transfer.

The NPs demonstrated colloidal stability in water, however in the body the NPs will encounter a more complex media containing proteins, lipids and salts. Consequently, it is imperative to assess their stability in this media, for which Dulbecco's Modified Eagle's medium (DMEM) supplemented with 10% fetal bovine serum (FBS) and PBS are used as standard comparisons. To assess their stability

in DMEM and PBS, the hydrodynamic diameters of representative BSA-coated NPs were measured. As shown in figure 4.11, there was no significant difference in d_H of 2.5 nm $CoFe_2O_4$@BSA NPs in water, PBS or DMEM, indicating good stability in physiological media.

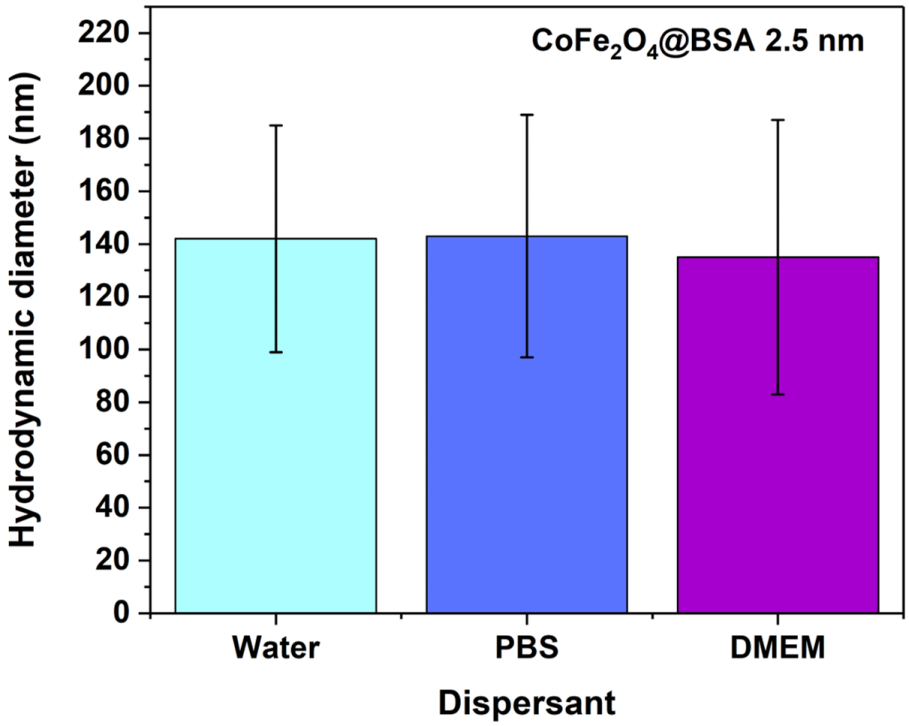


Figure 4.11: Hydrodynamic diameter of $CoFe_2O_4$@BSA clusters in different medium.

Magnetic properties of $CoFe_2O_4$@BSA NPs

SQUID measurements of $CoFe_2O_4$@BSA NPs were conducted to assess the effect of BSA on their magnetic properties. Room temperature hysteresis curves (figure 4.12(A)) show that the magnetisation saturation of 4.3 nm $CoFe_2O_4$@BSA NPs was 12 emu/g, which is 73% lower than that of $CoFe_2O_4$@OLA NPs (44 emu/g). The blocking temperature of $CoFe_2O_4$@BSA NPs was also lower in comparison to $CoFe_2O_4$@OLA NPs, with 91 K and 131 K respectively. The decrease in M_s for BSA-coated NPs could be due to the presence of the non-magnetic BSA layer and excess BSA. Similarly, Mikhaylova et al. observed a 40% reduction in M_s for amine-functionalised SPIONs following conjugation to BSA.[237] The decrease in T_B for $CoFe_2O_4$@BSA NPs suggests a reduction in the number of interparticle dipolar interactions, which is the interaction of the magnetic moments of the NP cores

in close proximity with one another.[7] Smaller dipolar interactions are known to decrease the T_B in superparamagnetic NPs.[238] The presence of large BSA proteins may have reduced the interaction between NPs. Similar surface coating effects on T_B have been reported by others.[239,240]

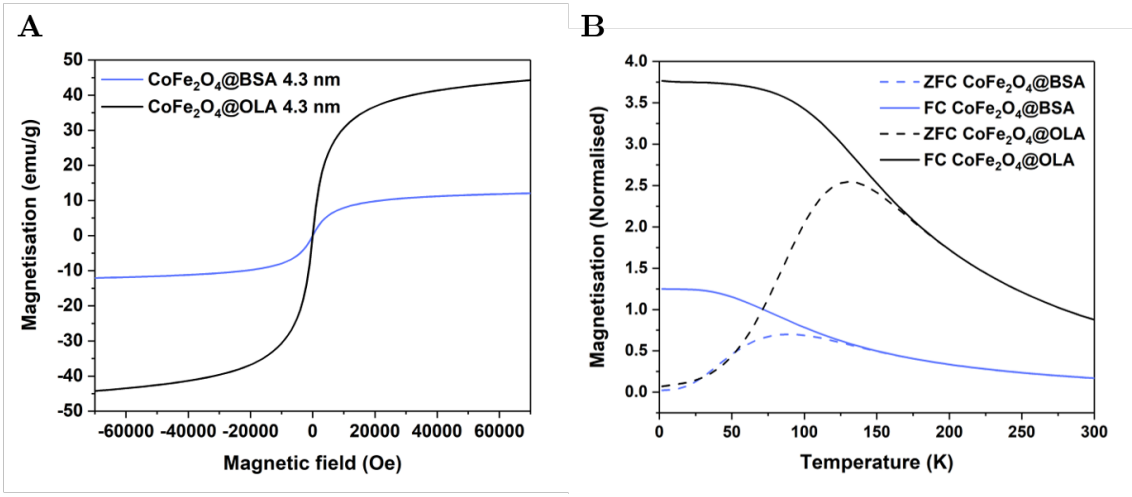


Figure 4.12: (A) Room-temperature (300 K) hysteresis curves of $CoFe_2O_4$ NPs with original OLA coating and after phase transfer with BSA. ZFC and FC curves at an applied field of 100 Oe.

In addition to the T_B and M_s, the coercivity of $CoFe_2O_4$ NPs reduced following phase transfer with BSA. At low temperature (4 K), the coercivity of $CoFe_2O_4$@BSA NPs was 13.6 Oe, in comparison to 14.5 Oe for $CoFe_2O_4$@OLA NPs (figure 4.13).

In terms of T_1 MRI applications, the reduction in M_s observed for $CoFe_2O_4$@BSA NPs is potentially beneficial, as lower M_s reduces effect on T_2. For this purpose, BSA-coated NPs may be suitable, however further development of the phase-transfer method to obtain monodisperse and stable NPs is a must before biomedical applications can be considered.

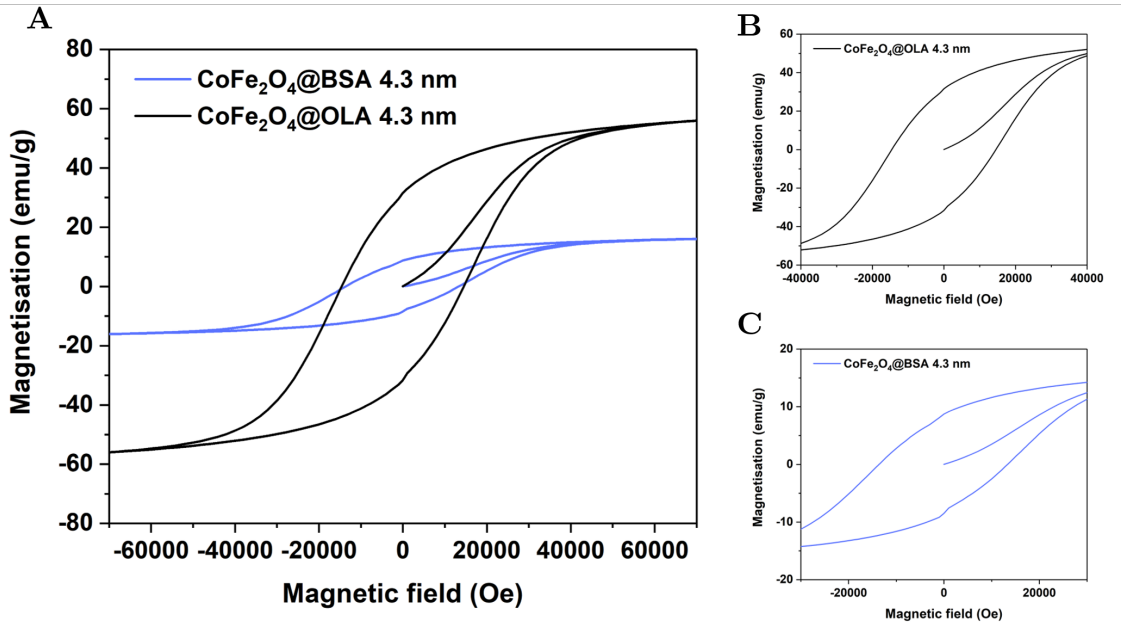


Figure 4.13: (A) Hysteresis curves of $CoFe_2O_4$ NPs with original OLA coating, and after phase transfer with BSA at 4 K. (B) Enlarged view of (B) $CoFe_2O_4$@OLA and (C) $CoFe_2O_4$@BSA NPs.

4.3.2 Ligand exchange with DMSA

In tandem with exploring BSA as a hydrophilic capping agent for transferring MFe_2O_4@OLA NPs to aqueous media, an alternative method using DMSA was investigated. DMSA ligand-exchange is a well-established method for transferring metal-oxide NPs from non-polar solvents to water. A summary of the synthesis and ligand exchange process is outlined in Fig.4.14.

Following ligand exchange with DMSA, water-dispersible Fe_3O_4@DMSA and $CoFe_2O_4$@DMSA NPs were obtained, however the dispersions visibly sedimented within a few days. DLS studies were conducted to assess the agglomeration state. Hydrodynamic diameters >100 nm were obtained which further indicated particle agglomeration (see table B.3 in section B.2.1). The anticipated d_H range was 10-20 nm (assuming monolayer coverage), based on the size of a DMSA molecule and previous reports.[78,241]

The formation of agglomerates was speculated to be caused by excess oleylamine hindering ligand exchange with DMSA. Oleylamine was used as both the surfactant and solvent during synthesis, thus the three washing steps performed post-synthesis may have been insufficient to remove the excess. A similar issue was reported by

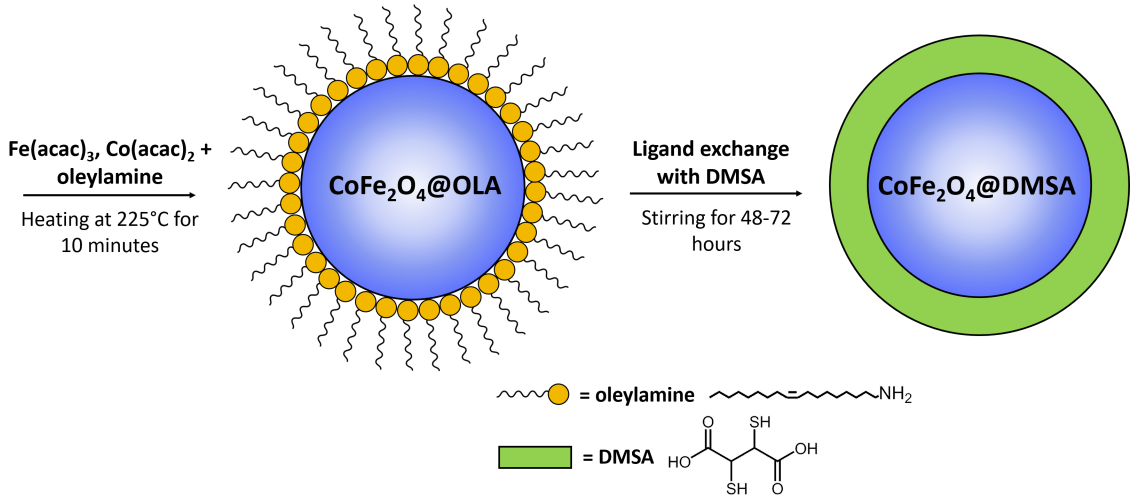


Figure 4.14: Oleylamine-coated $CoFe_2O_4$@DMSA and Fe_3O_4@DMSA NPs are obtained following synthesis with acetylacetonate precursors and oleylamine at 225°C for 10 minutes. Initially hydrophobic, the particles are rendered hydrophilic by stirring with DMSA for 48-72 hours. DMSA preferably binds to the metal oxide core replacing the oleylamine ligands.

Kumar et al. (2012) who detected residual oleic acid on particles post phase-transfer where agglomeration had occurred.[242] Evidence of agglomeration following DMSA ligand exchange with d_Hs in the range of 50-150 nm was also reported in other studies.[70,205,243,244]

To address this issue, ligand exchange was repeated using NPs that had been washed an additional three times in ethanol prior to ligand exchange, however this did not improve the results. Subsequently, a dialysis step was introduced to remove any excess oleylamine by diffusion across a selectively-permeable membrane (detailed in section 4.2.2). DLS studies comparing undialysed and dialysed particles after ligand exchange with DMSA showed a significant improvement in the dispersity of MFe_2O_4@DMSA particles for dialysed particles (table 4.3). The d_H of dialysed Fe_3O_4@DMSA NPs was 16.5 nm; the same sample without prior dialysis measured 115 nm. The d_H of OLA-coated NPs before and after dialysis suggested that excessive OLA was present on the particles, as a significant improvement was obtained following dialysis (d_H decreased from 87 to 11 nm). Removal of excess OLA thus facilitated the ligand exchange process.

TEM studies were conducted to further investigate the influence of dialysis on the agglomeration state of NPs following ligand exchange. TEM micrographs of undialysed Fe_3O_4@DMSA NPs show particles which appear to be trapped in an organic

Table 4.3: Hydrodynamic diameter measurements of Fe_3O_4 NPs before and after dialysis in chloroform.

Particle type	Core size (TEM) (nm)	Ligand	d_H before dialysis (nm)	d_H after dialysis (nm)
Fe_3O_4	4.7 ± 0.7	OLA	87 ± 2	11 ± 1
		DMSA	115 ± 54	17 ± 3

matrix (figure 4.15(A,B)). Another study investigating DMSA-SPIONs showed very similar TEM images and reported flocculation of these NPs over time.[242] Conversely, for dialysed particles the matrix appears noticeably reduced (figure 4.15 (C,D)).

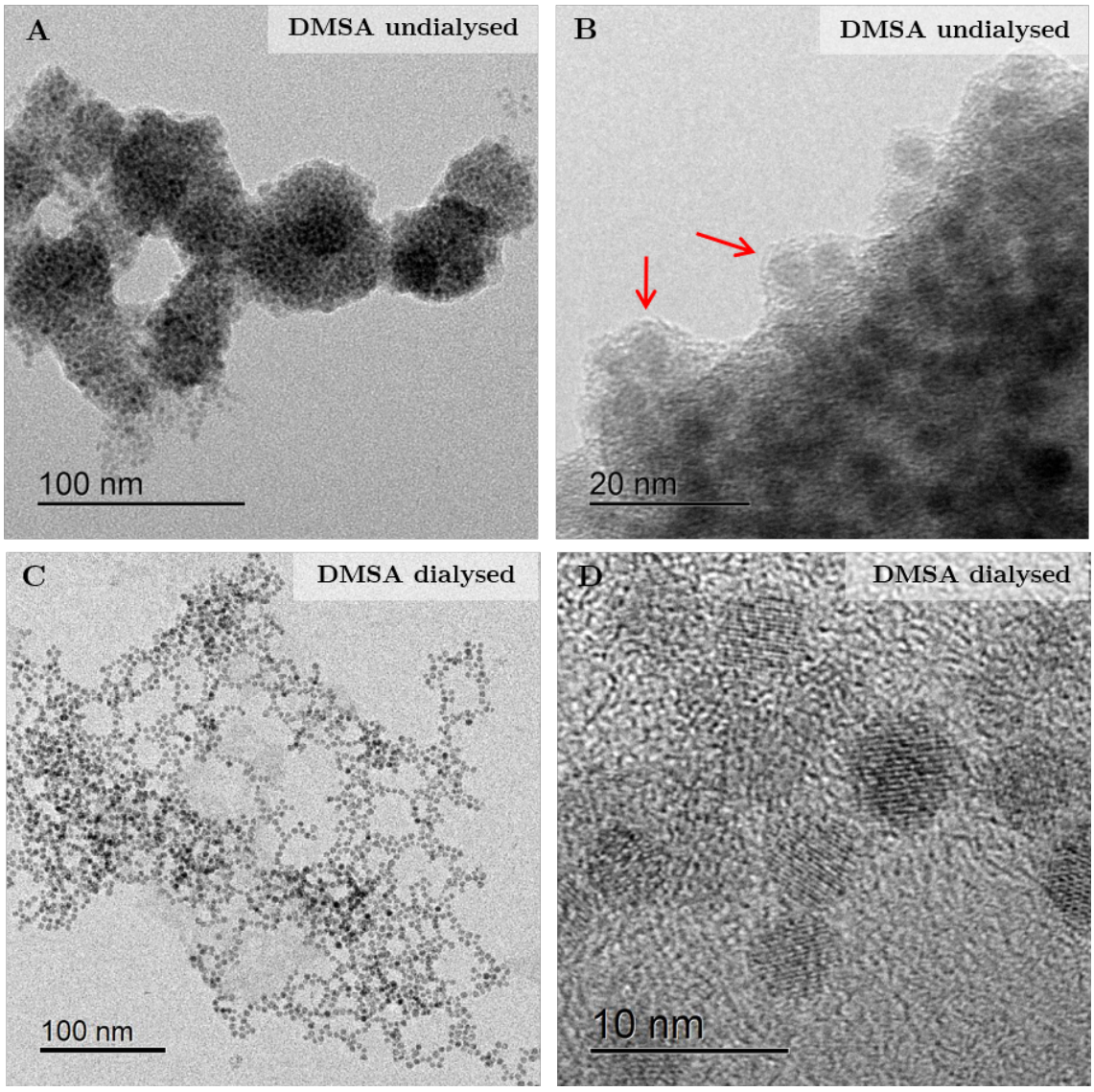


Figure 4.15: TEM micrographs of (A) Fe_3O_4@DMSA NPs that were not dialysed prior to ligand exchange, (B) TEM of undialysed Fe_3O_4@DMSA NPs, (C) Fe_3O_4@DMSA NPs that were dialysed prior to ligand exchange and (D) HR-TEM of dialysed Fe_3O_4@DMSA NPs.

Following the dialysis TEM and DLS studies, all subsequent ligand exchange experiments were performed including the pre-dialysis step. Accordingly, obtained suspensions in water appeared clear and no precipitation was visible (figure 4.16), indicating that DMSA was successfully stabilising the NPs and no agglomeration had occurred.

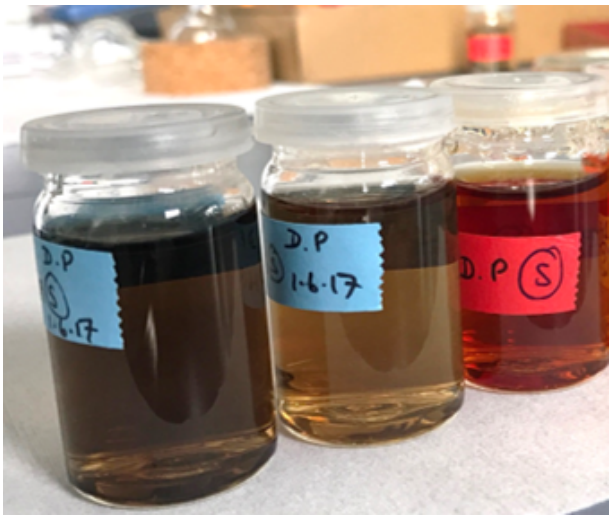


Figure 4.16: Representative samples of DMSA-coated cobalt-ferrite and iron-oxide NPs in water showing clear homogeneous dispersions.

Hydrodynamic diameters 7-23 nm in size were observed for all iron-oxide and cobalt-ferrite NPs, table 4.4 details the results. For 2.4 nm particles, d_Hs of 11 $\pm$2 nm and 8 $\pm$2 nm were measured for $CoFe_2O_4$@DMSA and Fe_3O_4@DMSA NPs respectively. Their zeta potentials were -31.8 $\pm$1.8 mV and -33.9 $\pm$0.7 mV, reflecting the negative charges from carboxylate moieties on the surface.

Representative TEM and d_H distribution graphs for 2.5 nm $CoFe_2O_4$@DMSA and 4.7 nm Fe_3O_4@DMSA NPs are shown in figure 4.17. The NPs retained their original core size and monodispersity post-phase transfer (figures 4.17(C,D)). Size distribution graphs comparing their average core diameter before and after ligand exchange are detailed in the appendix (see section B.2.2). HR-TEM revealed clear lattice fringes, showing crystallinity was also preserved (figures 4.17(E,F)). A similar study concerning oleylamine-only coated NPs described an increase in core size distribution after phase transfer with DMSA, owing to instability and aggregation occurring whilst the ligands were exchanging. Qi et al. reported an increase in core diameter from 4.3 to 9.5 nm after ligand-exchange.[241] Conversely, another report on oleic acid and oleylamine-coated NPs showed a decrease in core size caused by

the release of ferrous ions from the iron oxide surface, resulting in partial particle dissolution.[78]

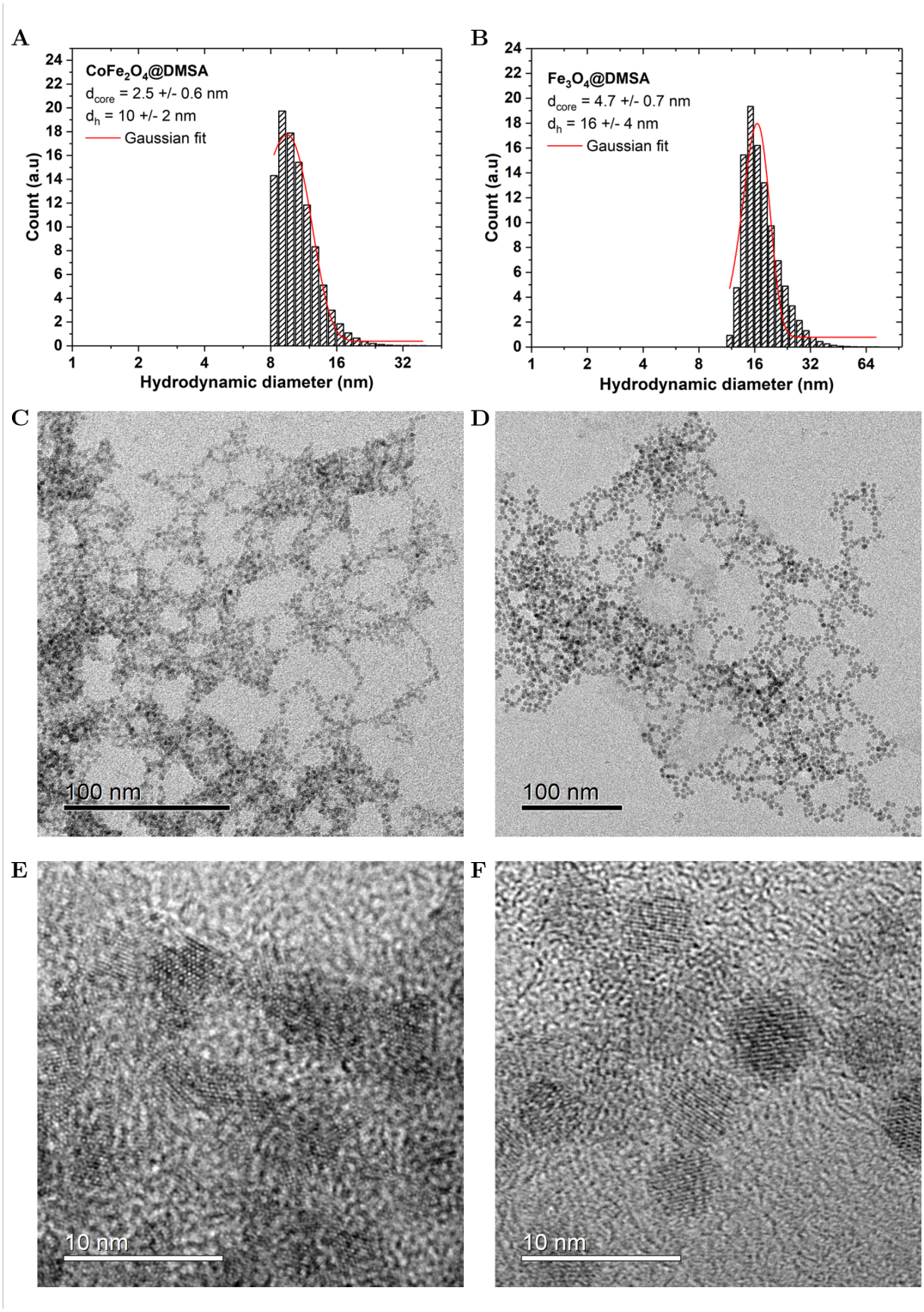


Figure 4.17: Hydrodynamic size distributions of (A) 2.5 nm $CoFe_2O_4$@DMSA and (B) Fe_3O_4@DMSA NPs showing good monodispersity. TEM micrographs of (C) 2.5 nm $CoFe_2O_4$@DMSA and (D) Fe_3O_4@DMSA NPs. HR-TEM micrographs of (E) 2.5 nm $CoFe_2O_4$@DMSA and (F) Fe_3O_4@DMSA NPs showing clear lattice fringes.

To confirm DMSA binding to the particles, TGA and FTIR studies were conducted. Figure 4.18 shows the weight loss profiles of $CoFe_2O_4$@OLA and $CoFe_2O_4$@DMSA NPs with a total weight loss of 60.5% and 36.4% respectively. The amount of ligands present on the surface of the NPs was estimated from the weight loss using equation 4.3 below.

$$N = \frac{\omega_l \rho \nu A}{\omega_c M} \tag{4.3}$$

where ω_l is the total weight (g) of the ligands calculated from TGA, ρ is the density of cobalt-ferrite (5.2957 g/cm^3), ν = volume of 2.4 nm particle, A is Avogadro's constant, ω_c is the total weight (g) of the particle core (calculated from TGA), M is the molar mass of ligand (oleylamine (267.5 g/mol) or DMSA (182.22 g/mol)) and N is the number of ligands per NP. The estimated number of DMSA ligands per NP is 90. Considering the surface area of a 2.4 nm NP is 18.1 nm^2, the ligand density is approximately 5 molecules per nm^2. Therefore the weight loss of 36.4% suggests a double-layer of DMSA is present on the NPs surface. The amount of OLA totalled 98 molecules per NP, thus the ligand density for a 2.4 nm NP is approximately 5.4 molecules per nm^2, suggesting a small amount of excess OLA was present after dialysis.

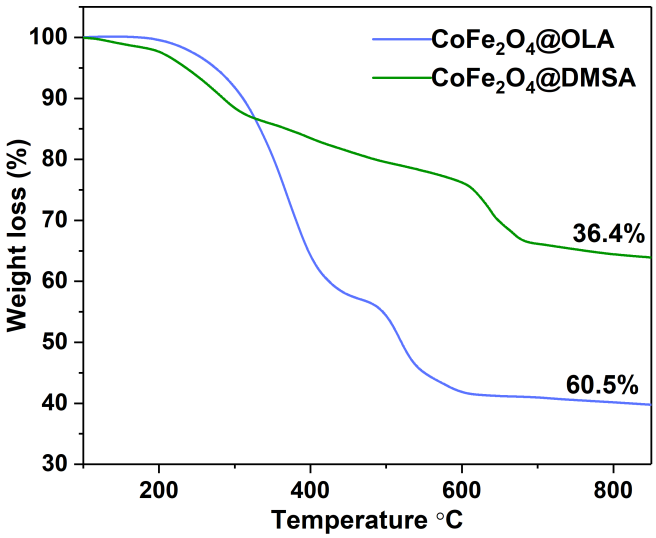


Figure 4.18: TGA weight loss profile of 2.4 nm $CoFe_2O_4$@OLA and $CoFe_2O_4$@DMSA NPs.

FTIR of $CoFe_2O_4$@OLA and $CoFe_2O_4$@DMSA NPs showed clear differences in their spectra (Figure 4.19). The first peak at 550 cm^{-1} was typical of the Fe-O stretching mode.[245] Broad peaks at 2922 and 2850 cm^{-1} were attributed to CH_2 asymmetric and symmetric stretching respectively[71].[246] The set of broad peaks between 1300 and 1650 cm^{-1} in $CoFe_2O_4$@OLA NPs were due to -NH_2 bending modes.[115][247] The strong broad band at 3340 cm^{-1} was due to -OH stretching. The presence of this band and the peak at 1135 cm^{-1} after ligand exchange was due to OH groups from remnant water[245].[248]

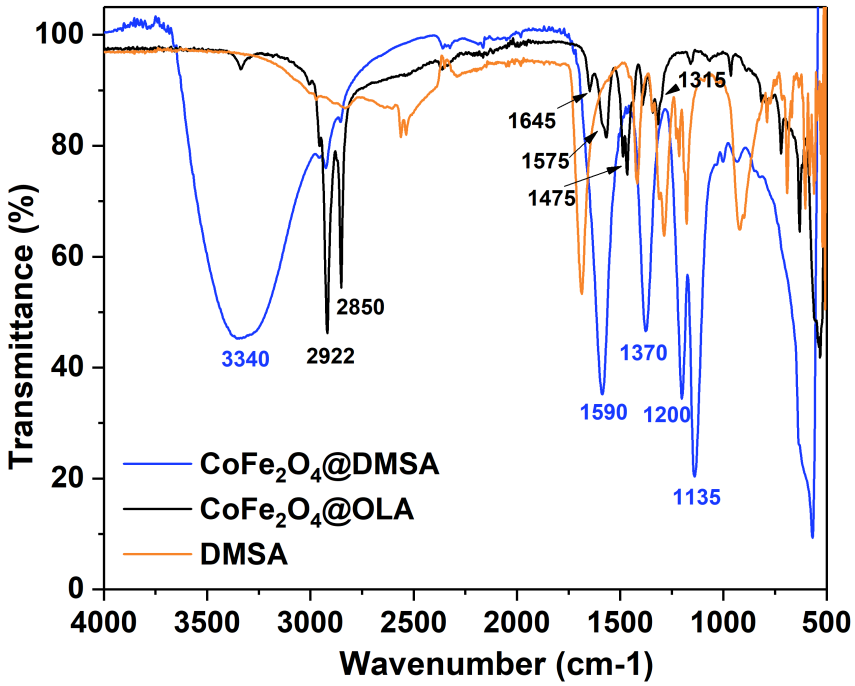


Figure 4.19: FTIR spectra of 2.4 nm $CoFe_2O_4$@OLA, $CoFe_2O_4$@DMSA NPs and DMSA. Sharpening and separation of the peaks at 1590 and 1370 cm^{-1} in the $CoFe_2O_4$@DMSA NPs' spectrum is due to asymmetric and symmetric stretching of carbonyl groups respectively, indicating that DMSA had bound to the surface.

Sharpening and separation of the peaks at 1590 and 1370 cm^{-1} appear from asymmetric and symmetric stretching of carbonyl groups respectively, indicating that DMSA was bound to the surface[229].[249] These new peaks were assigned to red shifting of carbonyl absorption bands typically observed at 1700 and 1750 cm^{-1}. Shifting occurred because the ligand had bound to the particles causing disassociation of the carboxyl group. Large splitting between these bands is associated with

a monodentate interaction between the carboxylate group of DMSA and the iron oxide NP.[78] FTIR confirmed that DMSA had replaced OLA on the surface of the NPs.

Stability of DMSA-coated NPs in different pH, buffer and over time

The stability of NPs is critical for biomedical applications, in particular MRI, as particle aggregation has a significant effect on relaxation rate. Aggregation of ultra-small iron oxide NPs has been shown to decrease the T_1 relaxation rate and increase the T_2 relaxation rate or nearby water protons, resulting in a dominant T_2 effect.[250] Cell toxicity is also affected by NP stability, as aggregation can influence uptake into cells, and NP degradation due to acidic pH can lead to leaching of ions.[251]

To address stability and reproducibility, DMSA ligand exchange was performed with a range of $CoFe_2O_4$@DMSA and Fe_3O_4@DMSA NPs 2-5 nm in size and their d_H and ζ-potential were measured in solutions from pH 3-10. Hydrodynamic diameters were re-measured following 3-12 months storage at 4 ℃. The d_H of the NPs ranged from 7 to 23 nm and ζ-potentials ranged from -28.0 to -43.2 mV, indicating monodisperse and stable dispersions were initially obtained for all samples (table 4.4). Following storage for 3-12 months, d_Hs increased slightly; the largest increase was from 8 to 46 nm after 12 months. Similarly, Zhang et al. found their DMSA particles were stable for 6 months, although they had initially large d_Hs (80 nm).[243]

The zeta-potential of both Fe_3O_4@DMSA and $CoFe_2O_4$@DMSA NPs increased as the pH decreased (figure 4.20(B)). The decrease in charge towards acidic pH is due to the protonation of free carboxylate and thiol groups on the NPs surface. Very similar results were reported by Palma et al.[78] Qi et al. also measured decreasing zeta-potential below pH 6 for Fe_3O_4@DMSA, with a nearly-neutral value of -5 mV at pH 3.[241] Interestingly, $CoFe_2O_4$@DMSA NPs were found to be stable in a wider pH range of 3-10 than Fe_3O_4@DMSA NPs, which began to flocculate below pH 5. As shown in figure 4.20(A) the d_H of $CoFe_2O_4$@DMSA NPs increased slightly from 8 ±2 nm at pH 7 to 17 ±4 nm at pH 3, whereas the d_H of Fe_3O_4@DMSA NPs increases from 7 ±2 nm to 79 ±25 nm. Fe_3O_4@DMSA NPs flocculation may have been caused by acid-induced reduction of Fe^{3+} to Fe^{2+}, which in turn caused oxidation of DMSA. Cobalt-ferrite is less prone to reduction than magnetite,[252] which may have

Table 4.4: Details of ligand exchange results with $CoFe_2O_4$@DMSA and Fe_3O_4@DMSA NPs. The hydrodynamic diameters were measured using DLS and repeated 3-12 months later. The pH stability range was determined by zeta-potential values that exceeded -25 mV.

Sample	Core size (nm)	d_H (nm)	Zeta (ζ) (pH 7)	pH stability range ($\zeta \geq$-25 mV)	d_H (+ no. of months after measurement)
$CoFe_2O_4$@DMSA 1	2.4 ±0.4	11 ±2	-31.8 ±1.8	3-9	25 ±7 (+12)
$CoFe_2O_4$@DMSA 2	2.4 ±0.4	13 ±3	-34.2 ±1.4	3-9	46 ±14 (+3)
$CoFe_2O_4$@DMSA 3	2.3 ±0.3	16 ±4	-28.0 ±0.3	3-9	15 ±5 (+3)
$CoFe_2O_4$@DMSA 4	2.3 ±0.3	8 ±2	-42.2 ±3.7	3-9	46 ±16 (+12)
$CoFe_2O_4$@DMSA 5	2.5 ±0.6	10 ±2	-36.4 ±4.1	-	-
$CoFe_2O_4$@DMSA 6	4.3 ±0.6	12 ±3	-38.4 ±0.9	3-9	36 ±7 (+12)
$CoFe_2O_4$@DMSA 7	4.3 ±0.6	23 ±7	-40.7 ±0.6	3-9	22 ±4 (+12)
Fe_3O_4@DMSA 1	2.4 ±0.5	7 ±2	-33.9 ±0.7	5-9	40 ±10 (+12)
Fe_3O_4@DMSA 2	4.0 ±0.8	12 ±2	-43.5 ±2.5	5-9	23 ±6 (+3)
Fe_3O_4@DMSA 3	4.2 ±0.7	12 ±2	-41.7 ±1.0	5-9	24 ±5 (+12)
Fe_3O_4@DMSA 4	4.7 ±0.7	16 ±4	-43.2 ±6.5	5-9	16 ±3 (+12)

reduced the extent of DMSA oxidation in acidic pH. Alternatively DMSA may have oxidised from oxygen in the solution. Oxidation of DMSA is a known phenomena that leads to the formation of interparticle disulphide bridges. Fauccioner et al. found that addition of an alkalisation step after ligand exchange improved colloidal stability significantly.[77] At pH 9, the free SH groups are deprotonated to thiolate groups which partially replace carboxylate groups at the surface of the particles. Free COO- groups then serve to stabilise the particle in a wide pH range. The observations in this work concur with that of Fauccioner; visible sedimentation of the particles occurred in the absence of an alkalisation step. Similar remarks were made by Chen (2008)[229] who observed sedimentation of DMSA-coated NPs in 5 days.

To view the NPs in their native liquid state, cryo-EM was employed. Figure 4.20(C) shows $CoFe_2O_4$@DMSA NPs arranged in a chain-like fashion, possibly due to magnetic interactions. Higher NP concentrations were used for cryo-EM than for hydrodynamic diameter measurements owing to the difficulty in locating such small-sized NPs in a suitably thin area of ice for optimum imaging. Magnetic NPs in high concentration are known to have weak magnetic dipole interactions resulting in linear chains.[213] Palma et al. also saw chaining after DMSA ligand exchange.[78] When dilute samples were used for cryo-EM, the micrographs revealed monodisperse

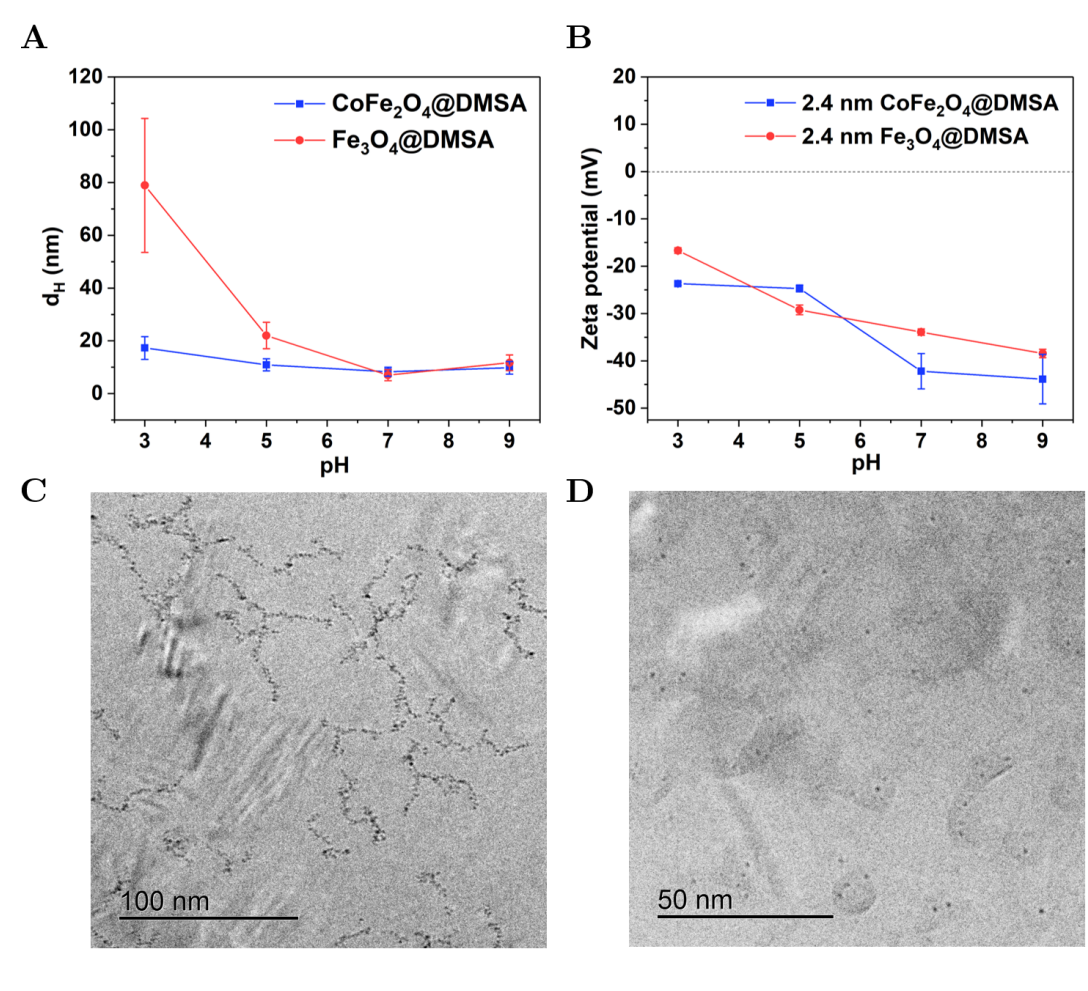


Figure 4.20: (A) Hydrodynamic diameter and (B) zeta potential of 2.4 nm $CoFe_2O_4$@DMSA and Fe_3O_4@DMSA NPs in pH range 3-9. Cryo-EM micrographs 2.4 nm $CoFe_2O_4$@DMSA NPs in water at a concentration of (C) ca. 300 µg/ml and (D) ca. 30 µg/ml.

NPs (figure 4.20(D)).

The stability of NPs in water is important for their general application and storage, however *in vivo* the NPs will encounter more complex media containing proteins, lipids, salts and other large molecules which may interact with the particle. The formation of a protein-particle complex, named the protein corona, can potentially alter the surface charge and hydrodynamic diameter of the particles, affecting their *in vivo* distribution.[253] As a first step to assess protein adsorption on MFe_2O_4@DMSA NPs, the d_H of the particles was measured in cell culture medium DMEM supplemented with 10% FBS. Figure 4.21(A) shows no significant change in d_H for $CoFe_2O_4$@DMSA NPs (8 ±2 nm in pure water to 11 ±3 nm in DMEM w/ 10% FBS), suggesting that protein adsorption was minimal. Fe_3O_4@DMSA NPs

suffered a larger increase from 7 ±2 nm to 30 ±8 nm, indicating protein adsorption. Cryo-EM of Fe_3O_4@DMSA NPs in DMEM revealed no additional agglomeration or aggregation in comparison to Fe_3O_4@DMSA NPs in water (figure 4.21(B)), suggesting that the increase in d_H was due to protein adsorption.

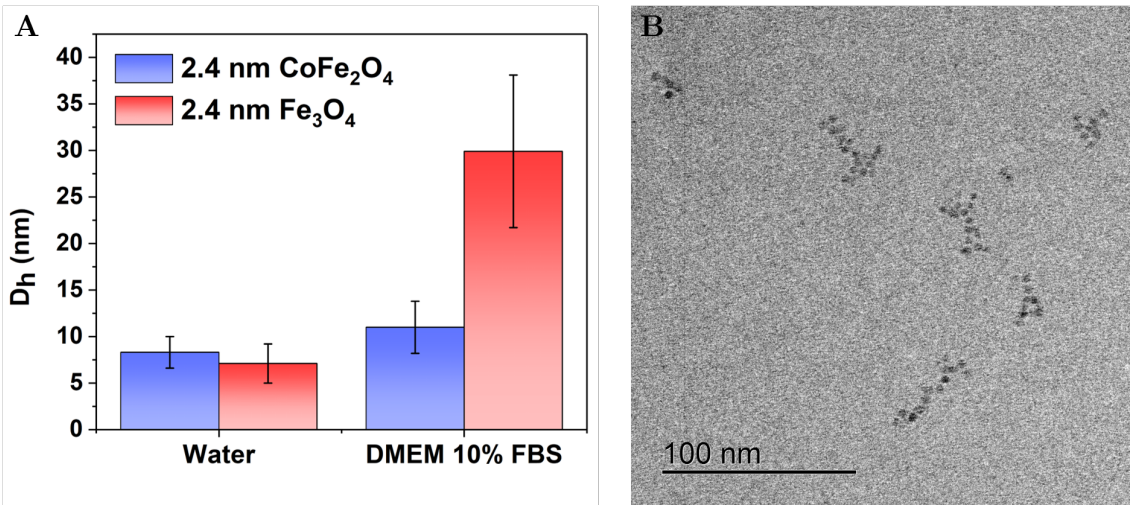


Figure 4.21: (A) Comparison of the NPs d_H in water DMEM supplemented with 10% FBS. (B) Cryo-EM micrograph of 4.2 nm Fe_3O_4@DMSA NPs in DMEM supplemented with 10% FBS.

Magnetic properties of NPs following DMSA ligand exchange

SQUID measurements of DMSA and OLA capped 4 nm $CoFe_2O_4$@DMSA and Fe_3O_4@DMSA NPs were compared to assess the effect of capping agent on the magnetic properties. The magnetisation saturation (M_s) of DMSA-coated NPs was lower in comparison to OLA-coated NPs. The M_s of OLA-coated NPs decreased from 44 to 7.8 emu/g for $CoFe_2O_4$@DMSA NPs and 55 to 23.8 emu/g for Fe_3O_4@DMSA NPs following ligand exchange with DMSA (figure 4.22(A)). The decrease can be explained by an increase in spin canting due to oxidation of the surface by DMSA. Daou et al. observed an increase in spin canting with carboxylate-coated magnetite NPs in comparison to bare particles owing to the contribution of an increase in the thickness of the oxidised layer and a canted surface layer in this oxidised layer.[254] Kim et al. also reported a decrease in M_s following DMSA ligand exchange due to surface oxidation.[244] Conversely, Mohapatra et al. found that OLA-coated $MnFe_2O_4$ NPs increased the M_s by 19% in comparison to trioctylphosphine oxide-coated NPs.[20] OLA served to increase spin-orbit coupling through coupling of the

amine to surface cations in $MnFe_2O_4$ NPs.

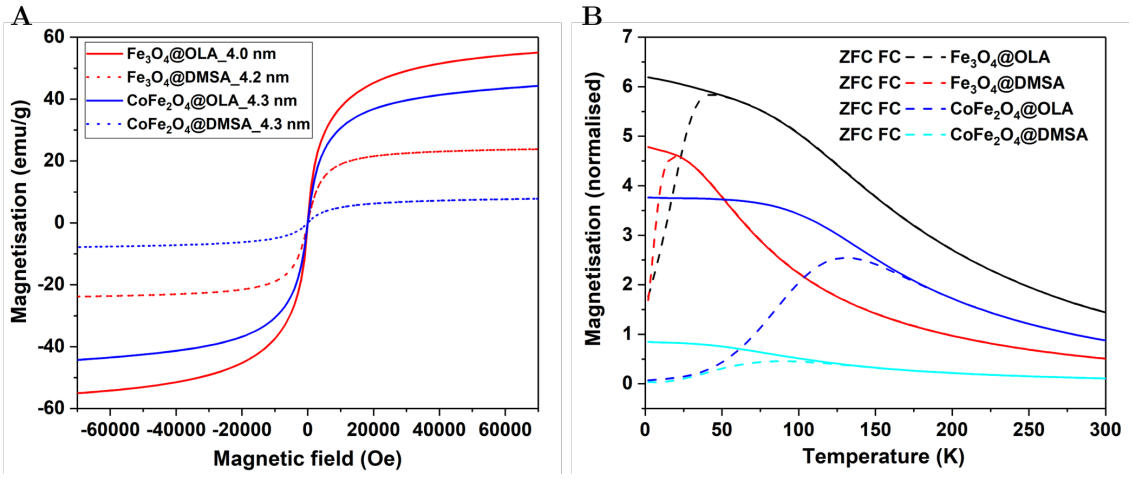


Figure 4.22: (A) Magnetisation curves of ca. 4 nm OLA and DMSA capped MFe_2O_4 NPs at 300 K. (B) Corresponding temperature-dependent magnetisation (zero-field cooling (ZFC) and field-cooling (FC)) curves. The FC curves were obtained at an applied field of 100 Oe.

The magnetic properties of 2.4 nm $CoFe_2O_4$@DMSA and Fe_3O_4@DMSA NPs were also measured after ligand exchange with DMSA. The M_s and T_B of $CoFe_2O_4$ and Fe_3O_4 NPs also decreased as anticipated in comparison to their as-synthesised measurements (see section 3.3.3). Figure 4.23 shows the magnetisation curves at 300 K, with both $CoFe_2O_4$@DMSA and Fe_3O_4@DMSA NPs displaying typical superparamagnetic behaviour evidenced by a loss of hysteresis. The magnetisation saturation of 2.4 nm Fe_3O_4@DMSA and $CoFe_2O_4$@DMSA NPs was 9.6 emu/g and 4.8 emu/g respectively. The blocking temperature (T_B) for 2.4 nm $CoFe_2O_4$@DMSA NPs was 102 K, which is markedly higher than that of Fe_3O_4@DMSA NPs at 12 K (Figure 4.23(B)). This rise in T_B is characteristic for $CoFe_2O_4$ due to an increase in anisotropy energy courtesy of Co^{2+} ions.[153] Their magnetic moments (m), calculated from Equation 4.4 were 38.8 μB for Fe_3O_4@DMSA NPs and 17.5 μB for $CoFe_2O_4$@DMSA NPs.

$$m = \frac{M\rho V}{\mu_B} \tag{4.4}$$

Where M is mass magnetisation, ρ is the material density, V is particle volume and μ_B is the Bohr magneton value.[30] The very small magnetic moment of 2.4 nm particles resulted from a high proportion of the particle being composed of surface

atoms and thus subject to spin canting effects.[185]

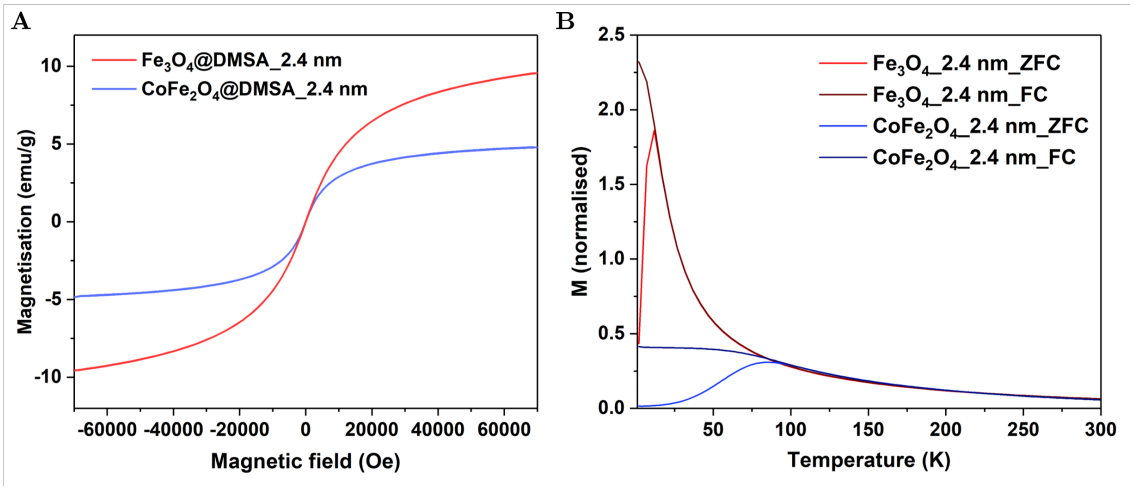


Figure 4.23: (A) Magnetisation curves of 2.4 Fe_3O_4@DMSA and $CoFe_2O_4$@DMSA NPs at 300 K. (B) Corresponding temperature-dependent magnetisation (zero-field cooling (ZFC) and field-cooling (FC)) curves. The FC curves were obtained at an applied field of 100 Oe.

4.3.3 Conclusions

Two routes to render MFe_2O_4@OLA NPs dispersible in water were explored: phase transfer with BSA and ligand exchange with DMSA. The aim was to achieve good colloidal stability, evidenced by small hydrodynamic diameters in water and physiological media at various pH, without affecting the crystallinity and size distribution of the cores. The BSA phase transfer method was unsuccessful for this purpose, yielding water-dispersible NPs that agglomerated in clusters. The clusters were stable in neutral and alkaline pH and physiological media, however had large hydrodynamic diameters (>100 nm).

Clusters are undesirable for biomedical applications for two major reasons: first clusters are likely to be quickly recognised and cleared by the RES. Secondly, clusters may adversely affect T_1 contrast in MRI as water molecules must be able to come into very close range of the NP cores in order for the exchange interaction which gives rise to T_1 relaxation to occur. The formation of clusters was speculated to be caused by excess OLA preventing effective adsorption of BSA. Particle dialysis was introduced to remove excess OLA, however this had no effect on the results, nor did varying the concentration of BSA. The formation of clusters may have been due to

the emulsion process itself, and thus further development of the method is required.

Phase transfer with DMSA on the other hand was successful for achieving monodisperse water-dispersible MFe_2O_4 NPs. Initially DMSA ligand exchange yielded large hydrodynamic diameters due to the presence of excess OLA. Small hydrodynamic diameters (ca. 12 nm) were subsequently achieved by the combination of an alkalisation step and particle dialysis. The method was reproducible and applicable to both $CoFe_2O_4$ and Fe_3O_4 NPs 2-5 nm in size. The NPs demonstrated good stability in pH 5-9 and physiological media. Furthermore, only minor flocculation was observed following 12 months in storage. Binding of DMSA to the NPs surface was confirmed with FTIR, and TGA studies revealed a double-layer of DMSA was present on the NPs surface. The DMSA coating affected the magnetic properties of the NPs due to oxidation of the surface: MFe_2O_4@DMSA NPs had significantly lower magnetisation saturation values in comparison to MFe_2O_4@OLA NPs. Low M_S values are nonetheless desirable for T_1-weighted MRI to reduce the effect of T_2 relaxation, which is the dominant mechanism for larger SPIONs. The small magnetic moments of 38.8 and 17.5 μB obtained for 2.4 nm Fe_3O_4@DMSA and $CoFe_2O_4$@DMSA NPs, in combination with the excellent colloidal stability in water, warrant investigation into their potential as T_1 MRI contrast agents. First however, the potential toxicity of the NPs must be assessed. The next chapter addresses biocompatibility with cytotoxicity and oxidative stress studies on MFe_2O_4@DMSA and MFe_2O_4@BSA NPs, comparing the effect of surface coating, core composition, and NP size.

Chapter 5

Cytotoxicity and oxidative stress of ultra-small MFe_2O_4@DMSA and MFe_2O_4@BSA NPs

Previous chapters have outlined the synthesis, characterisation and phase transfer of ultra-small iron oxide and cobalt-ferrite NPs. Two different phase transfer methods were explored, and either BSA or DMSA coated NPs resulted dispersible in water. This chapter details investigation into the toxicity of these particles towards HepG2 liver cells. HepG2 liver cells were chosen as the intended application of the particles is for liver-targeted MRI, and the liver is typically the accumulation site of metal-oxide NPs *in vivo*.[29,53]

Both iron-oxide and cobalt-ferrite NPs with different particle sizes, and either BSA or DMSA coatings were assessed for their toxicity in order to understand the effect of metal composition, core size and surface coating. Their toxicity was analysed with *in vitro* cytotoxicity and oxidative stress assays. For accuracy, it is important to determine the metal concentrations of the NPs, and to test for any interference the NPs may have with the assay components and optical measurements. The concentrations of the NPs were determined by inductively coupled plasma optical emission spectrometry (ICP-OES); section 5.3.1 details the results. Section 5.3.2 details the results of interference testing. The main results of cytotoxicity and oxidative stress assays are presented in sections 5.3.3 and 5.3.4. A discussion follows which compares the results obtained by the two different assays and how they relate to current

literature on the toxicity of metal-oxide NPs.

This work was carried out in collaboration with the Leibniz Institute for New Materials (INM): Cell culture, cytotoxicity and oxidative stress assays were performed by Dr. Jana Fleddermann, and ICP-OES was conducted by Andrea Jung.

5.1 Introduction to measuring nanotoxicity

The safety of NPs is one of the biggest concerns for their application in biomedicine. Their extremely small size enables them to interact on a sub-cellular level in the body, therefore evaluating their behaviour, distribution, and potential toxicity is extremely important for *in vivo* MRI applications. Currently there is no gold standard approach for assessing the toxicity of NPs; the optimal choice is dependent upon the type of NP, the intended application, the administration route, and the biological entities they are most likely to encounter.[60] *In vivo* studies are favoured as they provide a direct assessment of effect to human health. However, *in vitro* methods are more practical, rapid, and easy to use, and give a general sense of NP potential toxicity during the initial development of NPs.

Colorimetric/fluorometric toxicity assays are the most widely-used methods for initial screening of NP toxicity. For metal-oxide NPs, the tetrazolium dye 3-(4,5-dimethylthiazol-2-yl)-2,5-diphenyltetrazolium bromide (MTT) assay is frequently employed, which involves measuring the number of viable cells following exposure to NPs for a period of 1-3 days.[255] MTT is reduced to insoluble formazan by oxidoreductase enzymes in living cells, producing a purple colour. NP interference with the MTT assay is common, as iron-oxide NPs can absorb in the same UV-Vis range used for measurements.[60] To avoid interference, NPs are removed prior to measurements, however even careful extraction can remove cells in the process, leading to inaccuracies in the readings. Furthermore, the MTT compound itself can be cytotoxic as it uses energy from the cell, and the formazan crystals that form have been reported to damage cell membranes.[256] For this reason, CellTox™ Green, an assay that measures cell death as opposed to cell viability, was chosen for this study, and interference testing was conducted. In addition to measuring toxicity, it is important to measure non-lethal cellular changes such as metabolic abnormality

and inflammatory responses. One of the well-known issues with metal-oxide NPs is their ability to generate reactive oxygen species (ROS), which can cause oxidative stress to cells as discussed below.

5.1.1 Toxicity of ferrite NPs: oxidative stress and size-dependence

Iron oxide NPs are generally considered biocompatible and safe as iron is a natural product in the body and can be degraded and stored by ferritin. A recent study showed that cobalt (Co^{2+}) ions can also be degraded by ferritin.[53] However, the safety of both iron and cobalt-containing NPs is controversial, with concern regarding the degradation of NPs to release metal ions. The toxicity of Co^{2+} ions versus Co_3O_4 NPs was compared by Papis et al. who found that free Co^{2+} ions were more toxic to HepG2 cells, however Co_3O_4 NPs caused a rapid induction in ROS, whereas Co^{2+} ions did not.[257] Iron oxide NPs have also demonstrated toxic effects towards various cell types. A review by Singh et al. comprehensively covers the various toxicity mechanisms of iron-oxide NPs.[25] One of the principle causes of their toxicity is their ability to generate ROS by reducing hydrogen peroxide to hydroxyl radicals (.OH), dubbed the Fenton reaction.[258] The Fenton reaction mechanism is discussed in depth in section 5.3.4. ROS levels in cells are maintained by enzymes and antioxidants, however a burst of ROS can upset this redox homeostasis and induce deleterious effects to cells through oxidative damage of biomolecules (e.g., proteins, lipids, and nucleic acids) or disrupt cell signalling mechanisms, potentially causing cell death (apoptosis).[258]

The reaction rate of ROS generation by iron-oxide NPs has been shown to increase with an increase in surface area.[259] This implies ultra-small NPs could potentially enhance ROS production. The toxicity of USNPs is currently poorly understood; the majority of studies to date have been conducted on larger NPs (>20 nm).[26] Furthermore, studies on cobalt-ferrite NPs are generally lacking, and no studies have been conducted on cobalt-ferrite NPs smaller than 5 nm. Asides from their large surface area, USNPs could potentially have greater cytotoxic effects as their small size enables penetration into sub-cellular components.[26] Alternatively, their small size and thus reduced metal ion content may be favourable in reducing toxic effects.[260] For example, Xie et al. compared the toxicity of 6, 9 and 14 nm

Fe_3O_4 particles and found only 6 nm NPs avoided ROS generation when incubated with two human hepatoma cells.[56]

In this study, ultra-small iron oxide and cobalt-ferrite NPs were evaluated for their potential to induce cytotoxicity and oxidative stress to HepG2 liver cells to address the gap in knowledge regarding the toxicity of USNPs. As the same synthesis and ligand exchange conditions were used to prepare both Fe_3O_4 and $CoFe_2O_4$ NPs, their results could be directly compared to assess the effect of the metal ions. The surface coating is also known to influence toxicity, therefore both DMSA and BSA coated NPs were evaluated. Finally, two different particle sizes (2.4 nm and 4.2 nm) were compared to determine if ultra-small (2.4 nm) NPs were detrimental or beneficial in terms of toxicity.

5.2 Materials and methods

5.2.1 Chemicals

Sterile filters (Rotilab P668.1), sodium hydroxide (NaOH) (≥99%), and Triton X-100 (3051.3) were purchased from Carl Roth GmbH, and fetal bovine serum (FBS) from PAN-Biotech (3302-P291205). CellTox™Green Cytotoxicity Assay (Promega, Cat. G8742), Dulbecco's Phosphate Buffered Saline (D-PBS) (Invitrogen 14190169), Dulbecco's Modified Eagle Medium (DMEM) (1885023) and RPMI-1640 basal medium (21875-034) were purchased from Thermo Fisher Scientific. 2',7'-Dichlorofluorescin diacetate (ROS indicator, D6883), 3-Morpholinosydnonimine (SIN-1) and hydrogen peroxide (H1009) were purchased from Sigma Aldrich. Cellstripper with chelating agents (25-056-CI) was purchased from Corning. Unless otherwise specified, ultra-pure Milli-Q water was used throughout.

5.2.2 Nanoparticle preparation

MFe_2O_4@BSA or MFe_2O_4@DMSA NPs were filtered through sterile filters with a pore size of 0.22 μm to remove any bacterial contaminants and large aggregates, then diluted to concentrations of 100 μg/ml in 50% DMEM medium.

5.2.3 HepG2 cell culture

Adherent, epithelial human hepatocarcinoma cells (HepG2) (German Collection of Microorganisms and Cell Cultures (DSMZ, Braunschweig, Germany)) were cultured in an incubator under humidified atmosphere at 37 °C with 5% CO_2 in DMEM medium supplemented with 10% (v/v) FBS and dislodged using Cellstripper.

5.2.4 Cytotoxicity assay method

To evaluate the toxicity of the NPs towards HepG2 cells, the CellTox™Green assay was employed. This assay measures changes in membrane integrity that occur as a result of cell death with a cyanine dye indicator. The dye preferentially binds to DNA released from cells following disruption to the cell membrane, significantly enhancing its fluorescence upon binding. Viable cells do not increase the fluorescence signal, thus the signal obtained is proportional to the number of dead cells. To prepare cells for assay testing, the cells were dislodged using cell stripper, counted by an automated cell counter (CASY Model TT, OLS OMNI Life Science, Bremen, Germany) and seeded with a density of 75.000/ml (100 µl per well) in 96-well BRAND®plates (plastic bottom, black walls). HepG2 cells were incubated with NPs of different concentrations in RPMI-1640 medium supplemented with 10% FBS for 24 hours at 37 °C. Cell death was measured by the CellTox™Green assay (positive control = lysis solution from kit). Fluorescence measurements were obtained using a Tecan Infinite® M200 Pro plate reader (excitation = 490 nm, emission = 525 nm). Fluorescence values were normalised to the negative control (cell medium = 1), and corrected for optical interference using the percentage interference values from figure 5.2A. Three independent assays were performed, and for each assay samples were tested in triplicate. Particle-induced optical interference was assessed by repeating the protocol above in the absence of cells. To test for particle optical interference in the event of a positive result, 50 µl of 1% Triton X-100 was added per well and incubated with cells for 24 hours at 37 °C, following which NPs in RPMI-1640 medium supplemented with 10% FBS were added and fluorescence measurements performed as above.

5.2.5 Oxidative stress assay method

Nanoparticle-induced oxidative stress was measured by detecting the oxidation of 2',7'-dichlorofluorescin-diacetate (H_2DCF-DA) into the highly fluorescent compound 2',7' dichlorofluorescein (DCF) due to the presence of reactive oxygen species (ROS). H_2DCF-DA is the most popular probe used for measuring oxidative stress.[261] Cells were dislodged using cell stripper, counted by an automated cell counter (CASY Model TT, OLS OMNI Life Science, Bremen, Germany) and seeded with a density of 75.000/ml (100 µl per well) in 96-well BRAND®plates (plastic bottom, black walls). HepG2 cells were incubated with NPs of different concentrations in RPMI-1640 medium supplemented with 10% FBS for 24 hours at 37 °C. Hydrogen peroxide was used as the positive control. Following incubation, 100 µM of H_2DCF-DA diluted in DMEM medium (without phenol red) was added to each well and incubated for 30 minutes at 37 °C. Fluorescence measurements were obtained using a Tecan Infinite® M200 Pro plate reader (excitation = 492 nm, emission = 530 nm). Fluorescence values were normalised to the negative control (cell medium = 1), and corrected for optical interference using the percentage interference values from figure 5.3A. Three independent assays were performed, and for each assay samples were tested in triplicate. Interference testing was conducted by incubating particles with H_2DCF in the absence of cells. H_2DCF-DA was deacetylated with NaOH according to the protocol of Ivask et al.[58] NPs or controls (water, PBS or 10 µM 3-morpholinosydnonimine (SIN-1)) were incubated with 100 µl of H_2DCF for one hour at 21 °C in the dark. Fluorescence measurements were then performed as above. To assay for particle reduction of ROS signal, the interference test was repeated as above with the addition of 10 µM SIN-1 per well.

5.2.6 Inductively coupled plasma optical emission spectrometry

Inductively coupled plasma optical emission spectrometry (ICP-OES) is an quantitative analysis method used to detect metals at very low concentrations. A liquid sample is aspirated and its atoms ionised by a plasma source. The ions are then separated by their mass-to-charge ratio and detected by the mass spectrometer. ICP-

OES is a highly sensitive technique: both iron and cobalt can be detected down to the single part per trillion (ppt) level.[262] Thus, it is suitable for determining the amount of metal in the USNP samples.

To obtain elemental concentrations, ICP-OES measurements were conducted using a Horiba Jobin Yvon Ultima 2 (pressure: 2.15 bar, flow: 0.75 l/min, Co: λ = 238.892 nm, Fe: λ = 238.204 nm). Samples were diluted 1:100 in H_2O. Subsequent calculations were performed to estimate the particle concentration:

Particle concentration *(C_p)* (g/l), defined as the concentration of iron oxide or cobalt ferrite as opposed to single metal concentration, was estimated based on ICP-OES data on the elemental concentration of metals in the NPs. To estimate particle concentration, first the number of NPs per litre (n) was calculated:

$$n = \frac{CAV_{uc}}{N_{Fe}M_{Fe}v} \tag{5.1}$$

Where C is the iron concentration determined by ICP-OES (g/l), $N_{Fe/O/Co}$ is the number of iron, oxygen or cobalt atoms in a unit cell (assuming defect-free FCC Fe_3O_4 or $CoFe_xO_y$ spinel structure, for cobalt-ferrite particles the ratio was based on the ICP-OES data). $M_{Fe/O/Co}$ is molar mass of iron, oxygen or cobalt, A is Avogadro's constant, v is the NP volume, and V_{uc} is the volume of a unit cell (nm^3) (based on lattice parameters of 0.8397 nm for cobalt ferrite and 0.838 nm for magnetite). Particle concentration *(C_p)* (g/l), was then calculated by multiplying the number of particles (n) by the mass of a single iron oxide or cobalt ferrite NP (iron oxide example shown):

$$C_p = n((N_{Fe}M_{Fe}A^{-1}) + (N_OM_OA^{-1})\frac{v}{V_{uc}}) \tag{5.2}$$

Several assumptions were made when estimating the particle concentrations as detailed in section B.3.1 of the appendix.

5.3 Results and discussion

5.3.1 Determination of NP concentrations

ICP-OES measurements of the iron and cobalt concentration of MFe_2O_4@BSA and MFe_2O_4@DMSA NPs were used to estimate the concentration of the NPs (table 5.1). The stoichiometry of cobalt ferrite NPs did not correspond to $CoFe_2O_4$ as measured by EELS (chapter 3); the iron content was greater than double the amount of cobalt according to ICP-OES. The propensity to substitute cations is a feature of spinel ferrites, and different compositions are thus possible as described in chapter 3. The exact stoichiometry of the cobalt ferrite NPs was difficult to determine with EELS and ICP-OES, however it is clear that the NPs were composed of a mixture of Fe and Co. As NP-induced toxic effects have been associated with the available surface area,[251] the total number of NPs is also shown.

Table 5.1: Calculated particle concentrations compared to elemental ICP-OES concentrations

Particle type	Core size (TEM) (nm)	Coating ligand	ICP-OES elemental concentration (mg/l)		Calculated NP concentration (μg/ml)	Number of NPs in 1 ml
			Fe	Co		
Fe_3O_4	4.2 nm	DMSA	121.2 ± 0.2	n/a	167.5 ± 0.3	8.26×10^{14}
Fe_3O_4	2.4 nm	DMSA	179.2 ± 2.0	n/a	247.6 ± 0.3	6.55×10^{15}
$CoFe_2O_4$	4.3 nm	DMSA	158.9 ± 1.9	57.4 ± 0.3	297.87 ± 3.1	1.36×10^{15}
$CoFe_2O_4$	2.4 nm	DMSA	101.5 ± 1.4	34.5 ± 0.6	187.8 ± 2.0	4.95×10^{15}
$CoFe_2O_4$	2.4 nm	DMSA	192.5 ± 5.9	27.8 ± 0.3	303.9 ± 8.6	8.04×10^{15}
$CoFe_2O_4$	2.4 nm	BSA	48.4 ± 0.8	20.3 ± 0.3	94.5 ± 1.5	2.49×10^{15}

Using the calculated NP concentrations, the samples were diluted in DMEM medium to concentrations of 100 μg/ml for the toxicity assays, with the exception of $CoFe_2O_4$@BSA where the maximum concentration obtainable was 50 μg/ml (figure 5.1). Particle concentrations in the range of 1-100 μg/ml are typically used in ferrite NP toxicity testing. Prominent examples can be found in the widely-cited review article by Singh et al. (2010),[25] who summarised the toxicity of iron-oxide NPs. The dose of Feridex®, an iron-oxide based MRI contrast agent previously FDA-approved for liver MRI, approximates to an iron serum concentration level of 5.5 μg/ml.[263]

Thus 1-100 μg/ml was deemed appropriate for cytotoxicity testing. It is also worth noting that metal-oxide NP interference in assay fluorescence measurements above concentrations of 100 μg/ml is a widely-cited issue.

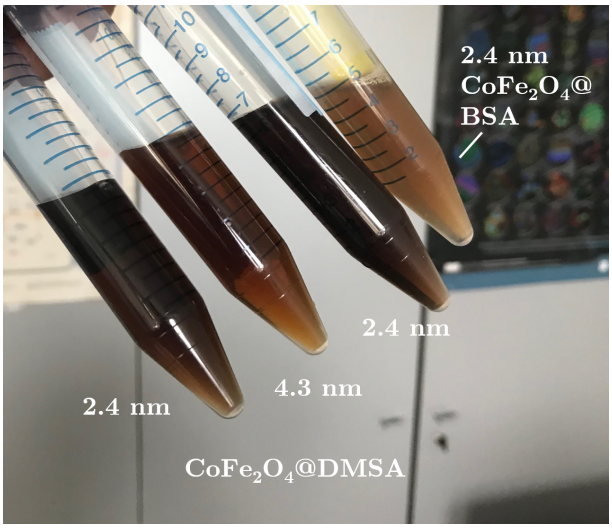


Figure 5.1: The concentrations of cobalt ferrite NP samples used for cytotoxicity testing following sterilisation and dilution (200 μg/ml ($CoFe_2O_4$@DMSA)) and (100 μg/ml ($CoFe_2O_4$@BSA)).

5.3.2 Evaluation of potential NP assay interference

NP interference with cytotoxicity assays is a common problem, particularly for metal-oxide NPs which can optically interfere with the fluorescence readings. Thus, any interference must be measured and taken into consideration when analysing toxicity data. To assess for NP-induced optical interference, fluorescence measurements of MFe_2O_4@DMSA and $CoFe_2O_4$@BSA NPs in cell medium alone (no cells or dye indicators used) were acquired. The fluorescence values were normalised to the negative control (cell medium) and were an average of three measurements. Figure 5.2(A) shows the fluorescence signal decreased as NP concentration increased. Both Fe_3O_4 and $CoFe_2O_4$ NPs caused a concentration-dependent reduction in fluorescence; neither NP size nor composition had an observable influence on the interference. Metal-oxide NP interference at high concentrations ($>$ 50 μg/ml) has been widely reported for other commonly-used methods such as MTT, LDH and DCF assays.[264,265]

To check if the NP optical interference would affect a positive signal in the event of cell death, cells were incubated with 1% triton X-100 (a positive control for

cell death) for 24 hours at 37 ℃, following which NPs were added. Figure 5.2(B) shows that particles did not cause an increase in signal, thus false positive results from particle interference are ruled out. However, fluorescence decreased as NP concentration increased as observed in the particles-only experiments (figure 5.2(A)). Thus, false negative results are possible due to the minor decrease in fluorescence caused by NP optical interference.

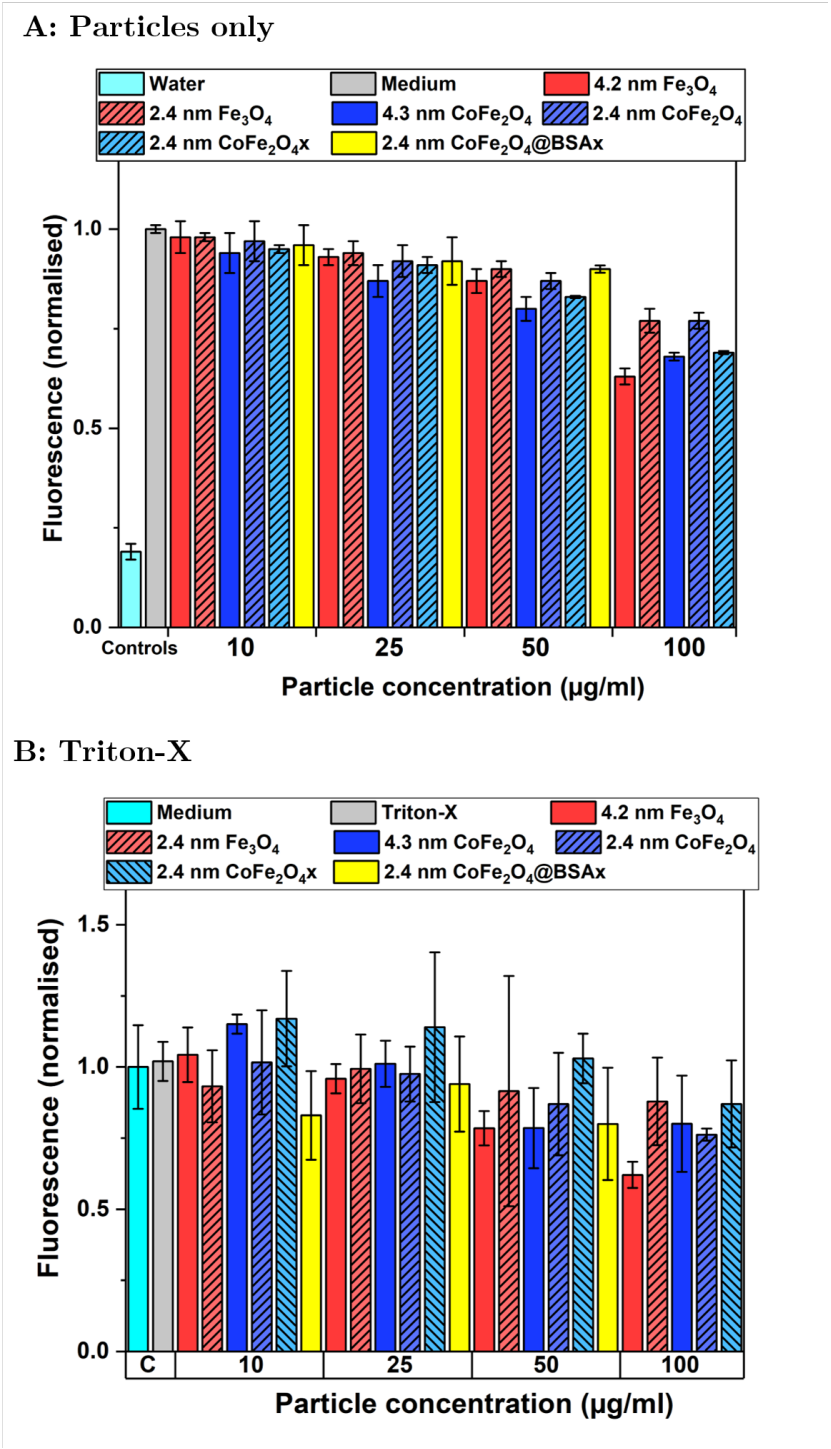


Figure 5.2: Interference testing of MFe_2O_4@DMSA and $CoFe_2O_4$@BSA NPs in CellTox™ Green assay; (A) Fluorescence measurements in response to particle concentration in the absence of cells (normalised to cell medium). $CoFe_2O_4$ samples labelled with an 'x' are the same synthesis batch but different surface coatings. (B) Particles exhibited negative optical interference with positive signal generated from Triton-X (normalised to control test = fluorescence values before addition of NPs).

Several possible strategies for correcting for NP interference have been reported. One route is to remove the NPs prior to optical measurements.[264] However, in this

assay the end measurement is the cell death of adherent cells, thus removing NPs would inevitably remove dead cells as-well, invalidating the results. Alternatively, the concentration range could be limited to the range which interference is not observed.[266] The third option is to subtract the absorbance of NPs in cell media from the absorbance data attained from NP-treated cells.[60] The latter was adopted in this study, and the cytotoxicity and ROS values obtained in subsequent experiments were corrected for the factor of negative interference to the range of the absolute values in the particles-only experiment (Figure 5.2(A)).

Next, the oxidative stress interference potential of the NPs was assessed using the reactive oxygen species dye indicator (2',7'-dichlorodihydrofluorescein (H_2DCF)). Particles were incubated with H_2DCF in the absence of cells. SIN-1 was used as the positive control as it can process H_2DCF in a cell-free environment.[267] As shown in figure 5.3, MFe_2O_4@DMSA NPs caused no increase or decrease in fluorescence signal and thus did not interfere with the ROS dye. However $CoFe_2O_4$@BSA NPs caused a significant concentration-dependent increase in fluorescence signal, within the same range as the positive control at the maximum concentration. The $CoFe_2O_4$@BSA NPs thus had intrinsic oxidative properties. Considering the presence of BSA in the cell medium used in all samples, the BSA surface coating is unlikely to be the cause of ROS dye conversion. In fact, BSA has known antioxidant properties.[268] The oxidative properties may have been caused by uncoated NPs present in the sample. Further characterisation of the BSA-coated NPs is required to understand their oxidative properties. Nonetheless, their interference prevents accurate measurements of NP-induced ROS generation, and thus BSA-coated NPs were not evaluated for oxidative stress with this method henceforth.

Further testing of the MFe_2O_4@DMSA NPs was conducted to assess for potential interference with the already-converted ROS dye after incubation with SIN-1 (in the absence of cells). Particles were incubated with 10 μM of SIN-1 for 1 hour at room temperature in the dark. As shown in figure 5.3(B), NPs did not cause a reduction or increase in ROS signal, and thus did not interfere with a positive ROS signal. Unlike in the cytotoxicity tests, particle optical interference was negligible in the oxidative stress measurements due to the high absolute values of fluorescence.

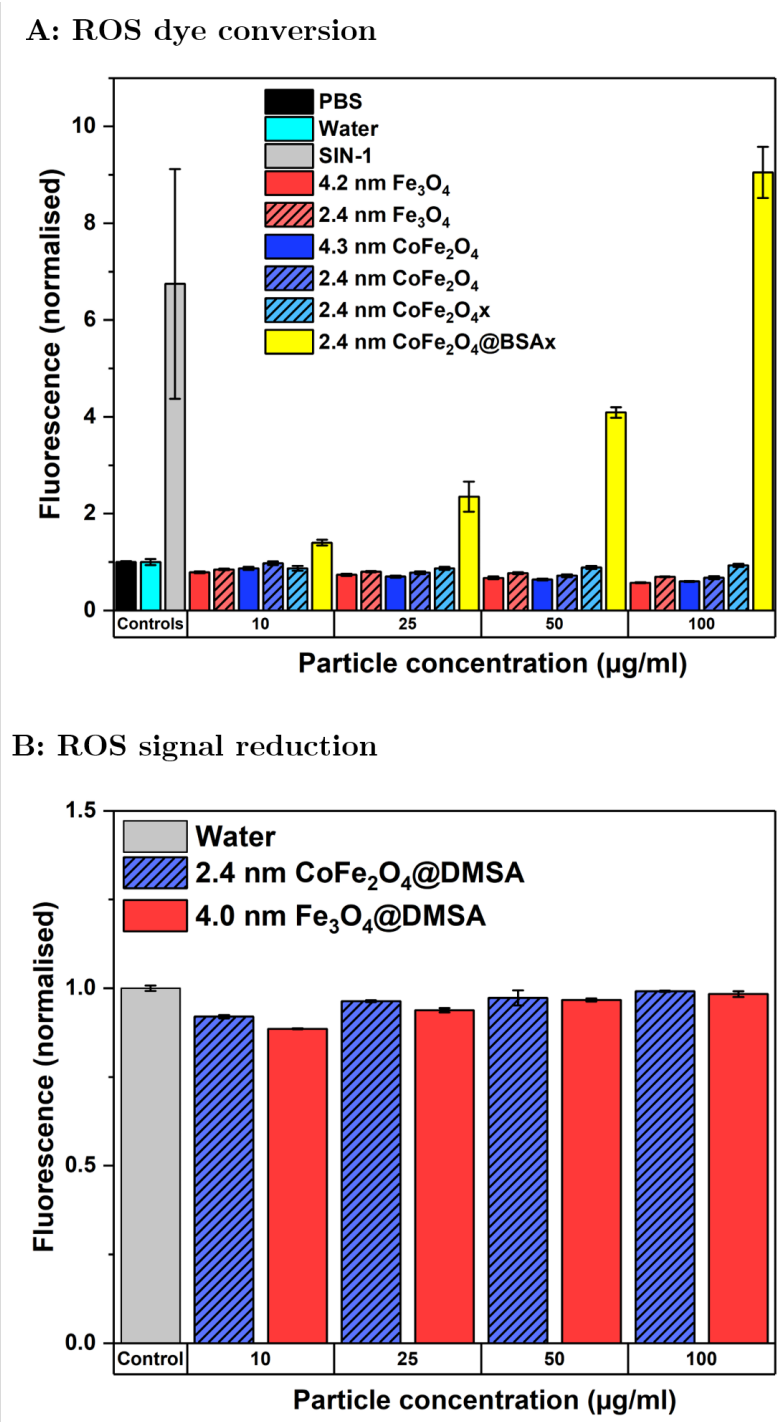


Figure 5.3: Interference testing of MFe_2O_4@DMSA and $CoFe_2O_4$@BSA NPs in ROS assay; (A) Interference test of NPs with ROS dye: NPs did not cause conversion of dye in absence of cells (normalised to PBS). (B) NPs did not interfere with SIN-1 (normalised to water). $CoFe_2O_4$ samples labelled with an 'x' are the same synthesis batch but different surface coatings.

5.3.3 Cytotoxicity of ultra-small NPs towards HepG2 cells

For biomedical applications, it is paramount that NPs are screened for potential cytotoxic effects. The cytotoxicity of MFe_2O_4@DMSA and $CoFe_2O_4$@BSA NPs towards HepG2 liver cells was evaluated using the CellTox™ Green assay which measures NP-induced cell death. Iron oxide and cobalt ferrite NPs of two different sizes (4.3 and 2.4 nm) were prepared using identical synthesis and ligand exchange conditions, enabling direct comparison of their toxicity to HepG2 liver cells. Figure 5.4 shows relative cell death for 2.4 and 4.3 nm MFe_2O_4@DMSA and $CoFe_2O_4$@BSA NPs at concentrations of up to 100 μg/mL. Relative cell death (fluorescence) was corrected for optical interference induced by the particles (see section 5.3.2). No cell death occurred with MFe_2O_4@DMSA, and there was no size or metal composition influence. However, $CoFe_2O_4$@BSA NPs produced appreciable concentration-dependent cell death. The clustered form of $CoFe_2O_4$@BSA NPs may have been a causation, leading to greater cellular uptake. Considering their cytotoxic effect and agglomerated form, extensive further investigation is required to optimise $CoFe_2O_4$@BSA NPs. Thus, the direct BSA-functionalisation route was no longer explored as a viable option to achieve biocompatible NPs, and all subsequent research efforts were directed towards MFe_2O_4@DMSA NPs.

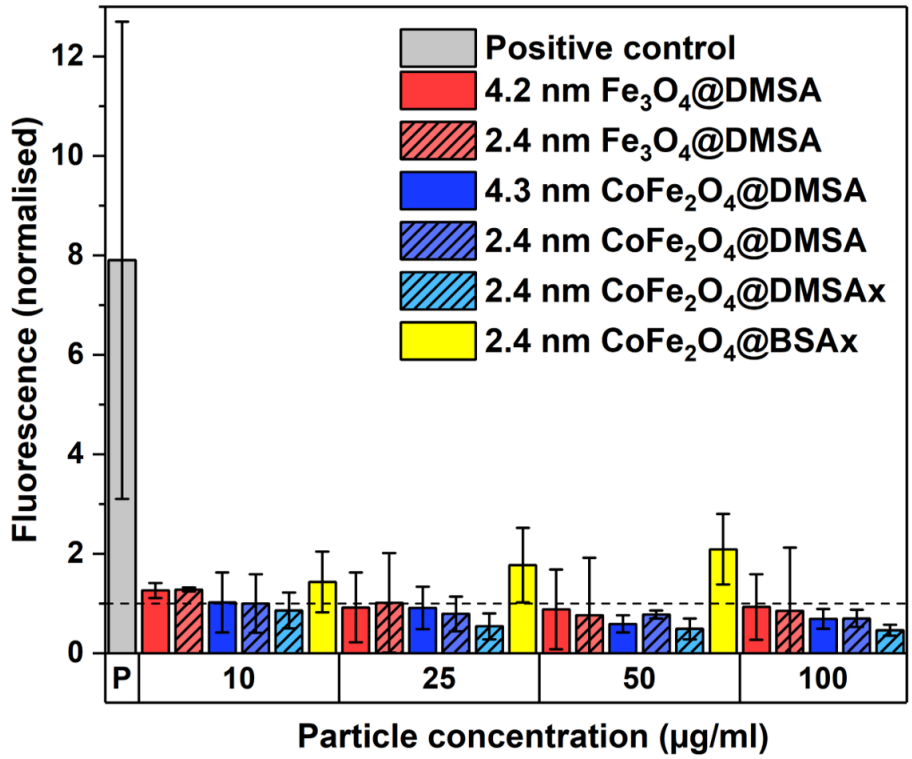


Figure 5.4: Cytotoxicity results of MFe_2O_4@DMSA and $CoFe_2O_4$@BSA NPs following incubation with HepG2 liver cells for 24 hours: relative cell death (fluorescence) in relation to particle concentration. Fluorescence values were normalised to the negative control (cell medium = 1 (dotted line)). No cell death was observed for any particle type. $CoFe_2O_4$ samples labelled with an 'x' are the same synthesis batch but different surface coatings. Positive control = lysis solution from kit. Results are shown as mean ± standard deviation from three independent experiments.

5.3.4 Oxidative stress of ultra-small NPs towards HepG2 cells

Tandem with cytotoxicity testing, NP-induced production of reactive oxygen species (ROS) was evaluated using 2',7'-dichlorofluorescin-diacetate (H_2DCF-DA). ROS have potentially harmful effects on cells, and have been linked to DNA damage, apoptosis, and even carcinogenesis.[54] Conversely, NP-induced ROS production can be harnessed for therapeutic application as treatment towards cancer cells through selective-induction of apoptosis[269].[270] Figure 5.5 shows the results of the ROS assay conducted with DMSA-coated NPs. Both Fe_3O_4@DMSA and $CoFe_2O_4$@DMSA NPs produced concentration-dependent ROS following incubation with HepG2 cells. Cobalt-ferrite NPs produced 48% higher ROS than iron-oxide at 100 µg/ml, with

2.4 nm particles producing the highest.

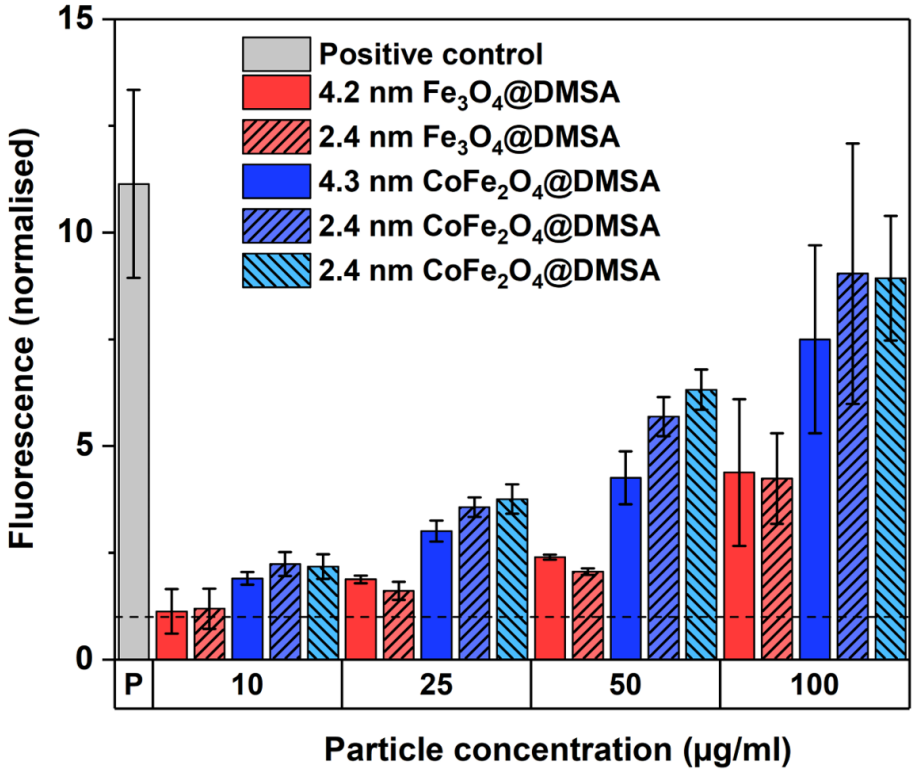


Figure 5.5: Relative ROS production (fluorescence) reactive oxygen species induced by the particles. Both Fe_3O_4@DMSA and $CoFe_2O_4$@DMSA NPs produced ROS, however $CoFe_2O_4$@DMSA NPs produced significantly higher amounts than Fe_3O_4@DMSA NPs. Positive control = hydrogen peroxide. Results are shown as mean ± standard deviation from three independent experiments.

5.4 Discussion

Iron-oxide and cobalt ferrite NPs coated in DMSA were not cytotoxic to HepG2 cells, however both produced significant amounts of ROS. Despite high ROS production levels, particularly for cobalt ferrite NPs, no cell membrane integrity was compromised. ROS can affect membrane integrity through peroxidation of membrane lipids; the consequence of which can lead to signalling of cell apoptosis under extreme stress, or initiate antioxidative processes.[271] Interestingly, a similar study by Liu et al. into the toxicity of DMSA-coated Fe_3O_4 NPs observed HepG2 cell apoptosis at NP concentrations of 100 µg/ml.[272] Conjunctively, they detected increased activity for malonyldialdehyde, a marker for oxidative stress, suggesting this

was the mechanism responsible for apoptosis. A comprehensive study into the toxicity of 6 nm cobalt ferrite NPs by Horev-Azaria et al. using *in vitro* assays on 7 different cell lines in combination with predictive modelling, found that ROS generation by $CoFe_2O_4$ NPs was dependent on the cell type.[273] Contradictory to the results of this study, Horev-Azaria found that HepG2 cells were the least affected by $CoFe_2O_4$ NPs compared to other cell types, with no cytotoxicity or ROS observed at concentrations up to 284 μg/ml. The discrepancies between our results may be due to the slightly different conditions used: Liu et al. used 11 nm NPs, an increased incubation time of 48 hours and the MTT cell viability assay. Horev-Azaria et al. used 6 nm cobalt-ferrite NPs with a diethylene glycol coating.

Metal-oxide induced production of ROS is linked to the Fenton reaction, whereby transition metal ions catalyze hydrogen peroxide decomposition and generate hydroxyl radicals.[274–276] The greater ROS production for $CoFe_2O_4$@DMSA NPs measured in this study may be due to the higher catalytic ability of Co^{2+} ions over Fe^{2+}. It may also be linked to the production of different ROS species; iron is known to produce .OH radicals whereas cobalt produces $.HO_2$ radicals.[277] A study comparing the fenton-like reactions of different transition metals ions when reacted with electrogenerated hydrogen peroxide generation using voltammetry measurements found that cobalt (Co^{2+}) has a higher .HO radical generating ability than iron (Fe^{3+}).[274]

ROS production generated by metal-oxide NPs has been widely published, however, others in the field have reported opposing results. Gao et al. published a claim in Nature Nanotechnology that magnetite NPs have intrinsic peroxidase-like properties: decomposing hydrogen peroxide and scavenging free radicals.[278] This widely-cited article generated many follow-up studies, including a report by Huang et al. that the peroxidase-like activity of Fe_3O_4 NPs was responsible for proliferating cell growth in human mesenchymal stem cells, determined by an increase in cell viability in MTT assays.[279] However, they did not assess for NP interference, therefore the increase in viability at high concentrations may not be valid. The results in this work showed a decrease in cell death (fluorescence) with increasing particle concentrations, which was due to interference and not NP-induced cell proliferation. More recently, Gumpelmayer et al. challenged the results of Huang and Gao by repeating their experiments, concluding that magnetite NPs do not have

peroxidase-like activity.[280] However, they also concluded that Fe_3O_4 NPs do not generate ROS in an oxidative stress assay (*in vitro* oxidation of ascorbate), which conflicts with the findings in this study.

Contradictory reports on the cytotoxicity and ROS potential of metal-oxide NPs are widespread in literature. Cytotoxic effects and ROS production induced by both Fe_3O_4 and $CoFe_2O_4$ NPs have been reported by others.[59,270] Wu et al. found DMSA-coated maghemite NPs induced ROS and had adverse effects on nematodes after 24 hour exposure.[281] Fe_3O_4 NPs coated with tetramethylammonium 11-aminoundecaonate were cytotoxic towards human glia, human breast cancer, and normal cell lines at concentrations above 10 μg/ml.[282] Filipova et al. recorded 20% cell death of human umbilical vein endothelial cells following exposure to polylactic acid-coated Fe_3O_4 NPs.[283] Ahamed et al. found 23 nm naked $CoFe_2O_4$ particles were cytotoxic against HepG2 cells and produced ROS.[284] Conversely, others have reported no cytotoxic effects or ROS production for $CoFe_2O_4$ NPs against HepG2 cells,[273] or other cell types.[285,286] Cytotoxicity and ROS can be avoided through functionalisation with a biocompatible surface. Finetti et al. performed MTT and H_2DCF-DA assays on cobalt ferrite NPs and originally found oxidative stress and cytotoxic effects towards endothelial cells.[55] These adverse effects were eliminated by loading the NPs into polysaccharide hydrogels, which were not toxic to endothelial, stromal and epithelial cells, and were safe and biodegradable *in vivo*. In section 6.2 of chapter 6, a method that significantly minimised ROS production of both Fe_3O_4@DMSA and $CoFe_2O_4$@DMSA NPs via surface functionalisation with a bile acid derivative is presented.

The disparities concerning metal-oxide NP toxicity highlight the importance of testing each new particle system against cells, as surface coating, preparation parameters, and other slight changes in particle characteristics can have a profound effect. Toxicity behaviour is complex, and vastly different results have been attained even for NPs composed of the same material and surface coatings. The lack of coherence between results is one of the greatest challenges facing the application of NPs, as their toxicity cannot be predicted and remains poorly understood. Centralisation of toxicity data would be beneficial to start identifying trends between NP design and toxicity behaviour, however this is inhibited by the use of different methods and

conditions to measure toxicity. Efforts are under way to standardise cytotoxicity testing: Farcal et al. proposed an 'Intelligent Testing Strategy' comprising a range of *in vitro* methods and cellular models to comprehensively evaluate NP toxicity.[287] They suggested this approach, in combination with detailed characterisation of the NPs in question, use of comparable and comprehensive dose metrics, use of reference NPs allowing comparisons between studies, implementation of NP interference controls and material characterization in the relevant biological matrix, is required to effectively assess toxicity behaviour before *in vivo* investigations. Their study was part of the FP7-MARINA program of the European Commission, which is dedicated towards assessing, developing and optimising methods for life cycle analysis, exposure, hazard identification and risk assessment of NPs.

5.5 Conclusions

Iron-oxide and cobalt-ferrite NPs of different sizes and surface coatings were evaluated for their toxicity towards HepG2 liver cells. BSA-coated $CoFe_2O_4$ NPs were found to be cytotoxic towards HepG2 cells; cell death increased as particle concentration increased. Unfortunately $CoFe_2O_4$@BSA NPs interfered with the oxidative stress assay, thus could not be evaluated for ROS production. Due to the combination of their unfavourable cytotoxicity results and agglomerated condition as reported in chapter 4, further investigation into BSA-coated NPs was abandoned.

DMSA-coated Fe_3O_4 and $CoFe_2O_4$ NPs indicated better suitability for biomedical applications, with no cytotoxic effects towards HepG2 cells for any particle sizes. However, elevated levels of ROS were measured following a 24 hour incubation period, particularly for $CoFe_2O_4$ NPs. ROS generation is a frequently-encountered issue with metal-oxide NPs. As an indicator for oxidative stress, ROS production should ideally be minimised as much as possible. To further evaluate the cytotoxicity and oxidative stress effects of the NPs, further *in vitro* assays and cell uptake studies should be conducted, followed by *in vivo* experiments.

Comprehensive cytotoxicity testing was beyond the scope of this work, however DMSA-coated NPs did demonstrate potential suitability for biomedical applications which warrants their further investigation. In chapter 6, the application of

ultra-small MFe_2O_4@DMSA NPs as MRI contrast agents is explored. Furthermore, preliminary studies into their functionalisation with a bile-acid derivative towards liver-targeted MRI demonstrates an effective route for significantly reducing their ROS generation to safe levels.

Chapter 6

Magnetic resonance imaging and bile-acid functionalisation studies of ultra-small MFe_2O_4@DMSA NPs towards liver-targeted MRI

Previous chapters have detailed the synthesis, characterisation, ligand exchange and cytotoxicity of ultra-small MFe_2O_4 NPs. This future work chapter is composed of two parts: first the MRI application of ultra-small MFe_2O_4 NPs (section 6.1), and second the bile-acid functionalisation of ultra-small MFe_2O_4 NPs towards liver-targeted MRI (section 6.2). Currently-used positive (T_1) contrast agents are composed of gadolinium, and toxicity concerns have recently led to their investigation. Ultra-small ferrite NPs may offer a more biocompatible and tailorable alternative to T_1 contrast enhancement. In this chapter, 2.4 nm Fe_3O_4@DMSA and $CoFe_2O_4$@DMSA NPs are investigated as contrast agents with MRI phantom studies using pre-clinical (9.4 T) and clinical (3.0 T) MRI scanners. Particular emphasis is placed on 2.4 nm $CoFe_2O_4$@DMSA NPs as this is the first time they have been explored for T_1-weighted MRI before, and their reduced magnetic saturation could be advantageous for T_1-weighted imaging. Section 6.1.1 provides background information on MRI and NP-based contrast agents. The methods used to assess the MRI behaviour of ultra-small MFe_2O_4@DMSA NPs are outlined in section 6.1.3. The results of 9.4 T and 3.0 T MRI phantom testing are detailed in section 6.1.4.

The second part of this chapter describes the conjugation of MFe_2O_4@DMSA NPs to a bile-acid derivative, cholic acid. Bile-acids are part of the hepatobilary system, and thus are naturally transported to and from the liver in the human body. In this context, functionalisation of MFe_2O_4@DMSA NPs with cholic acid is explored towards their application as liver-targeted MRI agents for the first time. Synthesis of amino cholate and its conjugation method to the NPs is described in section 6.2.2. Characterisation of the magnetic properties and stability of the new NPs is described in section 6.2.3. Cytotoxicity and oxidative stress of the MFe_2O_4@BA NPs is outlined in section 6.2.3, where the results show significant reduction of reactive oxygen species.

The work in this chapter was conducted in collaboration with several institutes. Operation of the 9.4 T pre-clinical MRI scanner and data processing was conducted by Dr. Mahon Maguire at the Wellcome Trust Centre for Human Genetics in Oxford. Operation of the 3.0 T clinical MRI scanner was conducted by Dr. Daniel Papp and Dr. Sebastian Reiger at the Oxford Centre for Human Brain Activity. Data processing was conducted by Dr. Mahon Maguire (Oxford), and Professor Evelio Rafael Gonzales Dalmau, Armando José Hernández Rodríguez and Israel Reyes Molina from the Cuban Neuroscience Centre in Havana, Cuba. Bile-acid functionalisation of the NPs was carried out in collaboration with Dr. Annette Krageloh, Dr. Isabella Tavernaro and Dr. Jana Fleddermann at the Leibniz Institute for New Materials in Germany.

6.1 MRI phantom testing of MFe_2O_4@DMSA NPs

6.1.1 Introduction to MRI

Magnetic resonance imaging (MRI) is a powerful tool used widely in clinics for the diagnosis and treatment of injuries and diseases. MRI uses high strength magnets, radio-frequency (RF) pulses and the magnetic moments of protons in water to generate a contrast-based internal image of the body. First, a magnetic field (B_0) aligns proton spins either parallel (lower energy) or anti-parallel (higher energy) to its direction. An RF pulse is then applied which excites some protons aligned parallel to the anti-parallel (spin-down state) alignment, simultaneously aligning their

spins in phase too. The RF pulse operates at the precession frequency of protons in that particular magnetic field strength, called the Larmor frequency. When the RF pulse is removed, protons relax back to their lower energy spin-up state by two separate processes: re-aligning with B_0, and losing phase coherence.[209] These relaxation mechanisms generate a radio signal which can be measured by receivers in the scanner and made into an image. Image contrast is achieved due to the variation in proton density and relaxation rates in different parts of the body such as fat, tissue, and blood.[288]

T_1 and T_2 relaxation

The two separate mechanisms by which protons relax following an RF pulse are termed longitudinal (T_1), or transverse (T_2 and $T_2{}^*$) relaxation. T_1 relaxation is known as spin-lattice relaxation, as the protons realign to the longitudinal plane (parallel to B_0), transferring energy to the surrounding lattice. T_2 relaxation is known as spin-spin, whereby the spins of protons in the transverse plane dephase, causing signal decay. An additional term $T_2{}^*$ was introduced to explain why T_2 times often appeared shorter in real experiments than what was predicted by molecular mechanisms.[289] $T_2{}^*$ results from local magnetic field inhomogeneities, which accelerate the decay of proton's spins.

T_1 and T_2 create different types of image contrast. T_1 generates positive contrast: fat appears bright (white) and water appears dark, as fat has a short T_1 relaxation time in comparison to water because it can transfer received energy to its surroundings more easily.[290] T_2 generates negative contrast, where fluid appears bright and fat and tissue appears dark. Different imaging modes are used depending on the type of diagnosis required. For example, T_1 is useful for identifying fatty tissue, characterizing focal liver lesions and in general for obtaining morphological information, whereas T_2 is favoured for imaging tumours and inflammation due to their high fluid content (figure 6.1).[46,291]

To improve contrast in MRI, contrast agents (CAs) are intravenously administered immediately prior to scanning. CAs are routinely used worldwide; approximately 30 million MRI scans per year involve the use of a CA.[292] The following section discusses contrast agents and their utility in MRI.

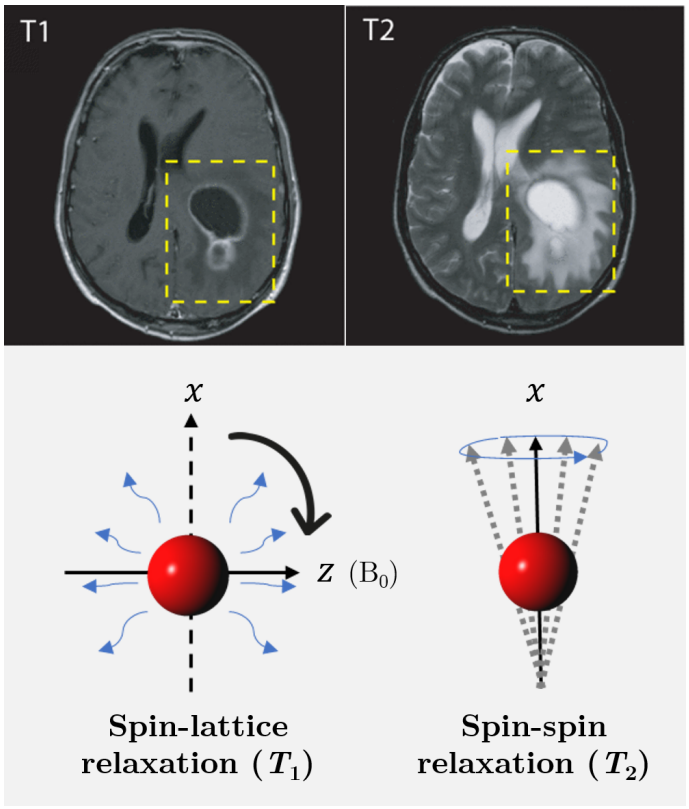


Figure 6.1: (Top) Example MRI of patient with brain tumour showing T_1 and T_2-weighted images. The tumour is more easily visible in the T_2 image as it is surrounded by fluid which appears bright (copyright © 2008 *IEEE*). (Bottom) schematic illustrating T_1 and T_2 relaxation.

6.1.2 MRI contrast agents: Gadolinium-based and magnetic NPs

Contrast agents are useful tools to enhance image contrast in MRI. CAs are typically paramagnetic materials, and the most frequently used are gadolinium-based (Gd), which shorten T_1 and are therefore known as T_1 contrast agents. Gd-CAs also shorten T_2, however the effect is negligible in comparison to T_1. T_2 CAs are composed of superparamagnetic iron-oxide nanoparticles (SPIONs) >5 nm in size. Similarly, SPIONs also shorten T_1, however to a significantly lesser extent than T_2. There is growing interest in developing dual T_1–T_2 contrast agents to combine the advantages of positive and negative contrasts.[293] However, this is very challenging, as CAs affect T_1, T_2 and/or T_2^* by different molecular mechanisms.

Gd effectively shortens T_1 though an *inner sphere relaxation mechanism*, which describes close-range dipole interactions between protons and Gd's unpaired electrons. The dipole interactions create magnetic fluctuations near the Larmor fre-

quency of protons, inducing T_1 relaxation. Simultaneously, water molecules around the periphery of Gd molecules undergo relaxation caused by the local magnetic field of Gd, called *outer sphere relaxation*. Both mechanisms contribute to T_1 relaxation (60% originates from inner sphere and 40% from outer sphere).[294] By shortening T_1, the amount of time required to acquire an image is reduced, consequently more lines of phase-encoding can be obtained (which increases image resolution). CAs also improve contrast and thus signal by differential uptake into different biological compartments. In order for a T_1 CA to be highly efficient, the CA should:

1. Have unpaired electrons. Gd possesses seven, exhibiting powerful paramagnetism. Co^{2+} cations have three unpaired electrons and Fe^{3+} ions have five, thus also provide paramagnetism.

2. Have a molecular tumbling rate close to the Larmor frequency. The molecular tumbling rate is the rotational rate of the molecule. Gd-DTPA (Magnevist®) has a smaller molecular weight than its albumin-conjugated version Ablavar®. Conjugation of Gd-DTPA to albumin increased relaxivity 4-5 times, as albumin slowed the rotational motion of the CA to a rate near the Larmor frequency. This is another reason why BSA-coated USNPs were explored in this thesis.

3. Allow close contact between the water molecules and paramagnetic centre. A distance within ∼0.25 nm is required for inner sphere relaxation to occur. Gd CAs are composed of Gd ions surrounded by a chelating shell which allows one binding site within this distance. A single layer of DMSA is reported to be 0.1 nm thick,[295] thus the double layer estimated on the surface of USNPs in this work (chapter 4) is within the distance required for close water contact (provided no protein adsorption occurs).

Less influential complex factors which influence T_1 are described elsewhere.[296] The mechanisms by which ultra-small iron oxide NPs shorten T_1 relaxation time are not entirely clear. In addition to the suppressed magnetisation of USNPs minimising their contribution to T_2 relaxation, it is hypothesised that their high surface-

to-volume ratio exposes iron ions which promote inner sphere relaxation.[297] Analogously to Gd, the water mobility around the USNPs also dictates their T_1 relaxation efficiency. Therefore, the coating ligand greatly influences the effectiveness of a T_1 CA.

Although Gd-based agents satisfy the criteria for an effective T_1 agent, Gd ions are extremely toxic and pose a significant health risk. To mitigate the toxicity of Gd ions, chelating agents are used to shield the body from exposure and encourage rapid renal clearance. However, in 2006 it was discovered that in patients with kidney failure, Gd-CAs circulate for longer which leads to their degradation *in vivo* and potential onset of fatal nephrogenic systemic fibrosis (NSF).[298] Thus, Gd-based agents can not be used on patients with kidney issues, which represent 16% of the UK population.[299] Fresh concerns were raised over the dechelation of Gd-CAs following a post-mortem study in 2015 by Mayo Clinic researchers who found Gd deposits in the brain tissue of patients who had received Gd-CA enhanced MRI scans.[40] In February 2018, the UK government suspended the licenses of Omniscan®and Magnevist®, two main commercial Gd-based contrast agents, until further investigation.[39]

The safety concerns surrounding Gd-based agents highlight the need to develop new, more biocompatible CAs. SPIONs are more biocompatible than Gd,[41] and have proven clinical utility for T_2 contrast enhancement. Their large magnetic moment induces local magnetic field inhomogeneities, which dephase nearby water protons shortening both T_2* and T_2 relaxation. As SPIONs are uptaken by the reticuloendothelial system and thus predominately accumulate in the liver,[29] they proved most suitable for liver-targeted MRI and two types of SPIONs received FDA approval (Feridex® and Resovist®),[300] However, Gd-based non-specific and hepatospecific agents demonstrated better practicality and diagnostic performance for liver cancer and thus are currently preferred by clinicians.[37] Consequently, due to a lack of clinical users, Feridex® was withdrawn from the market, and Resovist® is currently available in only a few countries.[35]

Recognising the limited commercial success of SPIONs as T_2 contrast agents, new research emerged investigating their application as T_1 agents instead. A small number of early studies identified that under certain conditions, iron oxide NPs could generate T_1-weighted contrast.[301–303] However in 2011, seminal work by Kim et al.

detailed the link between ultra-small NP size and T_1-weighted contrast.[30] Kim et al. found that T_1-weighted contrast could be achieved with maghemite NPs by reducing the particle size to 3 nm. In a size-dependent study with 1.5, 2.2, 3.0 and 12 nm NPs, they found that the magnetic core of NPs smaller than 3 nm was greatly reduced as they were composed mostly of surface atoms, which are magnetically disordered due to spin canting. The spin canting reduced their magnetisation saturation, which led to a decrease in T_2 effect, whilst the five unpaired electrons of the maghemite core provided effective shortening of T_1. Their 'extremely small-sized' iron-oxide NPs (ESIONs), proved useful for MR angiography with long-blood circulation times in rats.

Following Kim et al's work and the Mayo Clinic report on Gd retention in the brain, the number of research reports into ultra-small iron oxide NPs for T_1 imaging has grown. The research landscape is summarised by number of papers (figure 6.2) and by location (figure 6.3). In 2016, Rui et al. demonstrated T_1-weighted MR angiography with ultra-small poly(acrylic) acid coated Fe_3O_4 NPs (USPIO@PAAs) 4.5 nm in size.[43] Jia et al. (2016) demonstrated T_1-imaging of hepatic tumours with peptide-coated 4 nm Fe_3O_4 NPs.[304] In 2017, Wei et al. reported 'exceedingly small' (2.5 nm) maghemite NPs coated with a zwitterionic shell (ZES-SPIONs).[42] Their design was directed towards NPs that could be renally excreted, with a 1 nm thick dopamine sulfonate coating, yielding a hydrodynamic diameter of 4.7 nm. They conducted *in vivo* MR angiography studies which showed both the T_1-weighted properties of the NPs and their effective renal clearance. Inspired by Wei's study, Shen et al. used similar parameters to identify the optimum particle size, comparing 1.9, 2.6, 3.3 and 3.6 nm 'exceedingly small' Fe_3O_4 NPs.[305] They concluded that 3.6 nm was the optimum NP size for T_1-weighted contrast, however this study was conducted on a 7 T system which is not the clinical standard.

In addition to T_1-imaging, ultra-small NPs have been exploited for dual T_1 and T_2-weighted MRI. Bai et al. showed dual contrast with ultra small Fe_3O_4 NPs was possible through time-dependent *in vivo* aggregation.[306] Following initial administration in mice, T_1-weighted contrast was obtained. Over time, the NPs aggregated at a tumour site through active targeting with a peptide molecule. The aggregation affected their magnetic properties, leading to enhancement of T_2. Although

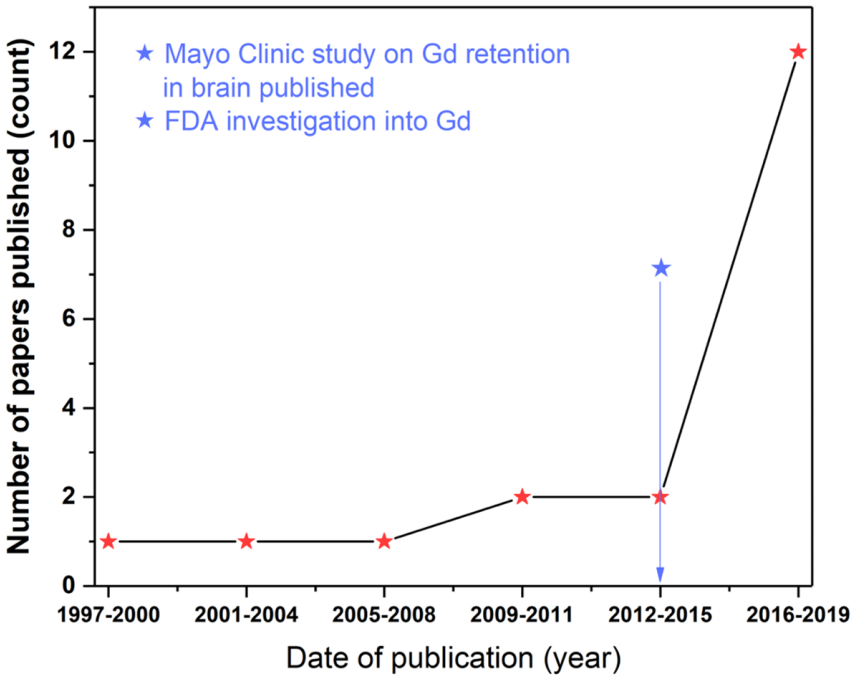


Figure 6.2: Timeline of publications on ultra-small iron oxide or ferrite NPs for T_1-weighted MRI.

this is an interesting idea for dual-imaging, the lack of control over aggregation *in vivo* may hamper their practical use. Another study approached dual-imaging by labelling SPIONS with Gd ions, however this approach does not avoid the toxicity concern with Gd ions.[307] In addition to iron oxide NPs, manganese oxide NPs have been explored as T_1 CAs with promising performance arising due to Mn's 5 unpaired electrons.[308] Zhang et al. compared 3 nm iron oxide NPs with manganese ferrite ($MnFe_2O_4$) NPs for T_1-weighted contrast enhancement. The $MnFe_2O_4$ NPs had the highest T_1 relaxivity, and proved effective for *in vivo* blood pool and liver-specific MRI.[44] However, high concentrations of Mn ions can cause a serious neurodegenerative disorder known as 'manganism', and thus presents toxicity issues similar to Gd.[8]

Although ultra small iron oxide NPs have demonstrated strong applicability for T_1-weighed imaging, their inherently strong magnetic moment still impairs their performance in comparison to gadolinium (table 6.2 in section 6.1.4 compares their properties). Furthermore, iron oxide NPs are prone to oxidation which can alter their surface properties, leading to potential changes in their stability, magnetic behaviour and toxicity.[24,25] The addition of cobalt ions may serve to increase the



Figure 6.3: Map of publications on ultra-small iron oxide or ferrite NPs for T_1-weighted MRI.

stability of iron oxide NPs as well as decrease their magnetic moment. As shown in chapter 4, 2.4 nm $CoFe_2O_4$@DMSA NPs had a smaller magnetic moment compared to Fe_3O_4@DMSA NPs of the same size.

Considering that lower M_s values reduce T_2 effects, and Co^{2+} cations have three unpaired electrons and Fe^{3+} has five, $CoFe_2O_4$ nanoparticles could be beneficial for T_1-weighted MRI, however they remain relatively unexplored as MRI contrast agents. A few reports exist detailing the potential of cobalt-ferrite NPs >3 nm as T_2 contrast agents owing to their large magnetic moment. Ghasemian et al. measured the relaxivity of DMSA-coated 16 nm cobalt-zinc-ferrite NPs and found their suitability for T_2 contrast enhancement with an r_2/r_1 ratio of 50.[309] Nidhin et al. reported an r_2/r_1 ratio of 6.9 for 7.2 nm cobalt-ferrite NPs.[310] However cobalt ferrite NPs smaller than 3 nm have not been tested for MRI applications before. In this context, ultra-small $CoFe_2O_4$ NPs could be promising candidates for T_1-weighted MRI applications. In this chapter, the MRI behaviour of 2.4 nm $CoFe_2O_4$@DMSA NPs are explored for the first time.

6.1.3 MRI phantom methods

9.4 T MRI phantom method

To evaluate the MRI contrast effect of MFe_2O_4@DMSA NPs, a phantom test was performed using a 9.4 T imaging system with 1 T/m imaging gradients and Direct-

Drive console (Agilent Technologies, USA), and a 39 mm i.d. quadrature driven birdcage resonator tuned to 400 MHz (Rapid Biomedical, Germany). MFe_2O_4@DMSA NPs were linearly diluted in agarose gel (1% TBE blend, Sigma Aldrich) and suspended in 1 ml syringes. The concentration of the NPs was determined from ICP-OES and calculations using the same method detailed in section 5.2.6 of chapter 5. Following calibration and manual shimming, slice-selective gradient echo scout images were acquired (TR=100 ms, TE=1.33 ms, 20° flip angle, 32 averages, 128x128 points, 40x40 mm^2 FOV, 6 mm slice thickness). T_1 mapping was carried out using a slice-selective inversion recovery sequence with gradient echo imaging readout (TR=20 s, TI=0.02-19 s in 48 steps, 2 averages, 128x128 points, 40x40 mm^2 field of view, 6 mm slice thickness). T_2 mapping was carried out using a slice-selective spin-echo imaging sequence with multiple echos in readout (TR=30 s, TE=8 ms, 4 averages, 512 echos, 128x128 points, 40x40 mm FOV, 6 mm slice thickness). All MR data were processed and fitted using IDL8.2 (Harris Geospatial Solutions, USA). Images were zero-filled to a matrix size of 256x256 points and masked based on the magnitude of the scout image before fitting. The mean and standard deviation for the T_1 and T_2 of each phantom were calculated over a region of interest (ROI) placed in the centre of each phantom. T_1 times were calculated using a non-linear least square fitting procedure (Levenberg-Marquardt algorithm) of the equation for inversion recovery (eq 6.1):[311]

$$M_z = M_0(1 - 2\ exp(-TI/T_1)) \tag{6.1}$$

Where M_0 is the magnetisation after complete relaxation, TI is the time delay between the 180° and 90° pulse (inversion time). M_z and M_0 correspond to the signal intensity *(SI)* after TI and $TI = \infty$ (complete relaxation) respectively. Thus,

$$SI_{TI} = SI_0(1 - 2\ exp(-TI/T_1)) \tag{6.2}$$

T_1 is determined by fitting the above equation to a plot of TI versus SI.

T_2 times were calculated with an exponential decay curve, where TE is the echo time:

$$M = M_0 \, e^{-TE/T_2} \tag{6.3}$$

T_2 times are determined from a plot of TE versus the SI from each NP phantom. The r_1 and r_2 relaxivity values were calculated from the slope of $1/T_{1/2}$ against particle concentration.

3.0 T MRI phantom method

To obtain clinically relevant relaxivity values for MFe_2O_4@DMSA NPs, a phantom test was performed on a 3.0 T Siemens Prisma MRI scanner equipped with a 32 channel receive only head coil. NPs were linearly diluted with agarose (1% TBE blend, Sigma Aldrich) and gelified in glass tubes. The concentration of the NPs was determined from ICP-OES and calculations using the same method detailed in section 5.2.6 of chapter 5. The glass tubes were then suspended in 1% agarose in a tank to enhance background signal and have a large enough volume for shimming. Following calibration, T_2 mapping was carried out by acquiring slice-selective turbo spin-echo images (TR=2020 ms, TE=8-397 ms in 24 steps, 3 averages, 150 degree flip angle, 320x320 points, 180x180 mm^2 FoV, 10 mm slice thickness). T_1 mapping was carried out using a slice-selective inversion recovery turbo spin echo sequence (TR=3 s, TI=25-2500 ms in 9 steps, TE=9.7 ms, 3 averages, 128x128 points, 129x180 mm^2 FoV, 6 mm slice thickness). The mean and standard deviation for the T_1 and T_2 of each phantom were calculated from the signal intensities over a region of interest (ROI) 3x3 voxels in size placed in the centre of each phantom. T_1 times were estimated using a non-linear least square fitting procedure (Levenberg-Marquardt algorithm) of the equation for inversion recovery (eq 6.1). T_2 data was analysed using the Cuban Neuroscience Centre's custom Matlab® (Mathworks) routines fitted to equation (6.3). The r_1 and r_2 relaxivity values were calculated from the slope of $1/T_{1/2}$ against particle concentration.

6.1.4 Results and discussion

9.4 T MRI phantom test

In order to evaluate any potential benefits for MRI contrast enhancement that arises from using cobalt ferrite NPs as opposed to iron-oxide NPs, 2.4 nm $CoFe_2O_4$@DMSA and Fe_3O_4@DMSA NPs were prepared using the synthesis and DMSA ligand exchange methods outlined in sections 2.2.2 of chapter 2 and section 4.2.3 of chapter 4 respectively. The core size, hydrodynamic diameter, zeta-potential and magnetic properties of the particles were determined according to the methods described in chapters 2 and 4. These parameters are important for determining their MRI contrast behaviour as outlined in section 6.1.2 of the introduction.

Figure 6.4 shows TEM micrographs of $CoFe_2O_4$@OLA and Fe_3O_4@OLA NPs, confirming that 2.4 nm monodisperse NPs were obtained as expected following the synthesis results detailed in chapter 2. The insets of figure 6.4 show the dispersions of $CoFe_2O_4$ and Fe_3O_4 NPs in water obtained following ligand exchange with DMSA. $CoFe_2O_4$@DMSA NPs appeared clear, but unfortunately Fe_3O_4@DMSA NPs appeared opaque, indicating that agglomeration had occurred during ligand exchange. Hydrodynamic measurements were acquired to assess the degree of agglomeration; the d_H of Fe_3O_4@DMSA NPs was 180 nm, confirming their agglomerated condition.

It is unclear why on this occasion Fe_3O_4@DMSA NPs agglomerated during ligand exchange, considering that reproducible results were obtained in previous studies (chapter 4). $CoFe_2O_4$@DMSA NPs had a d_H of 11 nm, which concurs with previous results. The agglomerated condition of Fe_3O_4@DMSA NPs is important to note as it may affect their MRI contrast behaviour: aggregation of ultra-small iron oxide NPs has been shown to decrease the T_1 relaxation rate and increase the T_2 relaxation rate of nearby water protons, resulting in a dominant T_2 effect.[250] Table 6.1 shows the full properties of the NPs used in the 9.4 T MRI study.

Table 6.1: Properties of NPs used in 9.4T MRI phantom study

Particle type	Core size (TEM) (nm)	Coating ligand	d_H (nm)	Zeta-potential (mV) (pH 7)	M_s (emu/g)	T_B (K)
Fe_3O_4	2.4 ± 0.3	DMSA	180 ± 46	-54 ± 1.2	9.6	12
$CoFe_2O_4$	2.4 ± 0.4	DMSA	11 ± 2	-34 ± 1.4	4.8	102

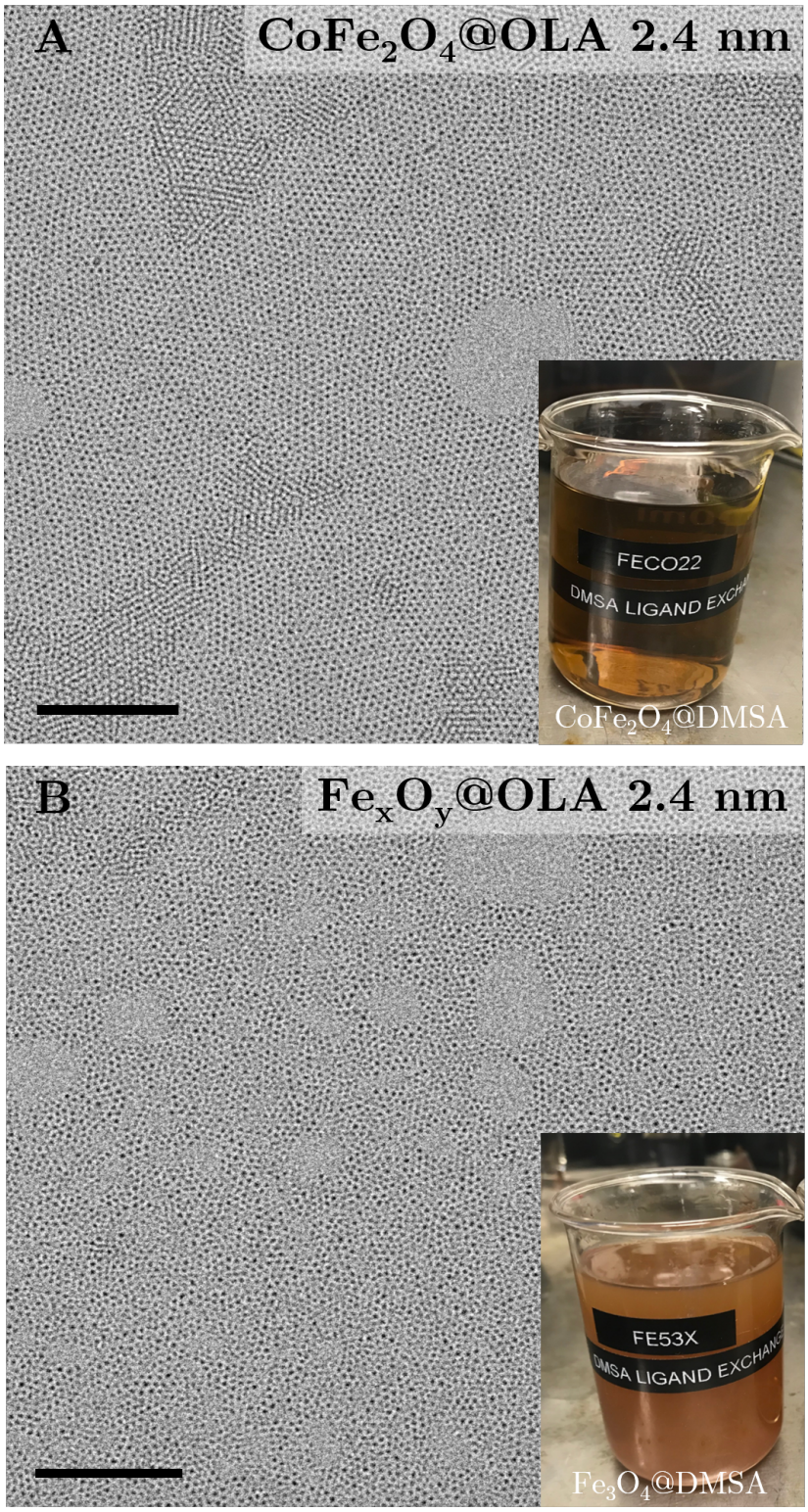


Figure 6.4: TEM micrographs of (A) $CoFe_2O_4$@OLA NPs and inset $CoFe_2O_4$@DMSA NPs in water after ligand exchange and (B) Fe_3O_4@OLA NPs and inset Fe_3O_4@DMSA NPs in water after ligand exchange. Both NP types showed monodisperse NPs 2.4 nm in size following synthesis in OLA. However, following ligand exchange, $CoFe_2O_4$@DMSA NPs appeared clear whereas the dispersion of Fe_3O_4@OLA NPs appeared opaque, indicating agglomeration had occurred during ligand exchange.

The NPs were prepared for MRI phantom testing by embedding them in agarose gel into syringes. Agarose gel was used as its texture and relaxation times are comparable to that of human tissue.[312] Care was taken to avoid the presence of air bubbles which can generate image artefacts.[313] The set-up of the phantom is depicted in figure 6.5. The syringes were positioned so that all NP samples could be imaged in a single slice.

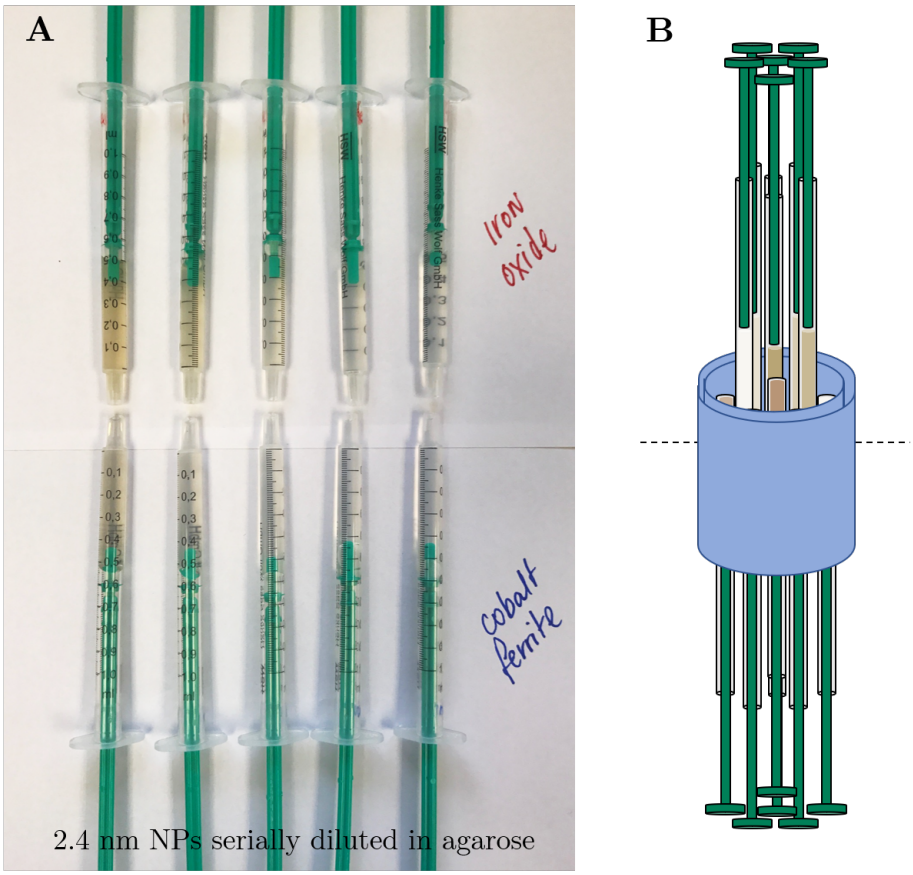


Figure 6.5: (A) NP samples were embedded in agarose gel in syringes. (B) Set-up of NP phantom for MRI scan. The dotted line indicates the position of the image slice

Figure 6.6 shows the T_1-weighted and T_2-weighted phantom images of 2.4 nm $CoFe_2O_4$@DMSA and Fe_3O_4@DMSA NPs obtained at 9.4 T. Un-doped agarose was used as a control. The $CoFe_2O_4$@DMSA NP phantoms show a visible increase in positive T_1 image contrast as the NP concentration increases. Their effect on negative T_2 image contrast was less pronounced; as NP concentration increases, image contrast decreases only slightly. Contrarily, Fe_3O_4@DMSA NP phantoms show a slight increase in positive T_1 image contrast as the NP concentration increases, whereas significant enhancement of negative T_2 image contrast can be observed.

Thus 2.4 nm $CoFe_2O_4$@DMSA NPs demonstrated T_1-weighted MRI contrast enhancement, whereas Fe_3O_4@DMSA NPs demonstrated T_2-weighted MRI contrast enhancement.

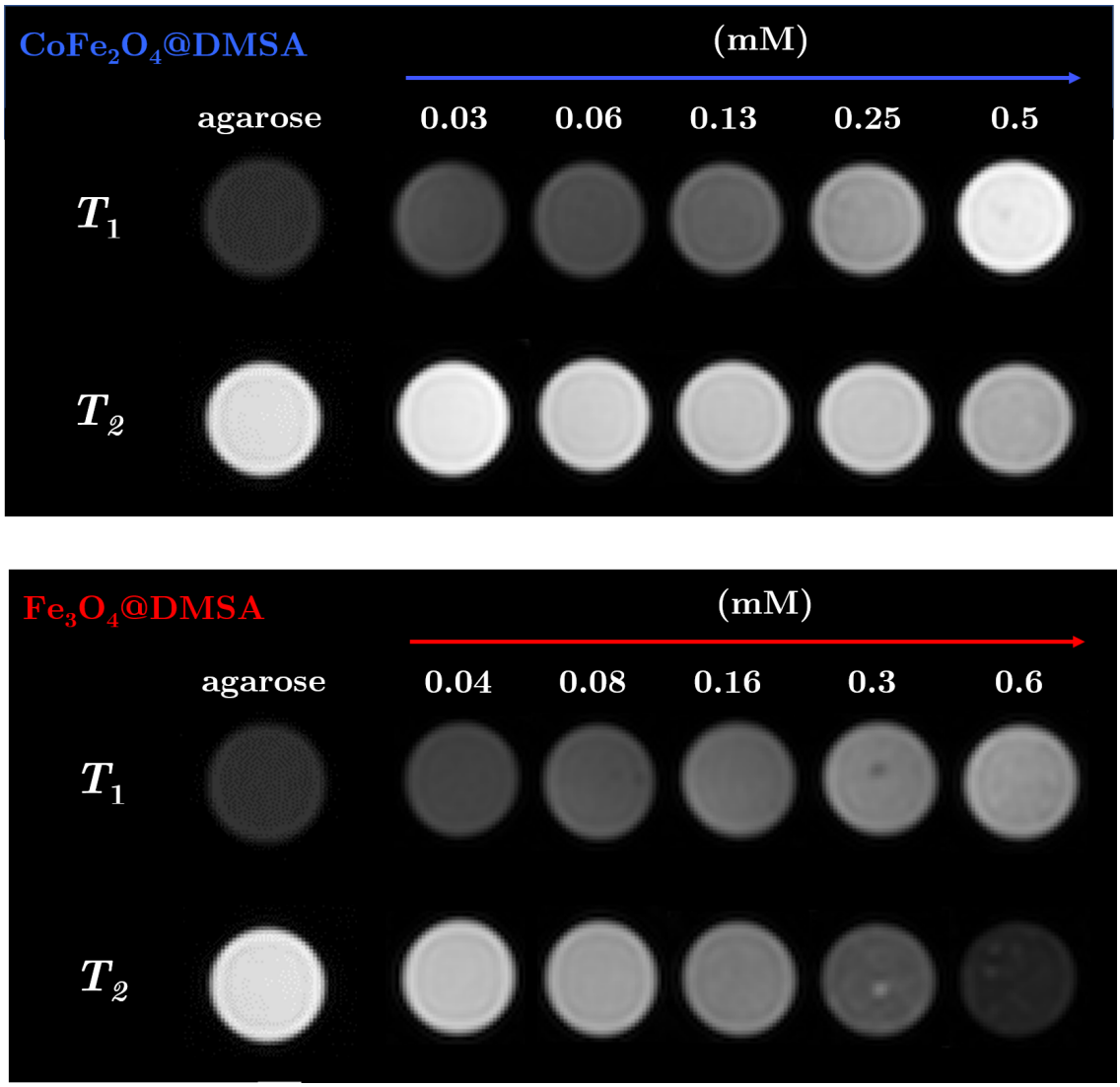


Figure 6.6: 9.4T MRI phantom scout images of 2.4 nm $CoFe_2O_4$@DMSA and Fe_3O_4@DMSA NPs embedded in 1% agarose gel. $CoFe_2O_4$@DMSA phantoms show an increase in T_1 (positive) contrast with increasing particle concentration. The particles have less influence on the T_2 (negative) contrast, decreasing slightly with increasing concentration. Conversely, Fe_3O_4@DMSA NPs show a slight increase in T_1 (positive) contrast with increasing particle concentration, whereas their influence on T_2 (negative) contrast is visibly more pronounced. The phantom at 0.3 mM concentration shows a small artefact caused by an air bubble.

The signal intensities of the NP phantom scout images were used to calculate the T_1 and T_2 relaxation times of the NPs to quantify their influence on MR image contrast. Experimental T_1 and T_2 relaxation times are listed in the appendix (section B.4.1). The inverse of T_1 and T_2 relaxation times gives the relaxation rates ($1/T_1$)

and $(1/T_2)$ respectively. Plotting $1/T_1$ and $1/T_2$ against the molar concentration (C) of the NPs gives their *relaxivities*, denoted as r_1 and r_2 (figure 6.7). The r_1 and r_2 relaxivities of $CoFe_2O_4$@DMSA NPs were 0.75 $mM^{-1}s^{-1}$ and 48.7 $mM^{-1}s^{-1}$ respectively. The r_1 and r_2 relaxivities of Fe_3O_4@DMSA NPs were 0.54 $mM^{-1}s^{-1}$ and 102.4 $mM^{-1}s^{-1}$ respectively. The higher r_1 relaxivity of $CoFe_2O_4$@DMSA NPs confirms their greater influence on positive contrast in compared to Fe_3O_4@DMSA NPs. In contrast, the two-fold higher T_2 relaxivity of Fe_3O_4@DMSA NPs reflects a significantly greater effect on T_2 image contrast in comparison to $CoFe_2O_4$@DMSA NPs.

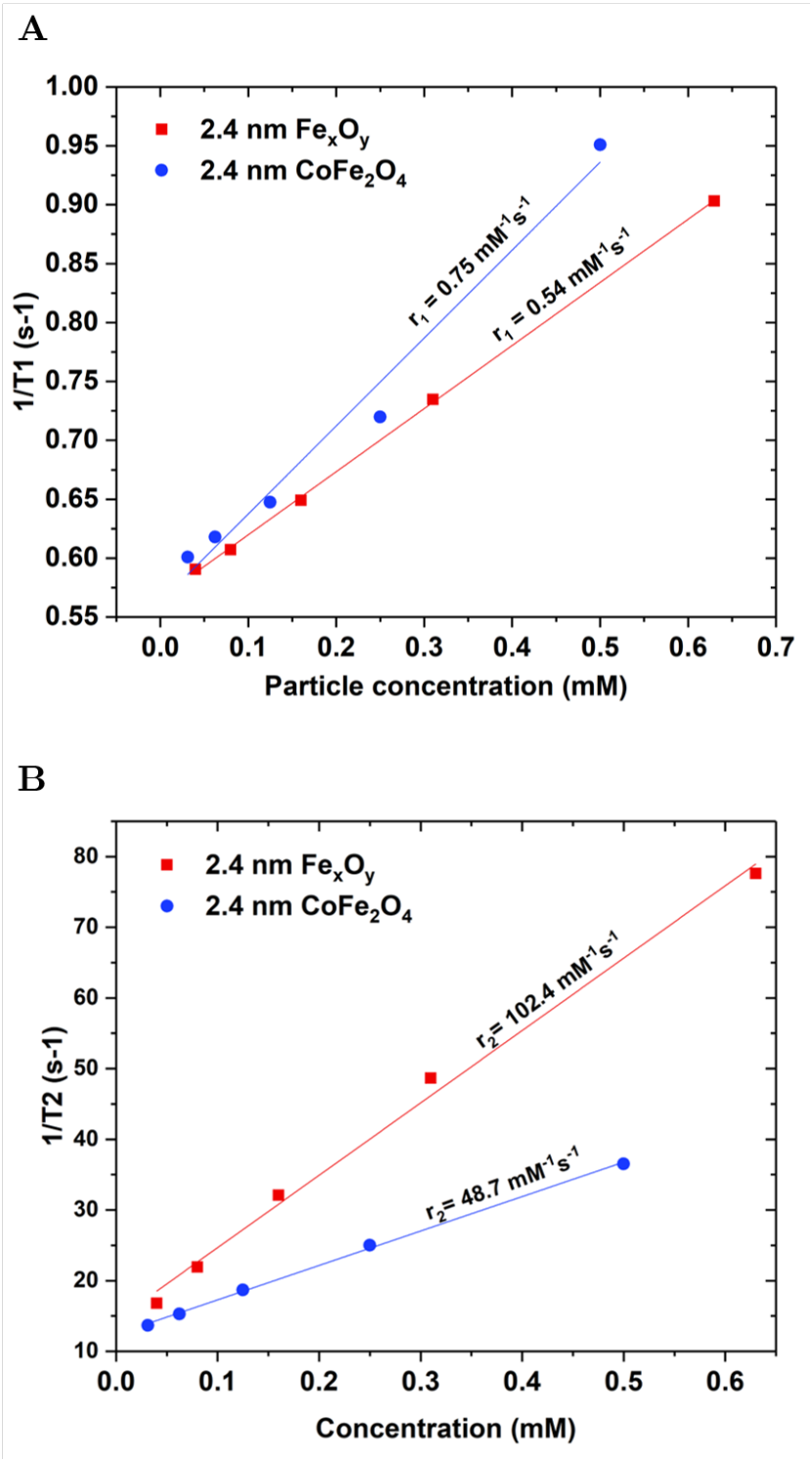


Figure 6.7: Plot of (A) T_1 relaxation rates and (b) T_2 relaxation rates of 2.4 nm $CoFe_2O_4$@DMSA and Fe_3O_4@DMSA NPs against particle concentration (mM). r_1 and r_2 relaxivities were calculated from the linear slope.

The low r_1 relaxivity and high r_2 relaxivity of Fe_3O_4@DMSA NPs could be due to their large hydrodynamic diameter of 180 nm. Shortening of T_1 relaxation time is achieved through energy exchange of protons in water after coming into close contact

with the paramagnetic species. A hydrodynamic diameter of 180 nm indicates the particles were agglomerated, thus the available surface area of Fe_3O_4@DMSA NPs for energy exchange was reduced, and water molecules were prevented from coming into close contact with the NPs. This effect has been reported by others. Ta et al. studied the effect of aggregation on the r_1 and r_2 relaxivity of 3.7 nm iron oxide NPs. Their results concur with the findings in this study: r_1 decreased dramatically whilst r_2 significantly increased as the hydrodynamic diameter of the NPs increased from 7 nm to 45 nm.[250] Similarly, Tao et al. compared the MRI contrast behaviour of 4 nm BSA and poly(acrylic) acid-poly(methacrylic acid) (PMAA-PTTM) coated Fe_3O_4 NPs and found that the Fe_3O_4@BSA NPs aggregated *in vivo*, changing their contrast performance from T_1 *in vitro* to T_2-weighted *in vivo*.[314]

These findings highlight the importance of colloidal stability on the MRI behaviour of NP-based contrast agents. Particle aggregation not only influences their distribution *in vivo*, but also their effect on T_1 and T_2 relaxation rates. Although the NPs flocculated during ligand exchange, aggregation can also occur *in vivo* as a result of protein adsorption. Thus for clinical application, the stability of MFe_2O_4@DMSA NPs *in vivo* needs to evaluated. Alternatively, aggregated Fe_3O_4@DMSA NPs, and also the aggregated Fe_3O_4@BSA NPs discussed in chapter 4, could be harnessed for T_2-weighted MRI. Another contributing factor to their higher r_2 relaxivity compared to $CoFe_2O_4$@DMSA NPs is their larger magnetic saturation of 9.6 emu/g versus 4.8 emu/g. A larger magnetisation saturation influences T_2 through greater induction of local field inhomogeneities which facilitate T_2 spin-spin relaxation.

The r_2/r_1 ratio is an important parameter for determining the effectiveness of a contrast agent towards r_1 or r_2 relaxation rates: the lower the ratio, the more effective the agent is towards enhancing T_1 contrast. Gadolinium-based contrast agents, such as Magnevist®, have an r_2/r_1 ratio in the range of 1.41. At 9.4 T, the r_2/r_1 obtained for $CoFe_2O_4$@DMSA NPs was 64.9. The r_2/r_1 obtained for Fe_3O_4@DMSA NPs was 189.6. The considerably higher ratio of Fe_3O_4@DMSA NPs in comparison to $CoFe_2O_4$@DMSA again reflects their greater influence on T_2 relaxation. The ratio is comparable to that of Resovist® (224.3 at 9.4 T), which is a T_2 contrast agent composed of 5 nm iron-oxide NPs agglomerated into larger clusters. Resovist® was developed for the purpose of liver-targeted MRI.

It is possible that if the Fe_3O_4@DMSA NPs had been monodisperse, the r_2/r_1 ratio obtained could have been considerably lower. Ultra-small iron oxide NPs have demonstrated T_1-weighted contrast enhancement with low r_2/r_1 ratios in several studies by others (see table 6.2 in the next section). Repetition of the MRI phantom study with un-agglomerated NPs is necessary to understand whether the high ratio obtained is due to the particle size and crystal structure, or their agglomerated condition.

The r_2/r_1 ratio of 64.9 achieved with $CoFe_2O_4$@DMSA NPs appears significantly higher than that of Gadolinium-based agents, despite evident T_1-weighted contrast enhancement as seen in figure 6.6. This is due to the large magnetic field strength of the system used: r_1 decreases and r_2 increases with an increase in magnetic field strength, leading to a higher r_2/r_1 ratio.[315] For example, Sinerem®, a contrast agent previously developed for MRI consisting of 35 nm iron oxide NPs, had an r_2/r_1 ratio of 83.6 at 7 T, 19.4 at 3.0 T and 6.5 at 1.5 T.[316] A study by Kovar et al. on 2 nm γ-Fe_2O_3@citrate NPs obtained an r_2/r_1 ratio of 49.6 at 9.4 T,[317] which is comparable to that achieved with $CoFe_2O_4$@DMSA NPs in this study.

In the MRI community, there is a desire to increase the field strength of clinical systems from the currently-used 1.5 T and 3.0 T systems to 7 T and above in order to achieve better signal-to-noise ratio and thus higher spatial resolution.[318] As such, it is important to measure the behaviour of contrast agents in higher field strengths in consideration for future applications. Efforts are under-way to improve the performance of Gd-based agents at higher field strengths without having to increase the dose, considering Gd's problematic toxicity.[319] Ferrite nanoparticles could present a more promising route considering their size, composition and magnetic properties can be tailored and thus optimised towards the desired application. Currently, the highest field strength of systems used in clinics is 3.0 T. To assess the performance of $CoFe_2O_4$@DMSA NPs under current clinically-relevant conditions, an MRI phantom study was conducted using an 3.0 T system, the results of which are detailed in the following section.

3.0 T MRI phantom test

To investigate the contrast enhancement ability of $CoFe_2O_4$@DMSA NPs with a clinical MRI scanner, an MRI phantom was created using NPs serially diluted in agarose and set in tubes. Due to the lower magnetic field strength of 3.0 T, a background signal is required, thus the tubes were set in a tub of agarose as depicted in figure 6.8(A).

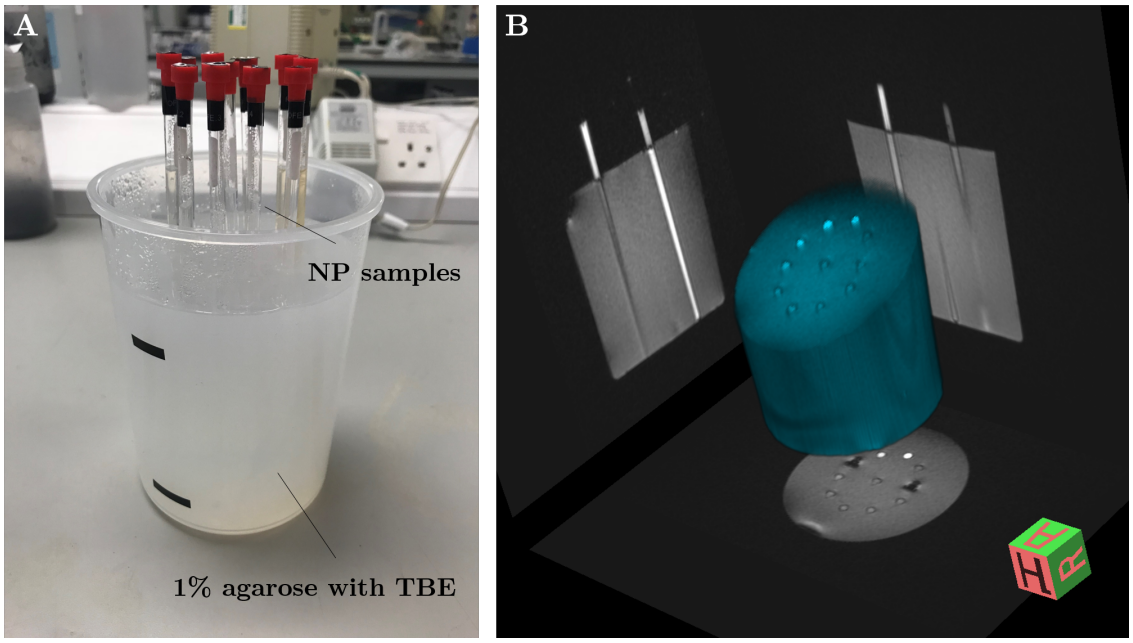


Figure 6.8: (A) Setup of MRI phantom for 3.0 T study: NPs dispersed in agarose were gelified in glass tubes and set in a tub of agarose. (B) 3D MRI image of the phantom demonstrating a slice.

T_1 and T_2-weighted images of the phantom were acquired as outlined in section 6.1.3. In this experiment, a faster approximation technique was used for the T_1 mapping. Thus the T_1 relaxation times acquired are consistently underestimated.[320] This technique is widely used to do myocardial T_1 mapping as it significantly reduces scan time.[321] Similar MR parameters were also used by related studies evaluating ultra-small iron oxide NPs as T_1 contrast agents.[30,43] As the purpose of this experiment was to determine the change in relaxation rate due to the increasing concentration of $CoFe_2O_4$@DMSA NPs, the actual T_1 relaxation times were not required. Nonetheless, in order to verify the validity of the data, Dr. Mahon Maguire ran Bloch equation simulations of the MR parameters used to compare the experimental values obtained to theoretical values. His results, which show ex-

cellent agreement between the theoretical and experimental data, are shown in the appendix (section B.4.2). Similar post-processing of MR sequence parameters to obtain accurate T_1 values has been described by Gai et al.[322] The results show the relaxation rate (r_1) was unaffected by the underestimation as anticipated.

The MRI scan of $CoFe_2O_4$@DMSA NPs at 3.0 T showed a concentration-dependent visible increase in positive T_1 contrast (figure 6.9). The estimated r_1 and r_2 relaxivities for $CoFe_2O_4$@DMSA NPs were 2.11 $mM^{-1}s^{-1}$ and 7.81 $mM^{-1}s^{-1}$ respectively (Figure 6.10). As anticipated, the r_1 increased with the decrease in field strength from 9.4 T to 3.0 T whilst the r_2 decreased. This resulted in an estimated r_2/r_1 ratio of 3.70. The r_2/r_1 ratio is very similar to that achieved by Kim et al. with 2.2 nm maghemite NPs,[30] and close to commercially available Gd-based contrast agents Magnevist® (Gd-DTPA) and Gadovist® (Gd-DO3A-butrol) with r_2/r_1 ratios of 1.41 and 1.42 at 3.0 T respectively. Table 6.2 details the r_2/r_1 ratios of other comparable agents.

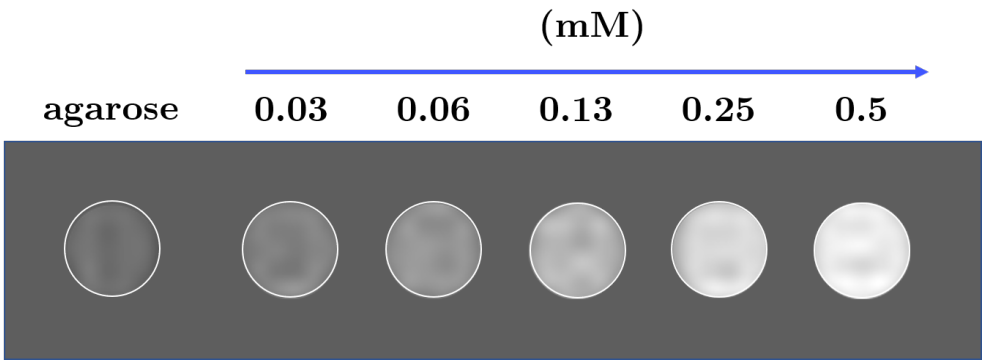


Figure 6.9: 3.0 T MRI phantom test of 2.4 nm $CoFe_2O_4$@DMSA NPs embedded in 1% agarose gel. MRI scout image showing an increase in T_1 (positive) contrast with increasing NP concentration.

The low r_2 value of $CoFe_2O_4$@DMSA NPs can be attributed to their very small magnetic moment, influenced by the addition of Co^{2+} ions and the small NP size. This likely minimised the magnetic induction of local magnetic field inhomogeneities and prevented $CoFe_2O_4$@DMSA NPs from having a pronounced effect on T_2 relaxation. NP concentration-dependent T_1 relaxation was achieved from the unpaired electrons of Co^{2+} and Fe^{3+} ions and the stability of the particles provided by the DMSA coating. An alternative approach to decreasing the magnetic moment of iron oxide NPs was explored by Starsich et al. who coated Fe_3O_4 NPs with a SiO_2

shell in order to reduce magnetic coupling and thus decrease the overall magnetisation.[323] However, this was not as effective as using cobalt ferrite proved in this work, as their r_2/r_1 ratio was two-fold higher at 5.4, owing to the retained superparamagnetic properties of iron oxide. These results demonstrate the potential of $CoFe_2O_4$@DMSA NPs for T_1 contrast enhancement for the first time.

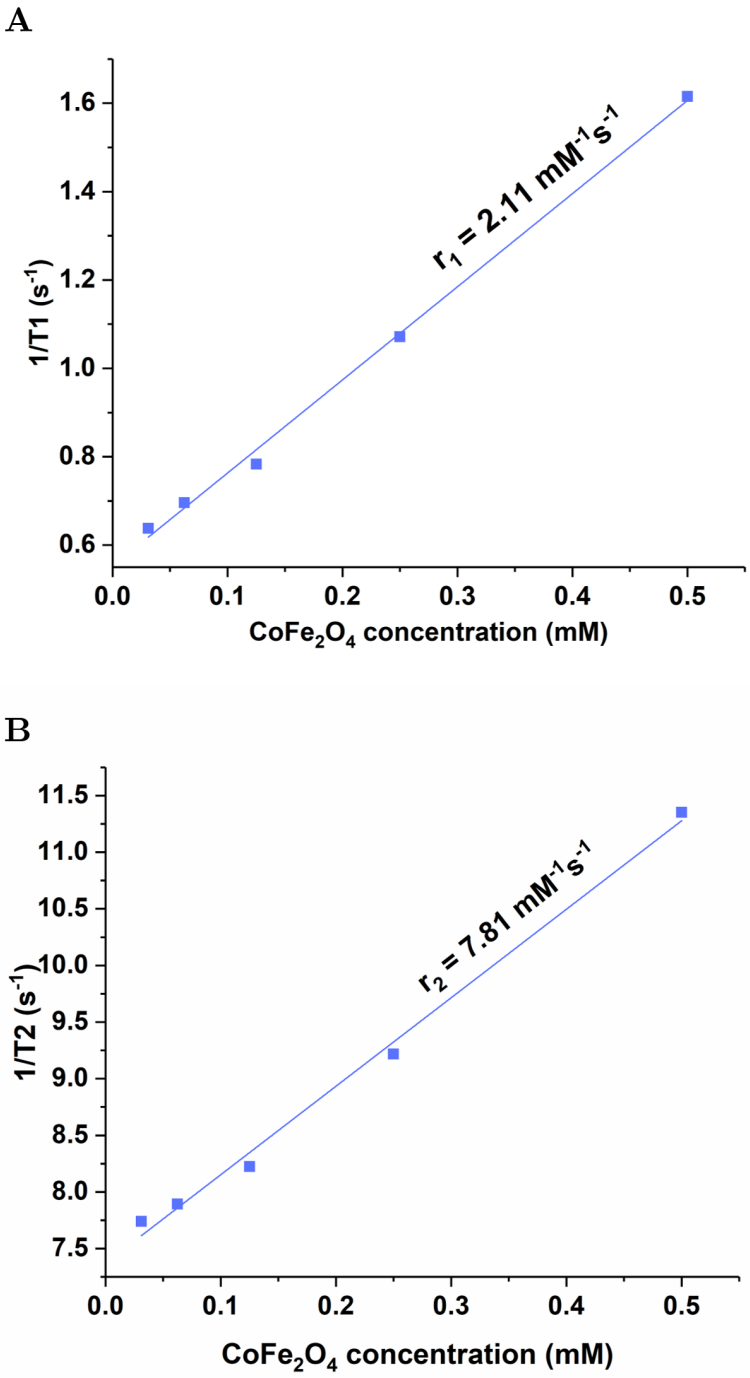


Figure 6.10: 3.0 T MRI phantom test of 2.4 nm $CoFe_2O_4$@DMSA NPs embedded in 1% agarose gel. (A) Plot of r_1 relaxation rate and (B) r_2 relaxation rate against $CoFe_2O_4$@DMSA NP concentration.

Table 6.2: Comparison of the relaxation properties of ultra-small ferrite NPs systems and commercially available Gd-based contrast agents at different magnetic field strengths. Data obtained for $CoFe_2O_4$@DMSA NPs in this study is highlighted in **bold**.

Contrast agent	$\mathbf{D_{TEM}}$ **(nm)**	$\mathbf{D_h}$ **(nm)**	r_1 **($mM^{-1}s^{-1}$)**	r_2 **($mM^{-1}s^{-1}$)**	r_2/r_1	$\mathbf{B_0}$ **(T)**	**Ref**
Fe_3O_4@BSA	5.3	-	39.3	179.8	4.58	0.5	[314]
Fe_3O_4@PMAA-PTTM	4.3	-	24.2	67.2	2.78	0.5	[314]
Fe_3O_4	4.0	-	5.99	15.53	2.59	0.5	[324]
USPIO@PAA	4.5	24	8.67	25.36	2.93	1.41	[43]
Fe_3O_4@PEG	4.0	10	7.3	17.52	2.4	1.41	[325]
γ-Fe_2O_3@citrate	4.8	18	14.50	66.90	4.61	1.41	[302]
Fe_3O_4@PAA	1.7	5.8	8.20	16.67	2.03	1.41	[326]
Fe_3O_4@PAA	2.2	-	6.15	28.62	4.65	1.41	[326]
Magnevist®	Gd^{3+}	1.8	4.8	5.1	1.1	1.5	[42]
ZES-SPIONs	2.5	4.7	5.2	10.5	2.0	1.5	[42]
ES-MION@PAA	2.5	-	8.80	22.7	2.6	1.5	[305]
$CoFe_2O_4$@DMSA	**2.4**	**11**	**2.11**	**7.81**	**3.70**	**3.0**	**[45]**
Magnevist®	Gd^{3+}	-	3.7	5.2	1.41	3.0	[315]
Gadovist®	Gd^{3+}	-	5.0	7.1	1.42	3.0	[315]
Fe_2O_3@PO-PEG	2.2	15	4.77	17.5	3.67	3.0	[30]
$MnFe_2O_4$@mPEG	2.0	8	8.43	21.02	2.49	3.0	[44]
$MnFe_2O_4$@mPEG	3.0	9	8.23	21.97	2.67	3.0	[44]
γ-Fe_2O_3@mPEG	3.0	-	4.96	28.59	5.76	3.0	[44]
Fe_3O_4@c(RGDyK)	5.3	10	7.74	21.67	2.8	3.0	[304]
Fe_xO_y@$SiO2_2$-BSA	3.9	100	2.3	12.4	5.4	3.0	[323]
$CoFe_2O_4$@DMSA	**2.4**	**11**	**0.75**	**48.7**	**65**	**9.4**	**[45]**
VSION@PEG750	3.5	19.8	1.74	40.7	23.4	9.4	[327]
VSION@PEG2000	3.5	22.2	1.12	31.11	27.8	9.4	[327]
γ-Fe_2O_3/citrate	2.0	4	0.25	12.4	49.6	9.4	[317]
Resovist®	5	63	1.67	374.6	224.3	9.4	[316]

6.1.5 Conclusions

The performance of ultra-small MFe_2O_4@DMSA NPs as contrast agents for MRI was evaluated with phantom testing at 9.4 T. $CoFe_2O_4$@DMSA NPs were found to effectively enhance T_1 positive contrast, whilst having little effect on T_2 negative contrast, demonstrating suitability as a T_1-weighted contrast agent. Fe_2O_4@DMSA NPs were found to enhance both T_1 and T_2 contrast, with a predominant effect on T_2, thus demonstrating better suitability as a T_2-weighted contrast agent. However, the Fe_2O_4@DMSA NPs were in an agglomerated condition, which is known to significantly affect contrast agent behaviour. In order to comparatively assess the behaviour of 2.4 nm Fe_2O_4@DMSA NPs and $CoFe_2O_4$@DMSA NPs, further phantom testing with monodisperse NPs should be conducted. The 2.4 nm $CoFe_2O_4$@DMSA NPs were further evaluated with a 3.0 T MRI scanner. Phantom testing confirmed their T_1-weighted contrast enhancement at a clinical magnetic field strength, with a low r_2/r_1 ratio of 3.70 suitable for a T_1 contrast agent. The r_2/r_1 ratio could potentially be optimised further by fine-tuning the NP size and cobalt composition.

The phantom testing served as a preliminary assessment of the contrast enhancement properties of ultra-small MFe_2O_4@DMSA NPs. Imperative for full evaluation of their clinical potential are *in vivo* animal studies. Their circulation time, clearance pathway, and general performance under physiological conditions are deciding factors in their clinical utility (asides from toxicity considerations). If the NPs were found to have long blood circulation times and effectively enhance contrast *in vivo*, they could be suitable for cardiovascular imaging such as angiography. Short circulation times and thus rapid uptake by the reticuloendothelial system would indicate better suitability for liver MRI. In addition to *in vivo* evaluation, it would be useful to assess their MRI performance at the lower field strength of 1.5 T, which is routinely used in clinics.

This study is a first step towards evaluating ultra-small $CoFe_2O_4$@DMSA NPs for application as T_1 MRI contrast agents. The question of whether cobalt ferrite NPs are more suitable for this purpose than iron oxide NPs or other ferrite NPs remains unanswered. The hypothesised potential benefit of greater resistance to oxidation and thus stability in storage and retention of characterised properties, in combination with their lower magnetic saturation and thus reduced T_2 effect, would

need to be weighed up against their potential disadvantage of increased toxicity in comparison to iron oxide. This could be achieved through combined systematic MRI and long-term toxicity *in vivo* studies with ultra-small ferrite NPs with a range of metal compositions. Nevertheless, this study reports for the first time the potential of $CoFe_2O_4$@DMSA NPs for application as T_1 MRI contrast agents.

6.2 Bile-acid functionalisation of MFe_2O_4@DMSA NPs

6.2.1 Introduction

Iron oxide and cobalt ferrite NPs are promising candidates for improving image contrast in MRI and could provide a safer alternative to Gd-based agents. In addition to improving the biocompatibility, the design of target-specific agents to improve image resolution in specific biological regions is desired for the early detection of disease. Hepatospecific MRI contrast agents are extremely useful for detecting focal liver lesions in the diagnosis of metastatic liver disease.[46] Commercialised iron oxide NPs such as Resovist® have been marketed as liver-specific T_2 contrast agents due to their uptake into the reticuloendothelial system (RES), and thus passive liver-targeting ability by accumulation in the liver.[29] Contrast between liver and liver lesions is improved since hepatic tumours do not contain RES cells.[328] However, Gd-based hepatospecific agents demonstrated better practicality and diagnostic performance for liver cancer.[37] Eovist® (gadolinium-EOB-DTPA) is an example of a Gd-based hepatospecific contrast agent. The presence of the ethoxybenzyl (EOB) group causes this compound to be selectively up-taken by hepatocytes.[328] Only normal functioning hepatocytes take up hepatospecific contrast agents and excrete them to the biliary tree, which provides very useful diagnostic information and allows the differentiation of lesion type.[291] Figure 6.11 shows the detection of multiple small liver metastases following administration of Eovist®in a patient.

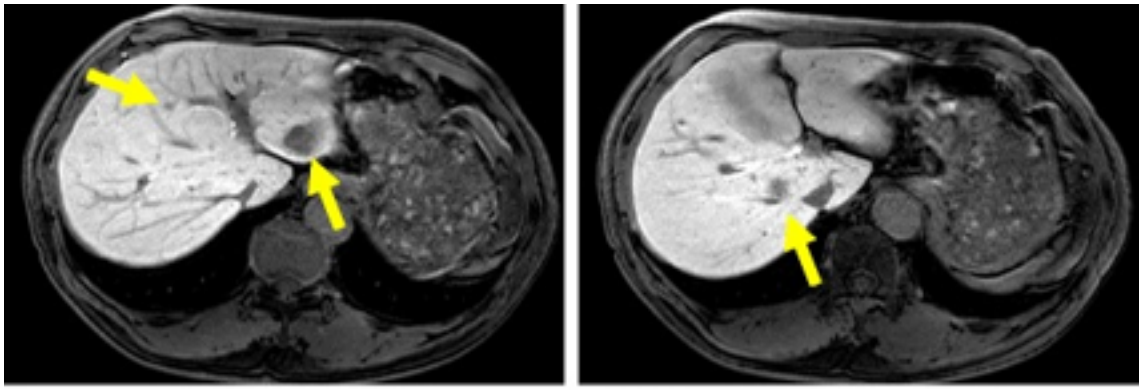


Figure 6.11: T_1 MRI of liver enhanced with Eovist®-enhanced MRI for detection of liver metastases showing multiple liver metastases (yellow arrows). Source:[329]

Contrast agents for detecting tissue abnormalities must be able to cross the hepatocyte membrane.[330] Due to their ultra-small 2.4 nm core and hydrodynamic size of 12 nm, the $CoFe_2O_4$@DMSA NPs developed in this study may not passively accumulate in the liver, and instead may be secreted renally as other ultra-small NPs have demonstrated.[42] Thus, for liver-targeted T_1 MRI, conjugation to a hepatospecific functional group could be beneficial. Bile acids, amphipathic molecules composed of a sterol scaffold with hydroxyl groups and a carboxyl-terminated side chain, are transported to and from the liver via the enterohepatic circulation system[47,51] (figure 6.12). As such they have been proposed as ideal surface modifiers for liver-targeted *in vivo* applications.

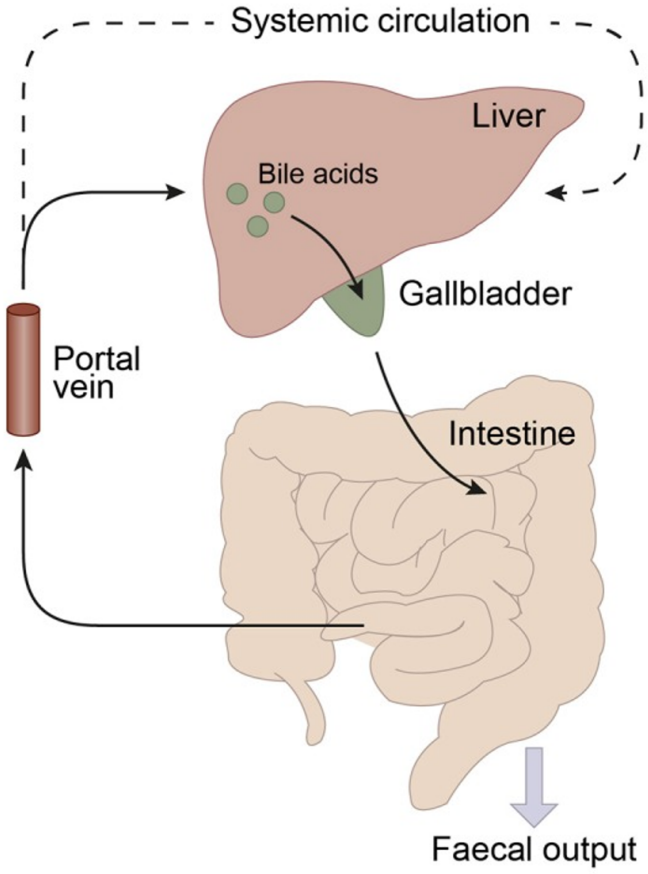


Figure 6.12: Schematic of the enterohepatic circulation system. Bile acids are synthesised within hepatocytes, then secreted into bile stored in the gallbladder. Following absorption into the small intestine, bile acids are transported back to the liver via the portal vein. Here, they are re-taken up by hepatocytes and their circulation restarts. Source:[331]

Kramer et al. effectively demonstrated the use of bile acids as 'Trojan horses' to deliver drugs specifically into the liver.[48] Similarly, Zhang et al. found that func-

tionalising chitosan nanoparticles with cholic acid, a primary bile acid, remarkably improved the efficacy of insulin delivery, owing to cholic acid's liver-targeting properties.[49] Anelli et al. tested whether cholic acid, cholylglycine or cholyltaurine linked to Gd-DOTA chelates could encourage hepatospecificity, and found that cholic acid was an efficient carrier for uptake by hepatocytes.[332] Others have also functionalised Gd-chelates with cholic acid towards liver-targeted MRI.[50,51]

Bile acids could offer a promising route to add liver-targeting functionality to NP contrast agents. However, bile acid-functionalised metal-oxide NPs have not been explored before. The next section describes the methods used to functionalise MFe_2O_4@DMSA NPs with cholic acid towards their application as liver-targeted MRI agents.

6.2.2 Materials and methods

Chemicals

Cholic acid (C1129-25 g), acetonitrile (271004-1 L), N,N'-Dicyclohexylcarbodiimide (DCC) (D8002-25 g), N-hydroxysuccinimide (NHS) (130672-25 g), dimethylformamide (DMF) (227056-250 ml), ammonia (ammonium hydroxide solution 25%), lithium aluminium hydride solution (($LiAlH_4$)) in THF (212776), ethyl acetate (270989-1 L), 1-Ethyl-3-(3-dimethylaminopropyl)-carbodiimide (EDC), sulfo-NHS (≥98% (HPLC), 56485-1 g) and ninhydrin (ACS reagent ≥98%, 72490-10 g) were purchased from Sigma Aldrich. Hydrochloric acid (HCl) (37% technical grade), ethanol (ROTIPURAN® ≥99.8%, 9065.4), acetic acid (ROTIPURAN® 100%, 3738.1) and dichloromethane (DCM) (≥99.5%, p.a., ACS, ISO) were purchased from Carl Roth GmbH. Silica 60 (0.063 - 0.2 mm) (Macherey-Nagel GmbH & Co.), methanol (reagent Ph. Eur.) (VWR International), tetrahydrofuran (THF) (T2394) (TCI Chemicals,) and triethylamine (AB109928) (ABCR GmbH) were purchased as stated. Unless otherwise specified, ultrapure Milli-Q water was used throughout.

Synthesis of amino cholate from cholic acid

Synthesis of amino cholate was carried out by Dr. Isabella Tavernaro from the INM. In order to conjugate bile acid to the NPs, an amino-group was required. Conversion of cholic acid to amino cholate was achieved by modifying the protocol of Zhou et

al. (2007).[333] Cholic acid was converted to an NHS ester using DCC as the coupling reagent. The activated ester was transformed into cholate amide, which was reduced by lithium aluminium hydride solution to afford the amino cholate. A Schlenk line was used for all synthesis reactions and solvents were extracted under argon. Cholic acid (535 mg), DCC (295 mg), and NHS (218 mg) were dissolved in anhydrous THF (25 ml) and acetonitrile (2.5 ml). After 8 h at room temperature, the colourless solid formed was filtered out and the filtrate was concentrated *in vacuo* to give a colourless foam (741 mg, 71% yield). A portion of this solid (370 mg) was dissolved in anhydrous DMF (10 ml) and 30 ml of ammonia was added. After 12 h at 50 °C, the precipitate was filtered and collected by suction filtration, washed with water (2 x 10 ml), and purified with column chromatography over silica gel using DCM and methanol (8:1 ratio) as the eluent to give a white powder (122 mg, 41% yield). The solid (100 mg) was dissolved in anhydrous THF (20 ml) under N_2. $LiAlH_4$ (15.2 ml in THF) was added slowly via a syringe. The reaction mixture was heated to reflux for 24 h. A small amount of ethyl acetate was added and the solvent was concentrated *in vacuo*. Finally, the residue was purified with column chromatography over silica gel using DCM/methanol (10:1), pure methanol and methanol/triethylamine (50:1) as the eluents to give a colourless solid.

Conjugation of amino cholate to MFe_2O_4@DMSA nanoparticles

The DMSA-coated nanoparticles were conjugated to amino cholate via EDC-NHS coupling. 8 ml of nanoparticles in H_2O (300 μg/ml) were added to a glass vial and the pH lowered to 5 using HCl. EDC (22 μl) was added and stirred, then 100 mg of sulfo-NHS in 1 ml of H_2O was added and the solution stirred at room temperature for 20 minutes. Another 22 μl of EDC was added and following 20 minutes of further stirring, 20 mg of amino cholate in 2 ml of H_2O and 20 μl triethylamine was added dropwise to the NP solution and the solution stirred overnight. The NPs were collected via centrifugation (4,600 rpm, 15 minutes) and washed in H_2O. Finally the bile acid-functionalised NPs were dialysed against H_2O for 2 hours with one water change after one hour, then filtered through a sterile filter membrane (5 μm pore size).

Nanoparticle characterisation

Characterisation of the bile-acid functionalised (MFe_2O_4@BA, BA = bile-acid functionalised) NPs, was conducted in accordance with the protocols listed in section 4.2.5 of chapter 4.

Cytotoxicity and oxidative stress testing

Evaluation of the cytotoxicity and oxidative stress potential of MFe_2O_4@BA NPs to HepG2 liver cells was carried out in accordance with the protocols detailed in section 5.2 of chapter 5.

Nuclear magnetic resonance spectroscopy to verify synthesis of amino cholate

Nuclear magnetic resonance (NMR) spectroscopy is a widely-used method to identify compounds. The underlying principles are similar to MRI: a sample is subjected to a magnetic field and RF pulse, exciting the nuclei of atoms into a spin-up or spin-down state. Upon relaxing to ground state, the nuclei release energy in the form of an RF signal. The amount of energy released depends upon their electronic structure and chemical environment. ^{1}H and ^{13}C NMR spectroscopy provide information about the number of protons and carbons in the sample respectively.[334] In this study, NMR spectroscopy was carried out to verify the conversion of cholic acid to amino cholate. NMR spectra were recorded using a Bruker Avance II multi-core liquid NMR spectrometer with a proton resonance frequency of 300 MHz. Chemical shifts (δ) are listed in parts per million (ppm) and are reported relative to solvent residual signals: $CDCl_3$ (^{1}H: δ = 7.26 ppm, ^{13}C: δ = 77.2 ppm), DMSO-d_6 (^{1}H: δ = 2.50 ppm, ^{13}C: δ = 39.5 ppm) or D_2O (^{1}H: δ = 4.79 ppm). Multiplicity is indicated as follows: s (singlet), bs (broad singlet), d (doublet), t (triplet), q (quartet), m (multiplet), bm (broad multiplet).

Ninhydrin test

The ninhydrin-based Kaiser test is a fast and simple method to detect the presence or absence of primary amines or amides.[335] Ninhydrin reacts with free primary amines and amides to generate an amino derivative that has a characteristic purple

colour. The Kaiser test was employed to qualitatively indicate the presence of amino cholate in the MFe_2O_4@DMSA NP dispersions. Following drop casting of DMSA, MFe_2O_4@DMSA NPs, MFe_2O_4@BA NPs and amino cholate onto thin layer chromatography (TLC) plates, a ninhydrin solution of 0.2 g ninhydrin in 99.5 mL ethanol and 0.5 mL acetic acid was added and the plates were heated with a heat gun.

6.2.3 Results and discussion

Conjugation to MFe_2O_4@DMSA NPs

Bile acids could provide liver-targeting functionality to NPs. With this in mind, the functionalisation of cholic acid to ultra-small MFe_2O_4@DMSA NPs was explored for the first time as a step towards designing new liver-targeting T_1 MRI contrast agents. Both iron-oxide and cobalt-ferrite NPs were synthesised for comparative purposes. In order to attach cholic acid to the particles, first cholic acid was converted into amino cholate by adaption of an existing protocol.[333] Chiefly, cholic acid was converted to the N-hydroxysuccinimide ester using dicyclohexylcarbodiimide (DCC) as the coupling reagent. The activated ester was then transformed into the cholate amide, which was reduced by $LiAlH_4$ to afford the amino cholate. NMR studies were conducted to confirm the product of each step (see section B.5 in the appendix). The amino group of amino cholate was then conjugated to carboxylate groups on the surface of MFe_2O_4@DMSA NPs by EDC-NHS coupling. A schematic outlining the process of obtaining $CoFe_2O_4$@BA and Fe_3O_4@BA NPs is shown in figure 6.13.

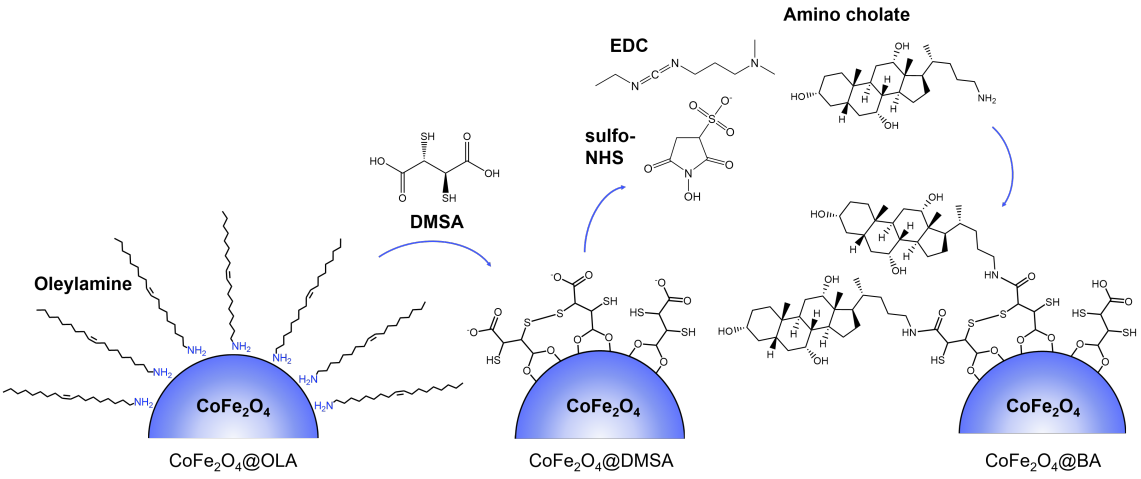


Figure 6.13: Schematic outlining the synthesis process for $CoFe_2O_4$@BA NPs. Firstly, hydrophobic oleylamine-coated particles were rendered hydrophilic via DMSA ligand exchange (as detailed in chapter 4). Then DMSA-coated nanoparticles were conjugated to amino cholate by EDC-NHS coupling.

To assess the conjugation of amino cholate to DMSA-NPs, FTIR was conducted. Figure 6.14 compares the FTIR spectra acquired for DMSA and BA functionalised $CoFe_2O_4$ and Fe_3O_4 NPs. Following conjugation with bile-acid, the broad peak at

3400 cm^{-1} (in the same region as OH stretching), sharpened due to NH stretching of the secondary amide group. Sharpening of the peaks at 2865 and 2930 cm^{-1} can be attributed to the symmetric and asymmetric CH_2 groups of amino cholate,[336] and the peak at 2970 cm^{-1} belongs to the asymmetric vibration of amino cholate's CH_3 groups. Additionally, the small peak at 1650 cm^{-1} is due to C=O amide stretching. The presence of NH and CH_3 stretching peaks indicated the presence of amino cholate in the NP dispersion. For further examination, the ninhydrin test was performed. Amino cholate and MFe_2O_4@BA NPs produced a purple colour, indicating the presence of an amine or amide (figure 6.15). Differentiating between amine and amide groups is not possible with FTIR or ninhydrin tests, however taking into consideration the multiple washing steps and dialysis performed, the results suggest that conjugation of amino cholate to MFe_2O_4@DMSA NPs had occurred.

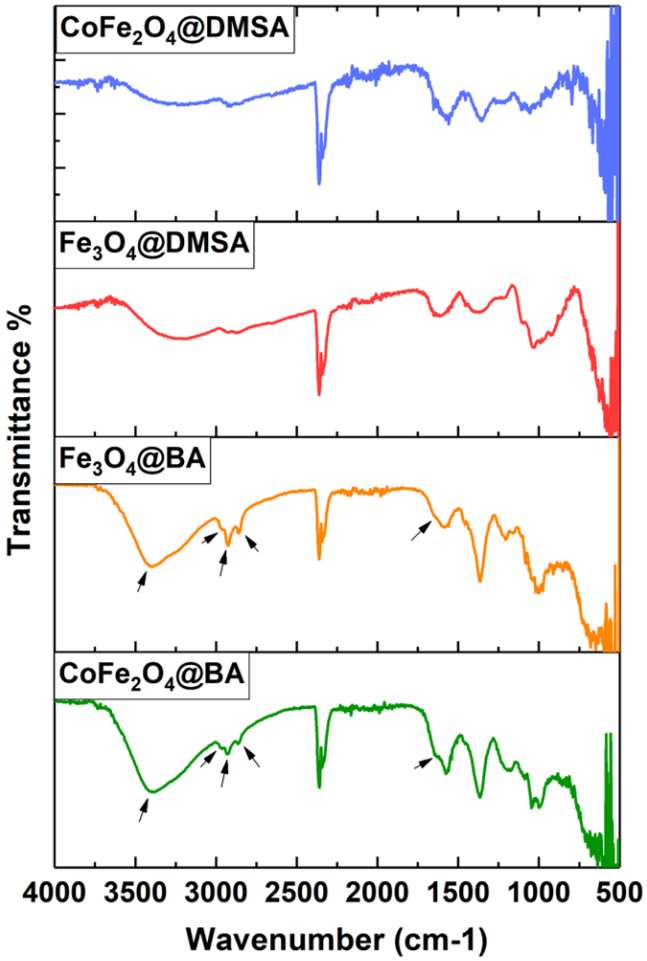


Figure 6.14: FTIR spectrum of DMSA and BA functionalised $CoFe_2O_4$ and Fe_3O_4 NPs

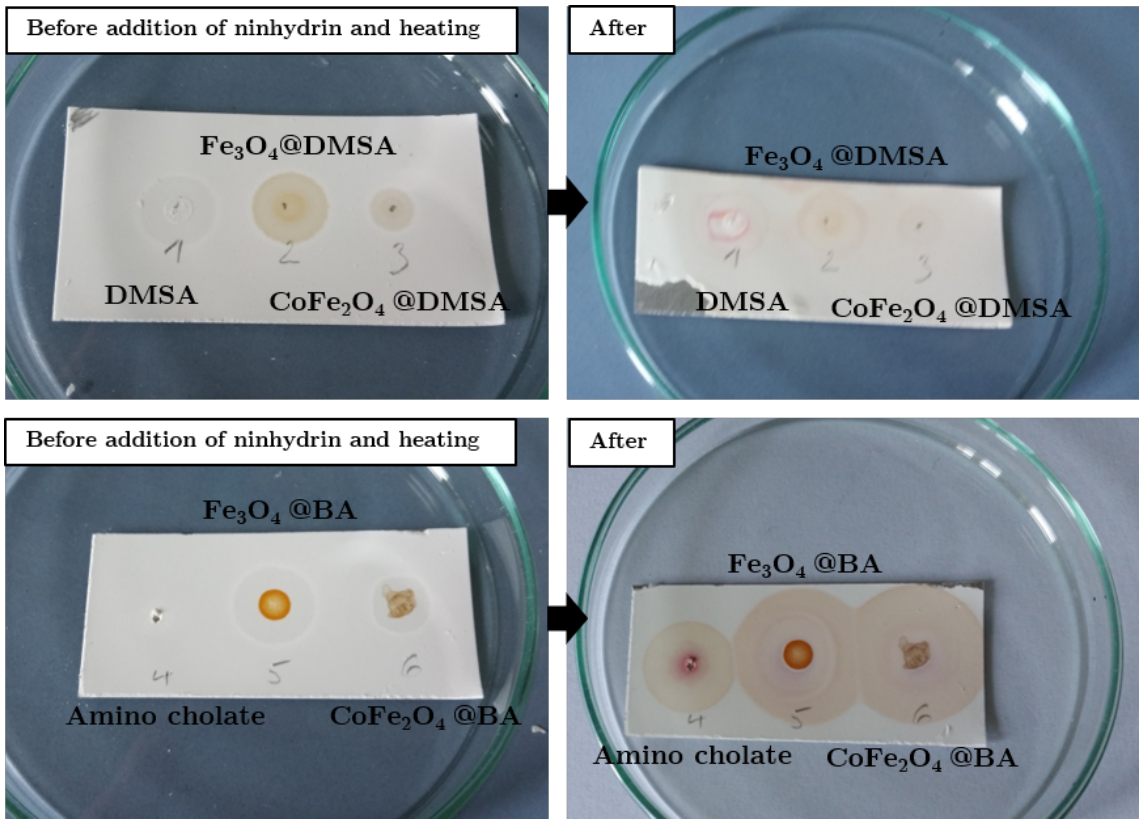


Figure 6.15: Images displaying the results of the Ninhydrin test conducted using thin layer chromatography. Following heating with a heat gun, amino cholate and MFe_2O_4@BA NPs produced a purple colour, indicating the presence of an amine.

To quantify the amount of bile-acid on the surface of the NPs, TGA measurements were performed. The weight loss profiles for Fe_3O_4@BA and $CoFe_2O_4$@BA NPs were almost identical, with total weight losses of 45% (figure 6.16). Considering that the weight loss for the same $CoFe_2O_4$ NPs prior to bile-acid functionalisation was 36.4% (see section 4.3.2 in chapter 4), approximately 8.6% of the total weight loss is due to the bile acid ligands. Using equation 4.3 from chapter 4, the number of bile-acid ligands per $CoFe_2O_4$@BA particle was estimated to be 28. The approximate radius of a bile acid molecule 3.5 Å,[47] and a single layer of DMSA is estimated to be 0.1 nm thick.[295] Thus assuming a double layer of DMSA on a 2.4 nm core, the total surface area would be 24.6 nm^2, suggesting a single layer of bile-acid was conjugated to the NPs surface.

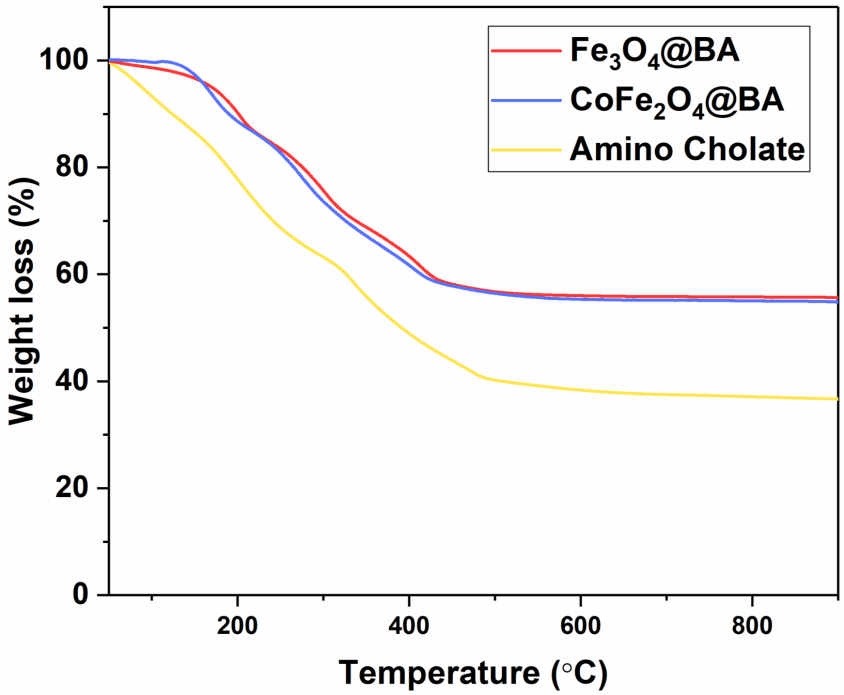


Figure 6.16: TGA weight loss profiles of Fe_3O_4@BA and $CoFe_2O_4$@BA NPs. Both particles had a weight loss of 45% and amino cholate shows a similar weight loss profile

Properties and stability of MFe_2O_4@BA NPs

The properties and stability of MFe_2O_4@BA NPs were evaluated with cryo-EM, DLS and zeta-potential studies under the same conditions used for MFe_2O_4@DMSA NPs in section 4.2.5 of chapter 4. Cryo-EM revealed networks of NPs similar to that observed for DMSA-coated NPs (Figure 6.17(A,B)). Although the appearance of MFe_2O_4@BA NPs under cryo-EM was similar to that observed for MFe_2O_4@DMSA NPs, noticeable NP sedimentation occurred after several days. To examine their stability, hydrodynamic diameter and zeta potential measurements were conducted in different pH. The average d_H for Fe_3O_4@BA and $CoFe_2O_4$@BA NPs at pH 7 was 476 ±128 nm and 369 ±74 nm respectively. The significant increase in d_H indicates NP agglomeration had occurred after functionalisation with bile acid. Bile acid is known to form helical aggregates due to its hydrophobic sterol backbone, which aids in its transport to the liver.[337] Below pH 5, the d_H of both Fe_3O_4@BA and $CoFe_2O_4$@BA NPs increased, showing the NPs were less stable in acidic conditions (Figure 6.17(C)). Zeta-potential measurements mirror these results; ζ values

of -36.5 ±1.5 mV and -38.7 ±1.0 mV were measured at pH 9 for Fe_3O_4@BA and $CoFe_2O_4$@BA NPs respectively (Figure 6.17(D)), whilst their ζ-potential increased in pH 3 to 19.1 ±0.6 mV -4.1 ±0.2 mV.

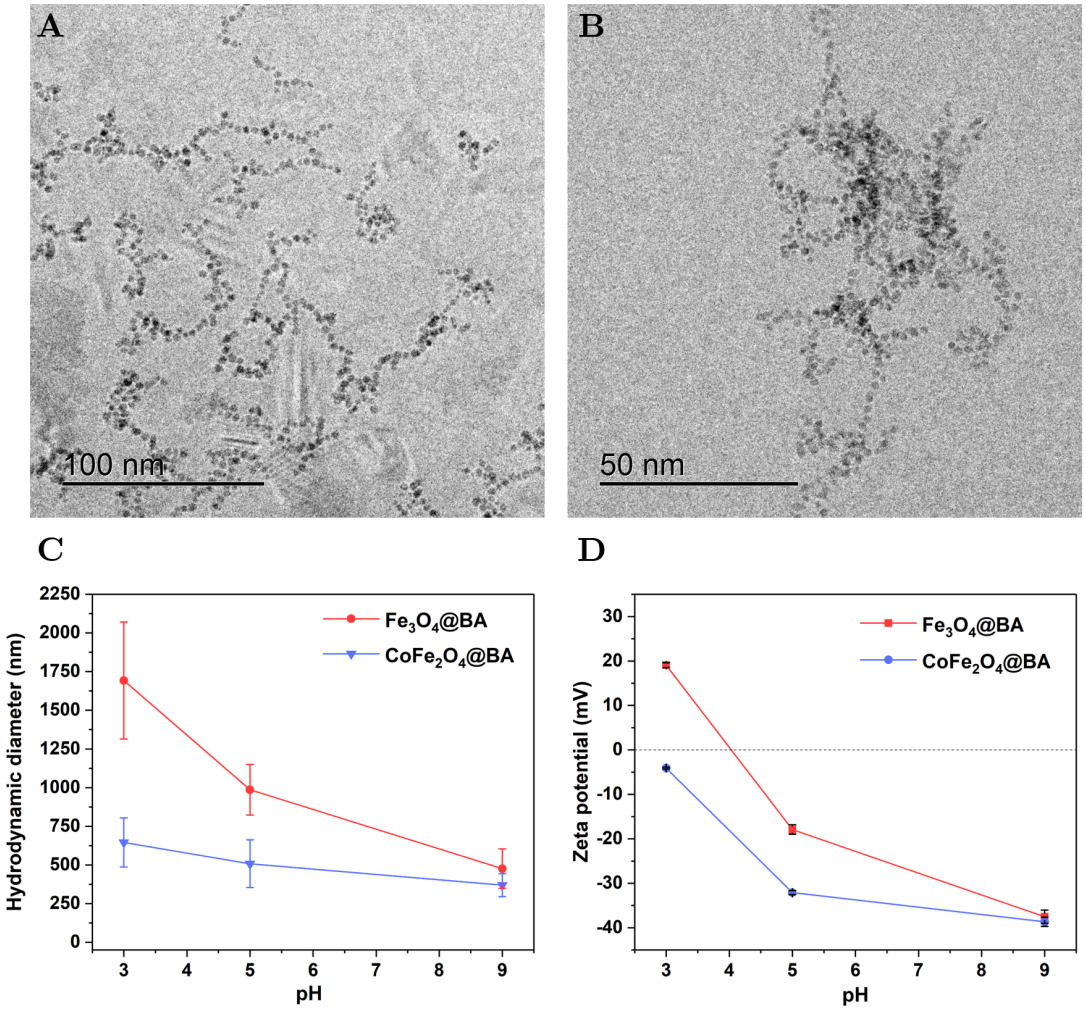


Figure 6.17: Cryo-EM micrographs of (A) Fe_3O_4@BA and (B) $CoFe_2O_4$@BA NPs. (C) pH dependent d_H measurements. (D) Zeta-potential measurements showing that MFe_2O_4@BA NPs were stable in neutral and alkaline pH, and that Fe_3O_4@BA NPs were less stable in acidic conditions than $CoFe_2O_4$@BA NPs.

Cytotoxicity and oxidative stress evaluation of MFe_2O_4@BA NPs

Determination of particle concentrations

ICP-OES measurements of the iron and cobalt concentration of MFe_2O_4@BA NPs were used to estimate the concentration of the NPs (table 6.3) following the same protocol used for MFe_2O_4@DMSA NPs described in section 5.2 of chapter 5. Using the calculated NP concentrations, the samples were diluted in DMEM

medium to concentrations of 100 μg/ml in preparation for the toxicity assays.

Table 6.3: Calculated particle concentrations compared to elemental ICP-OES concentrations

Particle type	Core size (TEM) (nm)	Coating ligand	ICP-OES elemental concentration (mg/l)		Calculated NP concentration (μg/ml)	Number of NPs in 1 ml
			Fe	Co		
Fe_3O_4	4.0	BA	296.0 ± 6.0	n/a	409.0 ± 8.3	2.34 x 10^{15}
$CoFe_2O_4$	2.4	BA	161.6 ± 1.5	36.1 ± 1.6	272.5 ± 4.3	8.18 x 10^{15}

Interference testing

Prior to evaluating the cytotoxic and oxidative stress potential of MFe_2O_4@BA NPs, interference testing was conducted following the same protocol detailed in section 5.2 of chapter 5 However, only the maximum NP concentration of 100 μg/ml was used in the cytotoxicity, optical interference and oxidative stress assays. To assess for NP-induced optical interference, fluorescence measurements of Fe_3O_4@BA and $CoFe_2O_4$@BA NPs in cell medium alone (no cells or dye indicators used) were acquired. The fluorescence values were normalised to the negative control (cell medium) and are an average of three measurements.

Figure 5.2(A) shows that at the maximum concentration of 100 μg/ml, $CoFe_2O_4$@BA NPs showed a reduction in fluorescence due to negative optical interference. Fe_3O_4@BA NPs showed a minor reduction in fluorescence. NP-induced optical interference has been discussed previously in section 5.3.2 of chapter 5. To correct for the factor of negative interference, the absorbance of NPs in cell media was subtracted from the absorbance data attained from particle-treated cells.

Next, the potential for the MFe_2O_4@BA NPs to cause conversion of the reactive oxygen species dye indicator (2',7'-dichlorodihydrofluorescein (H_2DCF)) was assessed, also following the same protocol detailed in section 5.2 of chapter 5. As shown in figure 5.3, MFe_2O_4@BA NPs caused no increase or decrease in fluorescence signal and thus did not interfere with the ROS dye. Further testing of the MFe_2O_4@BA NPs was conducted to assess for potential interference with the already-converted ROS dye after incubation with SIN-1 (in the absence of cells). As shown in figure 5.3(B), particles did not cause a reduction or increase in ROS signal, and thus did

not interfere with a positive ROS signal. Unlike in the cytotoxicity tests, particle optical interference was negligible in the oxidative stress measurements due to the high absolute values of fluorescence.

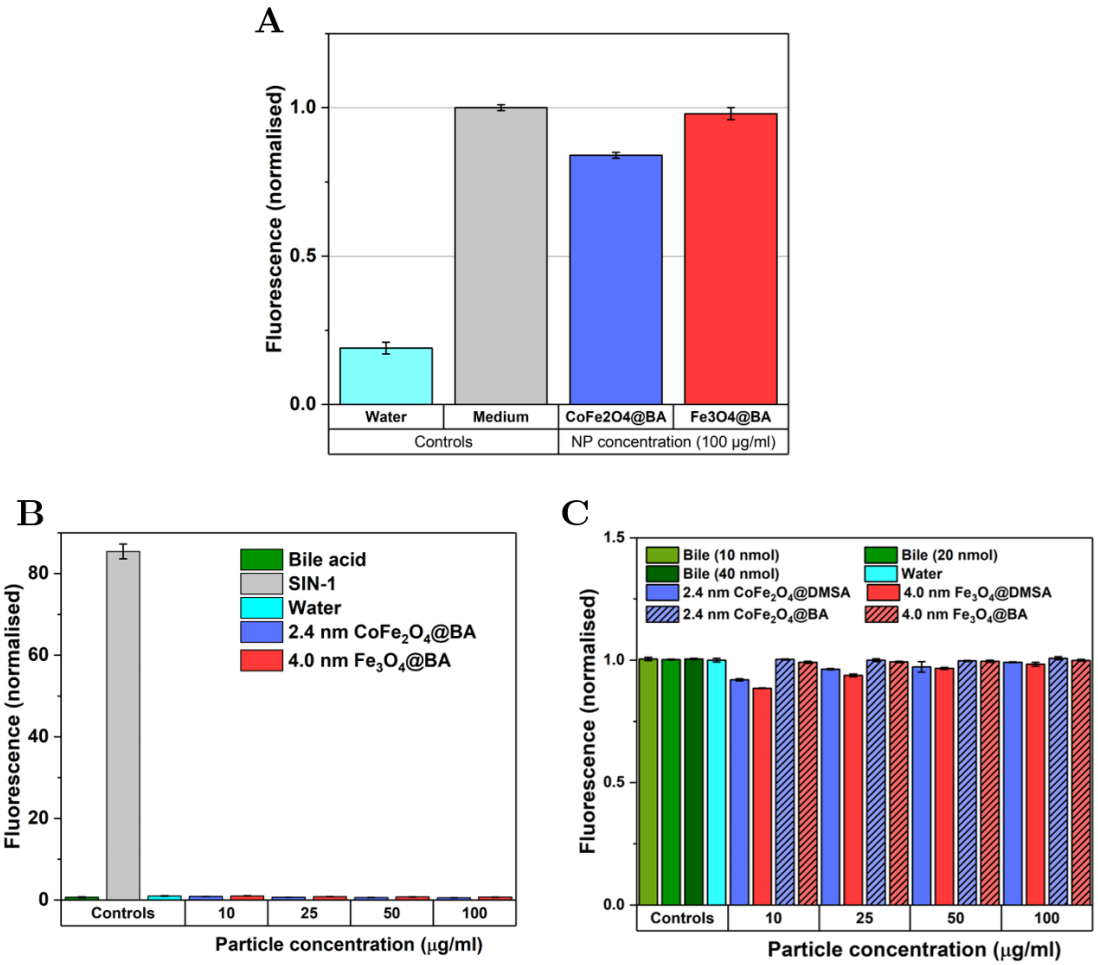


Figure 6.18: Interference testing of bile-acid functionalised NPs. A: Optical interference of NPs with fluorescence measurements (normalised to cell medium). The fluorescence of $CoFe_2O_4$@BA NPs decreased at a concentration of 100 µg/ml, thus these NPs caused negative interference. B: Interference test of NPs and bile acid with ROS dye: particles do not cause conversion of dye in absence of cells (C = normalised to PBS, D = normalised to water). C: Neither bile acid nor NPs interfered with SIN-1 (normalised to water).

Cytotoxicity and oxidative stress towards HepG2 cells

Cytotoxic and oxidative stress effects of Fe_3O_4@BA and $CoFe_2O_4$@BA NPs towards HepG2 cells were assessed using the same protocol and conditions used previously for DMSA-coated NPs (see section 5.2 of chapter 5). $CoFe_2O_4$@DMSA and Fe_3O_4@DMSA NPs were re-evaluated conjunctively to determine any differences

due to the presence of bile-acid. Figure 6.19A shows that at NP concentrations of 100 μg/ml, no cytotoxicity was observed with $CoFe_2O_4$@BA or Fe_3O_4@BA NPs. Figure 6.19(B) compares the ROS production for 2.4 and 4.0 nm NPs capped with DMSA, or DMSA and BA. Serendipitously, $CoFe_2O_4$@BA and Fe_3O_4@BA NPs significantly decreased the amount of ROS produced in comparison to $CoFe_2O_4$@DMSA and Fe_3O_4@DMSA NPs. The ROS production for $CoFe_2O_4$ NPs decreased by approximately 67% when bile-acid was conjugated to the NPs. Similarly, the ROS production of Fe_3O_4@BA NPs decreased by approximately 62%.

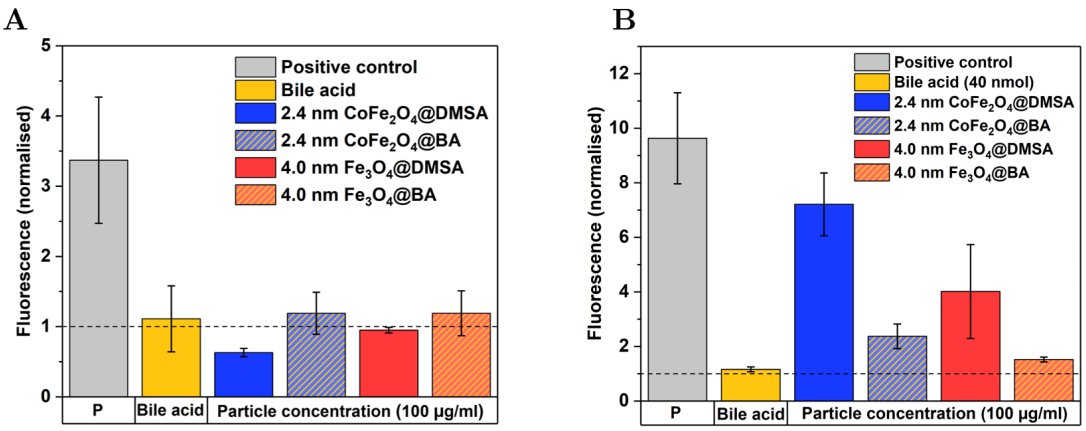


Figure 6.19: (A) Relative cell death (fluorescence) of HepG2 cells following exposure to DMSA and BA functionalised MFe_2O_4 NPs for 24 hours. As controls for comparison, free bile acid and triton-x 100 (positive control) were used. (B) Relative ROS production (fluorescence) of HepG2 cells following exposure to DMSA and BA functionalised MFe_2O_4 NPs for 24 hours. Significant decrease in ROS production is observed following functionalisation of $CoFe_2O_4$@DMSA and Fe_3O_4@DMSA NPs with a bile-acid derivative. Fluorescence was normalised to negative control (cell medium = 1) (positive control = hydrogen peroxide). Results are shown as mean ± standard deviation from three independent experiments.

The reduction in ROS observed suggests that bile-acid acted as an ROS scavenger, mitigating oxidative stress effects. Bile acids have demonstrated antioxidant properties by directly intercepting peroxy radicals in previous studies.[338] Contrarily, hydrophobic bile acids can induce ROS production through disruption of the mitochondrial membrane.[339] The hydrophobicity of bile-acids is linked to production of ROS, with deoxycholic acid (DCA) producing ROS, whilst hydrophilic ursodeoxycholic acid (UDCA) has antioxidant properties which are especially relevant towards Fe^{3+} induced oxidative damage.[340] UDCA was found to be an excellent scavenger of

.OH radicals generated by $FeCl_3$-EDTA, as well as nonchelated Fe^{2+} and Fe^{3+} ions, preferentially interacting with Fe^{3+}.[340] Notably, the rate constant for the reaction was 10-fold higher than that of well-known pharmacological scavengers. Considering the findings of this work and the order of bile-acid hydrophilicity (UDCA < CA < CDCA < DCA < LCA),[341] I propose that cholic acid shares similar antioxidant properties as UDCA, and could be an effective site-specific ROS scavenger for free radicals induced by iron-containing NPs. Further investigation to elucidate the mechanism of ROS scavenging by cholic acid is therefore warranted.

For liver-targeting biomedical applications, bile-acid functionalised NPs could offer a convenient route to obtain biocompatible ferrite NPs and mitigate their common issue of ROS generation. For potential application as T_1 contrast agents, the magnetic properties of bile-acid functionalised NPs should be evaluated, especially in consideration of their aggregation. The aggregation of bile-acid functionalisation could be addressed with further optimisation of the conjugation process.

6.2.4 Conclusions

MFe_2O_4@DMSA NPs were conjugated to a bile-acid derivative towards the design of biocompatible liver-targeted MRI contrast agents. In comparison to MFe_2O_4@DMSA NPs, bile-acid functionalised (MFe_2O_4@BA) NPs showed an improvement in biocompatibility, with a significant reduction of generated ROS following incubation with HepG2 liver cells. The results show that amino cholate, a derivative of cholic acid, potentially acts as an ROS scavenger. However, further research is necessary to elucidate the mechanism of ROS scavenging, and the physiological conditions in which amino cholate can scavenge. Suggested future experiments are detailed in the final chapter 7 of this thesis.

The conjugation of amino cholate to MFe_2O_4@DMSA NPs to achieve MFe_2O_4@BA NPs was successful, however the particles consequently agglomerated. The agglomeration of MFe_2O_4@BA NPs will likely affect their performance as MRI contrast agents. Therefore, in consideration for application as T_1 contrast agents, the conjugation process needs to be optimised to minimise agglomeration and obtain small hydrodynamic diameters. Optimisation could be achieved through a systematic study exploring different parameters such as bile-acid concentration, pH, and han-

dling procedures. In the event that the agglomeration is caused by bile acid itself and its inherent ability to form helical aggregates, then the application of bile-acid functionalised NPS for T_1 MRI may be redundant and instead the NPs may be better suited towards T_2 contrast enhancement. In order to assess their T_1 and T_2 contrast enhancement potential, MRI phantom studies with the MFe_2O_4@BA NPs are required. Following which, *in vivo* studies using mice would be highly important to evaluate whether the bile-acid functionalisation serves to target the liver as intended, and whether the NPs enhance T_1 and T_2 *in vivo*.

Bile-acid functionalised MFe_2O_4@BA NPs could offer a promising route for biocompatible liver-targeted MRI, and thus further research into this area is encouraged.

Chapter 7

Summary and Outlook

The main aim of this study was to develop ultra-small nanoparticles that were potentially suitable for application as T_1 MRI contrast agents. Current T_1 contrast agents are gadolinium-based, which present concerning toxicity issues. Safer alternatives and more targeted approaches are needed, of which ultra-small magnetic NPs are promising candidates. Quite often, research concerning NP synthesis, chemical functionalisation, toxicity and medical applications are conducted by separate research groups. This can lead to inconsistencies between experiments and incomplete data sets, which may convolute the evaluation of the suitability of the NPs. Considering that many factors should be taken into account when designing NPs for biomedical applications, a key strength of this study was its multidisciplinary approach, which provided a reliable and all-encompassing evaluation of the USNPs.

In this context, the first objective was to develop a synthesis method that could produce both iron oxide and cobalt-ferrite NPs below 3 nm with small magnetic moments. Ultra-small spinel ferrite NPs were successfully synthesised with sub-nm size precision using a simple thermal decomposition approach with oleylamine. Both iron oxide and cobalt ferrite NPs size was finely tuned from ca. 2-5 nm by varying the precursor-to-oleylamine ratio.

The general small NP sizes obtained suggested that OLA effectively lowered the free surface energy of the system through formation of an OLA-precursor complex, reducing the critical radius required for nucleation to occur. It was further hypothesised that varying the precursor-to-OLA ratio controlled NP size in the growth phase, as more OLA restricted growth by limiting the diffusion and reaction rate

of remaining monomers in the system. Further research is required to confirm the reaction mechanisms and how this varies depending on the parameters used. Future work could entail adopting a theoretical approach and modelling the thermodynamics of the reaction. Real-time and *in situ* spectroscopic analysis of the reaction would be highly beneficial, however this is beyond the capability of current characterisation tools.

Identifying the reaction mechanism may be useful to better understand NP nucleation and growth in the presence of oleylamine, and therefore potentially enable application of these principles to the controlled synthesis of other NP types. Research of this nature could permit a predictive approach to NP synthesis, as opposed to the trial and error approach that is currently taken. Attention should also be given to develop large-scale and ideally green synthesis methods, whilst still maintaining the level of control over NP size and crystallinity obtained in small batch synthesis approaches like that of this study. The practical use of USNPs is still hampered by the difficulty in synthesising them large-scale. Nevertheless, the synthesis method provided in this work provides a quick and simple route to produce USNPs, which could be used in fields beyond biomedicine. For example, as catalysts for the growth of single-walled carbon nanotubes.

The crystal structure of the USNPs was probed using atomic-resolution STEM, EELS and XRD analysis. Both iron oxide and cobalt ferrite USNPs displayed cubic spinel crystal structures. The composition of cobalt ferrite NPs was confirmed with EELS spectroscopy and XRD, however it was not possible to accurately confirm the oxidation state of the iron oxide NPs. The oxidation state can affect the magnetic properties and the toxicity of NPs *in vivo*, therefore it is important to identify. For this purpose, Mössbauer spectroscopy experiments may be worthwhile conducting in future studies.

The influence of NP size and composition on the magnetic properties was investigated in consideration for their application as T_1 MRI contrast agents, where small magnetic moments are desired. The magnetic saturation and blocking temperature of $CoFe_2O_4$@OLA NPs was shown to be highly sensitive to NP size, decreasing as NP size decreased from 4.5 to 2.4 nm. Fe_3O_4@DMSA and $CoFe_2O_4$@DMSA NPs 2.4 nm in size displayed superparamagnetic properties, with a weak magnetic moment ow-

ing to their small size and thus predominating effect of the magnetically disordered surface layer. Magnetic anisotropy introduced by Co^{2+} ions lowered the magnetic saturation for 2.4 nm $CoFe_2O_4$@DMSA NPs, which encouraged their application as T_1 MRI contrast agents.

In addition to possessing the ideal magnetic properties, it is extremely important that a contrast agent for T_1 MRI has good colloidal stability in water and physiological media. This is to prevent rapid clearance from the body, and allow close contact with water molecules *in vivo* so that T_1 relaxation can occur. With this objective in mind, two phase transfer methods were explored: DMSA ligand exchange and a new direct phase transfer method with BSA. Phase transfer with BSA proved ineffective, as large NP clusters were obtained. In addition, $CoFe_2O_4$@BSA NPs exhibited cytotoxicity towards HepG2 cells in subsequent toxicity tests, potentially due to large NP uptake or residual OLA and solvents in the clusters. The formation of clusters may have been due to the emulsion process itself, and thus further development of the method is necessary. Future work could entail trying different solvents, and using a nano-probe to create a nano-emulsion and thus smaller droplets. Furthermore, reducing the rate of evaporation by removing the water-bath heating step should be investigated. Although not suitable for the intended purpose of this work, the BSA-NP clusters could be exploited for alternative applications. For example, the Kraus group synthesise supraparticle SPION clusters via an emulsion process and discuss their potential for drug delivery applications.[342,343]

DMSA ligand exchange proved more suitable for obtaining water-dispersible NPs. One of the main drawbacks of using DMSA is its tendency to oxidise and form interparticle disulphide bridges, leading to rapid agglomeration. This issue was mitigated by dialysing the NPs before exchange, and alkalising the NPs after exchange. As a result, MFe_2O_4@DMSA NPs with reproducibly small hydrodynamic diameters $<$12 nm were obtained. The NPs were stable in a wide pH range, in DMEM cell culture and remained stable for up to 12 months. $CoFe_2O_4$@DMSA NPs were stable in a wider pH range than Fe_3O_4@DMSA NPs, potentially due to cobalt ferrite having less redox potential than magnetite. Producing NPs that are colloidally stable in water is important for many applications in biomedicine as well as other fields such as water filtration. This new improvement to the DMSA ligand exchange procedure through

minor modification could be beneficial for others to achieve colloidally stable NPs in water. In future work, it could be interesting to try ligand exchange techniques with other coatings such as citrate and PEG, and compare their effect on stability and toxicity.

The water-dispersible MFe_2O_4@DMSA NPs were evaluated for their biocompatibility with HepG2 liver cells by *in vitro* cytotoxicity and oxidative stress assays. The effects of NP size and metal composition were investigated. HepG2 liver cells were chosen as the liver is the accumulation site for NPs that are not cleared renally. Additionally, liver-targeted MRI was a specific application of interest. It was found that MFe_2O_4@DMSA NPs were not cytotoxic to HepG2 cells. There was no observable difference between 2.4 and 4.3 nm NPs, or between Fe_3O_4 and $CoFe_2O_4$ NPs. However, MFe_2O_4@DMSA NPs did produce significant amounts of ROS, with $CoFe_2O_4$@DMSA NPs producing more than Fe_3O_4@DMSA NPs. A possible explanation for this increase is the higher catalytic activity of Co^{2+} ions over Fe^{3+} ions.

The ability to direct compare the two NP types provided interesting insight into their composition-dependent toxicological behaviour. Although existing studies have described the toxicity of iron oxide NPs and cobalt ferrite NPs, it is not possible to directly compare results across different studies. Further *in vitro* assays comparing a range of NPs using different techniques, such as the MTT and LDH assay, and importantly across different cell lines, would be key next steps to gain a more comprehensive toxicological profile of the USNPs. Furthermore, cellular uptake studies employing electron or fluorescence microscopy techniques, could be beneficial to gain insight into cell interaction. Evaluating the short-term and long-term behaviour of NPs *in vivo* remains a major challenge for the application of nanomaterials in biomedicine. In general, it is difficult to gather a complete profile on nano-toxicity due to the complexity and breadth of the experiments required. A standardised set of guidelines and centralised database could provide better consistency and comparability between the efforts of different research groups.

In chapter 6 of this thesis, the application of ultra-small iron oxide and cobalt ferrite NPs for T_1 MRI contrast enhancement was explored in phantom studies. It was found that 2.4 nm $CoFe_2O_4$@DMSA NPs acted as T_1 contrast agents at pre-clinical

and clinical field strengths. Their r_2/r_1 ratio at 3.0 T was 3.70, which is close to that of commercially available Gd-based contrast agents. As hypothesised, the low magnetic moment of $CoFe_2O_4$ NPs proved effective for achieving T_1-weighted contrast. Due to the agglomerated condition of Fe_3O_4@DMSA NPs, it was not possible to directly compare the contrast behaviour of Fe_3O_4@DMSA and $CoFe_2O_4$@DMSA NPs. Therefore, further work should be conducted to weigh-up the benefits and drawbacks of using cobalt ferrite over iron oxide. Moreover, an ideal comprehensive study would consist of a panel of different NP sizes and compositions in order to identify the optimum NP for T_1 MRI. Additionally, fundamental studies on the relaxation mechanisms of USNPs are still needed to aid the design of NPs with optimal properties.

As a step towards their application for liver-targeted MRI, and in a bid to improve their biocompatibility, the NPs were conjugated to amino cholate, a derivative of bile acid, for the first time. Conjugation by EDC-NHS coupling was successful, however the NPs had large hydrodynamic diameters, thus the process requires further development to achieve monodisperse NPs. Additionally, characterisation of the magnetic properties following bile-acid functionalisation must be conducted.

Serendipitously, bile-acid functionalised NPs showed a significant reduction in the amount of ROS produced in contact with HepG2 cells in comparison to DMSA-coated NPs, with a 62 and 67% reduction for Fe_3O_4 and $CoFe_2O_4$ NPs respectively. This new insight indicates that bile-acid has the potential to act as an effective ROS scavenger for ferrite-NP induced free radicals. ROS production is a major issue facing the use of metal-oxide NPs *in vivo*. Considering that conjugation of amino cholate to the NPs was achieved using the widely-applied EDC-NHS coupling protocol, amino cholate could be beneficial to reduce ROS production for other types of NPs with intended biomedical applications.

To investigate the ROS scavenging potential of amino cholate further, it could be useful to conjugate amino cholate to other metal oxide NPs such as Co_3O_4, $MnFe_2O_4$ and $ZnFe_2O_4$, and measure ROS production to see if its ROS scavenging potential is applicable to other metal-oxides. Employing ROS assays using different cell types would also help to understand whether MFe_2O_4 NPs produce ROS in contact with other cells, and if so, whether ROS production is also minimised following function-

alisation to amino cholate. To elucidate the mechanism of ROS scavenging by amino cholate, one could perform electron spin resonance (ESR) spectroscopy, which can directly assess antioxidant quenching, ROS production (including what types of free radical are being produced), as well as ROS scavenging.[344] Yin et al's study is a good example of the application of ESR to identify ROS scavenging mechanisms.[345] To fully evaluate the biocompatibility of MFe_2O_4@BA NPs and their effect on ROS, *in vivo* studies, such as those described by Halliwell and Whiteman,[261] are necessary.

In addition to further toxicity research, *in vivo* MRI testing is a critical next step to identify if the bile-acid coating confers liver-targeting properties to the NPs as hypothesised. MRI studies with mice conducted at different time points following intravenous injections would allow direct visualisation of the position of NPs in the body. Late hepatobiliary phase acquisition would reveal if the NPs had active or passive liver-targeting properties, as the bile duct would be markedly enhanced in the event the NPs underwent biliary excretion.[291]

In closing, this thesis has detailed the synthesis, functionalisation and application of ultra-small ferrite NPs for T_1 MRI contrast enhancement. A summary of this research project and the main findings is provided in figure 7.1. The T_1 contrast potential of ultra small $CoFe_2O_4$ NPs was demonstrated for the first time, and further *in vivo* research into this exciting material is encouraged. The work presented in this thesis has contributed towards a deeper understanding of ultra-small nanoparticle design for biomedical applications. In particular, bile-acid functionalised 2.4 nm $CoFe_2O_4$ NPs were identified as a promising route for biocompatible liver-targeted T_1 MRI.

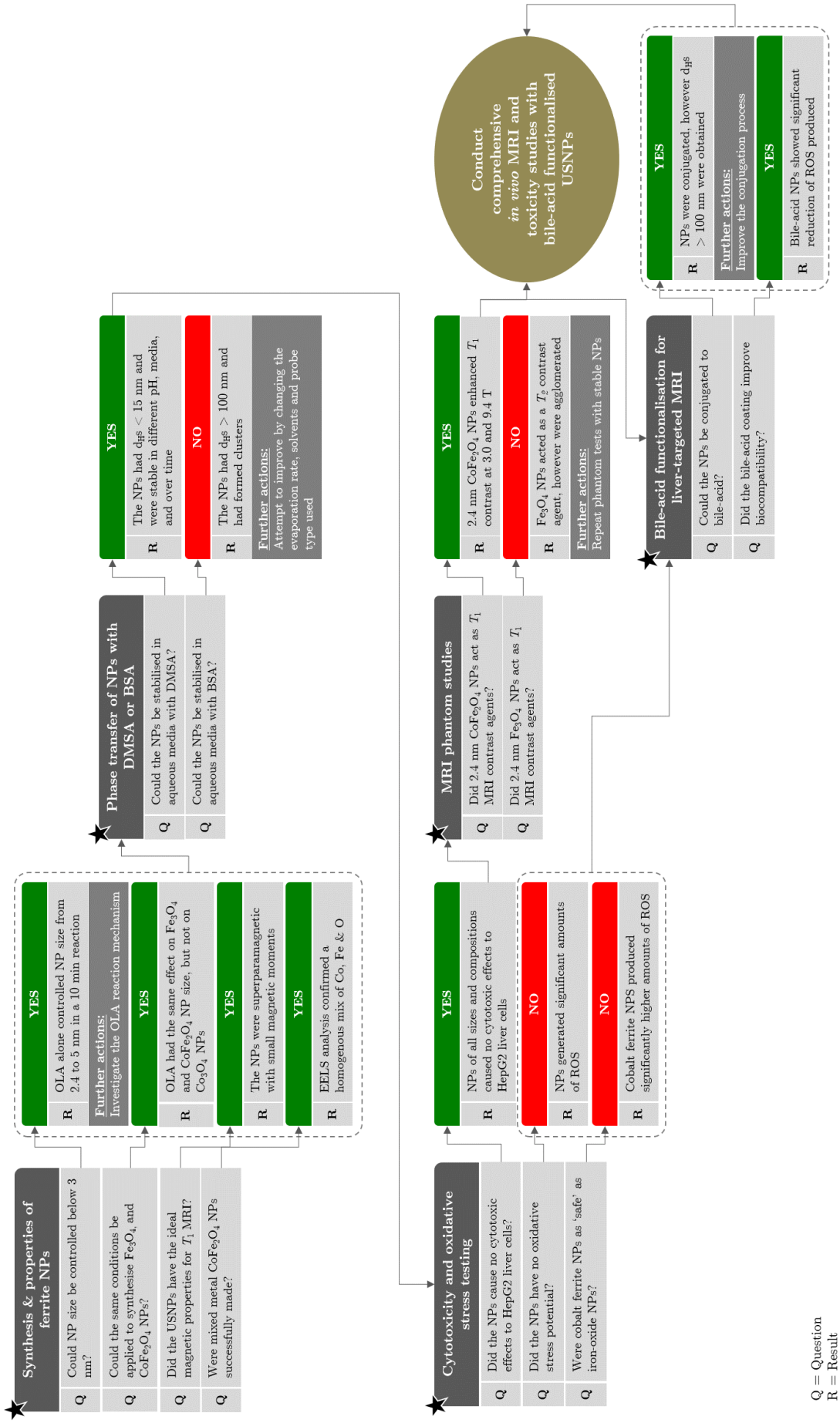


Figure 7.1: Flow chart summarising the main findings in this study

Bibliography

[1] S. Horikoshi and N. Serpone, "Introduction to Nanoparticles," in *Microwaves in Nanoparticle Synthesis*, pp. 1–24, John Wiley & Sons, Ltd, Apr. 2013.

[2] L. Zhang, F. X. Gu, J. M. Chan, A. Z. Wang, R. S. Langer, and O. C. Farokhzad, "Nanoparticles in Medicine: Therapeutic Applications and Developments," *Clinical Pharmacology & Therapeutics*, vol. 83, no. 5, pp. 761–769, 2008.

[3] Q. A. Pankhurst, J. Connolly, S. K. Jones, and J. Dobson, "Applications of magnetic nanoparticles in biomedicine," *Journal of Physics D: Applied Physics*, vol. 36, pp. R167–R181, June 2003.

[4] J. B. Haun, T.-J. Yoon, H. Lee, and R. Weissleder, "Magnetic nanoparticle biosensors," *Wiley Interdisciplinary Reviews: Nanomedicine and Nanobiotechnology*, vol. 2, pp. 291–304, May 2010.

[5] K. El-Boubbou, "Magnetic iron oxide nanoparticles as drug carriers: clinical relevance," *Nanomedicine*, vol. 13, pp. 953–971, Jan. 2018.

[6] M. Lewin, N. Carlesso, C.-H. Tung, X.-W. Tang, D. Cory, D. T. Scadden, and R. Weissleder, "Tat peptide-derivatized magnetic nanoparticles allow in vivo tracking and recovery of progenitor cells," *Nature Biotechnology*, vol. 18, pp. 410–414, Apr. 2000.

[7] I. M. Obaidat, B. Issa, and Y. Haik, "Magnetic Properties of Magnetic Nanoparticles for Efficient Hyperthermia," *Nanomaterials*, vol. 5, pp. 63–89, Jan. 2015.

[8] Y.-K. Peng, S. C. E. Tsang, and P.-T. Chou, "Chemical design of nanoprobes for T1-weighted magnetic resonance imaging," *Materials Today*, vol. 19, pp. 336–348, July 2016.

[9] P. Tartaj, M. a. d. P. Morales, S. Veintemillas-Verdaguer, T. G. l.-C. o, and C. J. Serna, "The preparation of magnetic nanoparticles for applications in biomedicine," *Journal of Physics D: Applied Physics*, vol. 36, pp. R182–R197, June 2003.

[10] Z. Sadowski and A. Pawlowska, "Synthesis of Metal Oxide Nanoparticles and Its Biomedical Applications," in *Nanotechnology Applied To Pharmaceutical Technology* (M. Rai and C. Alves dos Santos, eds.), pp. 91–111, Cham: Springer International Publishing, 2017.

[11] O. Fesenko and L. Yatsenko, *Nanophysics, Nanomaterials, Interface Studies, and Applications: Selected Proceedings of the 4th International Conference Nanotechnology and Nanomaterials (NANO2016), August 24-27, 2016, Lviv, Ukraine*. Springer, Sept. 2017.

[12] M. Wu, D. Zhang, Y. Zeng, L. Wu, X. Liu, and J. Liu, "Nanocluster of superparamagnetic iron oxide nanoparticles coated with poly (dopamine) for magnetic field-targeting, highly sensitive MRI and photothermal cancer therapy," *Nanotechnology*, vol. 26, no. 11, p. 115102, 2015.

[13] J. Baumgartner, L. Bertinetti, M. Widdrat, A. M. Hirt, and D. Faivre, "Formation of Magnetite Nanoparticles at Low Temperature: From Superparamagnetic to Stable Single Domain Particles," *PLOS ONE*, vol. 8, p. e57070, Mar. 2013.

[14] A. López-Ortega, E. Lottini, C. d. J. Fernández, and C. Sangregorio, "Exploring the Magnetic Properties of Cobalt-Ferrite Nanoparticles for the Development of a Rare-Earth-Free Permanent Magnet," *Chemistry of Materials*, vol. 27, pp. 4048–4056, June 2015.

[15] Wahajuddin and S. Arora, "Superparamagnetic iron oxide nanoparticles: magnetic nanoplatforms as drug carriers," *International Journal of Nanomedicine*, vol. 7, p. 3445, 2012.

[16] W. Lin, T. Hyeon, G. M. Lanza, M. Zhang, and T. J. Meade, "Magnetic Nanoparticles for Early Detection of Cancer by Magnetic Resonance Imaging," *MRS bulletin / Materials Research Society*, vol. 34, pp. 441–448, June 2009.

[17] B. Chertok, B. A. Moffat, A. E. David, F. Yu, C. Bergemann, B. D. Ross, and V. C. Yang, "Iron Oxide Nanoparticles as a Drug Delivery Vehicle for MRI Monitored Magnetic Targeting of Brain Tumors," *Biomaterials*, vol. 29, pp. 487–496, Feb. 2008.

[18] H. B. Na, I. C. Song, and T. Hyeon, "Inorganic Nanoparticles for MRI Contrast Agents," *Advanced Materials*, vol. 21, no. 21, pp. 2133–2148, 2009.

[19] E. Mazario, N. Menendez, P. Herrasti, M. Canete, V. Connord, and J. Carrey, "Magnetic Hyperthermia Properties of Electrosynthesized Cobalt Ferrite Nanoparticles," *The Journal of Physical Chemistry C*, vol. 117, pp. 11405–11411, May 2013.

[20] J. Mohapatra, A. Mitra, D. Bahadur, and M. Aslam, "Surface Controlled Synthesis of MFe2O4 (m = Mn, Fe, Co, Ni and Zn) Nanoparticles and Their Magnetic Characteristics," *CrystEngComm*, vol. 15, pp. 524–532, Dec. 2012.

[21] S. Amiri and H. Shokrollahi, "The role of cobalt ferrite magnetic nanoparticles in medical science," *Materials Science and Engineering: C*, vol. 33, pp. 1–8, Jan. 2013.

[22] H. M. Joshi, Y. P. Lin, M. Aslam, P. V. Prasad, E. A. Schultz-Sikma, R. Edelman, T. Meade, and V. P. Dravid, "Effects of Shape and Size of Cobalt Ferrite Nanostructures on Their Mri Contrast and Thermal Activation," *The Journal of Physical Chemistry. C, Nanomaterials and Interfaces*, vol. 113, no. 41, pp. 17761–17767, 2009.

[23] F. Liu, S. Laurent, H. Fattahi, L. Vander Elst, and R. N. Muller, "Superparamagnetic Nanosystems Based on Iron Oxide Nanoparticles for Biomedical Imaging," *Nanomedicine (London, England)*, vol. 6, pp. 519–528, Apr. 2011.

[24] P. Kucheryavy, J. He, V. T. John, P. Maharjan, L. Spinu, G. Z. Goloverda, and V. L. Kolesnichenko, "Superparamagnetic Iron Oxide Nanoparticles with Variable Size and an Iron Oxidation State as Prospective Imaging Agents," *Langmuir*, vol. 29, pp. 710–716, Jan. 2013.

[25] N. Singh, G. J. Jenkins, R. Asadi, and S. H. Doak, "Potential toxicity of superparamagnetic iron oxide nanoparticles (SPION)," *Nano Reviews*, vol. 1, Sept. 2010.

[26] K. Zarschler, L. Rocks, N. Licciardello, L. Boselli, E. Polo, K. P. Garcia, L. De Cola, H. Stephan, and K. A. Dawson, "Ultrasmall inorganic nanoparticles: State-of-the-art and perspectives for biomedical applications," *Nanomedicine: Nanotechnology, Biology and Medicine*, vol. 12, pp. 1663–1701, Aug. 2016.

[27] S. Ziemian, N. Löwa, O. Kosch, D. Bajj, F. Wiekhorst, and G. Schütz, "Optimization of Iron Oxide Tracer Synthesis for Magnetic Particle Imaging," *Nanomaterials*, vol. 8, Mar. 2018.

[28] B. Mehdaoui, A. Meffre, J. Carrey, S. Lachaize, L.-M. Lacroix, M. Gougeon, B. Chaudret, and M. Respaud, "Optimal Size of Nanoparticles for Magnetic Hyperthermia: A Combined Theoretical and Experimental Study," *Advanced Functional Materials*, vol. 21, pp. 4573–4581, Dec. 2011.

[29] H. Arami, A. Khandhar, D. Liggitt, and K. M. Krishnan, "In vivo delivery, pharmacokinetics, biodistribution and toxicity of iron oxide nanoparticles," *Chemical Society Reviews*, vol. 44, no. 23, pp. 8576–8607, 2015.

[30] B. H. Kim, N. Lee, H. Kim, K. An, Y. I. Park, Y. Choi, K. Shin, Y. Lee, S. G. Kwon, H. B. Na, J.-G. Park, T.-Y. Ahn, Y.-W. Kim, W. K. Moon, S. H. Choi, and T. Hyeon, "Large-Scale Synthesis of Uniform and Extremely Small-Sized Iron Oxide Nanoparticles for High-Resolution T1 Magnetic Resonance Imaging Contrast Agents," *Journal of the American Chemical Society*, vol. 133, pp. 12624–12631, Aug. 2011.

[31] L. M. Bauer, S. F. Situ, M. A. Griswold, and A. C. S. Samia, "High-performance iron oxide nanoparticles for magnetic particle imaging – guided hyperthermia (hMPI)," *Nanoscale*, vol. 8, pp. 12162–12169, June 2016.

[32] H. Shao, T.-J. Yoon, M. Liong, R. Weissleder, and H. Lee, "Magnetic nanoparticles for biomedical NMR-based diagnostics," *Beilstein Journal of Nanotechnology*, vol. 1, pp. 142–154, Dec. 2010.

[33] I. Koh and L. Josephson, "Magnetic Nanoparticle Sensors," *Sensors*, vol. 9, pp. 8130–8145, Oct. 2009.

[34] G. F. Goya, E. L. Jr, A. D. Arelaro, T. Torres, H. R. Rechenberg, L. Rossi, C. Marquina, and M. R. Ibarra, "Magnetic Hyperthermia With Fe_3O_4 Nanoparticles: The Influence of Particle Size on Energy Absorption," *IEEE Transactions on Magnetics*, vol. 44, pp. 4444–4447, Nov. 2008.

[35] Y.-X. J. Wang, "Current Status of Superparamagnetic Iron Oxide Contrast Agents for Liver Magnetic Resonance Imaging," *World Journal of Gastroenterology*, vol. 21, pp. 13400–13402, Dec. 2015.

[36] J. Estelrich, M. J. Sánchez-Martín, and M. A. Busquets, "Nanoparticles in magnetic resonance imaging: from simple to dual contrast agents," *International Journal of Nanomedicine*, vol. 10, pp. 1727–1741, Mar. 2015.

[37] J. Chanyaputhipong, S.-C. A. Low, and P. K. H. Chow, "Gadoxetate Acid-Enhanced MR Imaging for HCC: A Review for Clinicians," 2011.

[38] M. R. Prince, "Gadolinium-enhanced MR aortography.," *Radiology*, vol. 191, pp. 155–164, Apr. 1994.

[39] "Gadolinium-Containing Contrast Agents: Removal of Omniscan and Iv Magnevist, Restrictions to the Use of Other Linear Agents." https://www.gov.uk/drug-safety-update/gadolinium-containing-contrast-agents-removal-of-omniscan-and-iv-magnevist-restrictions-to-the-use-of-other-linear-agents.

[40] R. J. McDonald, J. S. McDonald, D. F. Kallmes, M. E. Jentoft, D. L. Murray, K. R. Thielen, E. E. Williamson, and L. J. Eckel, "Intracranial Gadolinium Deposition after Contrast-enhanced MR Imaging," *Radiology*, vol. 275, pp. 772–782, Mar. 2015.

[41] F. G. A. Moore and M. Levental, "The Usefulness of Gadolinium-Enhanced Images on a Follow-up Magnetic Resonance Image in Suspected Multiple Sclerosis," *Canadian Association of Radiologists Journal = Journal l'Association Canadienne Des Radiologistes*, vol. 64, pp. 358–362, Nov. 2013.

[42] H. Wei, O. T. Bruns, M. G. Kaul, E. C. Hansen, M. Barch, A. Wiśniowska, O. Chen, Y. Chen, N. Li, S. Okada, J. M. Cordero, M. Heine, C. T. Farrar, D. M. Montana, G. Adam, H. Ittrich, A. Jasanoff, P. Nielsen, and M. G. Bawendi, "Exceedingly Small Iron Oxide Nanoparticles as Positive MRI Contrast Agents," *Proceedings of the National Academy of Sciences*, vol. 114, pp. 2325–2330, Feb. 2017.

[43] Y.-P. Rui, B. Liang, F. Hu, J. Xu, Y.-F. Peng, P.-H. Yin, Y. Duan, C. Zhang, and H. Gu, "Ultra-Large-Scale Production of Ultrasmall Superparamagnetic Iron Oxide Nanoparticles for T1-Weighted Mri," *RSC Advances*, vol. 6, pp. 22575–22585, Feb. 2016.

[44] H. Zhang, L. Li, X. L. Liu, J. Jiao, C.-T. Ng, J. B. Yi, Y. E. Luo, B.-H. Bay, L. Y. Zhao, M. L. Peng, N. Gu, and H. M. Fan, "Ultrasmall Ferrite Nanoparticles Synthesized via Dynamic Simultaneous Thermal Decomposition for High-Performance and Multifunctional T1 Magnetic Resonance Imaging Contrast Agent," *ACS Nano*, vol. 11, pp. 3614–3631, Apr. 2017.

[45] D. Piché, I. Tavernaro, J. Fleddermann, J. G. Lozano, A. Varambhia, M. L. Maguire, M. Koch, T. Ukai, A. J. Hernández Rodríguez, L. Jones, F. Dillon, I. Reyes Molina, M. Mitzutani, E. R. González Dalmau, T. Maekawa, P. D. Nellist, A. Kraegeloh, and N. Grobert, "Targeted T1 Magnetic Resonance Imaging Contrast Enhancement with Extraordinarily Small CoFe2O4 Nanoparticles," *ACS Applied Materials & Interfaces*, vol. 11, pp. 6724–6740, Feb. 2019.

[46] N. Albiin, "MRI of Focal Liver Lesions," *Current Medical Imaging Reviews*, vol. 8, pp. 107–116, May 2012.

[47] M. J. Monte, J. J. Marin, A. Antelo, and J. Vazquez-Tato, "Bile Acids: Chemistry, Physiology, and Pathophysiology," *World Journal of Gastroenterology : WJG*, vol. 15, pp. 804–816, Feb. 2009.

[48] W. Kramer, G. Wess, G. Schubert, M. Bickel, F. Girbig, U. Gutjahr, S. Kowalewski, K. H. Baringhaus, A. Enhsen, and H. Glombik, "Liver-Specific Drug Targeting by Coupling to Bile Acids," *The Journal of Biological Chemistry*, vol. 267, pp. 18598–18604, Sept. 1992.

[49] Z. Zhang, H. Cai, Z. Liu, and P. Yao, "Effective Enhancement of Hypoglycemic Effect of Insulin by Liver-Targeted Nanoparticles Containing Cholic Acid-Modified Chitosan Derivative," *Molecular Pharmaceutics*, vol. 13, pp. 2433–2442, July 2016.

[50] H.-S. Chong, H. A. Song, S. Lim, K. Macrenaris, X. Ma, H. Lee, P. Bui, and T. Meade, "A Novel Cholic Acid-Based Contrast Enhancement Agent for Targeted MRI," *Bioorganic & Medicinal Chemistry Letters*, vol. 18, pp. 2505–2508, Apr. 2008.

[51] M. Assfalg, E. Gianolio, S. Zanzoni, S. Tomaselli, V. Lo Russo, C. Cabella, L. Ragona, S. Aime, and H. Molinari, "NMR Structural Studies of the Supramolecular Adducts between a Liver Cytosolic Bile Acid Binding Protein and Gadolinium (III)-Chelates Bearing Bile Acids Residues: Molecular Determinants of the Binding of a Hepatospecific Magnetic Resonance Imaging Contrast Agent," *Journal of Medicinal Chemistry*, vol. 50, pp. 5257–5268, Nov. 2007.

[52] E. Amstad, M. Textor, and E. Reimhult, "Stabilization and functionalization of iron oxide nanoparticles for biomedical applications," *Nanoscale*, vol. 3, pp. 2819–2843, July 2011.

[53] J. Volatron, J. Kolosnjaj-Tabi, Y. Javed, Q. L. Vuong, Y. Gossuin, S. Neveu, N. Luciani, M. Hémadi, F. Carn, D. Alloyeau, and F. Gazeau, "Physiological Remediation of Cobalt Ferrite Nanoparticles by Ferritin," *Scientific Reports*, vol. 7, p. 40075, Jan. 2017.

[54] P. P. Fu, Q. Xia, H.-M. Hwang, P. C. Ray, and H. Yu, "Mechanisms of Nanotoxicity: Generation of Reactive Oxygen Species," *Journal of Food and Drug Analysis*, vol. 22, pp. 64–75, Mar. 2014.

[55] F. Finetti, E. Terzuoli, S. Donnini, M. Uva, M. Ziche, and L. Morbidelli, "Monitoring Endothelial and Tissue Responses to Cobalt Ferrite Nanoparticles and Hybrid Hydrogels," *PLOS ONE*, vol. 11, p. e0168727, Dec. 2016.

[56] Y. Xie, D. Liu, C. Cai, X. Chen, Y. Zhou, L. Wu, Y. Sun, H. Dai, X. Kong, and P. Liu, "Size-dependent cytotoxicity of Fe3o4 nanoparticles induced by biphasic regulation of oxidative stress in different human hepatoma cells," *International Journal of Nanomedicine*, vol. 11, pp. 3557–3570, July 2016.

[57] Z. Chu, S. Zhang, B. Zhang, C. Zhang, C.-Y. Fang, I. Rehor, P. Cigler, H.-C. Chang, G. Lin, R. Liu, and Q. Li, "Unambiguous observation of shape effects on cellular fate of nanoparticles," *Scientific Reports*, vol. 4, p. 4495, Mar. 2014.

[58] A. Ivask, T. Titma, M. Visnapuu, H. Vija, A. Kakinen, M. Sihtmae, S. Pokhrel, L. Madler, M. Heinlaan, V. Kisand, R. Shimmo, and A. Kahru, "Toxicity of 11 Metal Oxide Nanoparticles to Three Mammalian Cell Types In Vitro," *Current Topics in Medicinal Chemistry*, vol. 15, no. 18, pp. 1914–1929, 2015.

[59] S. Naqvi, M. Samim, M. Abdin, F. J. Ahmed, A. Maitra, C. Prashant, and A. K. Dinda, "Concentration-dependent toxicity of iron oxide nanoparticles mediated by increased oxidative stress," *International Journal of Nanomedicine*, vol. 5, pp. 983–989, 2010.

[60] B. Kong, J. H. Seog, L. M. Graham, and S. B. Lee, "Experimental considerations on the cytotoxicity of nanoparticles," *Nanomedicine (London, England)*, vol. 6, pp. 929–941, July 2011.

[61] J. Dobson, "Remote control of cellular behaviour with magnetic nanoparticles," *Nature Nanotechnology*, vol. 3, pp. 139–143, Mar. 2008.

[62] D. S. Mathew and R.-S. Juang, "An overview of the structure and magnetism of spinel ferrite nanoparticles and their synthesis in microemulsions," *Chemical Engineering Journal*, vol. 129, pp. 51–65, May 2007.

[63] S. Akbar, S. K. Hasanain, N. Azmat, and M. Nadeem, "Synthesis of Fe2O3 nanoparticles by new Sol-Gel method and their structural and magnetic characterizations," *arXiv:cond-mat/0408480*, Aug. 2004. arXiv: cond-mat/0408480.

[64] S. Rashidi and A. Ataie, "One-Step Synthesis of CoFe2O4 Nano-Particles by Mechanical Alloying," *Advanced Materials Research*, vol. 829, pp. 747–751, Nov. 2013.

[65] T. Hyeon, S. S. Lee, J. Park, Y. Chung, and H. B. Na, "Synthesis of Highly Crystalline and Monodisperse Maghemite Nanocrystallites without a Size-Selection Process," *Journal of the American Chemical Society*, vol. 123, pp. 12798–12801, Dec. 2001.

[66] J. Park, K. An, Y. Hwang, J.-G. Park, H.-J. Noh, J.-Y. Kim, J.-H. Park, N.-M. Hwang, and T. Hyeon, "Ultra-large-scale syntheses of monodisperse nanocrystals," *Nature Materials*, vol. 3, pp. 891–895, Dec. 2004.

[67] S. Sun, H. Zeng, D. B. Robinson, S. Raoux, P. M. Rice, S. X. Wang, and G. Li, "Monodisperse MFe2O4 (m = Fe, Co, Mn) Nanoparticles," *Journal of the American Chemical Society*, vol. 126, pp. 273–279, Jan. 2004.

[68] L. T. Lu, N. T. Dung, L. D. Tung, C. T. Thanh, O. K. Quy, N. V. Chuc, S. Maenosono, and N. T. K. Thanh, "Synthesis of Magnetic Cobalt Ferrite Nanoparticles with Controlled Morphology, Monodispersity and Composition: The Influence of Solvent, Surfactant, Reductant and Synthetic Conditions," *Nanoscale*, vol. 7, pp. 19596–19610, Nov. 2015.

[69] M. Nakaya, R. Nishida, A. Muramatsu, M. Nakaya, R. Nishida, and A. Muramatsu, "Size Control of Magnetite Nanoparticles in Excess Ligands as a Function of Reaction Temperature and Time," *Molecules*, vol. 19, pp. 11395–11403, Aug. 2014.

[70] A. G. Roca, S. Veintemillas-Verdaguer, M. Port, C. Robic, C. J. Serna, and M. P. Morales, "Effect of Nanoparticle and Aggregate Size on the Relaxometric Properties of MR Contrast Agents Based on High Quality Magnetite Nanoparticles," *The Journal of Physical Chemistry B*, vol. 113, pp. 7033–7039, May 2009.

[71] R. A. Harris, P. M. Shumbula, and H. van der Walt, "Analysis of the Interaction of Surfactants Oleic Acid and Oleylamine with Iron Oxide Nanoparticles through Molecular Mechanics Modeling," *Langmuir*, vol. 31, pp. 3934–3943, Apr. 2015.

[72] J. Park, E. Lee, N.-M. Hwang, M. Kang, S. C. Kim, Y. Hwang, J.-G. Park, H.-J. Noh, J.-Y. Kim, J.-H. Park, and T. Hyeon, "One-Nanometer-Scale Size-Controlled Synthesis of Monodisperse Magnetic Iron Oxide Nanoparticles," *Angewandte Chemie International Edition*, vol. 44, pp. 2872–2877, May 2005.

[73] Y. Zhu, F. Y. Jiang, K. Chen, F. Kang, and Z. K. Tang, "Size-Controlled Synthesis of Monodisperse Superparamagnetic Iron Oxide Nanoparticles," *Journal of Alloys and Compounds*, vol. 509, pp. 8549–8553, Aug. 2011.

[74] J. Xie, S. Peng, N. Brower, N. Pourmand, S. X. Wang, and S. Sun, "One-Pot Synthesis of Monodisperse Iron Oxide Nanoparticles for Potential Biomedical Applications," *Pure and Applied Chemistry*, vol. 78, no. 5, pp. 1003–1014, 2006.

[75] Y. Yu, W. Yang, X. Sun, W. Zhu, X.-Z. Li, D. J. Sellmyer, and S. Sun, "Monodisperse MPt (M = Fe, Co, Ni, Cu, Zn) Nanoparticles Prepared from a Facile Oleylamine Reduction of Metal Salts," *Nano Letters*, vol. 14, pp. 2778–2782, May 2014.

[76] V. Georgiadou, C. Kokotidou, B. L. Droumaguet, B. Carbonnier, T. Choli-Papadopoulou, and C. Dendrinou-Samara, "Oleylamine as a Beneficial Agent for the Synthesis of Cofe2o4 Nanoparticles with Potential Biomedical Uses," *Dalton Transactions*, vol. 43, pp. 6377–6388, Apr. 2014.

[77] N. Fauconnier, J. N. Pons, J. Roger, and A. Bee, "Thiolation of Maghemite Nanoparticles by Dimercaptosuccinic Acid," *Journal of Colloid and Interface Science*, vol. 194, pp. 427–433, Oct. 1997.

[78] S. I. C. J. Palma, M. Marciello, A. Carvalho, S. Veintemillas-Verdaguer, M. d. P. Morales, and A. C. A. Roque, "Effects of Phase Transfer Ligands on Monodisperse Iron Oxide Magnetic Nanoparticles," *Journal of Colloid and Interface Science*, vol. 437, pp. 147–155, Jan. 2015.

[79] S. Laurent, D. Forge, M. Port, A. Roch, C. Robic, L. Vander Elst, and R. N. Muller, "Magnetic Iron Oxide Nanoparticles: Synthesis, Stabilization, Vectorization, Physicochemical Characterizations, and Biological Applications," *Chemical Reviews*, vol. 108, pp. 2064–2110, June 2008.

[80] V. K. LaMer and R. H. Dinegar, "Theory, Production and Mechanism of Formation of Monodispersed Hydrosols," *Journal of the American Chemical Society*, vol. 72, pp. 4847–4854, Nov. 1950.

[81] N. T. K. Thanh, N. Maclean, and S. Mahiddine, "Mechanisms of Nucleation and Growth of Nanoparticles in Solution," *Chemical Reviews*, vol. 114, pp. 7610–7630, Aug. 2014.

[82] J. Polte, "Fundamental growth principles of colloidal metal nanoparticles – a new perspective," *CrystEngComm*, vol. 17, no. 36, pp. 6809–6830, 2015.

[83] C. B. Murray, D. J. Norris, and M. G. Bawendi, "Synthesis and characterization of nearly monodisperse CdE (E = sulfur, selenium, tellurium) semiconductor nanocrystallites," *Journal of the American Chemical Society*, vol. 115, pp. 8706–8715, Sept. 1993.

[84] J. Rockenberger, E. C. Scher, and A. P. Alivisatos, "A New Nonhydrolytic Single-Precursor Approach to Surfactant-Capped Nanocrystals of Transition Metal Oxides," *Journal of the American Chemical Society*, vol. 121, pp. 11595–11596, Dec. 1999.

[85] H. Reiss, "The Growth of Uniform Colloidal Dispersions," *The Journal of Chemical Physics*, vol. 19, pp. 482–487, Apr. 1951.

[86] W. Ostwald, "Über die vermeintliche Isomeric des roten und gelben Quecksilberoxyds und die Oberflächenspannung fester Körper," *Zeitschrift fur Physikalische Chemie*, vol. 34, p. 495, 1900.

[87] I. M. Lifshitz and V. V. Slyozov, "The kinetics of precipitation from supersaturated solid solutions," *Journal of Physics and Chemistry of Solids*, vol. 19, pp. 35–50, Apr. 1961.

[88] C. Wagner, "Theorie der Alterung von Niederschlägen durch Umlösen (Ostwald-Reifung)," *Zeitschrift für Elektrochemie, Berichte der Bunsengesellschaft für physikalische Chemie*, vol. 65, pp. 581–591, Sept. 1961.

[89] J. Park, J. Joo, S. G. Kwon, Y. Jang, and T. Hyeon, "Synthesis of Monodisperse Spherical Nanocrystals," *Angewandte Chemie International Edition*, vol. 46, pp. 4630–4660, June 2007.

[90] A. Baldan, "Review Progress in Ostwald ripening theories and their applications to nickel-base superalloys Part I: Ostwald ripening theories," *Journal of Materials Science*, vol. 37, pp. 2171–2202, June 2002.

[91] K. Yoshida, A. Bright, and N. Tanaka, "Direct observation of the initial process of Ostwald ripening using spherical aberration-corrected transmission electron microscopy," *Journal of Electron Microscopy*, vol. 61, pp. 99–103, Apr. 2012.

[92] Y. Bao, W. An, C. H. Turner, and K. M. Krishnan, "The Critical Role of Surfactants in the Growth of Cobalt Nanoparticles," *Langmuir*, vol. 26, pp. 478–483, Jan. 2010.

[93] B. Jia and L. Gao, "Growth of Well-Defined Cubic Hematite Single Crystals: Oriented Aggregation and Ostwald Ripening," *Crystal Growth & Design*, vol. 8, pp. 1372–1376, Apr. 2008.

[94] C. Pacholski, A. Kornowski, and H. Weller, "Self-Assembly of ZnO: From Nanodots to Nanorods," *Angewandte Chemie International Edition*, vol. 41, pp. 1188–1191, Apr. 2002.

[95] J. Lee, J. Yang, S. G. Kwon, and T. Hyeon, "Nonclassical nucleation and growth of inorganic nanoparticles," *Nature Reviews Materials*, vol. 1, p. 16034, Aug. 2016.

[96] P. C. Hiemenz, R. Rajagopalan, and R. Rajagopalan, *Principles of Colloid and Surface Chemistry, Revised and Expanded*. CRC Press, Mar. 1997.

[97] L. G. Benning and G. A. Waychunas, "Nucleation, Growth, and Aggregation of Mineral Phases: Mechanisms and Kinetic Controls," in *Kinetics of Water-Rock Interaction* (S. L. Brantley, J. D. Kubicki, and A. F. White, eds.), pp. 259–333, New York, NY: Springer New York, 2008.

[98] A. G. Roca, M. P. Morales, and C. J. Serna, "Synthesis of Monodispersed Magnetite Particles From Different Organometallic Precursors," *IEEE Transactions on Magnetics*, vol. 42, pp. 3025–3029, Oct. 2006.

[99] A. Lassenberger, T. A. Grünewald, P. D. J. van Oostrum, H. Rennhofer, H. Amenitsch, R. Zirbs, H. C. Lichtenegger, and E. Reimhult, "Monodisperse Iron Oxide Nanoparticles by Thermal Decomposition: Elucidating Particle Formation by Second-Resolved in Situ Small-Angle X-ray Scattering," *Chemistry of Materials*, vol. 29, pp. 4511–4522, May 2017.

[100] P. Guardia, N. Pérez, A. Labarta, and X. Batlle, "Controlled Synthesis of Iron Oxide Nanoparticles over a Wide Size Range," *Langmuir*, vol. 26, pp. 5843–5847, Apr. 2010.

[101] D. Maity, S.-G. Choo, J. Yi, J. Ding, and J. M. Xue, "Synthesis of magnetite nanoparticles via a solvent-free thermal decomposition route," *Journal of Magnetism and Magnetic Materials*, vol. 321, pp. 1256–1259, May 2009.

[102] M. Unni, A. M. Uhl, S. Savliwala, B. H. Savitzky, R. Dhavalikar, N. Garraud, D. P. Arnold, L. F. Kourkoutis, J. S. Andrew, and C. Rinaldi, "Thermal Decomposition Synthesis of Iron Oxide Nanoparticles with Diminished Magnetic Dead Layer by Controlled Addition of Oxygen," *ACS Nano*, vol. 11, pp. 2284–2303, Feb. 2017.

[103] J. Y. Park, P. Daksha, G. H. Lee, S. Woo, and Y. Chang, "Highly water-dispersible PEG surface modified ultra small superparamagnetic iron oxide nanoparticles useful for target-specific biomedical applications," *Nanotechnology*, vol. 19, no. 36, p. 365603, 2008.

[104] F. Hu, K. W. MacRenaris, E. A. Waters, T. Liang, E. A. Schultz-Sikma, A. L. Eckermann, and T. J. Meade, "Ultrasmall, Water-Soluble Magnetite Nanoparticles with High Relaxivity for Magnetic Resonance Imaging," *The Journal of Physical Chemistry C*, vol. 113, pp. 20855–20860, Dec. 2009.

[105] R. Hufschmid, H. Arami, R. M. Ferguson, M. Gonzales, E. Teeman, L. N. Brush, N. D. Browning, and K. M. Krishnan, "Synthesis of phase-pure and monodisperse iron oxide nanoparticles by thermal decomposition," *Nanoscale*, vol. 7, pp. 11142–11154, June 2015.

[106] C. M. Phan and H. M. Nguyen, "Role of Capping Agent in Wet Synthesis of Nanoparticles," *The Journal of Physical Chemistry A*, vol. 121, pp. 3213–3219, May 2017.

[107] B. Derjaguin and L. Landau, "Theory of the stability of strongly charged lyophobic sols and of the adhesion of strongly charged particles in solutions of electrolytes," *Progress in Surface Science*, vol. 43, pp. 30–59, May 1993.

[108] E. J. W. Verwey, J. T. G. Overbeek, and J. T. G. Overbeek, *Theory of the Stability of Lyophobic Colloids*. Courier Corporation, 1999.

[109] W. S. Seo, J. H. Shim, S. J. Oh, E. K. Lee, N. H. Hur, and J. T. Park, "Phase- and Size-Controlled Synthesis of Hexagonal and Cubic CoO Nanocrystals," *Journal of the American Chemical Society*, vol. 127, pp. 6188–6189, May 2005.

[110] S. Mourdikoudis and L. M. Liz-Marzán, "Oleylamine in Nanoparticle Synthesis," *Chemistry of Materials*, vol. 25, pp. 1465–1476, May 2013.

[111] K.-S. Mandel, *Wet Chemical Synthesis of Transition Metal Nanoparticles for Carbon Nanotube Growth*. PhD thesis, University of Oxford; University of Saarbrucken, Sept. 2010. Unpublished.

[112] D. B. Williams and C. B. Carter, *Transmission Electron Microscopy: A Textbook for Materials Science*. Springer Science & Business Media, July 2009.

[113] H. Borchert, E. V. Shevchenko, A. Robert, I. Mekis, A. Kornowski, G. Grübel, and H. Weller, "Determination of Nanocrystal Sizes: A Comparison of TEM, SAXS, and XRD Studies of Highly Monodisperse CoPt3 Particles," *Langmuir*, vol. 21, pp. 1931–1936, Mar. 2005.

[114] T. J. Yoon, H. Lee, H. Shao, and R. Weissleder, "Highly magnetic core-shell nanoparticles with a unique magnetization mechanism.," *Angewandte Chemie (International ed. in English)*, vol. 50, pp. 4663–4666, May 2011.

[115] Z. Xu, C. Shen, Y. Hou, H. Gao, and S. Sun, "Oleylamine as Both Reducing Agent and Stabilizer in a Facile Synthesis of Magnetite Nanoparticles," *Chemistry of Materials*, vol. 21, pp. 1778–1780, May 2009.

[116] I. Galarreta, M. Insausti, I. Gil de Muro, I. Ruiz de Larramendi, and L. Lezama, "Exploring Reaction Conditions to Improve the Magnetic Response of Cobalt-Doped Ferrite Nanoparticles," *Nanomaterials*, vol. 8, p. 63, Jan. 2018.

[117] K. Mandel, F. Dillon, A. A. Koos, Z. Aslam, F. Cullen, H. Bishop, A. Crossley, and N. Grobert, "Customised transition metal oxide nanoparticles for the controlled production of carbon nanostructures," *RSC Advances*, vol. 2, pp. 3748–3752, Apr. 2012.

[118] M. A. Ramos-Docampo, B. Rivas-Murias, B. Rodríguez-González, and V. Salgueiriño, "Thermodynamically driven oxidation-induced Kirkendall effect in octahedron-shaped cobalt oxide nanocrystals," *CrystEngComm*, vol. 19, pp. 5542–5548, Sept. 2017.

[119] K. M. Nam, W. S. Seo, H. Song, and J. T. Park, "Non-native transition metal monoxide nanostructures: unique physicochemical properties and phase transformations of CoO, MnO and ZnO," *NPG Asia Materials*, vol. 9, p. e364, Mar. 2017.

[120] J. G. Railsback, A. C. Johnston-Peck, J. Wang, and J. B. Tracy, "Size-Dependent Nanoscale Kirkendall Effect During the Oxidation of Nickel Nanoparticles," Apr. 2010.

[121] D.-H. Ha, L. M. Moreau, S. Honrao, R. G. Hennig, and R. D. Robinson, "The Oxidation of Cobalt Nanoparticles into Kirkendall-Hollowed CoO and Co3o4: The Diffusion Mechanisms and Atomic Structural Transformations," *The Journal of Physical Chemistry C*, vol. 117, pp. 14303–14312, July 2013.

[122] M. Mohapatra and S. Anand, "Synthesis and Applications of Nano-Structured Iron Oxides/Hydroxides – a Review," *International Journal of Engineering, Science and Technology*, vol. 2, Jan. 2010.

[123] C. B. De Boer, T. A. T. Mullender, and M. J. Dekkers, "Low-temperature behaviour of haematite: susceptibility and magnetization increase on cycling through the Morin transition," *Geophysical Journal International*, vol. 146, pp. 201–216, July 2001.

[124] R. M. Cornell and U. Schwertmann, *The Iron Oxides: Structure, Properties, Reactions, Occurrences and Uses*. John Wiley & Sons, Dec. 2006.

[125] D. Faivre, *Iron Oxides: From Nature to Applications*. John Wiley & Sons, Apr. 2016.

[126] J. Pedrosa, B. F. O. Costa, A. Portugal, and L. Duraes, "Controlled Phase Formation of Nanocrystalline Iron Oxides/Hydroxides in Solution – an Insight on the Phase Transformation Mechanisms," *Materials Chemistry and Physics*, vol. 163, pp. 88–98, Aug. 2015.

[127] C. Colliex, T. Manoubi, and C. Ortiz, "Electron-Energy-Loss-Spectroscopy Near-Edge Fine Structures in the Iron-Oxygen System," *Physical Review B*, vol. 44, pp. 11402–11411, Nov. 1991.

[128] H. K. Schmid and W. Mader, "Oxidation States of Mn and Fe in Various Compound Oxide Systems," *Micron*, vol. 37, pp. 426–432, July 2006.

[129] J. Santoyo Salazar, L. Perez, O. de Abril, L. Truong Phuoc, D. Ihiawakrim, M. Vazquez, J.-M. Greneche, S. Begin-Colin, and G. Pourroy, "Magnetic Iron Oxide Nanoparticles in 10-40 nm Range: Composition in Terms of Magnetite/Maghemite Ratio and Effect on the Magnetic Properties," *Chemistry of Materials*, vol. 23, pp. 1379–1386, Mar. 2011.

[130] R. Frison, G. Cernuto, A. Cervellino, O. Zaharko, G. M. Colonna, A. Guagliardi, and N. Masciocchi, "Magnetite–Maghemite Nanoparticles in the 5–15 nm Range: Correlating the Core–Shell Composition and the Surface Structure to the Magnetic Properties. A Total Scattering Study.," *Chemistry of Materials*, vol. 25, pp. 4820–4827, Dec. 2013.

[131] L. Signorini, L. Pasquini, L. Savini, R. Carboni, F. Boscherini, E. Bonetti, A. Giglia, M. Pedio, N. Mahne, and S. Nannarone, "Size-dependent oxidation in iron/iron oxide core-shell nanoparticles," *Physical Review B*, vol. 68, p. 195423, Nov. 2003.

[132] A. Goldman, "Crystal Structure of Ferrites," in *Handbook of Modern Ferromagnetic Materials* (A. Goldman, ed.), The Springer International Series in Engineering and Computer Science, pp. 207–227, Boston, MA: Springer US, 1999.

[133] S. C. Petitto, E. M. Marsh, G. A. Carson, and M. A. Langell, "Cobalt oxide surface chemistry: The interaction of CoO(100), Co3O4(110) and Co3O4(111) with oxygen and water," *Selected Papers from the Proceedings of the 4th San Luis Pan-American Conference on the Study of Surfaces, Interfaces and Catalysis*, vol. 281, pp. 49–58, Feb. 2008.

[134] T. Tatarchuk, M. Bououdina, J. Judith Vijaya, and L. John Kennedy, "Spinel Ferrite Nanoparticles: Synthesis, Crystal Structure, Properties, and Perspective Applications," in *Nanophysics, Nanomaterials, Interface Studies, and Applications* (O. Fesenko and L. Yatsenko, eds.), Springer Proceedings in Physics, pp. 305–325, Springer International Publishing, 2017.

[135] K. K. Kefeni, T. A. M. Msagati, and B. B. Mamba, "Ferrite nanoparticles: Synthesis, characterisation and applications in electronic device," *Materials Science and Engineering: B*, vol. 215, pp. 37–55, Jan. 2017.

[136] G. v. d. Laan, "Microscopic origin of magnetocrystalline anisotropy in transition metal thin films," *Journal of Physics: Condensed Matter*, vol. 10, no. 14, p. 3239, 1998.

[137] M. Nath, "Multifunctional Magnetic Nanomaterials for Diverse Applications," in *Nanotechnology: Delivering on the Promise Volume 2*, vol. 1224 of *ACS Symposium Series*, pp. 139–166, American Chemical Society, Jan. 2016.

[138] F. Stacey, *The Physical Principles of Rock Magnetism*. Elsevier, Dec. 2012.

[139] C. J. Goss, "Saturation magnetisation, coercivity and lattice parameter changes in the system Fe3o4-yFe2o3, and their relationship to structure," *Physics and Chemistry of Minerals*, vol. 16, pp. 164–171, Nov. 1988.

[140] V. A. M. Brabers, "Chapter 3 Progress in spinel ferrite research," in *Handbook of Magnetic Materials*, vol. 8, pp. 189–324, Elsevier, Jan. 1995.

[141] M. Goodarz Naseri, E. B. Saion, and A. Kamali, "An Overview on Nanocrystalline ZnFe2o4, MnFe2o4, and CoFe2o4 Synthesized by a Thermal Treatment Method," 2012.

[142] V. S. Coker, N. D. Telling, G. van der Laan, R. A. D. Pattrick, C. I. Pearce, E. Arenholz, F. Tuna, R. E. P. Winpenny, and J. R. Lloyd, "Harnessing the extracellular bacterial production of nanoscale cobalt ferrite with exploitable magnetic properties," *ACS nano*, vol. 3, pp. 1922–1928, July 2009.

[143] N. S. Gajbhiye, G. Balaji, and M. Ghafari, "Magnetic Properties of Nanostructured MnFe2o4 Synthesized by Precursor Technique," *physica status solidi (a)*, vol. 189, pp. 357–361, Feb. 2002.

[144] X. Zuo, A. Yang, S.-D. Yoon, J. A. Christodoulides, V. G. Harris, and C. Vittoria, "Large induced magnetic anisotropy in manganese spinel ferrite films," *Applied Physics Letters*, vol. 87, p. 152505, Oct. 2005.

[145] R. Saravanan, *Ferrite Materials for Memory Applications*. Materials Research Forum LLC, Nov. 2017.

[146] A. S. Teja and P.-Y. Koh, "Synthesis, properties, and applications of magnetic iron oxide nanoparticles," *Progress in Crystal Growth and Characterization of Materials*, vol. 55, pp. 22–45, Mar. 2009.

[147] M. Tachiki, "Origin of the Magnetic Anisotropy Energy of Cobalt Ferrite," *Progress of Theoretical Physics*, vol. 23, pp. 1055–1072, June 1960.

[148] L. Martín-García, G. Chen, Y. Montaña, A. Mascaraque, B. M. Pabón, A. K. Schmid, and J. d. l. Figuera, "Memory effect and magnetocrystalline anisotropy impact on the surface magnetic domains of magnetite(001)," *Scientific Reports*, vol. 8, p. 5991, Apr. 2018.

[149] G. Baldi, D. Bonacchi, C. Innocenti, G. Lorenzi, and C. Sangregorio, "Cobalt ferrite nanoparticles: The control of the particle size and surface state and their effects on magnetic properties," *Journal of Magnetism and Magnetic Materials*, vol. 311, pp. 10–16, Apr. 2007.

[150] C. L. Dennis and R. Ivkov, "Physics of heat generation using magnetic nanoparticles for hyperthermia," *International Journal of Hyperthermia*, vol. 29, pp. 715–729, Dec. 2013.

[151] D. L. Leslie-Pelecky and R. D. Rieke, "Magnetic Properties of Nanostructured Materials," *Chemistry of Materials*, vol. 8, pp. 1770–1783, Jan. 1996.

[152] T. Q. Bui, S. N.-C. Ton, A. T. Duong, and H. T. Tran, "Size-dependent magnetic responsiveness of magnetite nanoparticles synthesised by co-precipitation and solvothermal methods," *Journal of Science: Advanced Materials and Devices*, vol. 3, pp. 107–112, Mar. 2018.

[153] K. Maaz, A. Mumtaz, S. K. Hasanain, and A. Ceylan, "Synthesis and Magnetic Properties of Cobalt Ferrite (CoFe2O4) Nanoparticles Prepared by Wet Chemical Route," *Journal of Magnetism and Magnetic Materials*, vol. 308, pp. 289–295, Jan. 2007.

[154] K. Woo, J. Hong, S. Choi, H.-W. Lee, J.-P. Ahn, C. S. Kim, and S. W. Lee, "Easy Synthesis and Magnetic Properties of Iron Oxide Nanoparticles," *Chemistry of Materials*, vol. 16, pp. 2814–2818, July 2004.

[155] T. Iwasaki, N. Mizutani, S. Watano, T. Yanagida, and T. Kawai, "Size control of magnetite nanoparticles by organic solvent-free chemical coprecipitation at room temperature," *Journal of Experimental Nanoscience*, vol. 5, pp. 251–262, June 2010.

[156] S. Mørup, E. Brok, and C. Frandsen, "Spin Structures in Magnetic Nanoparticles," *Journal of Nanomaterials*, 2013.

[157] J. M. D. Coey, "Noncollinear Spin Arrangement in Ultrafine Ferrimagnetic Crystallites," *Physical Review Letters*, vol. 27, pp. 1140–1142, Oct. 1971.

[158] D. Peddis, N. Yaacoub, M. Ferretti, A. Martinelli, G. Piccaluga, A. Musinu, C. Cannas, G. Navarra, J. M. Greneche, and D Fiorani, "Cationic distribution and spin canting in CoFe 2 O 4 nanoparticles," *Journal of Physics: Condensed Matter*, vol. 23, no. 42, p. 426004, 2011.

[159] M. P. Morales, S. Veintemillas-Verdaguer, M. I. Montero, C. J. Serna, A. Roig, L. Casas, B. Martínez, and F. Sandiumenge, "Surface and Internal Spin Canting in y-Fe2o3 Nanoparticles," *Chemistry of Materials*, vol. 11, pp. 3058–3064, Nov. 1999.

[160] W. Baaziz, B. P. Pichon, S. Fleutot, Y. Liu, C. Lefevre, J.-M. Greneche, M. Toumi, T. Mhiri, and S. Begin-Colin, "Magnetic Iron Oxide Nanoparticles: Reproducible Tuning of the Size and Nanosized-Dependent Composition, Defects, and Spin Canting," *The Journal of Physical Chemistry C*, vol. 118, pp. 3795–3810, Feb. 2014.

[161] H. Nukala, "Quantitative Thickness Mapping In High-angle Annular Dark-field (haadf) Scanning Transmission Electron Microscopy (stem)," *Electronic Theses and Dissertations*, Jan. 2008.

[162] S. J. Pennycook and P. D. Nellist, eds., *Scanning Transmission Electron Microscopy: Imaging and Analysis*. New York: Springer-Verlag, 2011.

[163] D. H. Anjum, "Characterization of nanomaterials with transmission electron microscopy," *IOP Conference Series: Materials Science and Engineering*, vol. 146, no. 1, p. 012001, 2016.

[164] D. R. G. Mitchell, "Contamination mitigation strategies for scanning transmission electron microscopy," *Micron*, vol. 73, pp. 36–46, June 2015.

[165] L. Jones, H. Yang, T. J. Pennycook, M. S. J. Marshall, S. Van Aert, N. D. Browning, M. R. Castell, and P. D. Nellist, "Smart Align—a New Tool for Robust Non-Rigid Registration of Scanning Microscope Data," *Advanced Structural and Chemical Imaging*, vol. 1, p. 8, July 2015.

[166] R. F. Egerton, *Electron Energy-Loss Spectroscopy in the Electron Microscope*. Springer Science & Business Media, July 2011.

[167] F. Hofer, F. P. Schmidt, W. Grogger, and G. Kothleitner, "Fundamentals of electron energy-loss spectroscopy," *IOP Conference Series: Materials Science and Engineering*, vol. 109, no. 1, p. 012007, 2016.

[168] R. D. Leapman, L. A. Grunes, and P. L. Fejes, "Study of the ${L}_{23}$ edges in the $3d$ transition metals and their oxides by electron-energy-loss spectroscopy with comparisons to theory," *Physical Review B*, vol. 26, pp. 614–635, July 1982.

[169] P. Rez, "Cross-Sections for Energy Loss Spectrometry," *Ultramicroscopy*, vol. 9, no. 3, pp. 283–287, 1982.

[170] Young-Min Kim, J.-M. Jeong, J.-G. Kim, and Y.-J. Kim, "Image processing of atomic resolution transmission electron microscope images," *Journal of the Korean Physical Society*, vol. 48, pp. 250–255, Feb. 2006.

[171] R. Kleiner, D. Koelle, F. Ludwig, and J. Clarke, "Superconducting quantum interference devices: State of the art and applications," *Proceedings of the IEEE*, vol. 92, pp. 1534–1548, Oct. 2004.

[172] R. L. Fagaly, "Superconducting quantum interference device instruments and applications," *Review of Scientific Instruments*, vol. 77, p. 101101, Oct. 2006.

[173] *Quantum Design MPMS3 Magnetic Property Measurement System*. https://qd-uki.co.uk/product/magnetometers.

[174] L. Angeloni, D. Passeri, S. Corsetti, D. Peddis, D. Mantovani, and M. Rossi, "Single nanoparticles magnetization curves by controlled tip magnetization magnetic force microscopy," *Nanoscale*, vol. 9, pp. 18000–18011, Nov. 2017.

[175] C. Granata and A. Vettoliere, "Nano Superconducting Quantum Interference device: A powerful tool for nanoscale investigations," *Physics Reports*, vol. 614, pp. 1–69, Feb. 2016.

[176] M. F. Hansen and S. Mørup, "Estimation of blocking temperatures from ZFC/FC curves," *Journal of Magnetism and Magnetic Materials*, vol. 203, pp. 214–216, Aug. 1999.

[177] M. Birkholz, *Thin Film Analysis by X-Ray Scattering*. John Wiley & Sons, May 2006.

[178] R. Sharma, D. P. Bisen, U. Shukla, and B. G. Sharma, "X-ray diffraction: a powerful method of characterizing nanomaterials," *Recent Research in Science and Technology*, Oct. 2012.

[179] U. Holzwarth and N. Gibson, "The Scherrer equation versus the 'Debye-Scherrer equation'," *Nature Nanotechnology*, vol. 6, p. 534, Sept. 2011.

[180] T. P. Almeida, T. Kasama, A. R. Muxworthy, W. Williams, L. Nagy, T. W. Hansen, P. D. Brown, and R. E. Dunin-Borkowski, "Visualized Effect of Oxidation on Magnetic Recording Fidelity in Pseudo-Single-Domain Magnetite Particles," *Nature Communications*, vol. 5, p. 5154, Oct. 2014.

[181] Q. Li, C. W. Kartikowati, S. Horie, T. Ogi, T. Iwaki, and K. Okuyama, "Correlation between particle size/domain structure and magnetic properties of highly crystalline Fe 3 O 4 nanoparticles," *Scientific Reports*, vol. 7, p. 9894, Aug. 2017.

[182] O. Nedelko and A. Ślawska Waniewska, "Role of the Surface Anisotropy in Magnetization Reversal of a Spherical Nanoparticle," *Physica Scripta*, vol. 2005, no. T118, p. 261, 2005.

[183] D. A. Dimitrov and G. M. Wysin, "Effects of surface anisotropy on hysteresis in fine magnetic particles," *Physical Review. B, Condensed Matter*, vol. 50, pp. 3077–3084, Aug. 1994.

[184] S. Oyarzún, A. Tamion, F. Tournus, V. Dupuis, and M. Hillenkamp, "Size effects in the magnetic anisotropy of embedded cobalt nanoparticles: from shape to surface," *Scientific Reports*, vol. 5, p. 14749, Oct. 2015.

[185] D. Peddis, M. V. Mansilla, S. Morup, C. Cannas, A. Musinu, G. Piccaluga, F. D'Orazio, F. Lucari, and D. Fiorani, "Spin-Canting and Magnetic Anisotropy in Ultrasmall CoFe2o4 Nanoparticles," *The Journal of Physical Chemistry B*, vol. 112, pp. 8507–8513, July 2008.

[186] J. W. M. Bulte and M. M. J. Modo, *Design and Applications of Nanoparticles in Biomedical Imaging*. Springer, Nov. 2016.

[187] S. Mornet, S. Vasseur, F. Grasset, and E. Duguet, "Magnetic nanoparticle design for medical diagnosis and therapy," *Journal of Materials Chemistry*, vol. 14, pp. 2161–2175, July 2004.

[188] E. Blanco, H. Shen, and M. Ferrari, "Principles of nanoparticle design for overcoming biological barriers to drug delivery," *Nature biotechnology*, vol. 33, pp. 941–951, Sept. 2015.

[189] Y. Liu, H. Zhu, H. Hong, W. Wang, and F. Liu, "Can zinc protect cells from the cytotoxic effects of cobalt ions and nanoparticles derived from metal-on-metal joint arthroplasties?," *Bone & Joint Research*, vol. 6, pp. 649–655, Dec. 2017.

[190] L. Gu, R. H. Fang, M. J. Sailor, and J.-H. Park, "In Vivo Clearance and Toxicity of Monodisperse Iron Oxide Nanocrystals," *ACS nano*, vol. 6, pp. 4947–4954, June 2012.

[191] U. Sakulkhu, M. Mahmoudi, L. Maurizi, G. Coullerez, M. Hofmann-Amtenbrink, M. Vries, M. Motazacker, F. Rezaee, and H. Hofmann, "Significance of surface charge and shell material of superparamagnetic iron oxide nanoparticle (SPION) based core/shell nanoparticles on the composition of the protein corona," *Biomaterials Science*, vol. 3, pp. 265–278, Jan. 2015.

[192] L. A. Lane, X. Qian, A. M. Smith, and S. Nie, "Physical Chemistry of Nanomedicine: Understanding the Complex Behaviors of Nanoparticles in Vivo," *Annual Review of Physical Chemistry*, vol. 66, no. 1, pp. 521–547, 2015.

[193] A. Verma and F. Stellacci, "Effect of surface properties on nanoparticle-cell interactions," *Small (Weinheim an Der Bergstrasse, Germany)*, vol. 6, pp. 12–21, Jan. 2010.

[194] A. J. Cole, A. E. David, J. Wang, C. J. Galbán, H. L. Hill, and V. C. Yang, "Polyethylene glycol modified, cross-linked starch-coated iron oxide nanoparticles for enhanced magnetic tumor targeting," *Biomaterials*, vol. 32, pp. 2183–2193, Mar. 2011.

[195] N. Hoshyar, S. Gray, H. Han, and G. Bao, "The effect of nanoparticle size on in vivo pharmacokinetics and cellular interaction," *Nanomedicine*, vol. 11, pp. 673–692, Mar. 2016.

[196] G. Stepien, M. Moros, M. Pérez-Hernández, M. Monge, L. Gutiérrez, R. M. Fratila, M. d. Las Heras, S. Menao Guillén, J. J. Puente Lanzarote, C. Solans, J. Pardo, and J. M. de la Fuente, "Effect of Surface Chemistry and Associated Protein Corona on the Long-Term Biodegradation of Iron Oxide Nanoparticles In Vivo," *ACS applied materials & interfaces*, vol. 10, pp. 4548–4560, Feb. 2018.

[197] J. Tan, S. Shah, A. Thomas, H. D. Ou-Yang, and Y. Liu, "The influence of size, shape and vessel geometry on nanoparticle distribution," *Microfluidics and nanofluidics*, vol. 14, pp. 77–87, Jan. 2013.

[198] G. Fullstone, J. Wood, M. Holcombe, and G. Battaglia, "Modelling the Transport of Nanoparticles under Blood Flow using an Agent-based Approach," *Scientific Reports*, vol. 5, p. 10649, June 2015.

[199] R. Toy, P. M. Peiris, K. B. Ghaghada, and E. Karathanasis, "Shaping cancer nanomedicine: The effect of particle shape on the in vivo journey of nanoparticles," *Nanomedicine (London, England)*, vol. 9, pp. 121–134, Jan. 2014.

[200] D. F. Moyano, M. Goldsmith, D. J. Solfiell, D. Landesman-Milo, O. R. Miranda, D. Peer, and V. M. Rotello, "Nanoparticle Hydrophobicity Dictates Immune Response," *Journal of the American Chemical Society*, vol. 134, pp. 3965–3967, Mar. 2012.

[201] R. Singh and J. W. Lillard, "Nanoparticle-based targeted drug delivery," *Experimental and molecular pathology*, vol. 86, pp. 215–223, June 2009.

[202] L. Bu, J. Xie, K. Chen, J. Huang, Z. P. Aguilar, A. Wang, K. W. Sun, M.-S. Chua, S. So, Z. Cheng, H. S. Eden, B. Shen, and X. Chen, "Assessment and comparison of magnetic nanoparticles as MRI contrast agents in a rodent model of human hepatocellular carcinoma," *Contrast Media & Molecular Imaging*, vol. 7, pp. 363–372, July 2012.

[203] E. D. Smolensky, H.-Y. E. Park, T. S. Berquó, and V. C. Pierre, "Surface functionalization of magnetic iron oxide nanoparticles for MRI applications - effect of anchoring group and ligand exchange protocol," *Contrast Media & Molecular Imaging*, vol. 6, pp. 189–199, Aug. 2011.

[204] Y.-W. Jun, Y.-M. Huh, J.-S. Choi, J.-H. Lee, H.-T. Song, S. Yoon, K.-S. Kim, J.-S. Shin, J.-S. Suh, and J. Cheon, "Nanoscale Size Effect of Magnetic Nanocrystals and Their Utilization for Cancer Diagnosis via Magnetic Resonance Imaging," *Journal of the American Chemical Society*, vol. 127, pp. 5732–5733, Apr. 2005.

[205] M. Galli, A. Guerrini, S. Cauteruccio, P. Thakare, D. Dova, F. Orsini, P. Arosio, C. Carrara, C. Sangregorio, A. Lascialfari, D. Maggioni, and E. Licandro, "Superparamagnetic iron oxide nanoparticles functionalized by peptide nucleic acids," *RSC Advances*, vol. 7, pp. 15500–15512, Mar. 2017.

[206] V. Kalidasan, X. L. Liu, T. S. Herng, Y. Yang, and J. Ding, "Bovine Serum Albumin-Conjugated Ferrimagnetic Iron Oxide Nanoparticles to Enhance the Biocompatibility and Magnetic Hyperthermia Performance," *Nano-Micro Letters*, vol. 8, pp. 80–93, Jan. 2016.

[207] A. Aires, S. M. Ocampo, D. Cabrera, L. d. l. Cueva, G. Salas, F. J. Teran, and A. L. Cortajarena, "BSA-coated magnetic nanoparticles for improved therapeutic properties," *Journal of Materials Chemistry B*, vol. 3, pp. 6239–6247, July 2015.

[208] B. X. Huang, H.-Y. Kim, and C. Dass, "Probing three-dimensional structure of bovine serum albumin by chemical cross-linking and mass spectrometry," *Journal of the American Society for Mass Spectrometry*, vol. 15, pp. 1237–1247, Aug. 2004.

[209] A. Elster, *Paramagnetic relaxation.* http://mriquestions.com/paramagnetic-relaxation.html.

[210] M. Jansch, P. Stumpf, C. Graf, E. Rühl, and R. H. Müller, "Adsorption kinetics of plasma proteins on ultrasmall superparamagnetic iron oxide (USPIO) nanoparticles," *International Journal of Pharmaceutics*, vol. 428, pp. 125–133, May 2012.

[211] B. Samanta, H. Yan, N. O. Fischer, J. Shi, D. J. Jerry, and V. M. Rotello, "Protein-passivated Fe3o4 nanoparticles: low toxicity and rapid heating for thermal therapy," *Journal of materials chemistry*, vol. 18, no. 11, pp. 1204–1208, 2008.

[212] J. Stetefeld, S. A. McKenna, and T. R. Patel, "Dynamic light scattering: a practical guide and applications in biomedical sciences," *Biophysical Reviews*, vol. 8, pp. 409–427, Oct. 2016.

[213] J. Lim, S. P. Yeap, H. X. Che, and S. C. Low, "Characterization of magnetic nanoparticle by dynamic light scattering," *Nanoscale Research Letters*, vol. 8, p. 381, Sept. 2013.

[214] E. M. Claesson, *Magnetic core-shell silica particles*. Dissertation, June 2007. http://dspace.library.uu.nl/handle/1874/21523.

[215] *Refractive index of Fe3O4 (Iron(II,III) oxide, Magnetite)*. https://refractiveindex.info/?shelf=main&book=Fe3O4&page=Querry.

[216] L. Blaney, *Magnetite (Fe3O4): Properties, Synthesis, and Applications*, 2007. https://preserve.lehigh.edu/cas-lehighreview-vol-15/5.

[217] T. Pradeep, *A Textbook of Nanoscience and Nanotechnology*. Tata McGraw-Hill Education, 2003.

[218] S. Bhattacharjee, "DLS and zeta potential – What they are and what they are not?," *Journal of Controlled Release*, vol. 235, pp. 337–351, Aug. 2016.

[219] R. J. Anderson, D. J. Bendell, and P. W. Groundwater, *Organic Spectroscopic Analysis*. Royal Society of Chemistry, 2004.

[220] B. C. Smith, *Fundamentals of Fourier Transform Infrared Spectroscopy*. CRC Press, Mar. 2011.

[221] H. A. Saroff, N. R. Rosenthal, E. R. Adamik, N. Hages, and H. A. Scheraga, "The Methylation of Bovine Serum Albumin," *Journal of Biological Chemistry*, vol. 205, pp. 255–270, Nov. 1953.

[222] T. Topala, A. Bodoki, L. Oprean, and R. Oprean, "Bovine Serum Albumin Interactions with Metal Complexes," *Clujul Medical*, vol. 87, no. 4, pp. 215–219, 2014.

[223] G. E. Shears, D. A. Ledward, and R. J. Neale, "Iron complexation to carboxyl groups in a bovine serum albumin digest," *International Journal of Food Science & Technology*, vol. 22, pp. 265–272, June 1987.

[224] Q. Yang, J. Liang, and H. Han, "Probing the interaction of magnetic iron oxide nanoparticles with bovine serum albumin by spectroscopic techniques," *The Journal of Physical Chemistry. B*, vol. 113, pp. 10454–10458, July 2009.

[225] H. T. M. Phan, S. Bartelt-Hunt, K. B. Rodenhausen, M. Schubert, and J. C. Bartz, "Investigation of Bovine Serum Albumin (BSA) Attachment onto Self-Assembled Monolayers (SAMs) Using Combinatorial Quartz Crystal Microbalance with Dissipation (QCM-D) and Spectroscopic Ellipsometry (SE)," *PLoS ONE*, vol. 10, Oct. 2015.

[226] S. Chatterjee and T. K. Mukherjee, "Spectroscopic investigation of interaction between bovine serum albumin and amine-functionalized silicon quantum dots," *Physical Chemistry Chemical Physics*, vol. 16, pp. 8400–8408, Apr. 2014.

[227] H. P. Erickson, "Size and Shape of Protein Molecules at the Nanometer Level Determined by Sedimentation, Gel Filtration, and Electron Microscopy," *Biological Procedures Online*, vol. 11, pp. 32–51, May 2009.

[228] W. Minor, *Serum albumin structure 2*. https://images.nigms.nih.gov/Pages/DetailPage.aspx?imageID2=3745.

[229] Z. P. Chen, Y. Zhang, S. Zhang, J. G. Xia, J. W. Liu, K. Xu, and N. Gu, "Preparation and Characterization of Water-Soluble Monodisperse Magnetic Iron Oxide Nanoparticles Via Surface Double-Exchange with Dmsa," *Colloids and Surfaces A: Physicochemical and Engineering Aspects*, vol. 316, pp. 210–216, Mar. 2008.

[230] Z. P. Chen, Y. Zhang, K. Xu, R. Z. Xu, J. W. Liu, and N. Gu, "Stability of Hydrophilic Magnetic Nanoparticles Under Biologically Relevant Conditions," *Journal of Nanoscience and Nanotechnology*, vol. 8, pp. 6260–6265, Dec. 2008.

[231] S. Dominguez-Medina, L. Kisley, L. J. Tauzin, A. Hoggard, B. Shuang, A. S. D. S. Indrasekara, S. Chen, L.-Y. Wang, P. J. Derry, A. Liopo, E. R. Zubarev, C. F. Landes, and S. Link, "Adsorption and Unfolding of a Single Protein Triggers Nanoparticle Aggregation," *ACS Nano*, vol. 10, pp. 2103–2112, Feb. 2016.

[232] J. Lacava, P. Born, and T. Kraus, "Nanoparticle Clusters with Lennard-Jones Geometries," *Nano Letters*, vol. 12, pp. 3279–3282, June 2012.

[233] V. Vetri, M. D'Amico, V. Foderà, M. Leone, A. Ponzoni, G. Sberveglieri, and V. Militello, "Bovine Serum Albumin protofibril-like aggregates formation: Solo but not simple mechanism," *Archives of Biochemistry and Biophysics*, vol. 508, pp. 13–24, Apr. 2011.

[234] T. E. Finn, A. C. Nunez, M. Sunde, and S. B. Easterbrook-Smith, "Serum Albumin Prevents Protein Aggregation and Amyloid Formation and Retains Chaperone-like Activity in the Presence of Physiological Ligands," *The Journal of Biological Chemistry*, vol. 287, pp. 21530–21540, June 2012.

[235] P. Sarangapani, S. Hudson, R. Jones, J. Douglas, and J. Pathak, "Critical Examination of the Colloidal Particle Model of Globular Proteins," *Biophysical Journal*, vol. 108, pp. 724–737, Feb. 2015.

[236] A. Michnik, K. Michalik, and Z. Drzazga, "Stability of bovine serum albumin at different pH," *Journal of Thermal Analysis and Calorimetry*, vol. 80, pp. 399–406, May 2005.

[237] M. Mikhaylova, D. K. Kim, C. C. Berry, A. Zagorodni, M. Toprak, A. S. G. Curtis, and M. Muhammed, "BSA Immobilization on Amine-Functionalized Superparamagnetic Iron Oxide Nanoparticles," *Chemistry of Materials*, vol. 16, pp. 2344–2354, June 2004.

[238] J. Garcia-Otero, M. Porto, J. Rivas, and A. Bunde, "Influence of dipolar interaction on magnetic properties of ultrafine ferromagnetic particles," *Physical Review Letters*, vol. 84, pp. 167–170, Jan. 2000.

[239] A. Repko, J. Vejpravová, T. Vacková, D. Zákutná, and D. Nižňanský, "Oleate-based hydrothermal preparation of CoFe2o4 nanoparticles, and their magnetic properties with respect to particle size and surface coating," *Journal of Magnetism and Magnetic Materials*, vol. 390, pp. 142–151, Sept. 2015.

[240] V. N. Nikiforov, A. N. Ignatenko, and V. Y. Irhin, "Magnetism of magnetite nanoparticles: Effects of finite size and coating," *Bulletin of the Russian Academy of Sciences: Physics*, vol. 78, pp. 1081–1085, Oct. 2014.

[241] M. Qi, K. Zhang, S. Li, J. Wu, C. Pham-Huy, X. Diao, D. Xiao, and H. He, "Superparamagnetic Fe 3 O 4 Nanoparticles: Synthesis by a Solvothermal Process and Functionalization for a Magnetic Targeted Curcumin Delivery System," *New Journal of Chemistry*, vol. 40, no. 5, pp. 4480–4491, 2016.

[242] M. Kumar, G. Singh, V. Arora, S. Mewar, U. Sharma, N. R. Jagannathan, S. Sapra, A. K. Dinda, S. Kharbanda, and H. Singh, "Cellular interaction of folic acid conjugated superparamagnetic iron oxide nanoparticles and its use as contrast agent for targeted magnetic imaging of tumor cells," *International Journal of Nanomedicine*, vol. 7, pp. 3503–3516, 2012.

[243] L. Zhang, X. Wang, J. Zou, Y. Liu, and J. Wang, "DMSA-Coated Iron Oxide Nanoparticles Greatly Affect the Expression of Genes Coding Cysteine-Rich Proteins by Their DMSA Coating," Oct. 2015.

[244] D.-H. Kim, Y. Tamada, T. Ono, S. D. Bader, E. A. Rozhkova, and V. Novosad, "The effect of ligands on FePt-Fe3o4 core-shell magnetic nanoparticles," *Journal of Nanoscience and Nanotechnology*, vol. 14, pp. 2648–2652, Mar. 2014.

[245] L. N. Song, N. Gu, and Y. Zhang, "A Moderate Method for Preparation Dmsa Coated Fe 3 O 4 Nanoparticles," *IOP Conference Series: Materials Science and Engineering*, vol. 164, no. 1, p. 012026, 2017.

[246] J. He, P. Kanjanaboos, N. L. Frazer, A. Weis, X.-M. Lin, and H. M. Jaeger, "Fabrication and Mechanical Properties of Large-Scale Freestanding Nanoparticle Membranes," *Small*, vol. 6, pp. 1449–1456, July 2010.

[247] M. Amir, A. Baykal, H. Sozeri, H. Gungunes, and S. E. Shirsath, "Oleylamine Surface Functionalized FeCoyFe2-yO4 (0.0 y 1.0) Nanoparticles," *Arabian Journal of Chemistry*, Nov. 2016.

[248] Z. Chen, "Size and Shape Controllable Synthesis of Monodisperse Iron Oxide Nanoparticles by Thermal Decomposition of Iron Oleate Complex," *Synthesis and Reactivity in Inorganic, Metal-Organic, and Nano-Metal Chemistry*, vol. 42, pp. 1040–1046, Aug. 2012.

[249] A. Noori, K. Parivar, M. Modaresi, M. Messripour, M. H. Yousefi, and G. R. Amiri, "Effect of Magnetic Iron Oxide Nanoparticles on Pregnancy and Testicular Development of Mice," *African Journal of Biotechnology*, vol. 10, no. 7, pp. 1221–1227, 2011.

[250] H. T. Ta, Z. Li, Y. Wu, G. Cowin, S. Zhang, A. Yago, A. K. Whittaker, and Z. P. Xu, "Effects of Magnetic Field Strength and Particle Aggregation on Relaxivity of Ultra-Small Dual Contrast Iron Oxide Nanoparticles," *Materials Research Express*, vol. 4, no. 11, p. 116105, 2017.

[251] S. J. Soenen, P. Rivera-Gil, J.-M. Montenegro, W. J. Parak, S. C. De Smedt, and K. Braeckmans, "Cellular Toxicity of Inorganic Nanoparticles: Common Aspects and Guidelines for Improved Nanotoxicity Evaluation," *Nano Today*, vol. 6, pp. 446–465, Oct. 2011.

[252] M. Song, Y. Zhang, S. Hu, L. Song, J. Dong, Z. Chen, and N. Gu, "Influence of Morphology and Surface Exchange Reaction on Magnetic Properties of Monodisperse Magnetite Nanoparticles," *Colloids and Surfaces A: Physicochemical and Engineering Aspects*, vol. 408, pp. 114–121, Aug. 2012.

[253] P. d. Pino, B. Pelaz, Q. Zhang, P. Maffre, G. U. Nienhaus, and W. J. Parak, "Protein Corona Formation Around Nanoparticles – from the Past to the Future," *Materials Horizons*, vol. 1, pp. 301–313, Apr. 2014.

[254] T. J. Daou, J. M. Grenèche, G. Pourroy, S. Buathong, A. Derory, C. Ulhaq-Bouillet, B. Donnio, D. Guillon, and S. Begin-Colin, "Coupling Agent Effect on Magnetic Properties of Functionalized Magnetite-Based Nanoparticles," *Chemistry of Materials*, vol. 20, pp. 5869–5875, Sept. 2008.

[255] R. M. Patil, N. D. Thorat, P. B. Shete, P. A. Bedge, S. Gavde, M. G. Joshi, S. A. M. Tofail, and R. A. Bohara, "Comprehensive cytotoxicity studies of superparamagnetic iron oxide nanoparticles," *Biochemistry and Biophysics Reports*, vol. 13, pp. 63–72, Mar. 2018.

[256] T. L. Riss, R. A. Moravec, A. L. Niles, S. Duellman, H. A. Benink, T. J. Worzella, and L. Minor, "Cell Viability Assays," in *Assay Guidance Manual*, Bethesda (MD): Eli Lilly & Company and the National Center for Advancing Translational Sciences, 2004.

[257] E. Papis, F. Rossi, M. Raspanti, I. Dalle-Donne, G. Colombo, A. Milzani, G. Bernardini, and R. Gornati, "Engineered cobalt oxide nanoparticles readily enter cells," *Toxicology Letters*, vol. 189, pp. 253–259, Sept. 2009.

[258] H. Wu, J.-J. Yin, W. G. Wamer, M. Zeng, and Y. M. Lo, "Reactive oxygen species-related activities of nano-iron metal and nano-iron oxides," *Journal of Food and Drug Analysis*, vol. 22, pp. 86–94, Mar. 2014.

[259] W. P. Kwan and B. M. Voelker, "Rates of Hydroxyl Radical Generation and Organic Compound Oxidation in Mineral-Catalyzed Fenton-like Systems," *Environmental Science & Technology*, vol. 37, pp. 1150–1158, Mar. 2003.

[260] B. H. Kim, M. J. Hackett, J. Park, and T. Hyeon, "Synthesis, Characterization, and Application of Ultrasmall Nanoparticles," *Chemistry of Materials*, vol. 26, pp. 59–71, Jan. 2014.

[261] B. Halliwell and M. Whiteman, "Measuring reactive species and oxidative damage in vivo and in cell culture: how should you do it and what do the results mean?," *British Journal of Pharmacology*, vol. 142, pp. 231–255, May 2004.

[262] A. B. M. Helaluddin, R. S. Khalid, M. Alaama, and S. A. Abbas, "Main Analytical Techniques Used for Elemental Analysis in Various Matrices," *Tropical Journal of Pharmaceutical Research*, vol. 15, pp. 427–434–434, Jan. 2016.

[263] "Feridex - FDA prescribing information, side effects and uses." https://www.drugs.com/pro/feridex.html.

[264] C. Costa, F. Brandao, M. J. Bessa, S. Costa, V. Valdiglesias, G. Kilic, N. Fernandez-Bertolez, P. Quaresma, E. Pereira, E. Pasaro, B. Laffon, and J. P. Teixeira, "In vitro cytotoxicity of superparamagnetic iron oxide nanoparticles on neuronal and glial cells. Evaluation of nanoparticle interference with viability tests," *Journal of applied toxicology: JAT*, vol. 36, pp. 361–372, Mar. 2016.

[265] A. Kroll, M. H. Pillukat, D. Hahn, and J. Schnekenburger, "Interference of engineered nanoparticles with in vitro toxicity assays," *Archives of Toxicology*, vol. 86, pp. 1123–1136, July 2012.

[266] A. Kroll, C. Dierker, C. Rommel, D. Hahn, W. Wohlleben, C. Schulze-Isfort, C. Göbbert, M. Voetz, F. Hardinghaus, and J. Schnekenburger, "Cytotoxicity screening of 23 engineered nanomaterials using a test matrix of ten cell lines and three different assays," *Particle and Fibre Toxicology*, vol. 8, p. 9, Feb. 2011.

[267] M. Roesslein, C. Hirsch, J.-P. Kaiser, H. F. Krug, and P. Wick, "Comparability of in Vitro Tests for Bioactive Nanoparticles: A Common Assay to Detect Reactive Oxygen Species as an Example," *International Journal of Molecular Sciences*, vol. 14, pp. 24320–24337, Dec. 2013.

[268] F. Kouoh, B. Gressier, M. Luyckx, C. Brunet, T. Dine, M. Cazin, and J. C. Cazin, "Antioxidant properties of albumin: effect on oxidative metabolism of human neutrophil granulocytes.," *Farmaco (Societa chimica italiana : 1989)*, vol. 54, pp. 695–699, Oct. 1999.

[269] M. J. Akhtar, M. Ahamed, S. Kumar, M. M. Khan, J. Ahmad, and S. A. Alrokayan, "Zinc oxide nanoparticles selectively induce apoptosis in human cancer cells through reactive oxygen species," *International Journal of Nanomedicine*, vol. 7, pp. 845–857, 2012.

[270] S. Klein, M. Kizaloglu, L. Portilla, H. Park, T. Rejek, J. Hummer, K. Meyer, R. Hock, L. V. R. Distel, M. Halik, and C. Kryschi, "Enhanced In Vitro Biocompatibility and Water Dispersibility of Magnetite and Cobalt Ferrite Nanoparticles Employed as ROS Formation Enhancer in Radiation Cancer Therapy," *Small*, vol. 14, no. 21, p. 1704111, 2018.

[271] S. Bhattacharjee, "Membrane lipid peroxidation and its conflict of interest: the two faces of oxidative stress," *Current Science*, vol. 107, pp. 1811–1823, Oct. 2014.

[272] Y. Liu, Z. Chen, and J. Wang, "Systematic evaluation of biocompatibility of magnetic Fe3o4 nanoparticles with six different mammalian cell lines," *Journal of Nanoparticle Research*, vol. 13, pp. 199–212, Jan. 2011.

[273] L. Horev-Azaria, G. Baldi, D. Beno, D. Bonacchi, U. Golla-Schindler, J. C. Kirkpatrick, S. Kolle, R. Landsiedel, O. Maimon, P. N. Marche, J. Ponti, R. Romano, F. Rossi, D. Sommer, C. Uboldi, R. E. Unger, C. Villiers, and R. Korenstein, "Predictive Toxicology of Cobalt Ferrite Nanoparticles: Comparative in-Vitro Study of Different Cellular Models Using Methods of Knowledge Discovery from Data," *Particle and Fibre Toxicology*, vol. 10, p. 32, July 2013.

[274] A. Chumakov, V. Batalova, and Y. Slizhov, "Electro-Fenton-Like Reactions of Transition Metal Ions with Electrogenerated Hydrogen Peroxide," *AIP Conference Proceedings*, vol. 1772, p. 040004, Oct. 2016.

[275] C. C. Winterbourn, "Toxicity of Iron and Hydrogen Peroxide: The Fenton Reaction," *Toxicology Letters*, vol. 82-83, pp. 969–974, Dec. 1995.

[276] S. Leonard, P. M. Gannett, Y. Rojanasakul, D. Schwegler-Berry, V. Castranova, V. Vallyathan, and X. Shi, "Cobalt-Mediated Generation of Reactive Oxygen Species and Its Possible Mechanism," *Journal of Inorganic Biochemistry*, vol. 70, pp. 239–244, July 1998.

[277] T. Porwol, W. Ehleben, K. Zierold, J. Fandrey, and H. Acker, "The Influence of Nickel and Cobalt on Putative Members of the Oxygen-Sensing Pathway of Erythropoietin-Producing HepG2 Cells," *European Journal of Biochemistry*, vol. 256, no. 1, pp. 16–23, 2001.

[278] L. Gao, J. Zhuang, L. Nie, J. Zhang, Y. Zhang, N. Gu, T. Wang, J. Feng, D. Yang, S. Perrett, and X. Yan, "Intrinsic peroxidase-like activity of ferromagnetic nanoparticles," *Nature Nanotechnology*, vol. 2, pp. 577–583, Sept. 2007.

[279] D.-M. Huang, J.-K. Hsiao, Y.-C. Chen, L.-Y. Chien, M. Yao, Y.-K. Chen, B.-S. Ko, S.-C. Hsu, L.-A. Tai, H.-Y. Cheng, S.-W. Wang, C.-S. Yang, and Y.-C. Chen, "The promotion of human mesenchymal stem cell proliferation by superparamagnetic iron oxide nanoparticles," *Biomaterials*, vol. 30, pp. 3645–3651, Aug. 2009.

[280] M. Gumpelmayer, M. Nguyen, G. Molnár, A. Bousseksou, B. Meunier, and A. Robert, "Magnetite Fe3o4 Has no Intrinsic Peroxidase Activity, and Is Probably not Involved in Alzheimer's Oxidative Stress," *Angewandte Chemie International Edition*, vol. 57, no. 45, pp. 14758–14763, 2018.

[281] Q. Wu, Y. Li, M. Tang, and D. Wang, "Evaluation of Environmental Safety Concentrations of DMSA Coated Fe2o3-NPs Using Different Assay Systems in Nematode Caenorhabditis elegans," *PLOS ONE*, vol. 7, p. e43729, Aug. 2012.

[282] B. Ankamwar, T. C. Lai, J. H. Huang, R. S. Liu, M. Hsiao, C. H. Chen, and Y. K. Hwu, "Biocompatibility of Fe 3 O 4 nanoparticles evaluated by in vitro cytotoxicity assays using normal, glia and breast cancer cells," *Nanotechnology*, vol. 21, no. 7, p. 075102, 2010.

[283] M. Filipova, O. K. Elhelu, S. H. De Paoli, Z. Fremuntova, T. Mosko, D. Cmarko, J. Simak, and K. Holada, "An effective "three-in-one" screening assay for testing drug and nanoparticle toxicity in human endothelial cells," *PLoS ONE*, vol. 13, Oct. 2018.

[284] M. Ahamed, M. J. Akhtar, M. A. M. Khan, H. A. Alhadlaq, and A. Alshamsan, "Cobalt Iron Oxide Nanoparticles Induce Cytotoxicity and Regulate the Apoptotic Genes Through Ros in Human Liver Cells (HepG2)," *Colloids and Surfaces B: Biointerfaces*, vol. 148, pp. 665–673, Dec. 2016.

[285] H. Wu, G. Liu, X. Wang, J. Zhang, Y. Chen, J. Shi, H. Yang, H. Hu, and S. Yang, "Solvothermal synthesis of cobalt ferrite nanoparticles loaded on multiwalled carbon nanotubes for magnetic resonance imaging and drug delivery," *Acta Biomaterialia*, vol. 7, pp. 3496–3504, Sept. 2011.

[286] J. S. Kim, T.-J. Yoon, K. N. Yu, B. G. Kim, S. J. Park, H. W. Kim, K. H. Lee, S. B. Park, J.-K. Lee, and M. H. Cho, "Toxicity and Tissue Distribution of Magnetic Nanoparticles in Mice," *Toxicological Sciences*, vol. 89, pp. 338–347, Jan. 2006.

[287] L. Farcal, F. T. Andón, L. D. Cristo, B. M. Rotoli, O. Bussolati, E. Bergamaschi, A. Mech, N. B. Hartmann, K. Rasmussen, J. Riego-Sintes, J. Ponti, A. Kinsner-Ovaskainen, F. Rossi, A. Oomen, P. Bos, R. Chen, R. Bai, C. Chen, L. Rocks, N. Fulton, B. Ross, G. Hutchison, L. Tran, S. Mues, R. Ossig, J. Schnekenburger, L. Campagnolo, L. Vecchione, A. Pietroiusti, and B. Fadeel, "Comprehensive In Vitro Toxicity Testing of a Panel of Representative Oxide Nanomaterials: First Steps towards an Intelligent Testing Strategy," *PLOS ONE*, vol. 10, p. e0127174, May 2015.

[288] R. B. Buxton, *Introduction to Functional Magnetic Resonance Imaging: Principles and Techniques*. Cambridge University Press, Aug. 2009.

[289] A. Elster, "T2* vs T2 relaxation time." http://mriquestions.com/t2-vs-t2.html.

[290] A. van der Plas, *MRI technique - Startradiology*, Aug. 2016. http://www.startradiology.com/the-basics/mri-technique/.

[291] A. P. Matos, F. Velloni, M. Ramalho, M. AlObaidy, A. Rajapaksha, and R. C. Semelka, "Focal liver lesions: Practical magnetic resonance imaging approach," *World Journal of Hepatology*, vol. 7, pp. 1987–2008, Aug. 2015.

[292] J. Lohrke, T. Frenzel, J. Endrikat, F. C. Alves, T. M. Grist, M. Law, J. M. Lee, T. Leiner, K.-C. Li, K. Nikolaou, M. R. Prince, H. H. Schild, J. C. Weinreb, K. Yoshikawa, and H. Pietsch, "25 Years of Contrast-Enhanced MRI: Developments, Current Challenges and Future Perspectives," *Advances in Therapy*, vol. 33, pp. 1–28, 2016.

[293] A. Szpak, S. Fiejdasz, W. Prendota, T. Strączek, C. Kapusta, J. Szmyd, M. Nowakowska, and S. Zapotoczny, "T1–T2 Dual-modal MRI contrast agents based on superparamagnetic iron oxide nanoparticles with surface attached gadolinium complexes," *Journal of Nanoparticle Research*, vol. 16, no. 11, 2014.

[294] L. M. De León-Rodríguez, A. F. Martins, M. Pinho, N. Rofsky, and A. D. Sherry, ""Basic MR Relaxation Mechanisms & Contrast Agent Design"," *Journal of magnetic resonance imaging : JMRI*, vol. 42, pp. 545–565, Sept. 2015.

[295] P. Eriksson, *A New Synthesis of Nanoparticles Designed for Biomedical Imaging. a Pilot Study.* Dissertation, Linkoping University, 2013.

[296] P. Caravan, J. J. Ellison, T. J. McMurry, and R. B. Lauffer, "Gadolinium(III) Chelates as MRI Contrast Agents: Structure, Dynamics, and Applications," *Chemical Reviews*, vol. 99, pp. 2293–2352, Sept. 1999.

[297] Y. Bao, J. A. Sherwood, and Z. Sun, "Magnetic iron oxide nanoparticles as T1 contrast agents for magnetic resonance imaging," *Journal of Materials Chemistry C*, vol. 6, pp. 1280–1290, Feb. 2018.

[298] J. L. Abraham, C. Thakral, L. Skov, K. Rossen, and P. Marckmann, "Dermal inorganic gadolinium concentrations: evidence for in vivo transmetallation and long-term persistence in nephrogenic systemic fibrosis," *The British Journal of Dermatology*, vol. 158, pp. 273–280, Feb. 2008.

[299] A. Bello, A. Levin, M. Tonelli, I. Okpechi, J. Feehally, D. Harris, K. Jindal, B. Salako, A. Rateb, M. Osman, B. Qarni, S. Saad, M. Lunney, N. Wiebe, F. Ye, and D. Johnson, "Global Kidney Health Atlas: A report by the International Society of Nephrology on the current state of organization and structures for kidney care across the globe," tech. rep., International Society of Nephrology, Brussels, Belgium, 2017.

[300] Y. X. J. Wang and J.-M. Idee, "A Comprehensive Literatures Update of Clinical Researches of Superparamagnetic Resonance Iron Oxide Nanoparticles for Magnetic Resonance Imaging," *Quantitative Imaging in Medicine and Surgery*, vol. 7, pp. 88–122, Feb. 2017.

[301] S. Wagner, J. Schnorr, H. Pilgrimm, B. Hamm, and M. Taupitz, "Monomer-Coated Very Small Superparamagnetic Iron Oxide Particles as Contrast Medium for Magnetic Resonance Imaging," *Investigative Radiology*, vol. 37, pp. 167–177, Apr. 2002.

[302] E. Taboada, E. Rodríguez, A. Roig, J. Oró, A. Roch, and R. N. Muller, "Relaxometric and Magnetic Characterization of Ultrasmall Iron Oxide Nanoparticles with High Magnetization. Evaluation as Potential T1 Magnetic Resonance Imaging Contrast Agents for Molecular Imaging," *Langmuir*, vol. 23, pp. 4583–4588, Apr. 2007.

[303] K. E. Kellar, D. K. Fujii, W. H. Gunther, K. Briley-Saebø, M. Spiller, and S. H. Koenig, "'NC100150', a preparation of iron oxide nanoparticles ideal for positive-contrast MR angiography," *Magma (New York, N.Y.)*, vol. 8, pp. 207–213, Aug. 1999.

[304] Z. Jia, L. Song, F. Zang, J. Song, W. Zhang, C. Yan, J. Xie, Z. Ma, M. Ma, G. Teng, N. Gu, and Y. Zhang, "Active-target T1-weighted MR Imaging of Tiny Hepatic Tumor via RGD Modified Ultra-small Fe3o4 Nanoprobes," *Theranostics*, vol. 6, pp. 1780–1791, July 2016.

[305] Z. Shen, T. Chen, X. Ma, W. Ren, Z. Zhou, G. Zhu, A. Zhang, Y. Liu, J. Song, Z. Li, H. Ruan, W. Fan, L. Lin, J. Munasinghe, X. Chen, and A. Wu, "Multifunctional Theranostic Nanoparticles Based on Exceedingly Small Magnetic Iron Oxide Nanoparticles for T1-Weighted Magnetic Resonance Imaging and Chemotherapy," *ACS Nano*, vol. 11, pp. 10992–11004, Nov. 2017.

[306] C. Bai, Z. Jia, L. Song, W. Zhang, Y. Chen, F. Zang, M. Ma, N. Gu, and Y. Zhang, "Time-Dependent T1–T2 Switchable Magnetic Resonance Imaging Realized by c(RGDyK) Modified Ultrasmall Fe3o4 Nanoprobes," *Advanced Functional Materials*, vol. 28, p. 1802281, Aug. 2018.

[307] H. Yang, Y. Zhuang, Y. Sun, A. Dai, X. Shi, D. Wu, F. Li, H. Hu, and S. Yang, "Targeted dual-contrast T1- and T2-weighted magnetic resonance imaging of tumors using multifunctional gadolinium-labeled superparamagnetic iron oxide nanoparticles," *Biomaterials*, vol. 32, pp. 4584–4593, July 2011.

[308] H. B. Na, J. H. Lee, K. An, Y. I. Park, M. Park, I. S. Lee, D.-H. Nam, S. T. Kim, S.-H. Kim, S.-W. Kim, K.-H. Lim, K.-S. Kim, S.-O. Kim, and T. Hyeon, "Development of a T1 Contrast Agent for Magnetic Resonance Imaging Using MnO Nanoparticles," *Angewandte Chemie*, vol. 119, no. 28, pp. 5493–5497, 2007.

[309] Z. Ghasemian, D. Shahbazi-Gahrouei, and S. Manouchehri, "Cobalt Zinc Ferrite Nanoparticles as a Potential Magnetic Resonance Imaging Agent: An In vitro Study," *Avicenna Journal of Medical Biotechnology*, vol. 7, no. 2, pp. 64–68, 2015.

[310] M. Nidhin, S. S. Nazeer, R. S. Jayasree, M. S. Kiran, B. U. Nair, and K. J. Sreeram, "Flower Shaped Assembly of Cobalt Ferrite Nanoparticles: Application as T2 Contrast Agent in MRI," *RSC Advances*, vol. 3, pp. 6906–6912, Apr. 2013.

[311] M. A. Wilson, *NMR Techniques & Applications in Geochemistry & Soil Chemistry*. Elsevier, Oct. 2013.

[312] A. Hellerbach, V. Schuster, A. Jansen, and J. Sommer, "MRI Phantoms – Are There Alternatives to Agar?," *PLoS ONE*, vol. 8, Aug. 2013.

[313] M. Hájek, *Texture Analysis for Magnetic Resonance Imaging*. Texture Analysis Magn Resona, 2006.

[314] C. Tao, Q. Zheng, L. An, M. He, J. Lin, Q. Tian, and S. Yang, "T1-Weight Magnetic Resonance Imaging Performances of Iron Oxide Nanoparticles Modified with a Natural Protein Macromolecule and an Artificial Macromolecule," *Nanomaterials*, vol. 9, p. 170, Feb. 2019.

[315] M. Rohrer, H. Bauer, J. Mintorovitch, M. Requardt, and H.-J. Weinmann, "Comparison of Magnetic Properties of MRI Contrast Media Solutions at Different Magnetic Field Strengths," *Investigative Radiology*, vol. 40, pp. 715–724, Nov. 2005.

[316] A. Jedlovszky-Hajdu, E. Tombacz, I. Banyai, M. Babos, and A. Palko, "Carboxylated Magnetic Nanoparticles as Mri Contrast Agents: Relaxation Measurements at Different Field Strengths," *Journal of Magnetism and Magnetic Materials*, vol. 324, pp. 3173–3180, Sept. 2012.

[317] D. Kovar, A. Mala, J. Mlcochova, M. Kalina, Z. Fohlerova, A. Hlavacek, Z. Farka, P. Skladal, Z. Starcuk, R. Jirik, O. Slaby, and J. Hubalek, "Preparation and Characterisation of Highly Stable Iron Oxide Nanoparticles for Magnetic Resonance Imaging," *Journal of Nanomaterials*, vol. 2017, p. 8 pages, 2017.

[318] P. Caravan, C. T. Farrar, L. Frullano, and R. Uppal, "Influence of molecular parameters and increasing magnetic field strength on relaxivity of gadolinium- and manganese-based T1 contrast agents," *Contrast media & molecular imaging*, vol. 4, no. 2, pp. 89–100, 2009.

[319] G. E. Hagberg and K. Scheffler, "Effect of r1 and r2 relaxivity of gadolinium-based contrast agents on the T1-weighted MR signal at increasing magnetic field strengths," *Contrast Media & Molecular Imaging*, vol. 8, pp. 456–465, Dec. 2013.

[320] A. Elster, *Myocardial T1-Mapping*. http://mriquestions.com/t1-mapping.html.

[321] B. Marty, A. Vignaud, A. Greiser, B. Robert, P. L. de Sousa, and P. G. Carlier, "Bloch Equations-Based Reconstruction of Myocardium T1 Maps from Modified Look-Locker Inversion Recovery Sequence," *PLoS ONE*, vol. 10, May 2015.

[322] N. D. Gai and J. A. Butman, "Fast T1 mapping determined using incomplete inversion recovery look–locker 3d balanced SSFP acquisition and a simple two-parameter model fit," *Journal of Magnetic Resonance Imaging*, vol. 35, no. 6, pp. 1437–1444, 2012.

[323] F. H. Starsich, C. Eberhardt, K. Keevend, A. Boss, A. M. Hirt, I. K. Herrmann, and S. E. Pratsinis, "Reduced Magnetic Coupling in Ultrasmall Iron Oxide T1 MRI Contrast Agents," *ACS Applied Bio Materials*, vol. 1, pp. 783–791, Sept. 2018.

[324] L. Zeng, W. Ren, J. Zheng, P. Cui, and A. Wu, "Ultrasmall water-soluble metal- iron oxide nanoparticles as T 1 -weighted contrast agents for magnetic resonance imaging," *Physical Chemistry Chemical Physics*, vol. 14, no. 8, pp. 2631–2636, 2012.

[325] U. I. Tromsdorf, O. T. Bruns, S. C. Salmen, U. Beisiegel, and H. Weller, "A Highly Effective, Nontoxic T1 MR Contrast Agent Based on Ultrasmall PEGylated Iron Oxide Nanoparticles," *Nano Letters*, vol. 9, pp. 4434–4440, Dec. 2009.

[326] G. Wang, X. Zhang, A. Skallberg, Y. Liu, Z. Hu, X. Mei, and K. Uvdal, "One-step synthesis of water-dispersible ultra-small Fe 3 O 4 nanoparticles as contrast agents for T 1 and T 2 magnetic resonance imaging," *Nanoscale*, vol. 6, no. 5, pp. 2953–2963, 2014.

[327] T. Vangijzegem, D. Stanicki, S. Boutry, Q. Paternoster, L. V. Elst, R. N. Muller, and S. Laurent, "VSION as high field MRI T1 contrast agent: evidence of their potential as positive contrast agent for magnetic resonance angiography," *Nanotechnology*, vol. 29, p. 265103, May 2018.

[328] J. Mintorovitch and K. Shamsi, "Eovist Injection and Resovist Injection: two new liver-specific contrast agents for MRI," *Oncology (Williston Park, N.Y.)*, vol. 14, pp. 37–40, June 2000.

[329] T. Akiyama, Y. Miyamoto, Y. Sakamoto, R. Tokunaga, K. Kosumi, H. Shigaki, J. Kurashige, M. Iwatsuki, Y. Baba, N. Yoshida, and H. Baba, "Cancer-related multiple brain infarctions caused by Trousseau syndrome in a patient with metastatic colon cancer: a case report," *Surgical case reports*, vol. 2, pp. 91–91, Sept. 2016.

[330] D. A. Betebenner, P. L. Carney, A. M. Zimmer, J. M. Kazikiewicz, E. Brücher, A. D. Sherry, and D. K. Johnson, "Hepatobiliary Delivery of Polyaminopolycarboxylate Chelates: Synthesis and Characterization of a Cholic Acid Conjugate of EDTA and Biodistribution and Imaging Studies with Its Indium-111 Chelate," *Bioconjugate Chemistry*, vol. 2, pp. 117–123, Apr. 1991.

[331] K. L. Mertens, A. Kalsbeek, M. R. Soeters, and H. M. Eggink, "Bile Acid Signaling Pathways from the Enterohepatic Circulation to the Central Nervous System," *Frontiers in Neuroscience*, vol. 11, Nov. 2017.

[332] P. L. Anelli, L. Lattuada, V. Lorusso, G. Lux, A. Morisetti, P. Morosini, M. Serleti, and F. Uggeri, "Conjugates of Gadolinium Complexes to Bile Acids as Hepatocyte-Directed Contrast Agents for Magnetic Resonance Imaging," *Journal of Medicinal Chemistry*, vol. 47, pp. 3629–3641, July 2004.

[333] Y. Zhou, E.-H. Ryu, Y. Zhao, and L. K. Woo, "Solvent-Responsive Metalloporphyrins: Binding and Catalysis," *Organometallics*, vol. 26, pp. 358–364, Jan. 2007.

[334] M. Balci, *Basic 1H- and 13C-NMR Spectroscopy*. Elsevier, Jan. 2005.

[335] E. Kaiser, R. L. Colescott, C. D. Bossinger, and P. I. Cook, "Color test for detection of free terminal amino groups in the solid-phase synthesis of peptides," *Analytical Biochemistry*, vol. 34, pp. 595–598, Apr. 1970.

[336] R. Mendelsohn, C. R. Flach, and D. J. Moore, "Determination of Molecular Conformation and Permeation in Skin via IR Spectroscopy, Microscopy, and Imaging," *Biochimica et Biophysica Acta (BBA) - Biomembranes*, vol. 1758, pp. 923–933, July 2006.

[337] P. Babu, N. M. Sangeetha, and U. Maitra, "Supramolecular Chemistry of Bile Acid Derivatives: Formation of Gels," *Macromolecular Symposia*, vol. 241, no. 1, pp. 60–67, 2006.

[338] R. J. DeLange and A. N. Glazer, "Bile Acids: Antioxidants or Enhancers of Peroxidation Depending on Lipid Concentration," *Archives of Biochemistry and Biophysics*, vol. 276, pp. 19–25, Jan. 1990.

[339] Y. Fang, S. I. Han, C. Mitchell, S. Gupta, E. Studer, S. Grant, P. B. Hylemon, and P. Dent, "Bile Acids Induce Mitochondrial ROS Which Promote Activation of Receptor Tyrosine Kinases and Signaling Pathways in Rat Hepatocytes," *Hepatology (Baltimore, Md.)*, vol. 40, pp. 961–971, Oct. 2004.

[340] D. Lapenna, G. Ciofani, D. Festi, M. Neri, S. D. Pierdomenico, M. A. Giamberardino, and F. Cuccurullo, "Antioxidant Properties of Ursodeoxycholic Acid," *Biochemical Pharmacology*, vol. 64, pp. 1661–1667, Dec. 2002.

[341] M. J. Perez and O. Briz, "Bile-Acid-Induced Cell Injury and Protection," *World Journal of Gastroenterology : WJG*, vol. 15, pp. 1677–1689, Apr. 2009.

[342] T. Kister, M. Mravlak, T. Schilling, and T. Kraus, "Pressure-controlled formation of crystalline, Janus, and core–shell supraparticles," *Nanoscale*, vol. 8, pp. 13377–13384, July 2016.

[343] S. Wintzheimer, T. Granath, M. Oppmann, T. Kister, T. Thai, T. Kraus, N. Vogel, and K. Mandel, "Supraparticles: Functionality from Uniform Structural Motifs," *ACS Nano*, vol. 12, pp. 5093–5120, June 2018.

[344] W. He, Y. Liu, W. G. Wamer, and J.-J. Yin, "Electron spin resonance spectroscopy for the study of nanomaterial-mediated generation of reactive oxygen species," *Journal of Food and Drug Analysis*, vol. 22, pp. 49–63, Mar. 2014.

[345] J.-J. Yin, F. Lao, P. P. Fu, W. G. Wamer, Y. Zhao, P. C. Wang, Y. Qiu, B. Sun, G. Xing, J. Dong, X.-J. Liang, and C. Chen, "The scavenging of reactive oxygen species and the potential for cell protection by functionalized fullerene materials," *Biomaterials*, vol. 30, pp. 611–621, Feb. 2009.

[346] Z. Wang, X.-D. Wen, R. Hoffmann, J. S. Son, R. Li, C.-C. Fang, D.-M. Smilgies, and T. Hyeon, "Reconstructing a solid-solid phase transformation pathway in CdSe nanosheets with associated soft ligands," *Proceedings of the National Academy of Sciences*, vol. 107, pp. 17119–17124, Oct. 2010.

Appendix A

List of Abbreviations

ADF-STEM	angular dark-field scanning transmission electron microscopy
Acac	acetylacetonate
B_0	magnetic field
BA	bile acid
BSA	bovine serum albumin
CA	contrast agent
CDCA	chenodeoxycholic acid
$CDCL_2$	deuterochloroform
CNT	classical nucleation theory
Co	cobalt
Co_3O_4	cobalt oxide
$CoFe_2O_4$	cobalt ferrite
$Co(acac)_2$	cobalt acetylacetonate
CoO	cobalt oxide
COO	carboxyl
Cryo-EM	cryogenic electron microscopy
D	diameter
D_2O	deuterium oxide
d_H	hydrodynamic diameter
DCA	deoxycholic acid
DCC	N,N'-Dicyclohexylcarbodiimide
DCF	dichlorofluorescein
DCM	dichloromethane
DLS	dynamic light scattering
DMEM	Dulbecco's modified eagle medium
DMF	dimethylformamide
DMR	diagnostic magnetic resonance
DMSA	dimercaptosuccinic acid

DMSO	dimethyl sulfoxide
DNA	deoxyribonucleic acid
EDC	1-Ethyl-3-(3-dimethylaminopropyl)-carbodiimide
EDTA	ethylenediaminetetraacetic acid
EELS	electron energy loss spectroscopy
EOB	ethoxybenzyl
ESION	extremely small iron oxide nanoparticles
ESR	electron spin resonance
FBS	fetal bovine serum
FC	field cooling
FCC	face centered cubic
FDA	Food and Drug Administration
Fe	iron
Fe_2O_3	maghemite
Fe_3O_4	magnetite
$Fe(acac)_3$	iron acetylacetonate
FFT	fast Fourier transform
FITR	Fourier-transform infrared spectroscopy
FOV	field of view
Gd	gadolinium
Gd-agents	gadolinium contrast agents
Gd-DTPA	gadolinium diethylenetriamine penta-acetic acid
H_2O	water
H_2DCF-DA	2',7'-dichlorofluorescein-diacetate
HCl	hydrochloric acid
HCP	hexagonal close packed
HDD	hexadecanediol
HepG2	liver hepatocellular cells
HRTEM	high resolution transmission electron microscopy
ICP-OES	inductively coupled plasma optical emission spectroscopy
INM	Leibniz Institute for New Materials
LCA	lithocholic acid
LDH	lactate dehydrogenase
$LiAlH_4$	lithium hydride
LSW	Lifschiz, Slyozov and Wagner
MFe_2O_4	ferrite
MPI	magnetic particle imaging
MPS	mononuclear phagocyte system
MR	magnetic resonance

MRI	magnetic resonance imaging
M_s	magnetic saturation
MTT	(3-(4,5-dimethylthiazol-2-yl)-2,5-diphenyltetrazolium bromide)
NaOH	sodium hydroxide
NH_2	nitrogen hydride
NHS	N-hydroxysuccinimide
NMR	nuclear magnetic resonance
NPs	nanoparticles
OA	oleic acid
OH	hydroxyl
OLA	oleylamine
PAA	poly(acrylic) acid
PBS	phosphate buffered saline
PEG	polyethylene glycol
PMAA-PTTM	poly(acrylic) acid-poly(methacrylic acid)
r_1	longitudinal relaxivity
r_2	transverse relaxivity
Refs	references
RES	reticuloendothelial system
RF	radio-frequency
ROI	region of interest
ROS	reactive oxygen species
RPMI	Roswell Park Memorial Institute medium
SAXS	small angle x-ray scattering
SIN-1	3-Morpholinosydnonimine
SiO_2	silicon dioxide
SPION	superparamagnetic iron oxide nanoparticle
STEM	scanning transmission electron microscopy
SQUID	superconducting quantum interference device
T_1	spin-lattice / longitudinal relaxation time
T_2	spin-spin / transverse relaxation time
T_B	Blocking temperature
TE	echo time
TEM	transmission electron microscopy
TGA	thermogravimetric analysis
THF	tetrahydrofuran
TI	interval time
TLC	thin layer chromatography
TR	repetition time

UCDA	ursodeoxycholic acid
UK	united kingdom
USNPs	ultra-small nanoparticles
VSION	very small iron oxide nanoparticles
XRD	x-ray diffraction
ZFC	zero field cooling
ζ-potential	zeta-potential

Appendix B

Additional results

B.1 Nanoparticle synthesis

B.1.1 Synthesis parameters

Table B.1: Parameters used in the synthesis of iron oxide, cobalt ferrite and cobalt oxide nanoparticles described in chapter 2. Controlled parameters were the amount of OLA (60 mmol), reaction temperature (225 ℃) and time (10 minutes).

Precursor quantity (mmol)	Fe_xO_y size (nm)	$CoFe_2O_4$ size (nm) (2:1 ratio)	$CoFe_2O_4$ size (nm) (1.5:1 ratio)	CoO size (nm)
1.4	5.7 ± 3.0	4.3 ± 0.8	3.5 ± 1.2	13.8 ± 3.7
0.7	4.6 ± 0.6	4.0 ± 0.8	4.8 ± 1.1	11.8 ± 1.7
0.3	4.0 ± 0.4	3.5 ± 0.7	3.0 ± 1.7	11.2 ± 2.2
0.15	3.8 ± 0.5	3.3 ± 0.6	3.0 ± 0.6	10.6 ± 1.8
0.07	3.1 ± 0.5	3.0 ± 0.6	2.2 ± 0.6	10.9 ± 1.7
0.03	2.4 ± 0.4	2.4 ± 0.3	2.6 ± 0.6	11.9 ± 1.5

Table B.2: Additional parameters used for the synthesis of iron oxide nanoparticles chapter 2.

Precursor (mmol)	OLA (mmol)	Reaction temp (℃)	Reaction time (mins)	Heating rate (℃ min^{-1})	Particle size (nm)
1	15	225	10	12	6.4 ± 1.0
1	30	225	10	12	4.6 ± 0.7
1	60	225	10	12	3.6 ± 0.7
1	120	225	10	12	3.2 ± 0.6
0.03	60	225	10	12.6	2.4 ± 0.5
0.03	60	225	10	15.3	2.5 ± 0.5
0.03	60	225	10	16.7	2.4 ± 0.4
0.03	60	225	10	17.0	2.4 ± 0.4
0.03	60	230	10	15.3	2.5 ± 0.5
0.03	60	250	10	24.7	2.4 ± 0.4
0.85	60	225	10	8.6	4.4 ± 0.9
0.85	60	225	30	8.3	4.8 ± 0.9
0.85	60	225	60	8.5	4.3 ± 0.9

B.1.2 Fourier transform infrared studies on synthesis aliquots

Experiments were conducted in an attempt to detect the formation of an OLA:precursor complex during synthesis and thus identify how the synthesis conditions affected nanoparticle nucleation and growth. Cobalt ferrite nanoparticles were synthesised according to the standard conditions for 2.4 nm (detailed in section 2.2.2), and 1 ml aliquots were withdrawn during the reaction at 100, 150, 180, 200 and 220 ℃. FTIR of aliquots was conducted using a Varian Excalibur FTS 3500 FTIR. Figure B.1 shows no differences in the spectra of aliquots taken at different temperatures. The OLA-precursor complex was expected to be detected in the form of secondary amide peaks in the range of 3000-3400 cm^{-1} and only in aliquots withdrawn above 150℃. In all samples, a very small amine/amide peak is visible in this range. Thus the FTIR experiments were inconclusive.

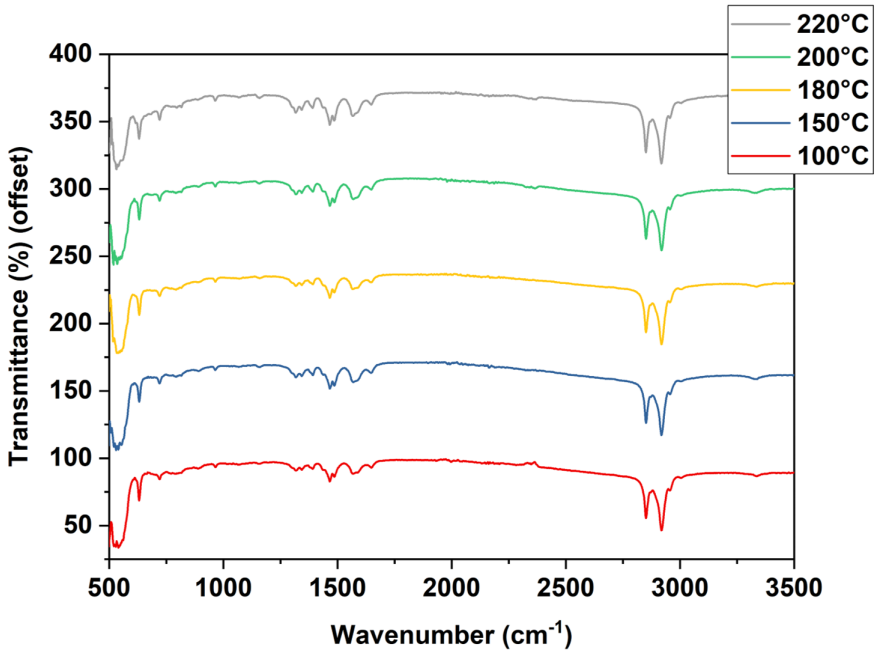


Figure B.1: *FTIR spectra of aliquots withdrawn at different temperatures during the synthesis of cobalt ferrite nanoparticles. No differences between spectra are visible.*

B.1.3 TEM of aliquot withdrawn during nanoparticle synthesis at 180℃

The synthesis experiment detailed below was carried out by Mai Mitzutani under my supervision. TEM was performed and analysed by the author. During synthesis of iron oxide nanoparticles in OLA, an aliquot was withdrawn at 180 ℃ to assess whether particles had already formed at this temperature. TEM (figure B.2) revealed the presence of nanoparticles in the aliquot, indicating that the precursor had decomposed and thus nucleation had occurred by 180 ℃.

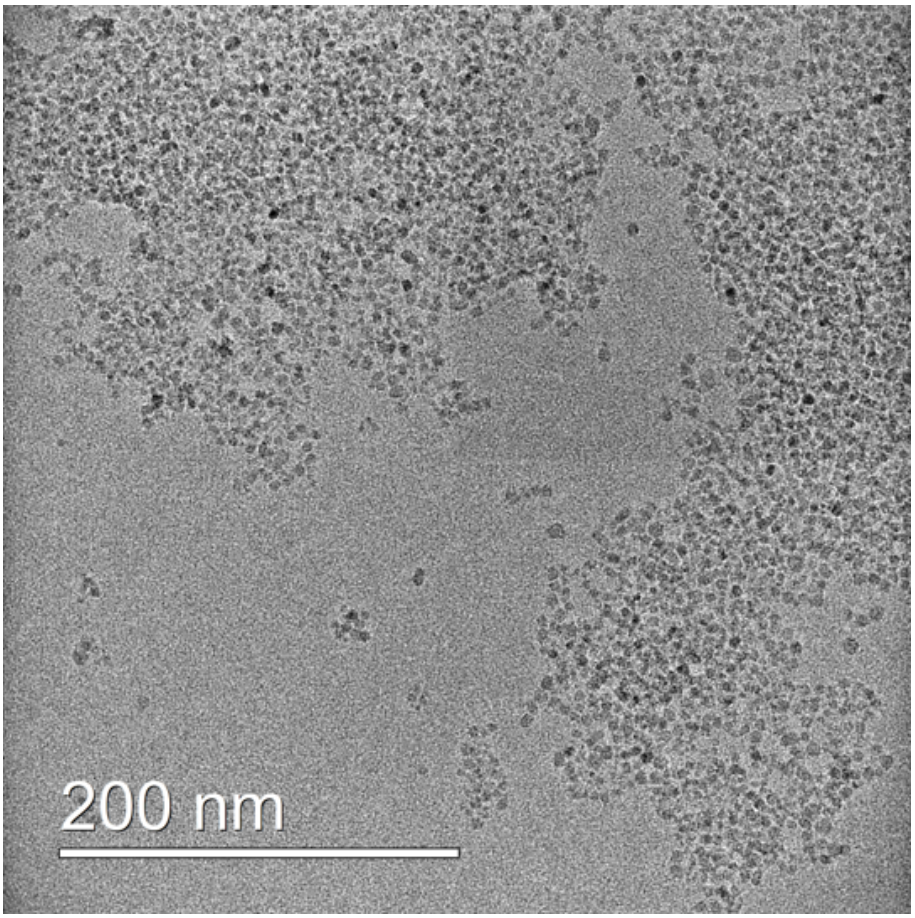
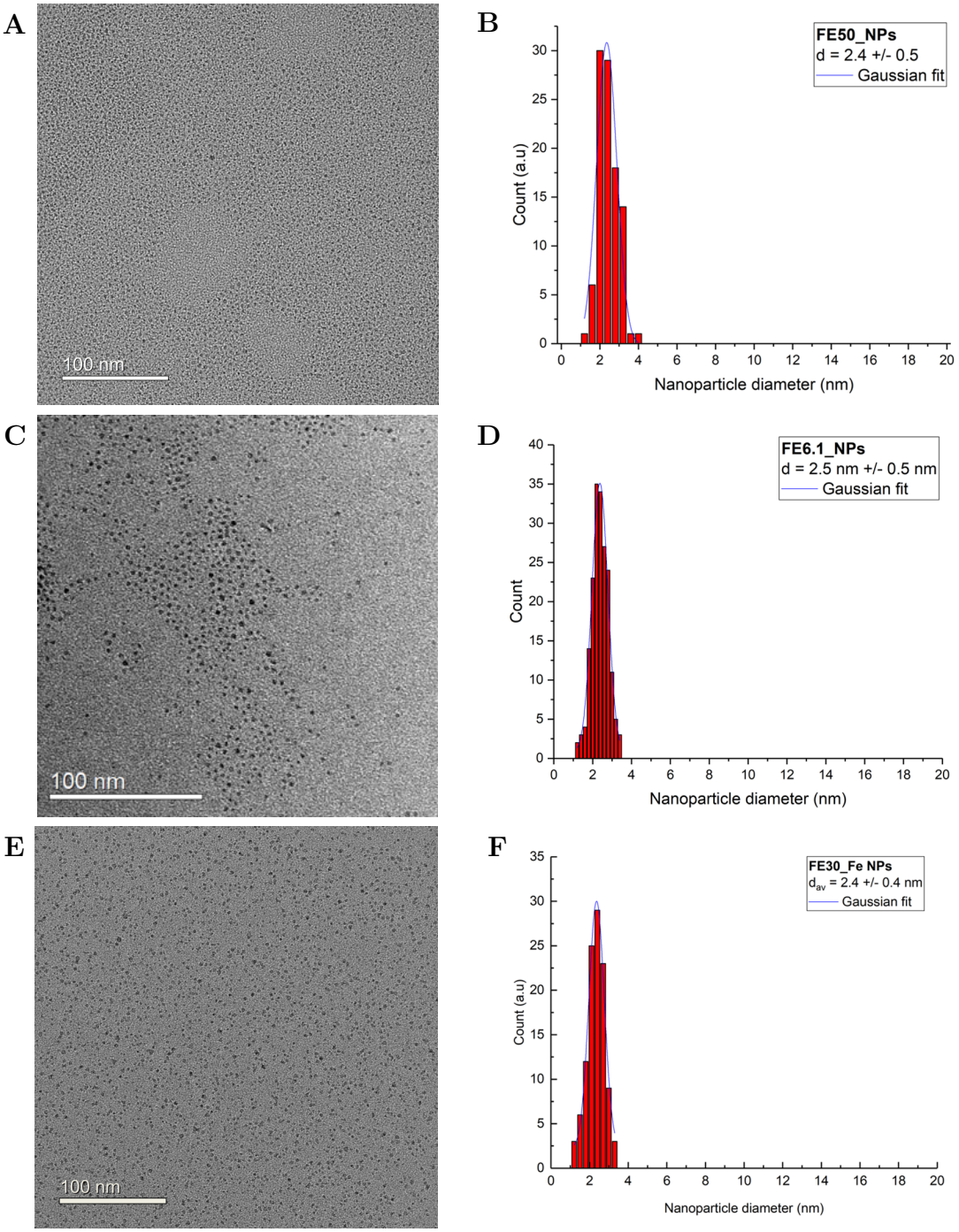


Figure B.2: *TEM micrograph of an aliquot withdrawn during the synthesis at 180 ℃ of iron oxide nanoparticles, showing that nanoparticles had already formed by this temperature point.*

B.1.4 TEM images of iron oxide nanoparticles synthesised at different heating rates



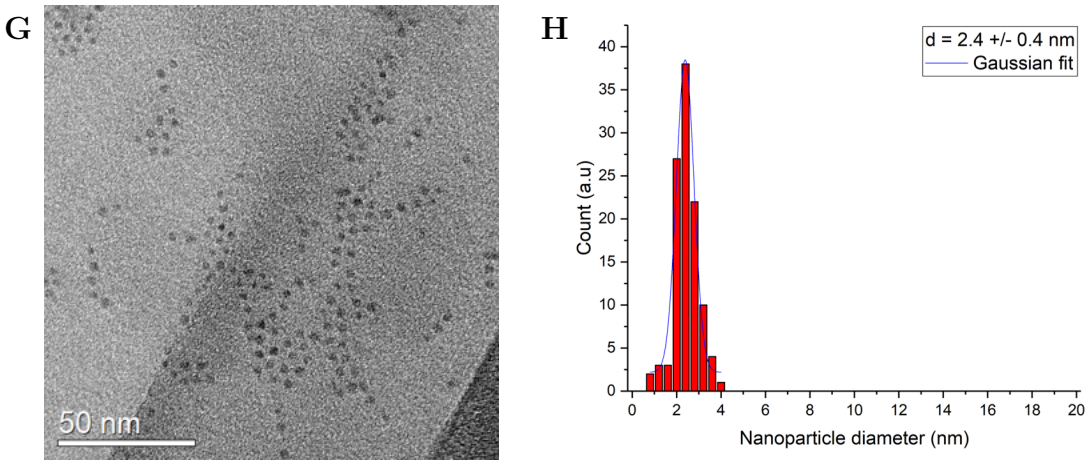
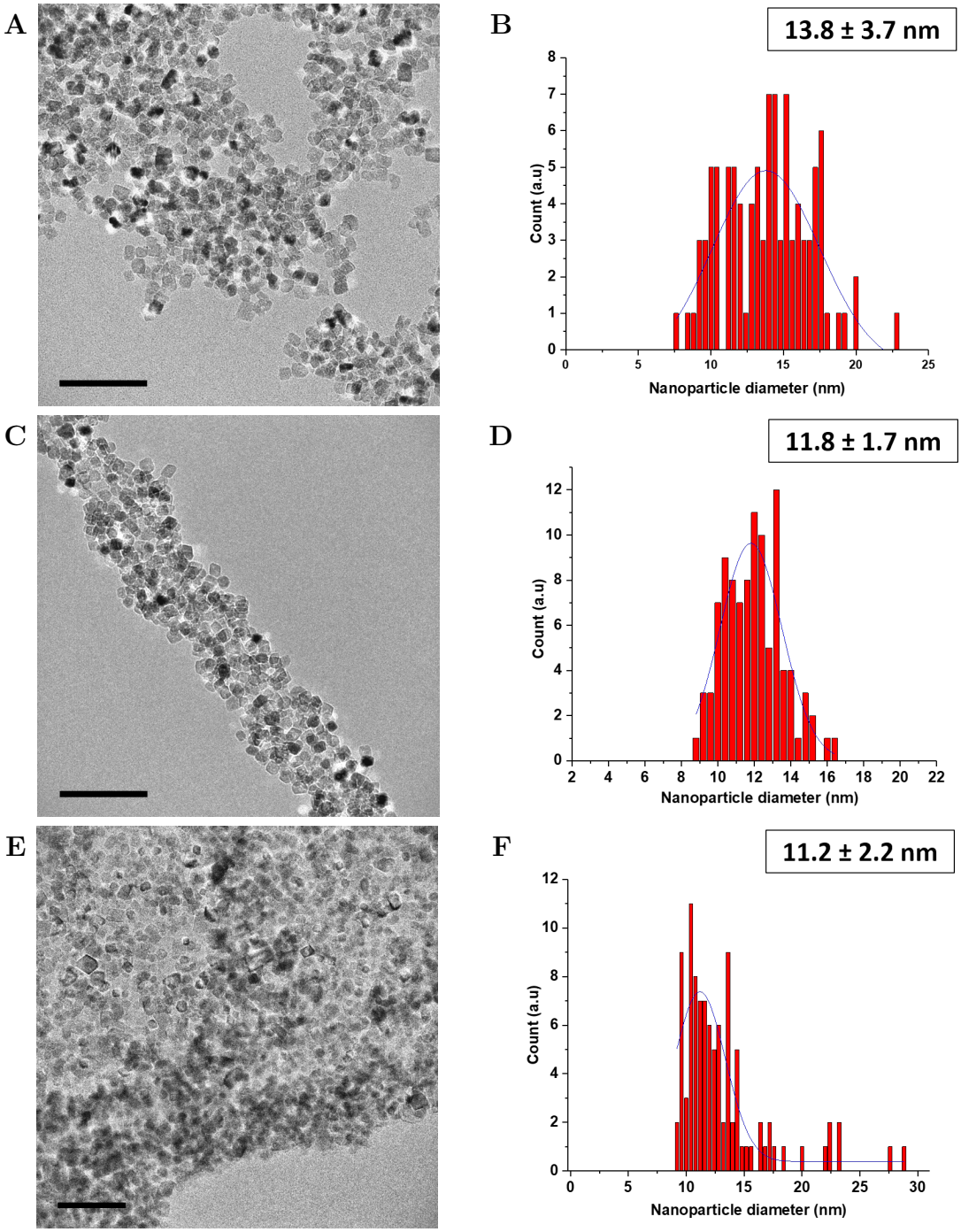


Figure B.4: TEM micrographs and corresponding size distribution graphs of iron-oxide nanoparticles synthesised with 60 mmol of OLA and 0.03 mmol of $Fe(acac)_3$ at different heating rates of A-B: 12.6 ℃ min^{-1}, C-D: 15.3 ℃ min^{-1}, E-F: 16.7 ℃ min^{-1}, G-H: 24.7 ℃ min^{-1}.

B.1.5 TEM images of cobalt oxide nanoparticles synthesised with different precursor-to-OLA ratios



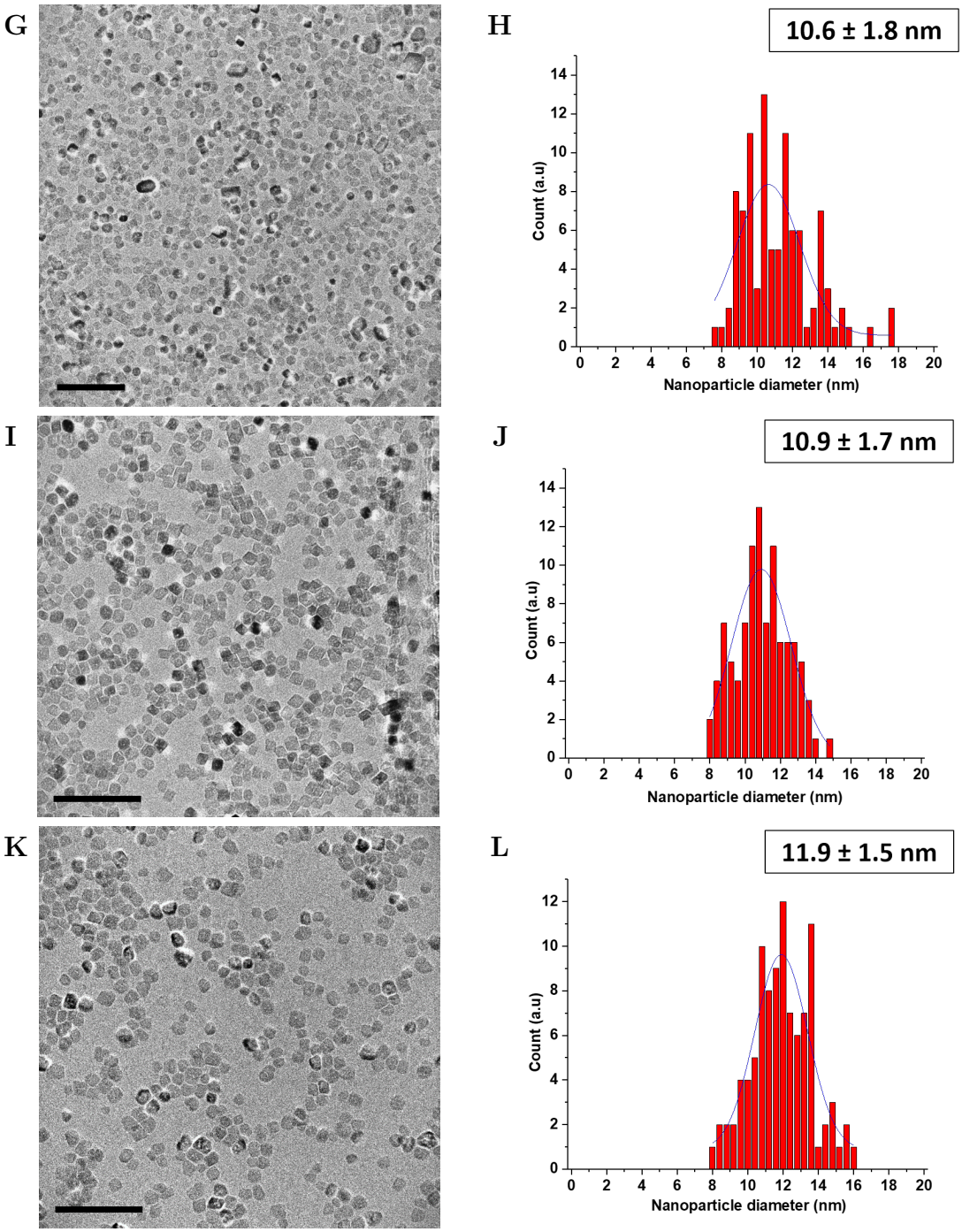


Figure B.6: TEM micrographs and corresponding size distribution graphs of cobalt oxide nanoparticles synthesised with 60 mmol of OLA and A-B: 1.4, C-D: 0.7, E-F: 0.3, G-H: 0.15, I-J: 0.07, and K-L: 0.03 mmol of $Co(acac)_2$ precursor. Scale bar is 100 nm.

B.2 Ligand exchange

B.2.1 Hydrodynamic diameter measurements of undialysed particles

Table B.3: Hydrodynamic diameter measurements of undialysed NPs following ligand exchange with DMSA.

Particle type	Ligand	Core size (TEM) (nm)	d_H (nm)
Fe_3O_4	DMSA	4.0 ± 0.3	136 ± 44
$CoFe_2O_4$	DMSA	4.1 ± 1.2	198 ± 33
Fe_3O_4	DMSA	4.0 ± 0.3	159 ± 49
$CoFe_2O_4$	DMSA	4.1 ± 1.2	187 ± 58

B.2.2 Core sizes before and after DMSA ligand exchange

The core size of particles before and after DMSA ligand exchange were measured from TEM micrographs. The average core diameter of both $CoFe_2O_4$ and Fe_3O_4 NPs did not change following ligand exchange from oleylamine to DMSA (figure B.7).

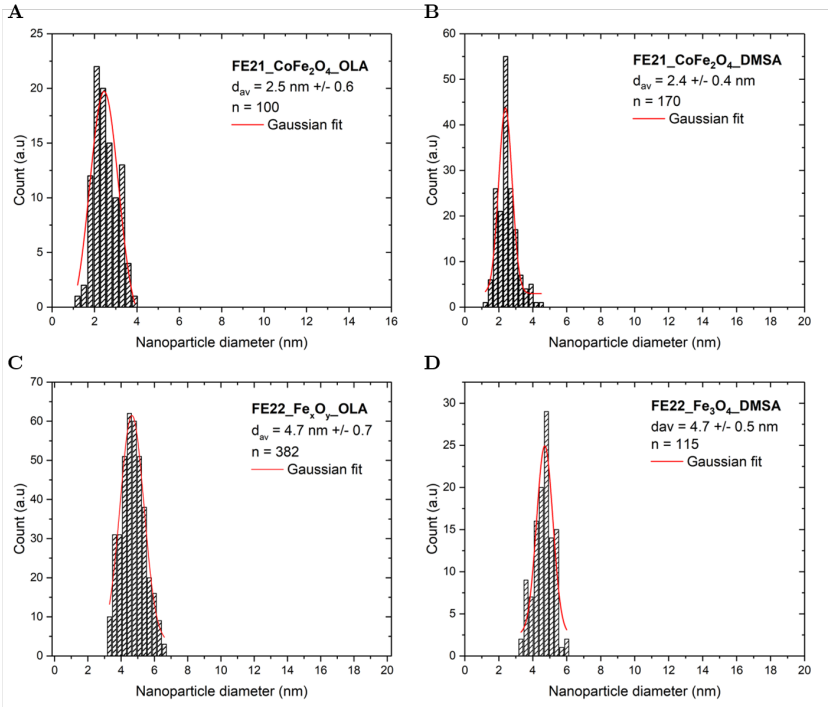


Figure B.7: Core particle size distributions of (A) $CoFe_2O_4$ NPs before DMSA ligand exchange, (B) $CoFe_2O_4$ NPs after DMSA ligand exchange, (C) Fe_3O_4 NPs before DMSA ligand exchange, and (D) Fe_3O_4 NPs after DMSA ligand exchange. Particles retained their original core size after ligand exchange.

B.2.3 Calculation of the excess amount of BSA

Calculations were made to estimate the excess amount of BSA if 80 mg or 160 mg was used. Several assumptions were made for the calculations as listed below:

- BSA coats the NPs fully in a monolayer.
- All BSA molecules bind in the same orientation, (either side-on or end-on).
- All nanoparticles are the same size and spherical.
- NPs are defect-free crystallites following the stoichiometric ratio of $CoFe_2O_4$ or Fe_3O_4.
- A monolayer of OLA is present on the particles.
- OLA is bound to the NPs by its polar group and has a chain length of 1.7 nm.[346]

Other parameters used for the calculation are listed in the table below:

Table B.4: Parameters used in BSA calculations

Density magnetite NPs (g/cm^3)	5.175	[216]
Density cobalt ferrite NPs (g/cm^3)	4.91	[214]
Molar mass OLA (g/mol)	267.5	-
Molar mass BSA (g/mol)	66463	-
Surface area OLA (nm^2)	0.26	-
Surface area BSA (side-on) (nm^2)	56	[225]
Surface area BSA (end-on) (nm^2)	16	[225]

Step 1: The number of NPs was estimated by:

$$n_{np} = \frac{m_t}{pv + (MA^{-1}SA_{ola}^{-1}SA_{npc})} \tag{B.1}$$

where m_t is the mass of NPs used for phase transfer, SA_{ola} is the surface area of OLA, SA_{npc} is the surface area of the NP core, M is the molar mass of OLA, and A is Avogadro's constant.

Step 2: Estimate the number of BSA molecules to coat a NP in a monolayer:

$$n_{bsa} = \frac{SA_{bsa}}{SA_{np}} \tag{B.2}$$

where SA_{bsa} is the surface area BSA occupies with either end-on or side-on binding, SA_{np} is the surface area of a NP including the OLA layer.

Step 3: Estimate the number of BSA molecules in 80/160/220 mg:

$$N_{bsa} = A\frac{m_{bsa}}{M_{bsa}} \tag{B.3}$$

where $m_{bsa}*$ is the mass of BSA and M_{bsa} the molar mass of BSA.

Step 4: Estimate the excess amount of BSA:

$$E = \frac{mol_{bsa}A}{n_{np}n_{bsa}} \tag{B.4}$$

Using the above calculations, the following results for excess amount of BSA were obtained:

Table B.5: Calculated excess of BSA in phase transfer experiments

		Particle type & size			
		Fe_3O_4		$CoFe_2O_4$	
Amount of BSA (mg)	BSA binding orientation	4 nm	2.5 nm	4 nm	2.5 nm
80	side-on	3.06	1.4	2.95	1.4
	end-on	0.9	0.4	0.8	0.4
160	side-on	6.1	2.8	5.91	2.7
	end-on	1.8	0.8	1.7	0.8

B.3 Cytotoxicity and Oxidative stress testing

B.3.1 Assumptions made in estimating NP concentrations from ICP-OES data

- All particles in a sample have the same diameter and are perfectly spherical.
- All particles are composed of the same number of unit cells.
- The particles' crystal structure is defect free.
- No surface states are considered.
- All iron-oxide nanoparticles are stoichiometric magnetite.

B.4 Data processing of MRI phantom studies

B.4.1 T_1 and T_2 relaxation times of MFe_2O_4@DMSA NPs at 9.4 T

Table B.6: Experimental T_1 and T_2 relaxation times and rates of MFe_2O_4@DMSA NPs at 9.4 T.

Sample	Particle concentration (mM)	T_1 (ms)	r_1 (s-1)	T_2 (ms)	r_2 (s-1)
FE1	0.63	1107	0.903	12.9	77.590
FE2	0.31	1361	0.735	20.6	48.640
FE3	0.16	1541	0.649	31.1	32.106
FE4	0.08	1646	0.607	45.6	21.935
FE5	0.04	1693	0.591	59.5	16.801
CO1	0.50	1051	0.951	27.4	36.543
CO2	0.25	1389	0.720	40.0	25.024
CO3	0.13	1544	0.648	53.5	18.699
CO4	0.06	1618	0.618	65.3	15.316
CO5	0.03	1664	0.601	73.0	13.694
Agarose	-	1707	0.586	84.0	11.908

B.4.2 Comparison of simulated and experimental T_1 relaxation times at 3.0 T

The T_1 relaxation times of $CoFe_2O_4$@DMSA NPs at 3.0 T were fitted to Bloch equations simulation of the MR parameters to assess the validity of the data considering that T_1 times are typically consistently underestimated in T_1 mapping when using the faster approximation technique. Table B.7 compares the experimental (raw) T_2 and T_1 data with the data fitted to the Bloch simulations (simulated). Samples CO1-CO5 reflect decreasing concentrations of $CoFe_2O_4$@DMSA NPs from 0.5 mM (CO1) to 0.03 mM (CO5). The control sample (undoped agarose) is included for comparison.

Table B.7: Experimental (raw) T_2 and T_1 relaxation times and rates of $CoFe_2O_4$@DMSA NPs at 3.0 T. T_1 times simulated from Bloch equations of the MR parameters used in the experiment are included for comparison.

Sample	T_2 (ms) (raw)	r_2 (s-1) (raw)	T_1 (ms) (raw)	r_1 (s-1) raw	T_1 (ms) (simulated)	r_1 (s-1) (simulated)
CO1	88	11.35	619	1.62	701	1.43
CO2	109	9.21	933	1.07	984	1.02
CO3	122	8.22	1277	0.78	1376	0.73
CO4	127	7.89	1437	0.70	1461	0.68
CO5	129	7.74	1568	0.64	1677	0.60
Agarose	105	9.51	1592	0.63	2144	0.47

The underestimation of T_1 values is consistent, thus should not affect the relaxivity of the contrast agent obtained from the linear slope of the relaxation rates. To confirm this, the simulated and experimental r_1 relaxation rates were plotted against particle concentration to calculate the relaxivity of $CoFe_2O_4$@DMSA NPs. As shown in figure B.8, the experimental and simulated relaxivity of $CoFe_2O_4$@DMSA NPs were identical at 2.11 $mM^{-1}s^{-1}$, confirming that underestimation of T_1 does not affect the relaxivity of $CoFe_2O_4$@DMSA NPs in this study.

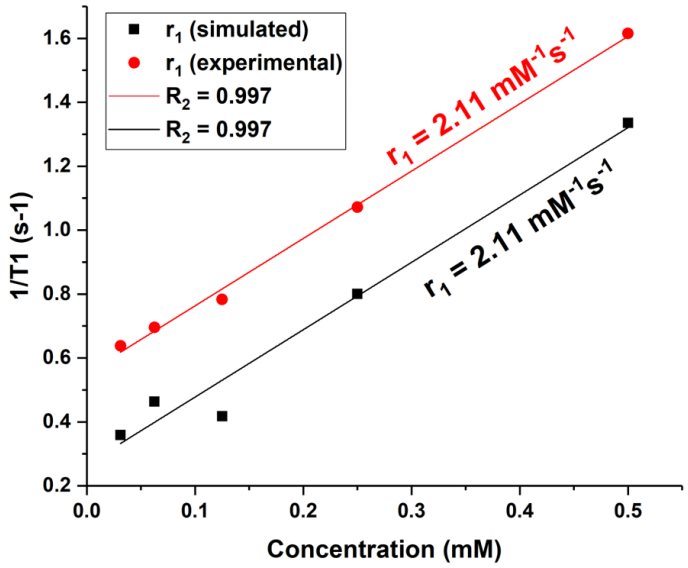


Figure B.8: Comparison of simulated and experimental relaxation rates of $CoFe_2O_4$@DMSA NPs at increasing concentrations. The simulated and experimental relaxivities, calculated from the linear slope of r_1, are in excellent agreement.

B.5 Bile-acid functionalisation: NMR studies to confirm synthesis of amino cholate

Cholic-acid-NHS ^{1}H-NMR (300 MHz, DMSO-d$_6$): δ = 0.61 (s,3H); 0.81 (s, 6H); 0.92-2.25 (bm, 23H), 2.64 (m, 4H), 3.61 (m, 1H); 4.02 (d, 1H); 4.13 (d, 1H); 4.32 (d, 1H) ppm. ^{13}C-NMR (75 MHz, DMSO-d$_6$): δ = 23.1 (CH); 23.3 (CH); 24.9 (CH); 25.9 (CH); 26.7 (CH); 27.7 (CH); 28.1 (CH); 29.0 (CH); 30.9 (CH); 31.1 (CH); 33.8 (CH); 34.9; 35.8; 40.6; 40.8; 41.9; 42.0; 46.6; 48.0; 66.7; (CO); 67.5 (CO); 71.5 (CO); 169.8 (COO); 170.7 (COO) ppm.

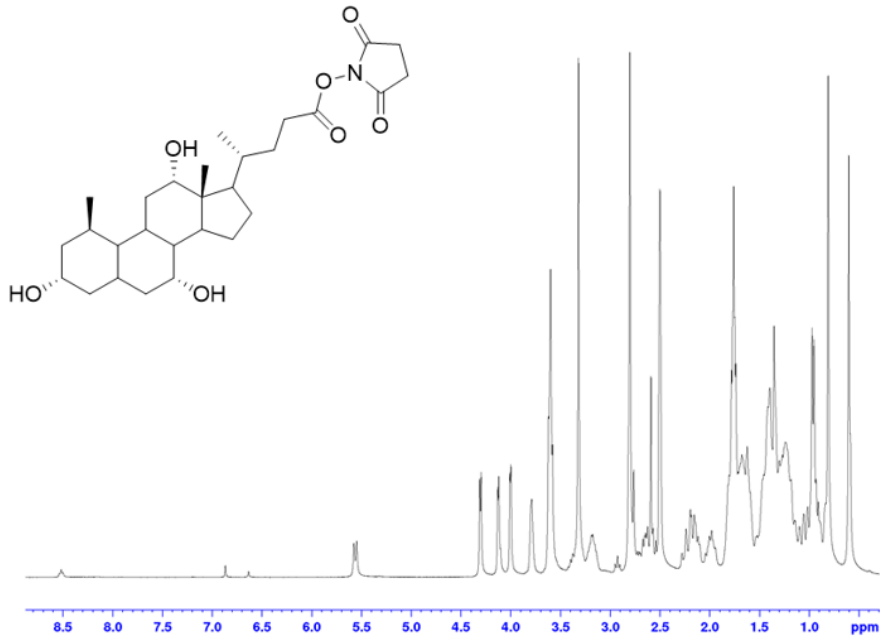


Figure B.9: ^{1}H-NMR spectrum (300 MHz) of cholic acid NHS in DMSO-d$_6$.

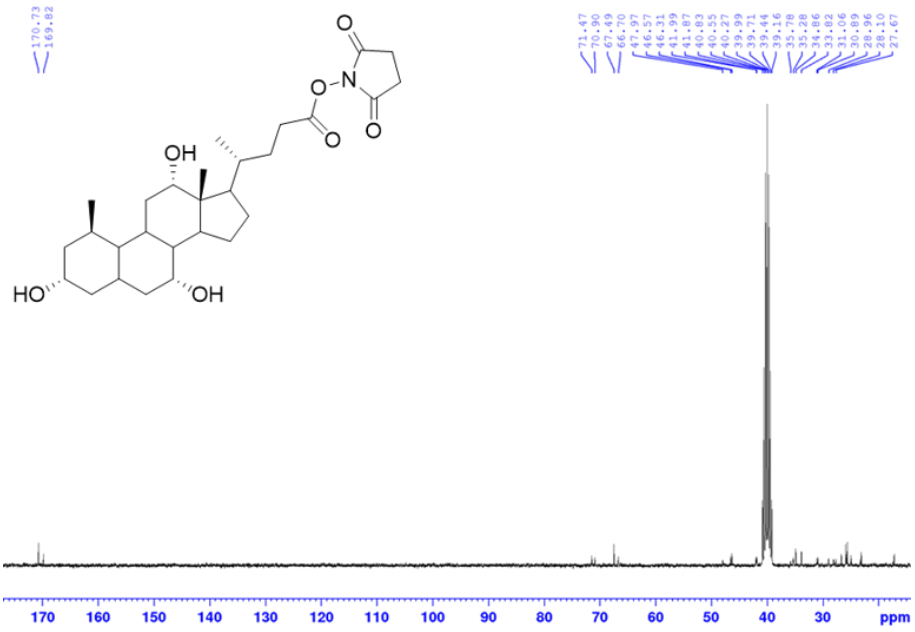


Figure B.10: ^{13}C-NMR spectrum (75 MHz) of cholic acid NHS in DMSO-d$_6$.

Cholate amide ^{1}H-NMR (300 MHz, $CDCl_3$): δ = 0.71 (s,3H); 0.85-2.20 (bm, 28H); 3.45 (m, 3H), 3.85 (d, 2H); 3.98 (d, 1H); 6.8 (s, 1H); 8.0 (2H) ppm. ^{13}C-NMR (75 MHz, CDCl3): δ = 22.6 (CH); 24.5 (CH); 25.6 (CH); 26.7 (CH); 28.4 (CH); 30.6 (CH); 34.7 (CH); 42.0 (CH); 46.6 (CH); 68.3 (CO); 169.2 (COO) ppm.

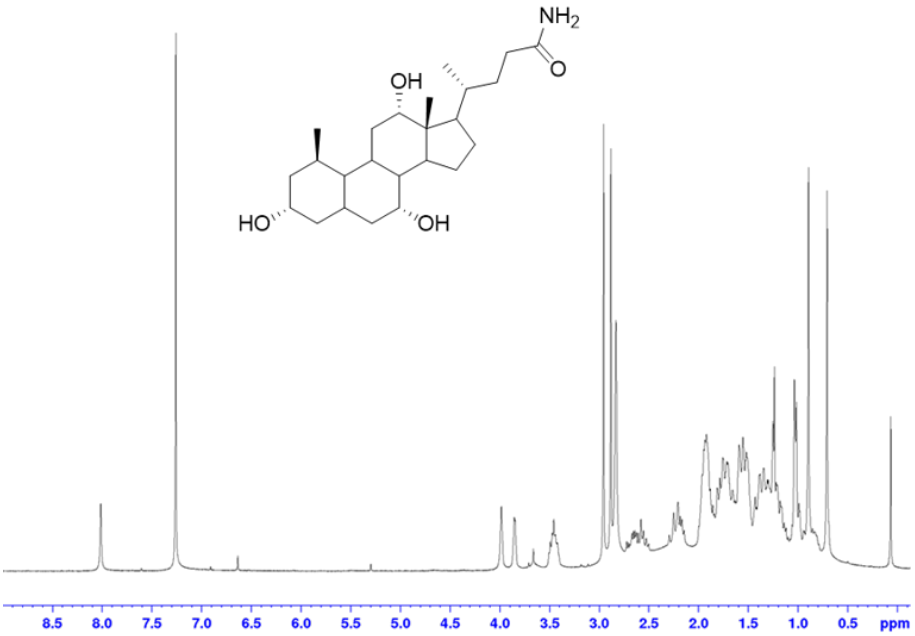


Figure B.11: ^{1}H-NMR spectrum (300 MHz) of cholate amide in DMSO-d$_6$.

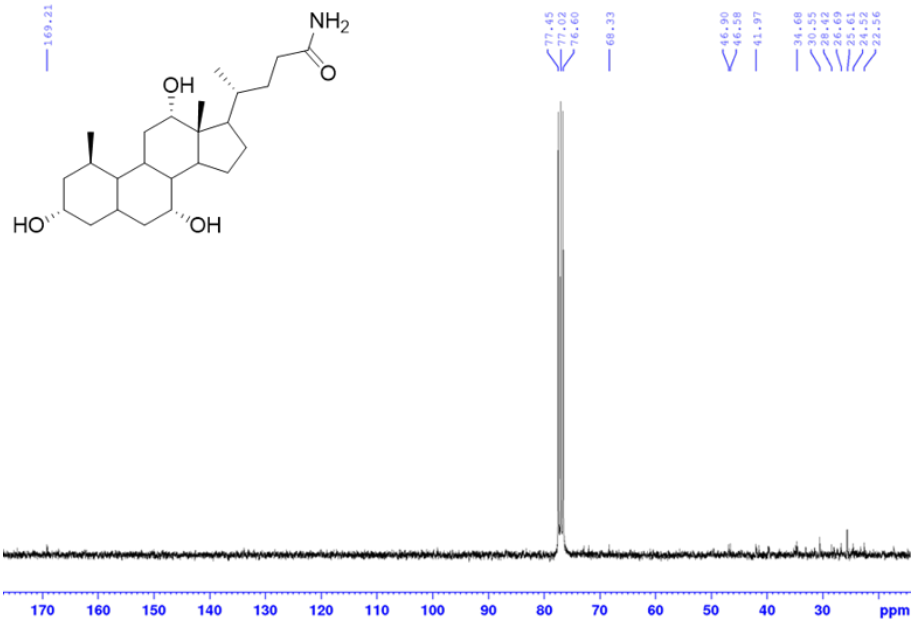


Figure B.12: ^{13}C-NMR spectrum (75 MHz) of cholate amide in DMSO-d_6.

Amino cholate ^{1}H-NMR (300 MHz; D2O): δ = 0.88-2.17 (bm, 33H); 2.51 (m, 2H); 3.11 (s, 1H); 3.62 (d, 2H); 3.95 (s, 1H) ppm.

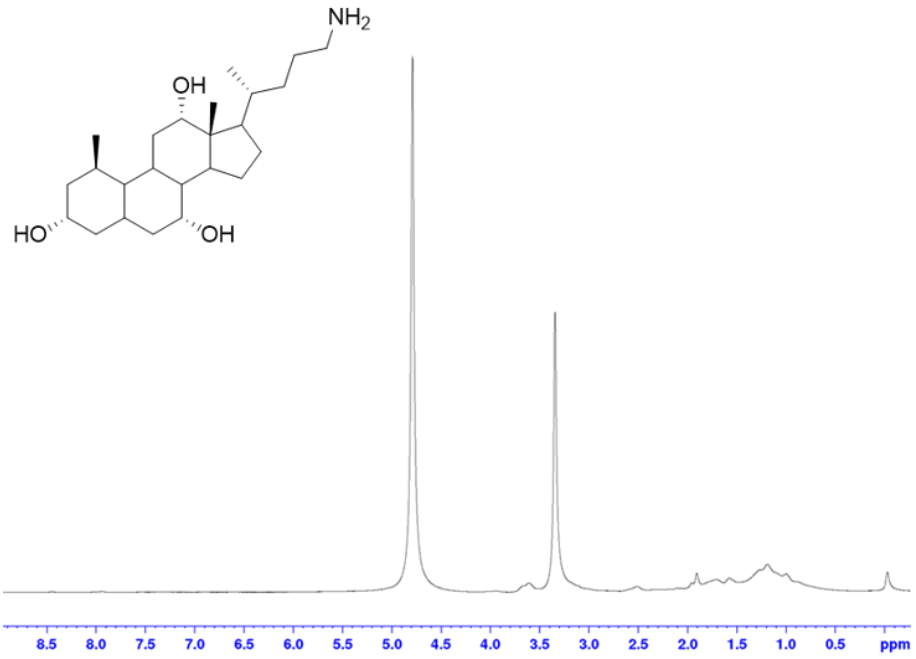


Figure B.13: ^{1}H-NMR spectrum (300 MHz) of amino cholate in D_2O.